REPORT DOCUMENTATION PAGE

Form Approved
OMB No 0704-0188

1. AGENCY USE ONLY (Leave blank)	2. REPORT DATE	3. REPORT TYPE AND DATES COVERED
	April 24, 1995	Final Report 7/20/91-3/19/95

4. TITLE AND SUBTITLE
Study of Photorefractive Fibers for Optical Interconnects, Switchings, Massive Memories, and Optical Properties

5. FUNDING NUMBERS
DAAL03-92-G-0328

6. AUTHOR(S)
Francis T.S. Yu

7. PERFORMING ORGANIZATION NAME(S) AND ADDRESS(ES)
Department of Electrical Engineering
The Pennsylvania State University
University Park, PA 16802

8. PERFORMING ORGANIZATION REPORT NUMBER
NA

9. SPONSORING/MONITORING AGENCY NAME(S) AND ADDRESS(ES)
U.S. Army Research Office
P. O. Box 12211
Research Triangle Park, NC 27709-2211

10. SPONSORING/MONITORING AGENCY REPORT NUMBER
ARO 30447.1-PH

11. SUPPLEMENTARY NOTES
The views, opinions and/or findings contained in this report are those of the author(s) and should not be construed as an official Department of the Army position, policy, or decision, unless so designated by other documentation.

12a. DISTRIBUTION/AVAILABILITY STATEMENT
Approved for public release; distribution unlimited.

12b. DISTRIBUTION CODE

13. ABSTRACT (Maximum 200 words)

The objective of this research is to study photorefractive (PR) fibers for optical interconnects, switchings, massive memories, and optical properties. The PR fibers can improve the electro-optic device technology, for which high capacity memories and interconnections can be developed. There are several reasons to select PR fibers over the bulk materials. It is more cost effective in terms of equivalent volume. It is much easier to grow single crystal fibers in long dimension (e.g., 5-10 cm). Because of long length, PR fiber holograms have very high angular and wavelength selectivities. We have, in this research demonstrated that a high capacity fiber-hologram memory can be developed using reflection-type holographic construction strategy. The important aspect of the specially doped Ce:Fe:$LiNbO_3$ fiber is that they have very high photosensitivities such that a low-power visible tunable laser can be used. We have also demonstrated numerous applications, e.g., tunable interconnection network, high density fiber hologram storage, as well as applied to correlators, neural networks and wavelet filtering.

14. SUBJECT TERMS	15. NUMBER OF PAGES
Single crystal photorefractive fibers, fiber holograms, specially doped fibers, application of PR fibers.	193
	16. PRICE CODE

17. SECURITY CLASSIFICATION OF REPORT	18. SECURITY CLASSIFICATION OF THIS PAGE	19. SECURITY CLASSIFICATION OF ABSTRACT	20. LIMITATION OF ABSTRACT
UNCLASSIFIED	UNCLASSIFIED	UNCLASSIFIED	UL

NSN 7540-01-280-5500

Standard Form 298 (Rev 2-89)
Prescribed by ANSI Std 239-18
298-102

30447-PH

FINAL REPORT

1. ARO PROPOSAL NUMBER: 30447-PH
2. PERIOD COVERED BY REPORT: 2 July 1992 - 19 March 1995
3. TITLE OF PROPOSAL: Study of Photorefractive Fibers for Optical Interconnects, Switchings, Massive Memories, and Optical Properties
4. CONTRACT OR GRANT NUMBER: DAAL03-92-G-0328
5. NAME OF INSTITUTION: The Pennsylvania State University
6. AUTHORS OF REPORT: Francis T.S. Yu

CONTENTS

7. LIST OF MANUSCRIPTS SUBMITTED OR PUBLISHED UNDER ARO SPONSORSHIP DURING THIS REPORTING PERIOD, INCLUDING JOURNAL REFERENCES:

S. Yin and F.T.S. Yu, "Specially Doped $LiNbO_3$ Crystal Holography Using a Visible-Light Low Power Laser Diode," IEEE Photonics Technology Letters, Vol. 5, pp. 581-582, May 1993.

F.T.S. Yu, S. Yin, and A. S. Bhalla, "Wavelength Multiplexed Holographic Construction Using a Ce:Fe: doped PR Fiber with a Tunable Visible-Light Laser Diode," IEEE Photonics Technology Letters, Vol. 5, pp. 1230-1233, October 1993.

F.T.S. Yu and S. Yin, "Applications of Photorefractive Crystals to Signal Processing," (Invited) International Journal of Optical Computing, Vol. 2, pp. 143-163, September 1993.

M. Wen, S. Yin, P. Purwosumarto and F.T.S. Yu, "Wavelet Matched Filtering using a Photorefractive Crystal," Optics Communications, Vol. 99, pp. 325-330, June 1993.

F.T.S. Yu, F. Zhao, H. Zhou and S. Yin, "Cross-Talk Noise in a Wavelength-Multiplexed Reflection-Type Photorefractive (PR) Fiber Hologram," Optics Letters Vol. 18, pp. 1849-1851, November 1993.

M. Wen, S. Yin and F.T.S. Yu, "Tunable Interconnection Network Using a Thick Photorefractive (PR) Crystal," Optics Communications, Vol. 99, pp. 325-330, June 1993.

F. Zhao, H. Zhou, S. Yin and F.T.S. Yu, "Wavelength-Multiplexed Holographic Storage by Using the Minimum Wavelength Channel Separation in a Photorefractive Crystal Fiber," to Optics Communications, Vol. 103, pp. 59-62, November 1993.

H. Zhou, F. Zhao and F.T.S. Yu, "Effects of Recording-Erasure Dynamics on Storage Capacity of a Wavelength-Multiplexed Reflection-Type Photorefractive Hologram," Applied Optics, Vol. 33, pp. 4339-4344, July 1994..

F.T.S. Yu and S. Yin, "Holographic Storage and Interconnection using a (Ce:Fe: Doped $LiNbO_3$) Photorefractive Crystal Fiber with a Tunable Visible-Light Diode Laser," Optical Memory and Neural Networks, Vol. 1, pp. 289-301, September 1993.

F.T.S. Yu, S. Yin and C. M. Uang, "A Content-Addressable Polychromatic Neural Net Using a Specially Doped $LiNbO_3$ Photorefractive Crystal," Optics Communications, Vol. 107, pp. 300-308, April 1994.

F.T.S. Yu (invited), "Application of Photorefractive Fiber Holograms to Interconnections, Switchings, and Massive Memories," Proceeding of International Conference on Holography, Correction Optics, and Recording Materials, SPIE Vol. 2108, Chernovtsy, Ukraine, May 10-14, 1993.

F.T.S. Yu and S. Yin (invited), "Holographic Storage and Interconnection Using a (Ce: Fe: Doped $LiNbO_3$) Photorefractive Crystal Fiber with a Tunable Visible-Light Diode Laser," in Photorefractive Materials, Effects, and Applications, Critical Review, edited by P. Yeh and C. Gu, SPIE, 1993.

F.T.S. Yu (invited), "Photorefractive Fiber Storage, Switching, Interconnects, and the Technological Challenges," Proceedings of the International Conference on Optical Information Processing, St. Petersburg, Russia, August 2-7, 1993.

F.T.S. Yu and S. Yin, "Specially Doped (Ce: Fe:) $LiNbO_3$ Based Crystal Holography," Proceedings of the International Conference on Optical Information Processing, St. Petersburg, Russia, August 2-7, 1993.

F.T.S. Yu and S. Yin, "Fiber Hologram Construction and Storage," Proceedings of World Optical Conference, Shanghai, China, August 30-September 3, 1993.

H. Zhou, F. Zhao and F.T.S. Yu, "Diffraction Properties of a Reflection-Type Photorefractive Hologram," Applied Optics, Vol. 33, pp. 4345-4352, July 1992.

D. Zhao, H. Zhou, F. Zhao and F.T.S. Yu, "Anisotropic Intrasignal Coupling in Photorefractive $LiNbO_3$," Microwave and Optical Technology Letters, Vol. 7, pp. 483-486, August 1994.

F.T.S. Yu, S. Yin, J. Zhang and R. Guo, "Application of Fiber Speckle Hologram to Fiber Sensing," Applied Optics, Vol. 33, pp. 5201-5202, August 1994.

F.T.S. Yu, J. Zhang and S. Yin, "Analysis of Fiber Specklegram Sensor (FSS) Using Mode-Coupling Theory," Applied Optics, Vol. 33, March 1995.

F.T.S. Yu, S. Yin and Z. H. Yang, "Thick Volume Photorefractive (PR) Crystal Wavelength-Multiplexed Reflection-Type Matched Filter," Optical Memory and Neural Networks, Vol. 3, pp. 207-215, May 1994.

F. Zhao, Z. Wu, F.T.S. Yu and D. K. McMillen, "Steady-State Nondegenerate Four-Wave Mixing in Photorefractive Ce:Fe:$LiNbO_3$," Applied Optics (in press).

F. Zhao, H. Zhou, Z. Wu, F.T.S. Yu and D. K. McMillen, "Temperature Dependency of Light-Induced Scattering and Noise Suppression in Ce:Fe:$LiNbO_3$ Photorefractive Crystal," Optical Engineering (in press).

H. Zhao, H. Zhou, Z. Wu, F.T.S. Yu, "Angular-Dependent Diffraction Efficiency in a Thick Photorefractive Hologram," Applied Optics, Vol. 34, pp. 1303-1309, March 1995.

F. Zhao, B. Yuan, H. Zhou, Z. Wu and F.T.S. Yu, "Photorefractive Enhancement Near 57°C, 70°C, and 110°C in Cerium-Fron-Doped Single Crystal Lithium Niobate," Optical Engineering (in press).

Z. Zhang, G. Lu and F.T.S. Yu, "Single Method for Measuring Phase Modulation in Liquid Crystal Televisions," Optical Engineering, Vol. 33, pp. 3018-3022, September 1994.

M. Lu, S. Yin, C. Chen, F.T.S. Yu, T. D. Hudson and D. K. McMillen, "Design of a Bipolar Composite Filter and its Optical Implementation," submitted to Optical Engineering.

S. Yin, G. Lu, J. Zhang, F.T.S. Yu and J. N. Mait, "A Kinoform Based Nipkow Disk for Confocal Microscope," Applied Optics (in press).

F.T.S. Yu, G. Lu, M. Lu and D. Zhao, "Application to Position Encoding to a Complex Joint Transform Correlator," Applied Optics, Vol. 34, pp. 1386-1388, March 1995.

F. Zhao, Z. Wu, F.T.S. Yu and D. K. McMillen, "Characterization of $LiNbO_3$ Materials: Singly-and-Doubly-Doped with Ce and Fe," Optical Memory and Neural Networks (in press).

D. McMillen, T. D. Hudson, F.T.S. Yu, J. Zhang, S. Yin and Z. Wu, "Anomalies of Photovoltaic Current in Ce: Fe: Doped $LiNbO_3$ Crystal at 55°C and 75°C temperature," Optical Engineering (in press).

S. Yin, M. Lu, C. Chen, F.T.S. Yu, T. D. Hudson and D. K. McMillen, "Design of a Bipolar Composite Filter Using a Simulated Annealing Algorithm," Optics Letters (in press).

F.T.S. Yu and S. Yin, "Bragg Diffraction Limited Photorefractive (PR) Based Correlators," (invited), Optical Engineering (in press).

F.T.S. Yu and S. Yin, "Photorefractive Fiber Holograms," (invited) submitted to Asian Journal of Physics.

F.T.S. Yu, S. Yin and Z. Yang, "Thick Volume Photorefractive (PR) Crystal Wavelength-Multiplexed Reflection-Type Matched Filter," Proceedings of SPIE on Optical Pattern Recognition V, Vol. 2237, April 1994.

F.T.S. Yu (invited), "Photorefractive Fiber Storage, Switching, Interconnects, and the Technical Challenges," Proceeding of ICO Frontiers in Information Optics, Kyoto, Japan, April 3-8, 1994.

F.T.S. Yu, A. S. Bhalla, S. Yin, F. Zhao, Z. Wu and D. M. Salerno, "Ce:Fe:$LiNbO_3$ Photorefractive Crystal: Material Properties and Applications, Proceeding of the Ninth IEEE International Symposium on the Applications of Ferroelectrics, August 7-10, 1994.

F.T.S. Yu, "Fiber Specklegram Sensors," Proceeding of the Second International Conference on Optoelectronics Science and Engineering '94. SPIE Vol. 2321, August 9-14, 1994.

8. SCIENTIFIC PERSONNEL SUPPORTED BY THIS PROJECT AND DEGREES AWARDED DURING THIS REPORTING PERIOD:

8.1 Scientific Personnel

F.T.S. Yu	- Principal Investigator
A. S. Bhalla	- Research Scientist
A. Mayers	- Research Assistant
Y. Yin	- Research Assistant
F. Zhao	- Research Assistant
M. Wen	- Research Assistant
Brett Guenther	- Research Assistant
W. Reeser	- Research Assistant
H. Zhou	- Research Assistant
P. Purwosumarto	- Research Assistant
J. P. Newman	- Research Assistant
A. V. Petrov	- Research Assistant
J. Zhang	- Research Assistant
M. Biao	- Research Assistant

8.2 Degrees Awarded

"Submicron Displacement Sensing Using Inner-Product Multimode Fiber Speckle Fields, "Meiyuan Wen, M.S. Degree, April 1993.

"Architecture and Design of a Polychromatic Optical Neural Network," Wade H. Reeser, M.S. Degree, completed December 1993.

"Optical Switching using a Fiber Speckle Hologram," Sumati Rajan, M.S. Degree, completed October 1993.

"A Simple Method of Measuring the Phase Modulating Property of LCTVs," Zheng Zhang, M.S. Degree, completed November 1993.

"Investigation of a Ce:Fe: Doped $LiNbO_3$ Photorefractive Crystal Hologram and its Applications to Optical Signal Processing," Shizhuo Yin, Ph.D. Degree, completed December 1993.

"Study of the Gray Scale, Polychromatic, Distortion Invariant Neural Networks using the IPA Model," Chii-Maw Uang, Ph.D. Degree, completed December 1993.

"Electro-Optic Amplitude Modulation Through A $LiNbO_3$ Crystal," Bruce H. Shultz, Jr., B.S. degree, April 1994.

"Optical Neural Networks: The Interpattern Association Model," Aurélia Secroun, M.S. degree, June 1994.

"Design and Fabrication of a Compact Electro-Optic Processing System," Andrew J. Milne, M.S. degree, December 1994.

"Alternative Approach to Adaptive RF Natch Filter using Photorefractive Two-Beam Coupling," Jeffery P. Newman, M.S. Degree, April 1995.

"Diffraction Properties of a Volume Photorefractive Hologram," Hanying Zhou, Ph.D. degree, February 1995.

"An Investigation of the Specially Doped Ce:Fe: $LiNbO_3$ Photorefractive Crystals: Optical Properties and Applications," Feng Zhao, Ph.D. degree, February 1995.

"Fiber Specklegram Sensing Using Hybrid Optical Information Processors," Kun Pan, Ph.D. degree, February 1995.

9. BRIEF OUTLINE OF RESEARCH FINDINGS

The aim of this research program is to investigate the applications of the photorefractive fibers to optical interconnections, Electro-Optic fiber switches, Large capacity fiber storage, and the optical properties of these fibers.

Photonics-based technology is expected to significantly influence the fields of communication, information processing, and computing. Photorefractive materials are considered important for light beam manipulation, control, and information storage in photonics technology. In recent years, photorefractive materials have been studied for applications to optical interconnections, photonic switching, real-time optical correlation, optical novelty filter, data storage, associative memory, spatial light modulator, and many others. These investigations show that photorefractive materials are promising for these applications. However, most of these investigations have shown that bulk materials pose significant limitations for at least three reasons: A high energy density of write-in light is required to achieve a required refractive index change, it is difficult to grow crystals larger than 1 cm^3, and a high applied voltage is needed to control electro-optic properties of the crystal. These drawbacks can be overcome by using a more flexible single crystal photorefractive fibers as will be discribed in the following:

Photorefractive fibers have the unique feature of combining the properties of both photorefractive materials and optical fibers for which the limitations of bulk materials as mentioned above can be alleviated. Since dynamic holograms can be written inside the photorefractive fibers, these fiber hologram images can be optically addressed. Hence, different kinds of holographic optical elements can be formed with the photorefractive fibers.

In addition, due to the longitudinal dimension of the fibers, the angular and wavelength multiplexing capabilities of the fiber holograms can be made extremely high. These will increase the storage capacity of the photorefractive fibers.

In this period, from July 20, 1992 to March 19, 1995, we have accomplished several major tasks on the research of the photorefractive fibers from the material aspects, physical properties as well as applications. Several of the findings have been subsequently published in open literatures. Sample copies of these published papers are included in the final technical, by which we shall provide a brief overview of our research work done. Some of the accomplishments will be highlighted and list the published papers are cited in the appendices.

9.1 Fiber Growth with Laser Heated Pedestal Growth System (Appendix 10.1)

The Laser Heated Pedestal Growth (LHPG) technique is a relatively new crystal fiber growth technology that can fabricate 50-1000 μm diameter and up to 5-10 cm long fibers. The groups at the Stanford University and The Pennsylvania State University have independently grown single crystal fibers by using this technique. The major advantages of growing single crystal fiber using the LHPG system are:

[1] It does not require any holding device (e.g., a crucible) so that the contamination from the holder can be avoided.

[2] Some growing limitations, such as the melting point, shape, etc. can be alleviated.

[3] Since the LHPG system used CO_2 laser as the heating source, the growing process is much easier to control. For example, the laser beam has an annular

taper form, such that the crystal fiber can be grown in the vertical direction, which is crucial for fiber growing.

[4] The LHPG technique can also be used in a variety of applications, for example, as applied to high temperature superconductor wire-rod and other novel devices.

A schematic diagram describing this system is shown in Fig. 1(a), in which a preformed PR crystal about 0.9 x 0.9 mm Ce: Fe: doped $LiNbO_3$ is placed in a holder that maintains at a precise vertical orientation. A 50 Watt CO_2 laser is brought to focus by first forming an annular beam with a reflaxicon. Then by steering the annular beam with a 45° flat mirror, a highly intensive focusing beam can be formed on the preformed PR rod using a concave parabolic mirror, as shown in Fig. 1(b). When a seed rod is brought in contact with the molten tip of the preform, the fiber growth can be initiated by slowly pulling the seed rod upward with a computer control driver, as illustrated in Fig. 1(c). Thus we see that a single crystal fiber can be drawn with the LHPG system [1].

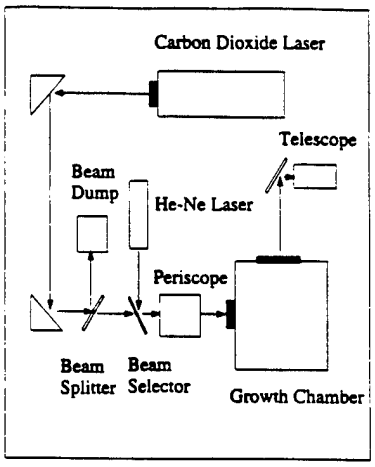

(a)

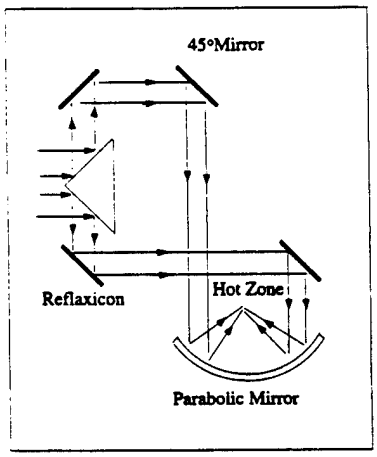

(b)

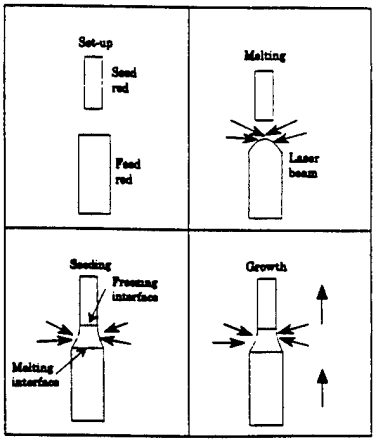

(c)

Fig. 1 The laser Heated Pedestal Growth (LHPG) System.

(a) Schematic diagram.

(b) The Growth chamber.

(c) Crystal fiber growth.

9.2 Specially Doped PR Materials (Appendix 10.2)

One of the major impediments prevents the wide spread of applications must be the high power requirement for the photorefractive fibers. For example, high power Ar^+ and He-Ne lasers are usually required for the conventional PR holographic process, which makes the processing system very cumbersome and expensive to operate. The features of the commercially available laser diode must be small size, easy to operate, and low cost. It would be for practical advantages, if high-photosensitive PR fibers are made available. In this period of research we have acquired pieces of specially doped Ce:Fe:$LiNbO_3$ PR crystals. We have found these crystals have a wide spectral response that covers the whole visible spectrum region (i.e., 400 nm to 700 nm). These crystals have a higher photo-sensitivity, as compared with the conventional $LiNbO_3$ photorefractive crystals. For example, using λ = 633 nm, the photo-sensitivity of these crystals can be as high as 10 mJ/cm^2, with a diffraction efficiency of about 1%. As in contrast with the conventional $LiNbO_3$ crystal, these crystals require several hundred mJ/cm^2 (at λ = 633 nm). If λ = 670 nm wavelength is used (e.g., typical wavelength for commercially available visible-light laser diodes), the sensitivity of these specially doped crystal can be as high as 15 mJ/cm^2 (with a diffraction efficiency of about 1%). Moreover, the mixed doping components contain Fe and Ce, in which the doping levels are about 500 ppm and 300ppm, respectively and the orientation of these crystals are z-cut.

We have used these PR crystals setup experiments to record reflection-type crystal holograms, using a commercially available low power diode laser. Excellent hologram images have obtained. To demonstrate the spectral response of these crystals, a green and

blue wavelength multiplexing crystal holograms have been constructed. To illustrate the low-power requirements, the exposure energy was adjusted to about 2 mJ/cm^2. The color hologram images obtained with the green and the red light have been reconstructed, by which the wide spectral response of the specially doped crystal are demonstrated. The detail of these research findings have been published in the IEEE Photonics Technology Letters [2].

9.3 Wavelength Selectivity (Appendix 10.3)

We have, in this period of research analyzed the wavelength selectivities of photorefractive volume holograms based on the coupled wave theory. We have shown that the wavelength multiplexed reflection-type hologram has a uniform selectivity than the angular multiplexed hologram and it is more sensitive as compared with the transmission-type hologram. Thus, the choice of using wavelength multiplexing reflection-type crystal fiber holograms would be optimum for data storage. We have experimentally demonstrated, the wavelength multiplexing for a PR fiber hologram, in which we have used a specially doped Ce:Fe:$LiNbO_3$ crystal fiber, having a diameter-to-length ratio about 1:10. A tunable laser diode (manufactured by New Focus Inc., model 6102) of wavelength λ = 670nm, output power ~ 5mW, and tuning range 12nm was used as the light source. The PR crystal fiber is about 7mm in length with a diameter of 700μm, at a-axis orientation. More than 100 wavelength-multiplexed holograms have been experimentally recorded with a diffraction efficiency of about 1%. The report of the wavelength multiplexing PR fiber crystal holography has been published in IEEE Photonics Technology Letters [3]. The same effects on PR crystal was also published in Optics Communications [4].

9.4 Channel Separation Hologram (Appendix 10.4)

The storage capacity of an angularly multiplexed bulk holographic memory is known to be limited by the total angular tuning range (which is about 4π solid angle), and the minimum channel separation. In a PR fiber, the angular tuning range is also limited by its small numerical aperture. However, in principle, there exists no upper tuning-range limit for the wavelength multiplexing, as in contrast with the angular multiplexing. Nevertheless, the practical limit must be the spectral photo-sensitivity of the PR material and of course the available tuning range of the light source. Thus, to achieve a larger storage capacity, the minimum wavelength channel separation should be fully utilized. Therefore one of our objectives is to investigate the minimum wavelength channel separation in a PR fiber. Thus in this period of research we have investigated the spectral bandwidth of the holographic channel of a holographic storage by using wavelength multiplexing/demultiplexing in a PR crystal fiber. The effect of the spectral width of the light source on the minimum channel separation and the cross-talk noise between the adjacent channels have been analyzed. Experimental results show the feasibility of using the minimum wavelength separation in wavelength multiplexed holographic storage in a PR fiber, for which a narrow linewidth (10 MHz) tunable diode laser is needed. When the minimum wavelength channel separation (15 GHz) is used, we have also shown that there is a $\sim 5\%$ cross-talk between adjacent channels. Detail of this analysis have been published in the Optics Communications [5].

9.5 Cross-Talk Noise (Appendix 10.5)

The upper bond of storage capacity of a thick-emulsion hologram was estimated by Van Heerden [6] to be equal to V/λ^3 (where V is the volume of the recording material and λ

is the wavelength), which is as high as 10^{12} bits. Recent advances in photorefractive (PR) materials have been provided a promising device for optical storage by which a massive holographic memory may be realized. However, there are some practical limiting factors hindering the achievement of this goal. For instance, One of the limiting factors is the cross-talk effect among the multiplexed channels. In other words, for wavelength-multiplexed holograms there are always some wavelength-spread intrusions from adjacent multiplexed channels that limit the storage capacity. It must be noted that the cross-talk noise for angular-multiplexed holograms was studied previously. In terms of wavelength-mutliplexed holograms, the effect that is due to wavelength spread was evaluated recently by Gu et al. [7] in a study that was based on the infinitesimal linewidth of the reading beam. We have , however, evaluated the cross-talk effect that is due to wavelength spread among the multiplexed channels in the wavelength-multiplexed PR fiber holograms. Since the wavelength selectivity is rather uniform and more efficient for the reflection-type hologram, we had focused our discussion primarily on reflection-type PR fiber holograms.

Since the cross-talk effect is dependent on the spectral width of the light source in a wavelength-multiplexed reflection-type PR fiber hologram. The spectral bandwith is a function of the recording wavelength, the refractive index, and the length of the PR fiber. The SNR_{CT} and cross-talk-limited storage capacity are also discussed. Compared with the results of Gu et al. [7], the SNR_{CT} described here differs significantly as the linewidth of the light source is considered. We have found that the SNR_{CT} is sensitive to the channel separation and to the spectral width of the light source. If the minimum channel separation is used, the SNR_{CT} has been shown to be uniformly distributed in the stored holographic

images. Using the minimum channel separation, we have estimated that the storage capacity of a wavelength-multiplexed PR fiber hologram can be as high as 1000 pages of holographic data, with a read-out SNR_{CT} ranging from 10 to 20 dB. The details of this analysis can be found in a paper published by Yu et al. in Optics Letters [8].

9.6 Recording-Erasure Dynamics (Appendix 10.6)

The use of the coupled-recording-wave approach is necessary in order to give an accurate estimation on the storage capacity of a multiplexed PR fiber hologram. In fact, all attempts to compensate the erasure effect and to give rise to a maximized storage capacity with detectable diffraction efficiencies yield similar recording schedules upon which the first tens of multiplexed holograms should be exposed at much longer times as compared with the rest. Consequently, the assumption of small index modulation for the first tens of holograms is no longer satisfied during recordings, and the beam coupling and the energy transferring that are due to the phase shift of the grating formed in the PR materials occurs, resulting in a nonuniform index modulation along the crystal thickness. As we know, Kogelnik's theory for volume holograms, which is based on a uniform refractive-index modulation ratio assumption, is not valid for the case of nonuniform index modulation ratios. We have, in this period of research applied the coupled-recording-wave approach to investigate the effects of recording-erasure dynamics on the storage capcity for this case. As energy transfer depends on the relative sign of the writing wave vectors, the behavior of a reflection-type hologram would be expected to be different from its transmission counterpart. We have derived a set of nonlinear coupled-wave equations that govern the holographic recording and reconstruction dynamics. A closed-form expression for the diffraction efficiency for on-

Bragg incidence is then formulated. The closed-form expression predicts a lower achievable diffraction efficiency for PR materials, as compared with Kogelnik's formula for non-PR materials. The dependence of the equalized diffraction efficiency on the number of multiplexed holograms have been analyzed. The results have shown that the storage capacity of the reflection-type hologram is roughly of the same order of magnitude as the transmission type but higher than the previous predictions obtained by an uncoupled-recording-wave theory. A paper reporting this analysis has been published in Applied Optics [9].

9.7 Diffraction Properties (Appendix 10.7)

Thick PR holograms have potential for widespread application in many areas, such as massive storage, optical interconnections, and switchings. However, to our knowledge, the diffraction properties have not yet been fully investigated, and so far have been described mostly by Kogelnik's theory, which was originally derived for non-PR holograms using an uncoupled-recording-wave approach. As applied to PR holograms, the theory shows its limitations and discrepancies when the index perturbation (i.e., coupling strength) is large. For example, the relative cross-talk noise obtained from the experiment reported by Rakuljic et al. [10] is much lower than in the analysis. The discrepancy is primarily caused by the beam coupling and the irreversible energy transfer affected by the phase shift of gratings formed in PR materials. The irreversible gratings formed in PR materials. The irreversible energy transfer results in a nonuniform index modulation ratio over the crystal thickness during recording, which affects the readout properties during reconstruction. In contrast, Kogelnik's theory begins with the assumption of a uniform refractive-index modulation ratio. In this period of research, we have studied the diffraction properties of a reflection PR

hologram using a coupled-recording-wave approach. A closed-form expression for the diffraction efficiency as a function of wavelength and angular deviation, as well as of temporal variation, is obtained. The new formula predicts a lower achievable diffraction efficiency and higher wavelength and angular sensitivities than Kogelnik's formula for non-PR holograms. This result offers an explanation for the apodization phenomenon previously found by Rakuljic et al. [9]. A paper reporting this calculation has been published in Applied Optics [11].

9.8 Intrasignal Couplings (Appendix 10.8)

PR materials have shown a wide range of applications such as large-capacity holographic memory, massive interconnection, spatial mode conversion, etc. These applications, however, usually involve intrasignal coupling as light beams propagate through a PR crystal. The intrasignal coupling problem has been addressed for PR crystals such as SBN or $BaTiO_3$ [12, 13], where the coupling was found symmetric with respect to the c axis of the crystal. The $LiNbO_3$ crystal is widely used, so this article will examine the intrasignal coupling in this type of crystal, which must be orientation dependent due to its anisotropic nature in terms of the effective electro-optic coefficient. Analytical solutions for one-dimensional intrasignal coupling are derived for a-axis and b-axis orientations, which enables us to estimate the maximum beam field angle and the maximum crystal thickness for a given intensity distortion due to the coupling. Thus in this period of research, we have investigated the intrasignal coupling in $LiNbO_3$. It has been shown that for this crystal, which has a point group symmetry of 3m, the anisotropy nature of the effective electro-optic coefficient results in an orientation-dependent intrasignal coupling. Analytical solutions for one-dimensional

intrasignal coupling are derived for the crystal of the a-axis and b-axis orientations. For the a-axis oriented crystal, the intrasignal coupling is symmetric with respect to the c-axis of the crystal. On the other hand, if the crystal is b-axis oriented, the coupling is asymmetric. Quantitatively, the relative intensity change in the b-axis oriented crystal would be much larger in the a-axis oriented crystal. Thus, for one-dimensional applications where intrasignal coupling is unwanted, case A is preferable due to less intrasignal coupling. For two-dimensional applications, however, the intrasignal coupling is generally orientation-dependent with a mixed coupling behavior of both case A and case B, and we should be cautious of the anistropy coupling behavior of $LiNbO_3$ in any event. Nevertheless, it is also worth noting that, in principle, the relative intensity distortion due to the intrasignal coupling can be compensated by using a phase-conjugation mirror (PCM) as pointed by Ito, Kitayama, and Oguri [14]. However, using a PCM would complicate the system, reduce the overall light efficiency, and the intrasignal coupling in the PCM is unavoidable. A paper reporting our studies has been published in Microwave and Optics Technology Letters [15].

9.9 Tunable Interconnection Network (Appendix 10.9)

Optical interconnections offer the advantage of transmitting a wide-band ultrahigh-frequency signal with high flexibility and negligible cross talk. Reconfigurable optical interconnects using photorefractive (PR) materials have been recently proposed by several investigators. PR materials offer higher diffraction efficiency and large storage capacity for massive interconnection networks. Because using wavelength multiplexing holograms in a thick recording material yields minimum cross talk as compared with the angular multiplexing technique, the interest in wavelength multiplexing in PR crystals has been

renewed. In this period of research, we have proposed an N x N interconnection network using a PR crystal with an array of tunable diode laser. We have shown that by using a wavelength multiplexing technique, an N x N interconnection network can be realized by using N multiplexed holograms, instead of N^2 holograms if the angular multiplexing scheme is used. In other words, by using an equal-volume PR crystal with the same tuning range of the laser diode, the wavelength multiplexing interconnection capacity would be N times larger than the angular multiplexing hologram. One of the obvious advantages of using an array of the tunable diode lasers is that the interconnection network can be reconfigured in the real-time mode. The rate of reconfiguration would be primarily imposed by the time response of the PR crystal. A paper of reporting this work has been published in Microwave and Optics Technology Letters [16].

9.10 Ce:Fe:$LiNbO_3$ Materials (Appendix 10.10)

Photorefractive lithium niobate ($LiNbO_3$) based materials have received broad promising applications in recent years, such as optical signal processing, random-access memories, large capacity interconnections, switching, etc. In these applications, high PR sensitivity and low scattering noise materials are needed. It is well-known that these PR properties are influenced by doping, annealing, and other crystalline processes. For example, the photo-induced charge transport process in $LiNbO_3$ can be enhanced by transmission-metal-dopants in different valence states. Fe, Cu, Cr, Mn, Ce, etc. dopants have been used to improve the PR properties of lithium niobate based materials. However, based on the approach by Yeh [17], the PR response time of a $LiNbO_3$ based material is in the order of a few seconds, which is much slower than the actual limit, which is in the order

of milliseconds. On the other hand, light-induced scattering noise (e.g., initiated by crystalline imperfections and non-uniform doping) through high (PR) gain amplification would affect the signal-to-noise ratio (SNR) of the material. Therefore to broaden the application of the $LiNbO_3$ based materials. PR sensitivity should be improved and scattering noise has to be minimized.

Both bulk and single crystal fiber $LiNbO_3$ based materials doped with Ce, Fe and Ce:Fe have been grown in the Material Research Laboratory (MRL) at the Pennsylvania State University, in which the conventional Czochralski technique has been used to grow the bulk crystals, and the Laser Heated Pedestal Growth (LHPG) technique is used to fabricate the single crystal fibers. Basically, this period of research, we have looked at a specially doped $LiNbO_3$ crystal (both bulk and fiber) and the PR effect due to dopants. We have found that double-doped Ce:Fe:$LiNbO_3$ crystal exhibits higher PR sensitivity, larger dynamic range, wider spectral bandwidth, and lower scattering noise, for which the crystal (bulk and fiber) would offer a variety of promising applications. In this study, we have rfound several anomalous PR sensitivities in the specially doped material, which occur at 57°C, 70°C and 110°C crystal temperatures. These anomalies are primarily due to the possible structural phase transitions of the crystal.

9.11 Steady State Nondegeneration (Appendix 10.11)

Among the methods of producing a phase-conjugate wave, four-wave mixing in a PR material is the most common technique since it requires a lower power source than other methods. Most of the work on four-wave mixing in photorefractive media has focused on the degenerate case, in which the phase conjugate wave has the same wavelength as all other

mixing beams. A frequency-varied phase conjugate wave (FVCW) is required for high capacity filter synthesis (such as wavelength-multiplexed filters). For FBCW, the phase conjugate wave is derived from a different wavelength than the input writing beam. A transient FVCW was generated by way of nondegenerate four-wave mixing (NFWM) in an Fe doped $LiNbO_3$ crystal, but a steady-state conjugate wave intensity was difficult to obtain due to the transient energy transfer effect and light-induced scattering. However, at a higher temperature, the thermally activated ions within the PR crystal can neutralize the electronic gratings, which reduces the light-induced scattering effect in the crystal. It is therefore apparent that an efficient steady-state nondegenerate phase-conjugation can be obtained by operating the PR crystal at a higher temperature. In this period of research we have investigated the temperature dependency of steady-state FVCW generation with a specially doped Ce:Fe:$LiNbO_3$ PR crystal. Our study shows evicence and an explanation of the strong temperature dependence of the NFWM in a specially doped Ce:Fe:$LiNbO_3$ PR crystal. We have found that an optimum steady-state FVCW output occurs at 120°C, which is attributed to the reduction of light-induced scattering due to neutralization of the electronic space charge field by thermally activated ions. The reduction in scattering allows more energy to go into the FVCW. We have also shown that a degenerate phase-conjugate wave is simultaneously generated at the higher temperature (e.g., 120°C). We further notice that there are potential uses of NFWM in specially doped Ce:Fe:$LiNbO_3$ PR crystals at an elevated temperature. For example, it can be used for wavefront correction, tunable complex spatial filtering, and others. A paper reporting these findings has been submitted to Optical Engineering for Publication [18].

9.12 Anomalies Photovoltaic Effect (Appendix 10.12)

To show the anomalies photovoltaic current, experiments are conducted in which an Ar+ laser is used to illuminate the crystal along the a-axis of the crystal. The photovoltaic current is measured by using a low-noise current pre-amplifier with an x-y recorder. Since the photovoltaic current from the crystal is in the order of a few pA, a copper chamber is used to isolate the specimen from external interference as shown in the figure. To vary the crystal temperature, an electric oven is used within the isolating chamber. The photovoltaic current also depends on its previous illumination history, we have found that a negative photoconductivity can be measured if the crystal had been long exposed to the laser light. When the crystal is heated to about 250°C for about 30 minutes, it can erase the previous influences due to laser illumination. The photovoltaic currents from room temperature (30°C) to 300°C are measured, in which we see that two anomalies peak currents occurred at 55°C and at 75°C. Although the photocurrent shows anomalies, the absorption of the crystal doesn't change with temperature. The lack of change indicates that the increase in photovoltaic current is not due to the increase of absorption, but rather there may be structural changes at anomalous temperatures.

When the crystal is heated above 180°C, the photovoltaic current increases very rapidly. However, the absorption change of the crystal is negligibly small. We believe that the rapid increase of photovoltaic current is primarily due to the detrapping of electrons in the crystal. In other words, when the crystal is illuminated by the laser, electrons in Fe^{2+} ions are excited into the conduction band, and then trapped by Fe^{3+} ions. As the temperature increases above 180°C, the electrons are detrapped from the recombination

center that causes the rise in photocurrent. Note that rapid increase in photovoltaic current at higher temperatures would cause the erasure of photorefractive grating. A paper reporting the anomalies of the photo-voltaic current is being submitted to Optical Engineering for publication [19].

9.13 Temperature Dependent Light-Induced Scattering (Appendix 10.13)

Light-induced scattering (beam-fanning) is a well-known photorefractive phenomena in which a coherent laser beam is scattered asymmetrically as it passes through a PR crystal. A typical scattering pattern in a $LiNbO_3$ crystal with an extraordinary polarization laser beam can be obtained. However, the light-induced scattering can be useful, for example, in self-pumped phase conjugators, photorefractive oscillators, optical limiting, etc., where a strong and fast light-induced scattering is desirable. However, it is an unwanted side-effect in many other cases such as image amplification, volume holographic storage, and multiplexed filter synthesis, where the scattering not only causes energy loss in the main beam (signal beam), but also contributes to noise, which results in a poor signal-to-noise ratio (SNR). Therefore, minimizing the light-induced scattering is an important issue for these applications. In this period of research, we have investigated the temperature dependent light-induced scattering in $LiNbO_3$. The scattering noise in a signal beam case has been effectively reduced by increaseing the temperature. The signal-to-noise ratio in a two-wave-mixing case is examined for different temperatures. The results suggest a new noise suppression technique by raising the crystal temperature, which is important in applications such as image amplification, holographic memory, and multiplexed filter synthesis. A paper reporting these findings will be published in Optical Engineering.

9.14 Bragg Diffraction Limited Correlators (Appendix 10.14)

In recent years, the use of photorefractive (PR) crystals to synthesize large capacity spatial filters has played a crucial role in the development of real-time correlators. The salient features of using the thick PR materials for the matched filter implementation must be the large information capacity, the real-time addressability, the high diffraction efficiency, and the high angular and wavelength selectivities. However, the thick PR crystals also impose the Bragg diffraction limitation, which reduces the shift-invariant capability of a PR based correlator. We have, in this period, investigated the Bragg diffraction limitation in a thick PR matched filter. The influences of Bragg diffraction on the angular and the wavelength selectivities are provided, in which we have shown that the reflection-type wavelength-multiplexed matched filter would be the best choice. Comparison among the thick PR crystal based correlators, we have shown that the reflection-type PR based correlator performs the best in terms of shift-tolerance among these three correlators. A detailed discussion of the Bragg limitation, as applied to various types of optical correlators in paper, which is currently submitted for publication [21].

9.15 As Applied to Wavelet Filtering (Appendix 10.15)

We have in this period of research applied wavelet transform with PP crystal matched filtering. Since the PR crystal is capable of storing a large number of wavelength multiplexed filters, the proposed system provides a large capacity identification in real time mode. Wavelet transform (WT) analysis is a viable alternative to Fourier transform (FT) analysis for pattern recognition. For instance, WT was utilized for multiresolution image analysis and several optical implementations of WT have been reported. In our application

of PR material, we have shown that the WMF performs better than the conventional matched filter. Since the performance of the wavelet matched filtering is affected by the dilation of the analyzing wavelet, an optimum dilation of the analyzing wavelet function can be found, which depends upon the feature of the input signal. The major advantage of the proposed system is that a large number of WMFs can be stored in a PR crystal, and therefore, the correlations of an input signal with respect to all the stored WMF's can be implemented in real time. A paper reporting these findings has been published in Optics Communications [22].

9.16 Application to Filter Sensors (Appendix 10.16)

Fiber-optic sensing has been shown to be one of the more important sensing technologies in recent years. A new type of fiber sensor called the fiber specklegram sensor (FSS) was proposed recently [23,24]. In other words, by taking advantage of the sensitivity of the complex speckle field that exits from a multimode fiber, a highly sensitive FSS can be developed. In previous work, we have proposed a multimode fiber-sensing system using photorefractive bulk crystal to construct a fiber-speckle hologram. However, using the bulk material for construction of the fiber-speckle hologram has some practical limitations: First, the physical size of the photorefractive (PR) crystal usually makes it awkward and inefficient for coupling with the sensing fiber. Second, the separation between the sensing fiber and the crystal hologram is vulnerable to misalignment and environmental changes. Third, bulk crystal is more expensive compared with equivalent-length PR fiber. Fourth, the large dimension of the buld material makes the fiber specklegram sensing system rather large, which limits its practical application.

To alleviate these limitations, we have used a FSS with a PR fiber. PR FSS offers the advantage of higher sensitivity, compact size, direct-coupling architecture, and more robustness during environmental changes. Because of the simplicity of the PR FSS system and its economical operation, we expect the proposed PR FSS to have widespread practical applications, such as in acoustic wave sensing and structure fatigue monitoring. A paper reporting on this concept with preliminary experiments had been published in Applied Optics [25].

9.17 Applied to Neural Network (Appendix 10.17)

We have in this period applied the specially doped PR crystal to a polychromatic neural network. We have proposed a two-level content-addressable polychromatic neural net for demonstration. The architecture is basically the combination of a polychromatic Hamming net with a mapping net, which is based on a hetero-association PR crystal holographic memory. The proposed neural net is not only increasing the storage capacity and reducing the interconnection links, but also provides the content addressable capability at the second mapping net level. Since the Ce:Fe:$LiNbO_3$ crystal volume hologram has a very large storage capacity, the number of the output neurons from the second mapping net level can be very large, which is in the order of 10^6. We have also experimentally demonstrated that the proposed content addressable polychromatic neural net can indeed perform the pattern translation in color. A paper reporting this application had been published in Optics Communications [26].

9.18 Remarks

The use of photorefractive (PR) materials for data storage and interconnection has led

to a myriad of applications in real-time optical signal processing and computing. The salient features of PR material are its large storage capacity, high diffraction efficiency, and high angular and wavelength selectivities. The increased use of PR fibers in recent years has also provided an alternative to a variety of applications. In this period of research we have grown special doped Ce:Fe:$LiNbO_3$ fiber using a laser heated pedestal growth (LHPG) technique at Penn State. We have introduced methods for constructing PR fiber holograms, in which the angular and the wavelength selectives have been evaluated. We have shown that the reflection-type wavelength-multiplexed fiber holograms are the best choice for most of the applications. The crosstalk noise for reflection-type wavelength-multiplexed fiber hologram has also been calculated, in which we see that the noise level is lowered by using a light source with a narrower linewidth. We have also proposed an application of PR fiber holograms to optical interconnection by which a high density holographic memory can be constructed. One of the important aspects of using the Ce:Fe:$LiNbO_3$ PR fiber is that low power tunable diode laser can be applied.

In short we have performed the major tasks proposed in the study of photorefractive fibers for optical interconnects, switchings, massive memories, and optical properties. We are confident that aim for wide-spread production application of the PR fibers is very promising, for which we are certain that it would happen in the near future.

References

1. J. Yamamoto and A. S. Bhalla, "Growth of $Sr_{1-x}Ba_xNb_2O_6$ Single Crystal Fibers," Mat. Res. Bull., 24, pp. 761-765, 1989.

2. S. Yin and F.T.S. Yu, "Specially Doped $LiNbO_3$ Crystal Holography Using a Visible-Light Low-Power Laser Divide," IEEE Photon. Tech. Lett., 5, pp. 581-582, 1993.

3. F.T.S. Yu, S. Yin and A. Bhalla, "Wavelength-Multiplexed Holographic Construction Using a Ge:Fe: Doped PR Fiber with a Tunable Visible-Light Laser Diode," IEEE Photon. Tech. Lett., 5, pp. 1230-1233, 1993.

4. S. Yin, H. Zhou, F. Zhao, M. Wen, Z. Yang, J. Zhang and F.T.S. Yu, "Wavelength Multiplexed Holographic Storage in a Sensitive Photorefractive Crystal Using a Visible-Light Tunable Diode Laser," Opt. Commun., 100, pp. 317-321, 1993.

5. F. Zhao, H. Zhou, S. Yin and F.T.S. Yu, "Wavelength-Multiplexed Holographic Storage by Using the Minimum Wavelength Channel Separation in a Photorefractive Crystal Fiber," Opt. Commun., 103, pp. 59-62, 1993.

6. P. J. Van Heerden, "Theory of Optical Information Storage in Solid," Appl. Opt., 2, pp. 393-400, 1963.

7. C. Gu, J. Hong, J. McMichael, R. Saxena, and F. Mok, "Cross-Talk-Limited Storage Capacity of Volume Holographic Memory," J. Opt. Soc. Am., A9, pp. 1978-1983, 1992.

8. F.T.S. Yu, F. Zhao, H. Zhou and S. Yin, "Cross-Talk Noise in a Wavelength-Multiplexed Reflection-Type Photorefractive Fiber Hologram," Opt. Lett., 21, pp. 1849-1851, 1995.

9. H. Zhou, F. Zhao and F.T.S. Yu, "Effects of Recording-Erasure Dynamics of Storage Capacity of a Wavelength-Multiplexed Reflection-Type Photorefractive Hologram," Appl. Opt., 33, pp. 4339-4343, 1994.

10. G. A. Rakuljic, V. Legva and A. Yariv, "Optical Data Storage by Using Orthogonal Wavelength-Multiplexed Volume Holograms," Opt. Lett., 17, pp. 1471-1473, 1992.

11. H. Zhou, F. Zhao and F.T.S. Yu, "Diffraction Properties of a Reflection Photorefractive Hologram," Appl. Opt., 33, pp. 4345-4352, 1994.

12. J. Ma, L. Liu, S. Wu, Z. Wang, L. Xu and B. Shu, "Multibeam Coupling in Photorefractive SBN:Ce," Opt. Lett., 13, pp. 1020-1022, 1988.

13. B. Fisher and M. Segev, "Photorefractive Waveguide and Nonlinear Mode Coupling Effects," Appl. Phys. Lett., 54, pp. 684-686, 1989.

14. F. Ito, K. Kitayama and H. Oguri, "Compensation of Fiber Holographic Image Distortion Caused by Intrasignal Photorefractive Coupling by Using a Phase-Conjugate Mirror," Opt. Lett., 17, pp. 215-217, 1992.

15. D. Zhao, H. Zhou, F. Zhao and F.T.S. Yu, "Anisotropic Intrasignal Coupling in Photorefractive $LiNbO_3$," Micro. and Opt. Tech. Lett., 7, pp. 483-486, 1994.

16. M. Wen, S. Yin and F.T.S. Yu, "Tunable Interconnection Network Using a Thick Photorefractive (PR) Crystal," Micro and Opt. Lett., 7, pp. 858-860, 1994.

17. P. Yeh, "Two-wave Mixing in Nonlinear Media," IEEE J. Quantum Electronics, QE-25, pp. 484-419, 1989.

18. F. Zhao, Z. Wu, F.T.S. Yu and D. K. McMillen, "Steady-state Nondegenerate Four-Wave Mixing in Photorefractive Ce:Fe:$LiNbO_3$," Opt. Eng. (in press).

19. F.T.S. Yu, J. Zhang, S. Yin and Z. Wu, "Anomalies of Photovoltaic Current in Ce:Fe: Doped $LiNbO_3$ Crystal at 55°C and 75°C Temperatures," Opt. Eng. (in press).

20. F. Zhao, H. Zhou, Z. Wu, F.T.S. Yu and D. K. McMillen, "Temperature Dependence of Light-Induced Scattering and Noise Suppression in Ce:Fe:$LiNbO_3$ Photorefractive Crystal," Opt. Eng. (in press).

21. F.T.S. Yu and S. Yin, "Bragg Diffraction Limited Photorefractive (PR) Crystal Based Correlators," Opt. Eng. (in press).

22. M. Wen, S. Yin, P. Purwardi and F.T.S. Yu, "Wavelet Matched Filtering Using a Photorefractive Crystal," Opt. Commun., 99, pp. 325-330, 1993.

23. S. Wu, S. Yin and F.T.S. Yu, "Sensing with Fiber Specklegrams," Appl. Opt., 30, pp. 4468-4470, 1991.

24. S. Wu, S. Yin, S. Rajan and F.T.S. Yu, "Multichannel Sensing with Fiber Specklegrams," Appl. Opt., 31, pp. 5975-5983, 1992.

25. F.T.S. Yu, S. Yin, J. Zhang and R. Guo, "Application of a Fiber-Speckle Hologram to Fiber Sensing," Appl. Opt., 33, pp. 5202-5203, 1994.

26. F.T.S. Yu, S. Yin and C.-M. Uang, "A Content-Addressable Polychromatic Neural Net Using a (Ce:Fe)-Doped $LiNbO_3$ Photorefractive Crystal," Opt. Commun., 107, pp. 300-308, 1994.

Appendix 10.1

Grown SBN and Ce:Fe: $LiNbO_3$ PR Fiber

Grown SBN and Ce:Fe: $LiNbO_3$ PR Fiber

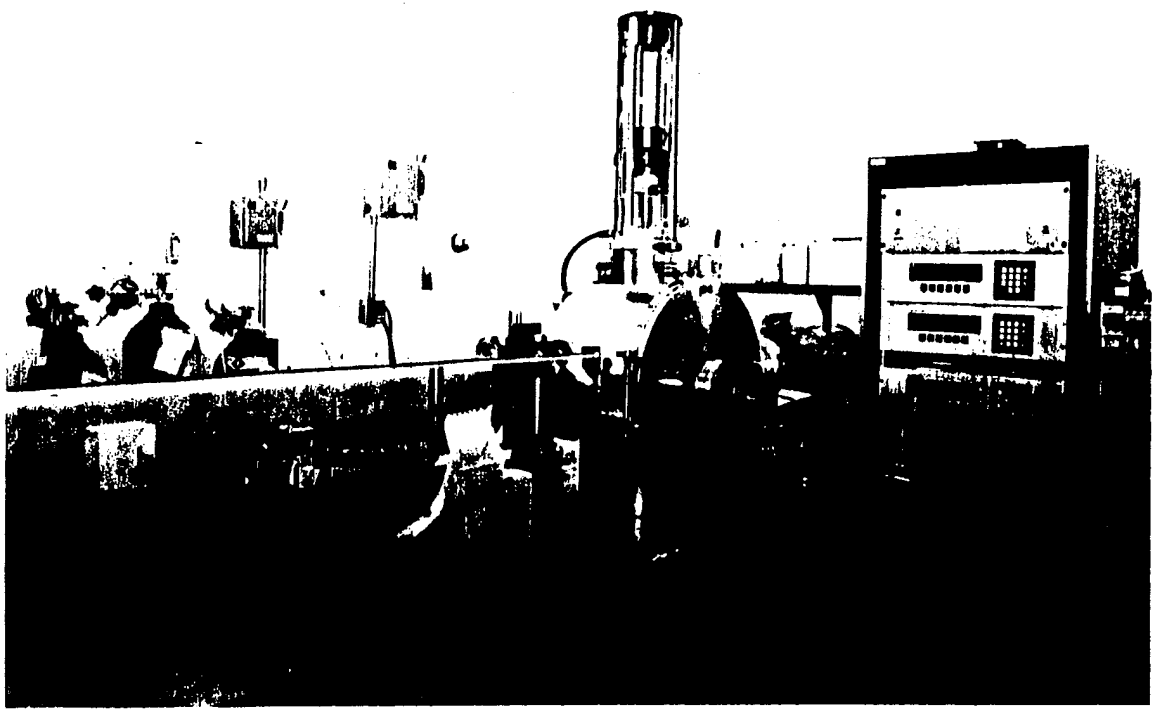

The Laser-Heated Pedestal Growth (LHPG) System

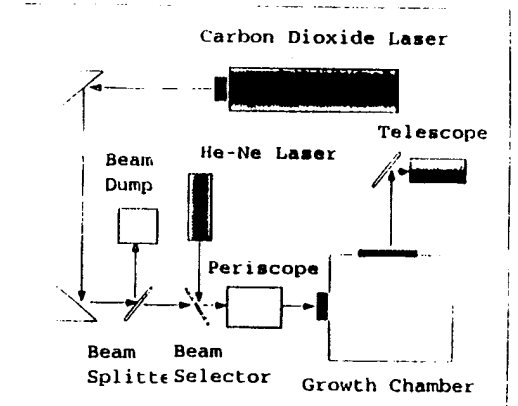

Schematic diagram of LHPG system

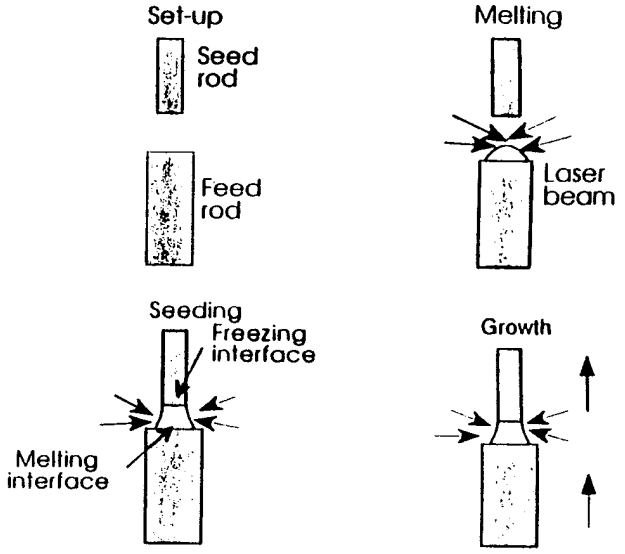

Schematic diagram of the melt zone

Appendix 10.2

Specially Doped $LiNbO_3$ Crystal Holography Using a Visible-Light Low-Power Laser Diode

Specially Doped $LiNbO_3$ Crystal Holography Using a Visible-Light Low-Power Laser Diode

Shizhuo Yin and Francis T. S. Yu, *Fellow, IEEE*

Abstract—**A special doped $LiNbO_3$ crystal holography using a visible-light low-power laser diode is presented. Since the crystal has a wide range of spectral response, it would offer practical applications to interconnects, switchings, massive storage, and many others.**

IN recent years, applications of photorefractive crystal to optical interconnections [1], optical signal processing [2], novelty filter [3], as well as storage [4], have been widely advocated. However, one of the major impediments prevents the wide spread of applications must be the high power requirement for the photorefractive crystals. For example, high power Ar^- and He–Ne lasers are usually required for the conventional $LiNbO_3$ crystal holographic process, which makes the processing system very cumbersome and expensive to operate. Although BSO crystal can have higher sensitivity, a high electric-voltage is required. Therefore, it is difficult to produce an acceptable device for practical implementation. In this letter, we report a specially doped $LiNbO_3$ crystal for the construction of photorefractive crystal hologram with a visible-light low power laser diode, by which practical application of this device can be realized.

The important features of the commercially available laser diode are the small size, easy to operate, and low cost, as compared with the high power Ar^+ and He–Ne lasers. Another feature of the laser diode is that the output wavelength is tunable (by controlling the output current from the power supply), by which it can be easily applied to wavelength multiplexed hologram.

In this letter, specially doped $LiNbO_3$ crystal is used as the volume hologram recording medium. The important aspect of this specially doped photorefractive crystal is the low power requirement which makes it possible to implement using a visible-light low power laser diode.

We have investigated the photosensitivity of this specially doped crystal. We found that it has a wide spectral response, which covers the whole visible spectrum region, i.e., 400–700 nm. The crystal has a higher photosensitivity, as compared with the conventional $LiNbO_3$ photorefractive crystals. For example, using $\lambda = 633$ nm, the photosensitivity of this crystal can be as high as 10 mJ/cm^2, with a diffraction efficiency about 1%. As in contrast with the conventional $LiNbO_3$ crystal, it requires several hundred mJ/cm^2 (at $\lambda = 633$ nm). If $\lambda = 670$ nm wavelength is used, (e.g., typical wavelength for commercially available visible-light laser diodes), the sensitivity of this specially doped crystal can be as high as 15 mJ/cm^2 (with a diffraction efficiency about 1%). Moreover, the mixed doping components of this crystal contain Fe and Ce, for which the doping levels are about 500 ppm and 300 ppm, respectively. The orientation of this crystal is z-cut.

The experimental setup for a reflection type crystal hologram using a low power laser diode is shown in Fig. 1. The diode laser is manufactured by Laser Max Inc., model 670-10, which emits a spectral line of about 670 nm with a power of about 10 mW and a coherence length of about 2 cm. Since the output beam from a single-mode semiconductor laser is astigmatic and elliptic, a correcting lens is required to collimate the light beam. The laser beam is divided into two parts by a beam splitter, for which the object and reference beams are measured about 1 mW. A piece of z-cut specially doped $LiNbO_3$ crystal of about 10 mm thick is used as the recording medium, as shown in the Fig. 1. We assume that the angle (outside the medium) of the writing beams is $2\alpha = 170°$, and the refractive index of $LiNbO_3$ is about 2.2 for $\lambda = 670$ nm. Then the angular and wavelength sensitivity can be calculated as $\{\Delta\alpha\}_r = 1.7 \times 10^{-3}$ radians, and $\{\Delta\lambda/\lambda\}_r = 3.0 \times 10^{-5}$, respectively [6]. Thus, we see that high angular and wavelength sensitivities of the crystal can be achieved. By properly adjusting the output wavelength of the laser diode, a wavelength multiplexed hologram, in the order of 10^3, can be constructed. To experimentally demonstrate the feasibility of using a low-power diode laser to record a hologram in the crystal, a letter C is used as the input pattern as shown in Fig. 2(a). The reconstructed holographic image is shown in Fig. 2(b), in which we see that relatively good result can be obtained.

To demonstrate the spectral response of this crystal, a green and blue wavelength multiplexing crystal hologram is constructed. The experimental setup is essentially the same as shown in Fig. 1, except an Ar^+ laser is added (which is tuned to about 1 mW) to provide the green and blue light. The exposure energy is adjusted to about 2 mJ/cm^2, by which a 1% diffraction efficiency is achieved. The corresponding holographic images are shown in Figs.

Manuscript received October 15. 1992; revised February 8, 1993.

The authors are with the Department of Electrical and Computer Engineering, Pennsylvania State University. University Park. PA 16802.

IEEE Log Number 9208321.

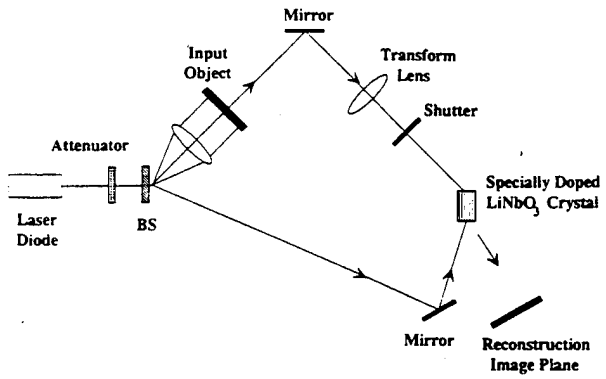

Fig. 1. Experimental Setup for reflection volume hologram with a laser diode.

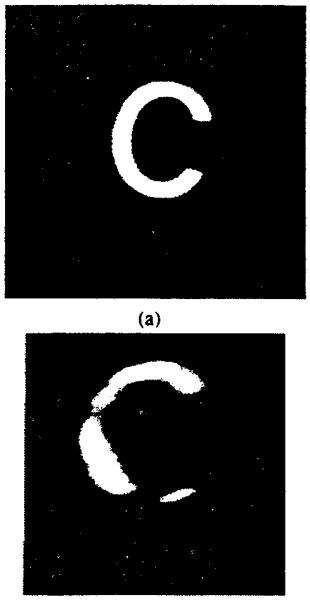

Fig. 2. Black-and-white holographic image obtained with red light (λ = 670 nm): (a) Input pattern "C"; (b) reconstructed output "C."

3 and 4, respectively. In the view of these results, we shown that the specially doped crystal indeed has a wide spectral response, which covers the whole visible light region.

In concluding this letter, we have shown that by using the specially doped $LiNbO_3$ crystal, a photorefractive

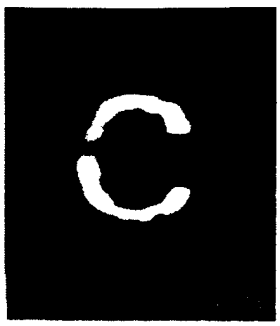

Fig. 3. Black-and-white reconstructed holographic image with green light (λ = 515 nm).

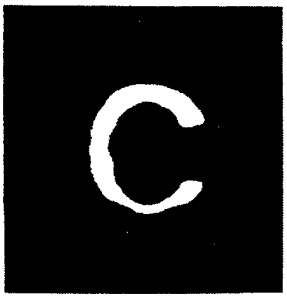

Fig. 4. Black-and-white reconstructed holographic image with blue light (λ = 488 nm).

crystal hologram can be made with a low power, low cost, visible-light laser diode. We emphasize that this letter could have significant effects on the applications of this specially doped crystal; namely, to optical interconnections, massive data storage switchings, as well as optical signal processing.

REFERENCES

[1] E. S. Manilott and K. M. Johnson, "Dynamic holographic interconnects using static holograms," in *Tech. Dig. OSA Annu. Meet. 1989*, Optical Society of America, Washington, D.C., 1989, p. 76.

[2] G. Gheen and L. J. Cheng, "Optical correlator with fast updating speed using photorefractive semiconductor materials," *Appl. Opt.*, vol. 27, pp. 2756–2760, 1988.

[3] D. Z. Anderson and J. Feinberg, "Optical novelty filter," *IEEE J. Quantum Electron.*, vol. 25, pp. 635–647, 1989.

[4] L. Solymar and D. J. Cooke, *Volume Holograph and Volume Gratings*. New York: Academic, 1981, p. 357.

[5] P. Günter and J. P. Huignard, *Photorefractive Materials and Their Applications*. Berlin: Springer-Verlag, 1988, p. 53.

[6] S. Wu, Q. Song, A. Mayers, and F. T. S. Yu, "Reconfigurable Interconnections using photorefractive holograms," *Appl. Opt.*, vol. 29, pp. 1118–1125, 1990.

Appendix 10.3

Wavelength-Multiplexed Holographic Construction Using a Ce:Fe: Doped PR Fiber with a Tunable Visible-Light Laser Diode

Wavelength-Multiplexed Holographic Construction Using a Ce: Fe: Doped PR Fiber with a Tunable Visible-Light Laser Diode

Francis T. S. Yu, *Fellow, IEEE,* Shizhuo Yin, and Amar S. Bhalla, *Member, IEEE*

Abstract—**A wavelength-multiplexed reflection-type photorefractive (PR) fiber hologram using a tunable visible-light laser diode is presented. We have shown that the wavelength-multiplexed PR fiber hologram offers a higher and more uniform wavelength selectivity than that of the transmission-type. Experimental demonstrations of wavelength-multiplexed reflection-type PR fiber hologram are provided, which are consistent with the theoretical analysis.**

Manuscript received June 22, 1993; revised July 29, 1993. This work was supported by the Defense Advanced Research Projects Agency through the U.S. Army Research Office under Contract DAAL 03-92-G-0328.

F. T. S. Yu, S. Yin, and A. S. Bhalla are with The Pennsylvania State University, Department of Electrical and Computer Engineering, University Park, PA 16802.

IEEE Log Number 9212448.

THE use of photorefractive (PR) materials for data storage and interconnection has attracted wide attention in optical signal processing and computing [1]–[8]. The salient features of PR material are the large storage capacity, high diffraction efficiency, and high angular and wavelength selectivities. The using of PR fibers [4], [9]–[11] to substitute PR bulk crystals in recent years has also provided an alternative to a variety of applications. In this paper, we shall first discuss the angular and the wavelength selectivities of PR fiber hologram, using the coupled wave theory of Kogelnik [12], in which we have noted that the estimated results are consistent with the experimental data, reported by Hesselink *et al.* [7]. Since the reflection-type wavelength multiplexed hologram offers a low crosstalk and a higher and uniform selectivity, [1], [13]

our discussion, in experimental part, will focus on this type.

From the previous works [1], [2] we know that the angular selectivities (in terms of the external write-in angle α) can be written as

$$\left\{\frac{1}{\Delta\alpha}\right\}_t = \frac{\text{Sin}\,\alpha\,\text{Cos}\,\alpha}{\sqrt{n^2 - \text{Sin}^2\,\alpha}}\frac{d}{\lambda}, \tag{1}$$

$$\left\{\frac{1}{\Delta\alpha}\right\}_r = \frac{\text{Sin}\,\alpha\,\text{Cos}\,\alpha}{\sqrt{n^2 - \text{Cos}^2\,\alpha}}\frac{d}{\lambda}. \tag{2}$$

To calculate the wavelength selectivities, k-vector diagrams (the detail discussions about it can be found in [1]) are considered as shown in Fig. 1. By referring to the moment conservation principle, a change in the diffraction beam angle θ (θ is the internal write-in angle) by $\Delta\theta$ is needed if the readout wavelength is deviated from the recording wavelength (λ) by $\Delta\lambda$. In view of Fig. 1(a), we have

$$(|\boldsymbol{k} + \Delta\boldsymbol{k}|)\,\text{Sin}\,\theta + (|\boldsymbol{k} + \Delta\boldsymbol{k}|)\,\text{Sin}\,(\theta - \Delta\theta) = 2|\boldsymbol{k}|\,\text{Sin}\,\theta \tag{3}$$

where $|\boldsymbol{k}| = 2\pi n/\lambda$. Thus, the wavelength selectivity for the transmission-type fiber hologram can be estimated as

$$\left|\frac{\lambda}{\Delta\lambda}\right| = 1 + \frac{2}{\dfrac{\text{Sin}\,\theta}{\text{Sin}\,(\theta - \Delta\theta)} - 1}. \tag{4}$$

By using the Snell's refraction law, the wavelength selectivity for the transmission-type is given by

$$\left\{\left|\frac{\lambda}{\Delta\lambda}\right|\right\}_t = 1 + \frac{2}{\dfrac{\text{Sin}\,\alpha/n}{\text{Sin}\left[\text{Sin}^{-1}\left(\dfrac{\text{Sin}\,\alpha}{n}\right) - \dfrac{\lambda}{d\,\text{Sin}\,\alpha}\right]} - 1} \tag{5}$$

which is a more exact solution as compared with the result that we have previously derived [1]. The previous result is the first-order approximation result, which is more valid for α in the range of 10°–80°. However, this result is more valid for α in the range of 22°–88°.

Similarly, for the reflection-type fiber hologram, as represented by the k-vector diagram in Fig. 1(b), the wavelength selectivity of the fiber hologram can be estimated as [1]

$$\left\{\left|\frac{\lambda}{\Delta\lambda}\right|\right\}_r = \frac{\sqrt{n^2 - \text{Cos}^2\,\alpha}}{\lambda}d. \tag{6}$$

To test the validity of these results as used for fiber holograms, we use the transmission-type angular-multiplexed type hologram as an example of comparing the theoretical analysis with the experimental data obtained by Hesselink [7] as tabulated in Table I. From this table, we see that the estimated results are closed to the experimental data (in the same order). The consistency may be explained as that the crystal fiber used in the experiment is several hundred microns in diameter and several millimeters in length. Thus, the performance of the fiber is similar to the performance of bulk crystals.

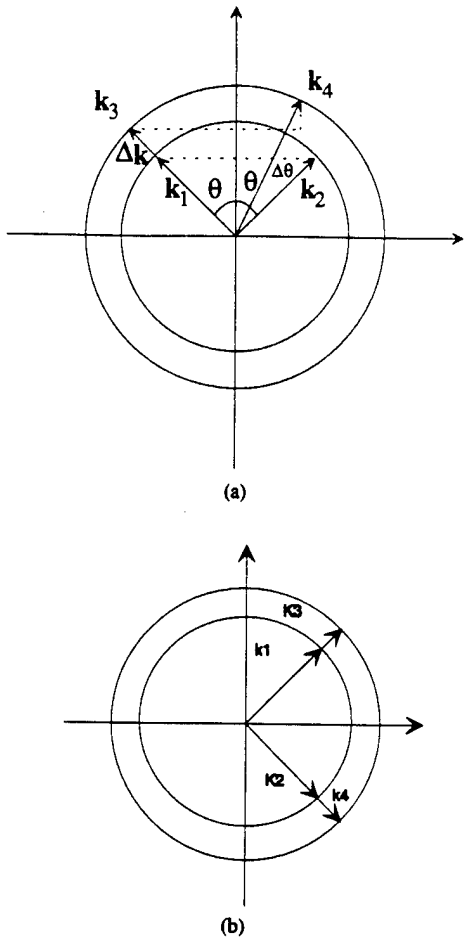

Fig. 1. Momentum conservation principle. k_1, k_2; writing wave vectors. k_3; readout wave vector. k_4; diffracted wave vector. Δk reading wavelength deviation. (a) For transmission-type hologram. (b) For reflection-type hologram.

TABLE I
CALCULATED AND EXPERIMENTAL DATA OF ANGULAR SELECTIVITY FOR FIBER HOLOGRAM λ = 515 NM N = 2.28, D = 4 MM

Recording Angle (2α)	Angular Selectivity Calculated Results (Degree)	Angular Selectivity Experimental Data (Degree)
0.7	2.41	1.43
3	0.64	0.86
5	0.39	0.57
10	0.19	0.44
20	0.098	0.26

Fig. 2 shows the normalized angular and wavelength selectivities for both types of fiber holograms, in which we see that the angular selectivities are limited by $15° \leq \alpha \leq 75°$ (FWHM). As in contrast, the wavelength selectivity for the reflection-type hologram is shown to be more sensitive and uniform. Moreover, it can also be shown that this type of hologram has a lower crosstalk noise [13]. Thus, it is the best choice for data storage. As a numerical

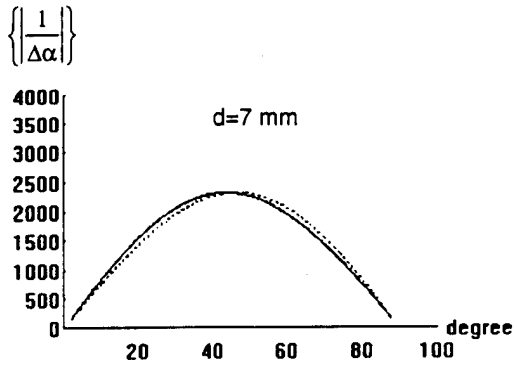

(a)

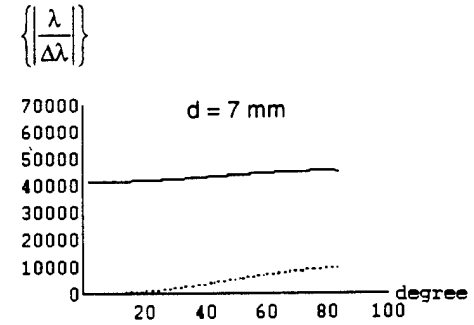

(b)

Fig. 2. (a) Normalized angular selectivity ($\lambda/d = 10^{-4}$, $n = 2.28$). (b) Normalized wavelength selectivity ($\lambda/d = 10^{-4}$, $n = 2.28$). Dashed line stands for transmission-type; solid line stands for reflection-type.

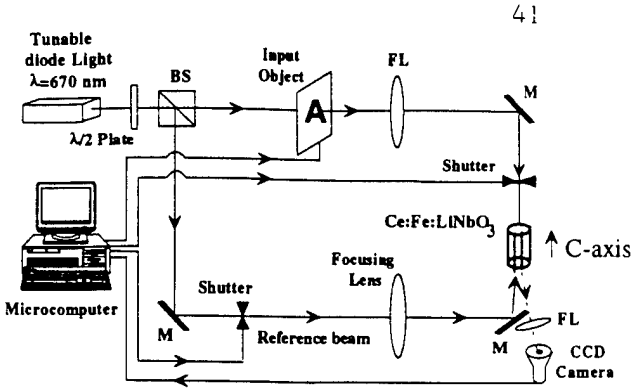

Fig. 3. Experimental setup for the construction of a wavelength-multiplexed PR crystal fiber hologram.

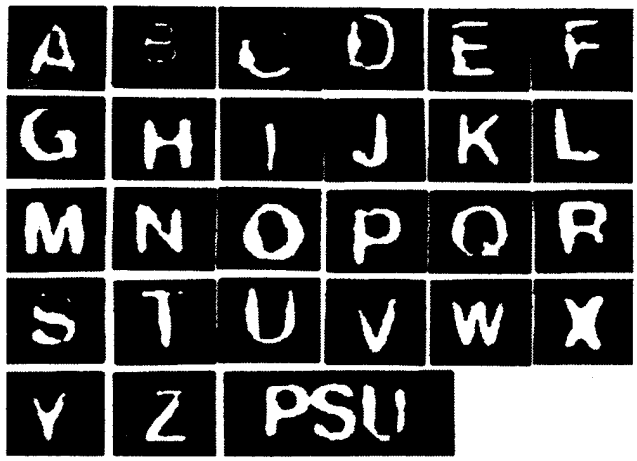

Fig. 4. Holographic images obtained from a Ce: Fe: doped $LiNbO_3$ PR fiber holograms.

example, we let the length and the recording wavelength be $d = 7$ mm and $\lambda = 0.7$ μm, the wavelength selectivity for a reflection fiber hologram is in the order of 10^4.

For experimental demonstration, we have used a Ce: Fe:-doped $LiNbO_3$ crystal fiber to construct a fiber hologram, as shown in Fig. 3. The crystal fiber was grown by a laser heated pedestal growth system in the Material Research Laboratory at Penn. State with a growing temperature about 1260 °C. The doping levels of Ce: Fe in the PR crystal fiber were measured to be about 300 ppm and 500 ppm, respectively, and the oxidizing and reducing temperature and the time were set about 700 °C and 5 h in the open air and $LiCO_3$ power environments, respectively. The size of the PR fiber is about 7 mm in length and 0.7 mm in diameter with a loss about 50%. Notice that the reason of using the Ce: Fe: doped $LiNbO_3$ PR fiber are: It has a higher photosensitivity in the red-light region, which is suitable for using a low-power visible-light tunable diode laser, and it has a high curie point of about 1200 °C, which is rather robust against the ambient temperature variation.

A 5-mw tunable laser diode (New Focus Inc. model 6102, $\lambda \approx 670$ nm, with a tuning range of 12 nm) is used as the light source. The object beam is measured to be about 2 mW/cm^2 with a write-in angle of $\alpha \approx 90°$. By using the wavelength tuning step of $\Delta\lambda = 0.1$ nm with about 5 s exposure time, a PR-fiber hologram is constructed. The diffraction efficiency for each multiplexed hologram is about 1%. By blocking the object beam and tuning the laser diode, a sequence of holographic images are reconstructed as depicted (in part) in Fig. 4.

From this figure, one can see that the obtained experimental results are relatively good. There are no obvious crosstalks among them, which is consistent with the theoretical evaluation. Notice that there are some distortions on the reconstructed images. Based on our experimental observation, the random distortions are mainly due to the nonuniform refractive index distribution within the fiber and the scattering effects coming from both the inside and not well-polished surface. And, the straight line distortion comes from the scanning lines of the receiver monitor. We do not believe that the distortion comes from the crosstalk noise. The reason is that we can get similar distortion for just recording only one hologram. We further want to note that there is no significant difference (about 20% deviation) in diffraction efficiency for each holographic channel if the same exposure energy is used in each channel. We believe that these adverse effects can

be alleviated if the PR fiber would have a more uniform refractive index distribution and been smoothly polished. At any rate, from these results, we have shown the feasibility of potential application of PR fibers to optical memory, interconnection, and others.

REFERENCES

[1] S. Wu, Q. Song, A. Mayers, D. Gregory, and F. T. S. Yu, "Reconfigurable interconnections using photorefractive holograms," *Appl. Opt.*, vol. 29, p. 1118, 1990.

[2] F. T. S. Yu and S. Jutamulia, "Optical Signal Processing," in *Computing and Neural Networks*. New York: Wiley-Interscience, ch. 7, 1992.

[3] P. A. Yeh, A. E. T. Chiou, and J. Hong, "Optical interconnection using photorefractive dynamic holograms," *Appl. Opt.*, vol. 27, p. 2093, 1988.

[4] L. Hesselink and S. Redfield, "Photorefractive holographic recording in strontium barium niobate fibers," *Opt. Lett.*, vol. 13, p. 877, 1988.

[5] F. Ito and K. Kitayama, "Real-time holographic storage of a temporal bit sequence by using angular multiple recording of spectral components," *Opt. Lett.*, vol. 17, p. 1152, 1992.

[6] Y. Qiao and D. Psaltis, "Sampled dynamic holographic memory," *Opt. Lett.*, vol. 17, p. 1376, 1992.

[7] L. Hesselink, "Photorefractive fibers for optical data storage and processing," *Int. J. Optoelectron.*, vol. J, p. 103, 1990.

[8] K. Kitayama and F. Ito, "Optical signal processing using photorefractive effect," *Multidimensional Systems and Signal Processing*, vol. 2, p. 401, 1991.

[9] J. K. Yamamoto and A. S. Bhalla, "Growth of $Sr_{1-x}Ba_xNB_2O_6$ single crystal fibers," *Mater. Res. Bull.*, vol. 24, p. 761, 1989.

[10] H. Yoshinaga, K. Kitayama, and H. Oguri, "Holographic image storage in iron-doped lithium niobate fibers," *Appl. Phys. Lett.*, vol. 56, p. 1728, 1990.

[11] Y. Sugiyama, S. Yagi, I. Yokomaha, and I. Hatakeyama, "Holographic recording in cerium doped strontium barium niobate a-axis single crystal fiber," Japan. *J. Appl. Phys.*, vol. 31, p. 708, 1992.

[12] H. Kogelnik, "Coupled wave theory for thick hologram grating," *Bell Syst. Tech. J.*, vol. 48, p. 2909, 1969.

[13] G. A. Rakuljic, V. Leyva, and A. Yariv, "Optical data storage by using orthogonal wavelength multiplexed volume holograms," *Opt. Lett.*, vol. 17, p. 1471, 1992.

Appendix 10.4

Wavelength Multiplexed Holographic Storage in a Sensitive Photorefractive Crystal Using a Visible-Light Tunable Diode Laser

Optics Communications 101 (1993) 317–321
North-Holland

OPTICS
COMMUNICATIONS

Wavelength multiplexed holographic storage in a sensitive photorefractive crystal using a visible-light tunable diode laser

S. Yin, H. Zhou, F. Zhao, M. Wen, Z. Yang, J. Zhang and Francis T.S. Yu

Electro-Optics Center, Department of Electrical & Computer Engineering, Pennsylvania State University, University Park, PA 16802, USA

Received 17 February 1993; revised manuscript received 29 April 1993

Wavelength multiplexed holograms using a Ce:Fe: doped $LiNbO_3$ crystal with a visible-light tunable diode laser are reported. The advantages of wavelength multiplexed reflection type holograms are discussed. It is shown that the wavelength multiplexed holograms offer a more uniform selectivity over all the construction angles, as compared with the angularly multiplexed crystal holograms.

1. Introduction

One of the important aspects of the photorefractive crystal holograms is their suitability for angular and wavelength multiplexing [1–4]. In the past decades, most of the research has focused on the angular multiplexing [5–8], due to the lack of suitable wavelength-tunable laser light sources. With the recent development of small size, wavelength-tunable diode lasers, wavelength multiplexing in crystal holography becomes easier and possible. Since the wavelength multiplexed holograms produce lower cross talk, as compared with the angularly multiplexed volume hologram [9], wavelength multiplexed crystal holography offers the possibility of higher density storage [2].

In this paper, we shall discuss the angular and the wavelength selectivity of a photorefractive crystal hologram using the coupled wave theory approach [1]. Mention must be made of the fact that the angular and the wavelength selectivities for a volume hologram have been previously evaluated based on the first-order approximation [3]. Thus the results reported, particularly for the transmission-type hologram, are only valid for moderate (external) write-in angles, ranging from 10° to 80°. Since higher signal-to-noise can be achieved as the write-in angle approaches 90° [9,10], it is important to investigate the angular and the wavelength selectivities of a crystal holography for write-in angles in the range of 80° to 90°.

2. Coupled wave theory

Referring to the coupled wave theory, the normalized diffraction efficiencies for unslanted transmission-type and reflection-type crystal holograms (as shown in fig. 1) can be shown to be [1]

$$\epsilon_t = \frac{\sin^2(v_t^2+\xi_t^2)^{1/2}}{1+\xi_t^2/v_t^2}, \tag{1}$$

$$\epsilon_r = \frac{1}{1+(1-\xi_r^2/v_r^2)/\sinh^2(v_r^2-\xi_r^2)^{1/2}}, \tag{2}$$

where

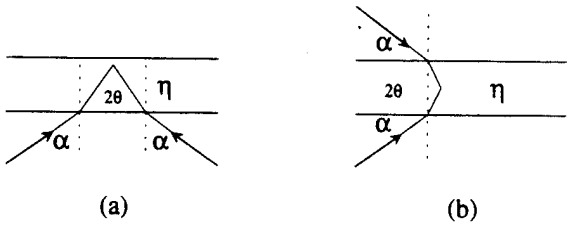

Fig. 1. Unslanted crystal holographic construction. (a) Transmission-type hologram (b) Reflection-type hologram.

$$v_t = \frac{\pi \Delta\eta\, d}{\lambda \cos\theta}, \quad \xi_t = \frac{2\pi\eta d \sin\theta}{\lambda}\Delta\theta,$$

$$v_r = \frac{\pi \Delta\eta\, d}{\lambda \sin\theta}, \quad \xi_r = \frac{2\pi\eta d \cos\theta}{\lambda}\Delta\theta,$$

with the subscripts t and r denoting the transmission and the reflection type holograms, respectively. Here, η is the refractive index of the recording material, 2θ is the internal angle, $\Delta\eta$ represents the amplitude of the modulation (refractive) index, and d is the thickness of the crystal.

We note that, in the weak coupling situation, i.e., $|v| \ll |\xi|$, the diffraction efficiencies for the transmission and reflection type holograms can be approximated by

$$\epsilon_t \approx v_t^2 \operatorname{sinc}^2 \xi_t, \tag{3}$$

$$\epsilon_r \approx v_r^2 \operatorname{sinc}^2 \xi_r. \tag{4}$$

In order to get a sense of the magnitude of weak coupling, we assume that the refractive index of a typical $LiNbO_3$ crystal is $\eta = 2.28$ and the amplitude of its modulation index is $\Delta\eta_{max} = 10^{-3}$–$10^{-5}$ [2]. Notice that for the multiplexed holograms, $\Delta\eta$ for each recorded hologram is much less than $\Delta\eta_{max}$. Thus for a given angular deviation $\Delta\theta = 1°$, the range of the internal construction angle under the weak coupling approximation would be

$$2° \leqslant \theta \leqslant 88°.$$

Since the angular selectivity of the hologram is inversely proportional to the width of the sinc factor, the angular selectivities for the transmission type and the reflective type crystal are

$$\Delta\theta_t = \frac{\lambda}{\eta d \sin\theta}, \tag{5}$$

$$\Delta\theta_r = \frac{\lambda}{\eta d \cos\theta}, \tag{6}$$

where θ is the internal write-in angle.

It is trivial to show that, by using Snell's law (see fig. 1),

$$\sin\alpha = \eta \sin\theta, \quad \text{for transmission hologram}, \tag{7}$$

$$\cos\alpha = \eta \cos\theta, \quad \text{for reflection hologram}, \tag{8}$$

the angular selectivities, as expressed in terms of external write-in angle α, can be written as [3,4]

$$\{\Delta\alpha\}_t = \frac{\sqrt{\eta^2 - \sin^2\alpha}}{\sin\alpha\cos\alpha}\frac{\lambda}{d}, \tag{9}$$

$$\{\Delta\alpha\}_r = \frac{\sqrt{\eta^2 - \cos^2\alpha}}{\sin\alpha\cos\alpha}\frac{\lambda}{d}. \tag{10}$$

To evaluate the wavelength selectivities for the transmission-type crystal hologram, we look at the k-vector diagram, as shown in fig. 2. From the principle of moment conservation, a change of the internal diffracted beam angle (θ) by $\Delta\theta$ corresponds to a shift in the readout wavelength from the recording wavelength (λ). Also, referring to fig. 2, we have

$$(|\boldsymbol{k}| + |\Delta\boldsymbol{k}|)\sin\theta + (|\boldsymbol{k}| + |\Delta\boldsymbol{k}|)\sin(\theta - \Delta\theta) = 2|\boldsymbol{k}|\sin\theta, \tag{11}$$

where $|\boldsymbol{k}| = 2\pi\eta/\lambda$. Therefore, the wavelength selectivity for the transmission-type holograms in terms of the internal write-in angle θ can be written as

$$\left|\frac{\lambda}{\Delta\lambda}\right| = 1 + 2\left(\frac{\sin\theta}{\sin(\theta - \Delta\theta)} - 1\right)^{-1}. \tag{12}$$

Thus, with eqs. (5) through (8), the wavelength selectivities for the transmission-type holograms can be written as

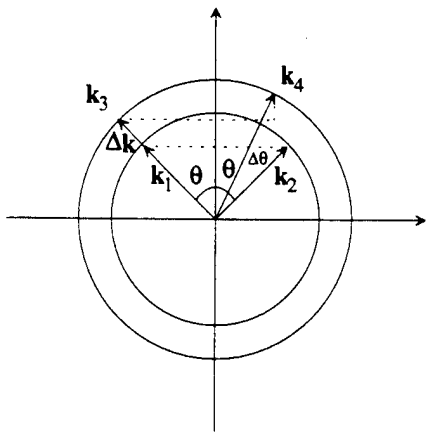

Fig. 2. Principle of momentum conservation in k-vector diagram. k_1, k_2, writing wave vectors. k_3, readout wave vector. k_4, diffracted wave vector. Δk, deviation of the reading wave vector.

$$\left\{\left|\frac{\lambda}{\Delta\lambda}\right|\right\}_t = 1 + 2\left(\frac{\sin\alpha/\eta}{\sin[\sin^{-1}(\sin\alpha/\eta)-\lambda/(d\sin\alpha)]} - 1\right)^{-1}. \quad (13)$$

Similarly, for the reflection-type hologram, it can be shown that the selectivity can be expressed as [3]

$$\left\{\left|\frac{\lambda}{\Delta\lambda}\right|\right\}_r = \frac{\sqrt{n^2-\cos^2\alpha}}{\lambda} d. \quad (14)$$

The angular and the wavelength selectivities for the transmission-type and reflection-type crystal holograms, eqs. (9), (10), (13), and (14) as a function of external write-in angle, are shown in figs. 3 and 4, respectively. From fig. 3, we see that with the variation of the angular selectivities for both the transmission-type and the reflection-type holograms, there is a limited range of external write-in angles to achieve high selectivity, i.e., $15° \leqslant \alpha \leqslant 75°$ (fwhm). In this figure we also see that angular selectivity increases as the thickness d of the crystal increases. In fig. 4, we see that the wavelength selectivity for the reflection-type hologram is higher than the transmission type, and that the selectivity of the reflection-type is rather more uniform than the transmission-type over the entire range of recording angles. Again it can be noted from this figure that the wavelength selectivity increases as the thickness of the crystal increases. These results suggest that the wavelength-multiplexed reflection-type crystal hologram would be preferable for massive data storage. In this connection, it was shown in a recent article by Rakuljic et al. [9] that the cross-talk in the wavelength multiplexed volume holograms is less severe than in the angular multiplexed holograms. Finally, to get a sense of magnitude, assuming a PR crystal thickness of $d=7$ mm and a construction wavelength $\lambda=0.7$ μm, the wavelength selectivity for a reflection type crystal hologram, $\{\lambda/\Delta\lambda\}_r$, would be in the order of 10^4.

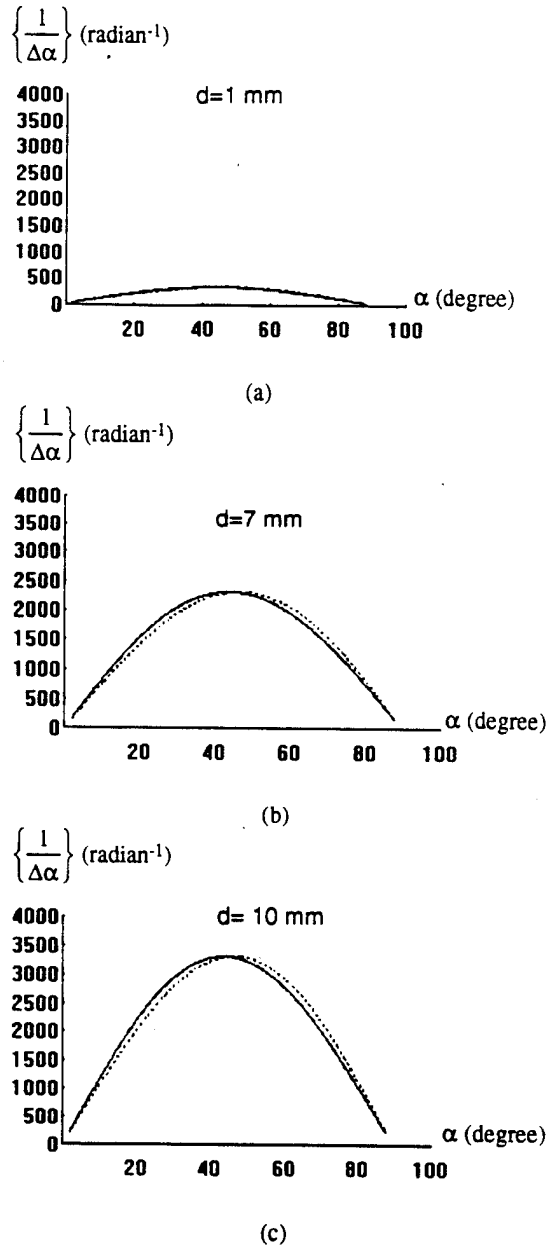

Fig. 3. Angular selectivity (dashed line for transmission-type hologram and solid line for reflection-type hologram). (a) $\lambda=0.7$, $d=1$ mm, $\eta=2.28$. (b) $\lambda=0.7$, $d=7$ mm, $\eta=2.28$. (c) $\lambda=0.7$, $d=10$ mm, $\eta=2.28$.

3. Experimental studies

In our experimental studies, we used a Ce:Fe: doped $LiNbO_3$ crystal, with doping levels about 500 ppm and 300 ppm, respectively, to construct a wavelength multiplexed reflection-type hologram, as

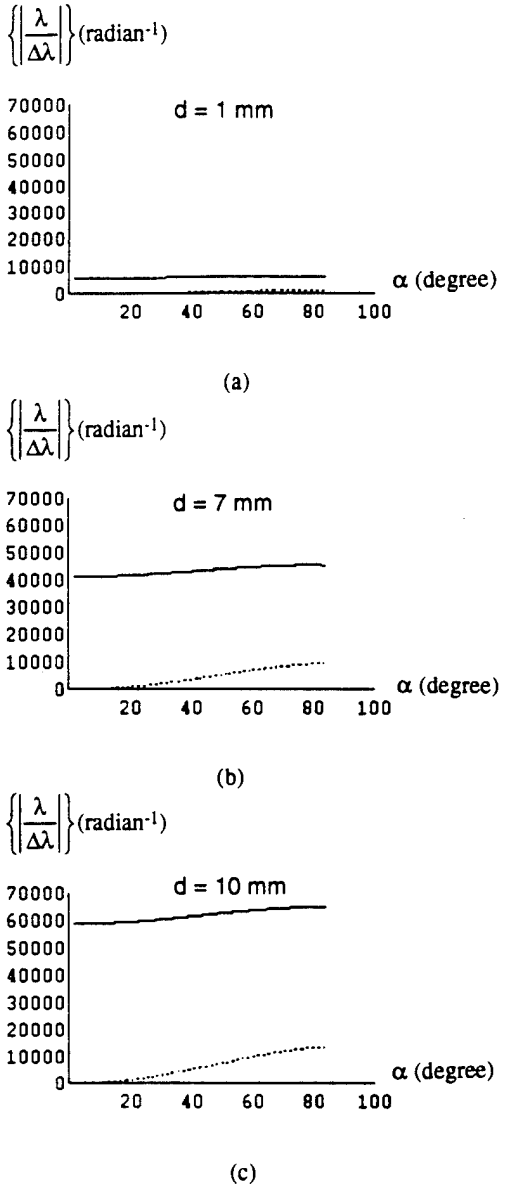

Fig. 4. Wavelength selectivity (dashed line for transmission-type hologram and solid line for reflection-type hologram). (a) $\lambda=0.7$, $d=1$ mm, $\eta=2.28$. (b) $\lambda=0.7$, $d=7$ mm, $\eta=2.28$. (c) $\lambda=0.7$, $d=10$ mm, $\eta=2.28$.

shown in fig. 5. The major advantages with using this specially-doped $LiNbO_3$ crystal are: (i) It has a high photosensitivity in red-light region, so that a low-power visible-light tunable diode laser can be used. For example, using $\lambda=670$ nm, the sensitivity of this

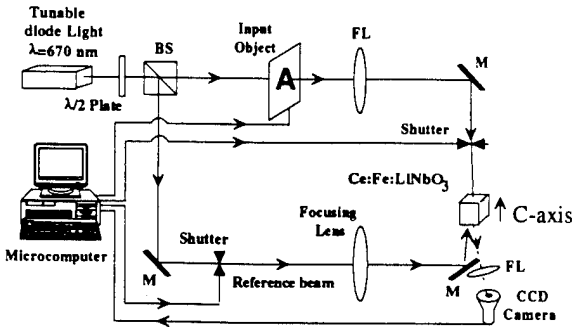

Fig. 5. Experimental set-up for the construction of wavelength multiplexing PR crystal hologram.

crystal was measured to be about 15 mJ/cm^2. (The diffraction light beam has an intensity of about 1% of the original object beam intensity.) (ii) The crystal has a high Curie point measured to be about 1200°C so it is quite robust against the temperature perturbation.

In the experiment, a tunable laser diode (New Focus Inc. Model 6102) with wavelength $\lambda=670$ nm, output power ≈ 5 mW, and tuning range about 12 nm, was used. The PR crystal was a one cubic centimeter cube and z-cut. The input beam intensity was measured to be about 2 mW/cm^2 and the wavelength multiplexed hologram was recorded at a fixed write-in angle of $\alpha \approx 90°$. Exposure times were each 5 seconds as the wavelength was stepped in $\Delta\lambda=0.1$ nm intervals. The hologram images were sequentially reconstructed (while blocking the input object beam) by tuning the laser diode through the same

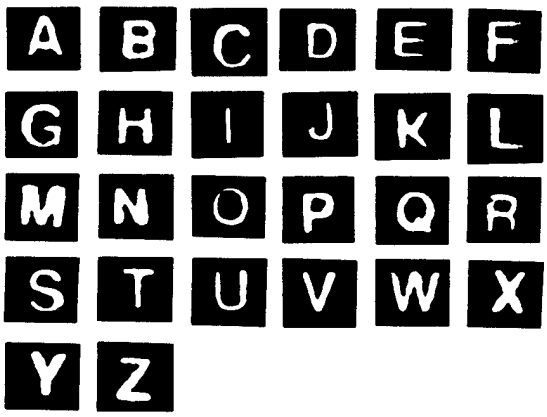

Fig. 6. Reconstructed holographic images using the specially doped Ce:Fe:$LiNbO_3$ PR crystal.

wavelength sequence. A CCD camera was used to pick up the reconstructed images which were then displayed on a TV monitor as shown in fig. 6. It is evident from the figure that cross-talk among the images is virtually non-existent. These results shown the feasibility of potentially practical implementation, in which a low power tunable laser diode can be used with a specially doped PR $LiNbO_3$ crystal.

4. Summary

We have analyzed the angular and the wavelength selectivities for the transmission-type and the reflection-type crystal holograms; our theoretical analysis indicates that the wavelength multiplexed reflection-type crystal hologram would offer higher and more uniform selectivities than the transmission-type hologram. Furthermore, the wavelength multiplexing technique offers a wider range of construction angle than the angular multiplexed hologram. Finally, we demonstrated that a series of wavelength multiplexed holograms can be recorded in a single Ce:Fe: doped crystal using a low power tunable visible-light laser diode. The reconstructed hologram images show no significant cross-talk among them.

Acknowledgements

The authors wish to acknowledge the support of Defense Advanced Research Projects Agency through the U.S. Army Research Office under Contract No. DAAL 03-92-G-0328.

References

[1] H. Kogelnik, Bell Syst. Tech. J. 48 (1969) 2909.
[2] P. Günter and J.P. Huiguard, Photorefractive materials and their applications. I (Springer, Berlin, 1988) p. 53.
[3] S.D. Wu, Q.W. Song, A.W. Mayers, D.A. Gregory and F.T.S. Yu, Appl. Optics 29 (1990) 1118.
[4] F.T.S. Yu and S. Jutamulia, Optical signal processing, computing and neural networks (Wiley-Interscience, 1992) ch. 7.
[5] J.J. Amodei and D.L. Staebler, RCA Review 33 (1972) 71.
[6] A.C. Strasser, E.S. Maniloff, K.M. Johnson and S.D. Goggin, Optics Lett. 14 (1989) 6.
[7] L. Staeble, W.J. Burke, W. Philips and J.J. Amodei, Appl. Phys. Lett. 26 (1975) 182.
[8] F.H. Mok, M.C. Tackitt and H.M. Stoll, Optics Lett. 16 (1991) 605.
[9] G.A. Rakuljic, V. Leyva and A. Yariv, Optics Lett. 17 (1992) 1471.
[10] C. Gu and J. Hong, in OSA Annual Meeting, 1992 OSA Technical Digest Series, Vol. 23 (OSA, Washington D.C., 1992) paper WT2, p. 111.

Appendix 10.5

Wavelength-Multiplexed Holographic Storage by Using the Minimum Wavelength Channel Separation in a Photorefractive Crystal Fiber

Optics Communications 103 (1993) 59–62
North-Holland

OPTICS
COMMUNICATIONS

Wavelength-multiplexed holographic storage by using the minimum wavelength channel separation in a photorefractive crystal fiber

F. Zhao, H. Zhou, S. Yin and F.T.S. Yu
Department of Electrical and Computer Engineering, The Pennsylvania State University, University Park, PA 16802, USA

Received 4 May 1993; revised manuscript received 29 June 1993

Estimated is the spectral bandwidth of the holographic channel in a wavelength multiplexed holographic storage in a PR crystal fiber. The effect of the spectral width of the light source on the minimum channel separation and the cross-talk between the adjacent channels have been analyzed. Experimental results have shown the feasibility of using the minimum wavelength separation in wavelength multiplexed fiber holograms. The cross-talk is measured to be about 5%. Also is shown that the reconstructed hologram images are in good fidelity with little cross-talk.

1. Introduction

The unique dynamic properties of photorefractive (PR) crystals offer an attractive solution to dynamic optical signal processing, such as massive data storage, interconnect, etc. The successful growth of photorefractive single crystal fibers [1–3] has provided us with an alternative approach with respect to bulk PR crystals in these applications. Among the various multiplexing/demultiplexing techniques, angular [4–8] and wavelength [4,7–9] multiplexing are two most prominent methods. Mok et al. have demonstrated 500 high-resolution reconstructed holograms by using the angular multiplexing/demultiplexing technique in a 1 cm^3 bulk crystal [5]. Angular multiplexing/demultiplexing has also been implemented in a photorefractive fiber [1,11], and Hesselink et al. have claimed that the angular selectivity is higher in a PR fiber than in a bulk crystal [1]. The wavelength multiplexing technique has recently gained much attention and been preferred, because of the lower cross-talk than the angular counterpart [9]. Experimental demonstrations have been provided in bulk crystals using wavelength multiplexing/demultiplexing [7–10]. We have recently shown that wavelength multiplexing can be implemented in a PR fiber hologram, in which more than 50 holographic images have been reconstructed [12].

The storage capacity of an angularly multiplexed bulk holographic memory is known to be limited by the total angular tuning range (which is about 4π solid angle), and the minimum channel separation [6]. In a PR fiber, the angular tuning range is also limited by its small numerical aperture. However, in principle, there exists no upper tuning-range limit for the wavelength multiplexing, as in contrast with the angular multiplexing. Nevertheless, the practical limit must be the spectral photo-sensitivity of the PR material and of course the available tuning range of the light source. Thus, to achieve a larger storage capacity, the minimum wavelength channel separation should be fully utilized. It is therefore our objective to investigate the minimum wavelength channel separation in a PR fiber. The effect due to the spectral width of the light source and the cross-talk between the adjacent channels are also discussed. A simple experiment is also provided to demonstrate the use of the minimum wavelength channel separation.

2. Theoretical background

Since the reflection-type holographic storage schemes with counter-propagating signal and refer-

ence beams are preferred [9,12], our analysis would only focus at the reflection-type fiber holographic process, as illustrated in fig. 1. Strictly speaking, a complete discussion on PR fiber holograms should include the nonlinear PR two-wave coupling, the intermodal linear coupling, and others. Since the PR fiber has a large number of modes (e.g., 10^4) with a limited length (e.g., 3–10 mm), it may be a good approximation and our discussion can be facilitated by using the Kogelnik's coupled-wave theory [4], for which the diffraction efficiency of a reflection-type volume hologram is given by

$$\eta(\Delta\lambda)=\left(1+\frac{1-\xi^2/\nu^2}{\sinh^2(\nu^2-\xi^2)^{1/2}}\right)^{-1}, \tag{1}$$

where

$$\xi=\frac{2\pi nL\Delta\lambda}{\lambda_0(\lambda_0+2\Delta\lambda)}, \tag{2a}$$

$$\nu=\frac{\pi n_1 L}{(\lambda_0+\Delta\lambda)\sqrt{1+2\Delta\lambda/\lambda_0}} \tag{2b}$$

can be obtained for an unslanted and a near-zero write-in angle case. L is the fiber length, n is the refractive index of the crystal fiber, n_1 is the induced refractive index due to recording light beams, λ_0 is the writing wavelength, and $\Delta\lambda$ is the wavelength mismatch of the reading beam with respect to the writing wavelength.

We note that eq. (1) describes the diffraction efficiency of a phase grating that was constructed by wavelength λ_0. Diffraction efficiency η as a function of wavelength mismatch $\Delta\lambda$ is plotted in solid lines, as shown in fig. 2, in which we assumed $L=5$ mm, $n=2.28$, $n_1=2\times10^{-6}$, and $\lambda_0=670$ nm. In view of this figure, we see that the diffraction efficiency is a fast decreasing function as $\Delta\lambda$ increases, for which it follows like a sinc function. We define the separation between the center of the main-lobe and the first null

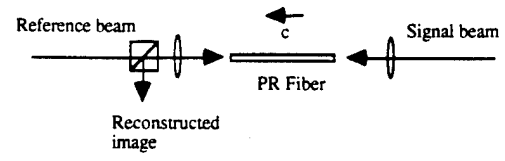

Fig. 1. Reflection-type wavelength multiplexed fiber holographic storage.

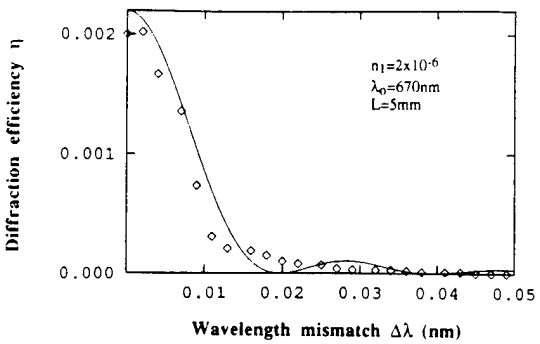

Fig. 2. Diffraction efficiency η as a function of wavelength mismatch $\Delta\lambda$ at $\eta(\Delta\lambda=0)=0.2\%$ ($n=2.29$, $n_1=2\times10^{-6}$, $\lambda_0=670$ nm, $L=5$ mm). Solid line: theoretical, and dotted line: experimental.

value as the spectral bandwidth of the holographic channel and shall use it as the minimum wavelength channel separation.

To evaluate the spectral bandwidth of the holographic channel (i.e., the location of the first null value), we simply set $\eta(\Delta\lambda)=0$ and solve for the smallest $\Delta\lambda$, for which we obtain

$$\Delta\lambda_{\min}=\frac{\lambda_0^2}{2nL}\sqrt{1+(n_1L/\lambda_0)^2}\,. \tag{3}$$

By assuming weak coupling condition (i.e., $(n_1L/\lambda_0)^2<10^{-3}$), the spectral bandwidth of the holographic channel can be approximated by

$$\Delta\lambda_{\min}\approx\lambda_0^2/2nL\,, \tag{4}$$

which is in the order of 10^{-2} nm for a typical PR fiber. For example, given $\lambda_0=670$ nm, $n=2.28$ and $L=5$ mm, it can be shown that $\Delta\lambda_{\min}=0.02$ nm. In view of eq. (4), the spectral bandwidth of the holographic channel, or the minimum channel separation, is inversely proportional to the fiber length L. It is apparent by using a longer PR fiber, in principle, a larger storage capacity can be obtained. Equation (1) is derived by the assumption of a monochromatic wavelength λ_0. However in practice, the writing beam has a finite spectral width $\Delta\lambda_{\text{laser}}$. The main-lobe of $\eta(\Delta\lambda)$ is expected to be broader which can be described by the convolution of eq. (1) with respect to the lineshape of the laser. It is obvious that the width of the main lobe $\eta(\Delta\lambda)$ is approximately equal to $\Delta\lambda_{\min}+\Delta\lambda_{\text{laser}}$. Thus we see that the spectral bandwidth, or the minimum wavelength channel sepa-

ration, will be about $\Delta\lambda_{min}+\Delta\lambda_{laser}$. Therefore, it is clear that a narrow linewidth tunable laser is needed for a wavelength multiplexed hologram.

Figure 3 illustrates the scheme of using the minimum wavelength channel separation in the wavelength domain in a fiber hologram, in which we assume five holographic gratings are recorded using λ_{-2}, λ_{-1}, λ_0, λ_1, and λ_2, respectively. Now we let the diffraction of the hologram image from the grating (main lobe) written by the same wavelength (as the reading beam) be the signal, and the diffraction from other gratings that spread into this channel be the cross-talk noise. To minimize the cross-talk noise, the read-out light source should have a spectral width much smaller than the half-width of the first null. To ensure a low-level cross-talk, for example, using the same data $L=5$ mm, $n=2.28$, and $\lambda_0=670$ nm, a single-mode laser with a linewidth $\Delta\lambda_{laser}<10^{-4}$ nm ($\sim$66 MHz) is needed.

3. Experimental results

To provide a demonstration for the wavelength-multiplexed reflection-type fiber hologram using the minimum channel separation, a Ce:Fe:$LiNbO_3$ crystal fiber is used as the recording medium. The doping concentration for Ce and Fe are 300 ppm and 500 ppm, respectively. The size of the fiber is about 0.7 mm in diameter, 5 mm long, with the *c* axis along

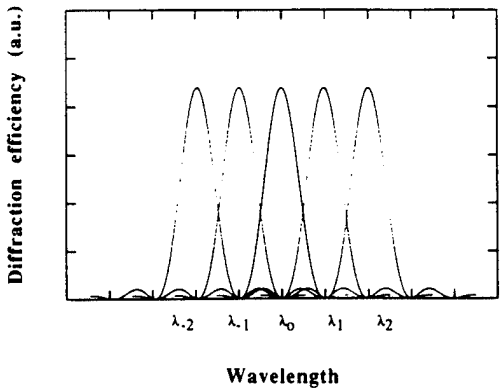

Fig. 3. Wavelength-division description of the wavelength-multiplexed holograms. Five holograms (wavelength channels) are recorded with a wavelength separation of $\Delta\lambda_{min}$, which is equal to the separation between the main-lobe and the first null.

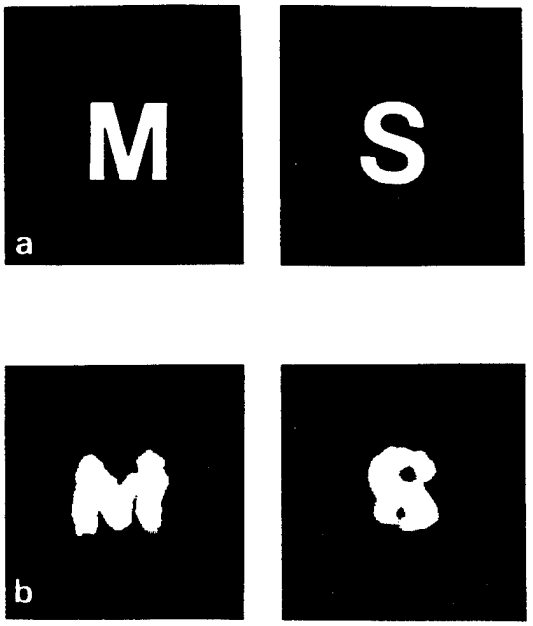

Fig. 4. Input images (a), and reconstructed images (b) for "M" and "S" with wavelength separation of 0.02 nm (15 GHz) and peak diffraction efficiency $\eta(\Delta\lambda=0)=0.2\%$.

with the crystal fiber. A 3 mW tunable diode laser (manufactured by New Focus, Model 6102) having a center wavelength of 670 nm with a 12 nm tunable range is used. The linewidth of the laser is about 2 MHz for an averaging time of 5 s and a drift smaller than 10 MHz/min. The signal beam intensity is about 100 mW/cm^2, and the exposure time is about 5 s. For the reconstruction process, the signal beam is blocked and the reference beam is attenuated to about 1/10 to lower the erasure effect on the PR hologram. The diffraction efficiency as a function of wavelength mismatch $\Delta\lambda$ is measured and plotted in dotted line in fig. 2, in which we see that the experimental data fit well with our analysis. Notice that both curves are for the case of a single hologram, and the cross-talk noise is measured to be about 5% at the first null where the second hologram will be located. For cases where multiple holograms are recorded, as shown in fig. 3, the total cross-talk noise for the center channel is expected to be slightly higher than for only two holograms. This is because all the neighboring holograms will contribute as cross-talk. Among all the neighboring channels, the farther the channel is, the smaller the cross-talk contribution. Detailed

discussion on cross-talk in a wavelength-multiplexed fiber hologram is given in a recent paper by Yu et al. [13], in which they have shown that the total cross-talk for the center channel will saturate as the total number of multiplexed holograms increases.

Two object-letters "M" and "S" are sequentially recorded in the PR fiber using a wavelength separation of about 0.02 nm ($\sim$15 GHz), which is correspondent to the calculated limit as given in eq. (5). The reconstructed hologram images are shown in fig. 4 as well as input images, in which we see that the images are in good fidelity with no severe cross-talk noise between them. The resolution of the hologram images has been estimated to be about 4 lp/mm. However, there is a severe hologram image distortion, which is primarily caused by the scattering centers and the nonhomogeneity of the material.

4. Conclusions

In summary, we have estimated the spectral bandwidth of the holographic channel of a holographic storage by using wavelength multiplexing/demultiplexing in a PR crystal fiber. The effect of the spectral width of the light source on the minimum channel separation and the cross-talk noise between the adjacent channels have been analyzed. Experimental results show the feasibility of using the minimum wavelength separation in wavelength multiplexed holographic storage in a PR fiber, for which a narrow linewidth (10 MHz) tunable diode laser is needed. When the minimum wavelength channel separation (15 GHz) is used, we have also shown that there is a $\sim$5% cross-talk between adjacent channels.

Acknowledgements

The authors would like to thank F. Luecke and M. Chang of New Focus Inc. for helpful discussions on the tunable diode laser. This work is supported by the Defense Advanced Research Projects Agency through the U.S. Army Research Office under Contract No. DAAL 03-92-G-0328.

References

[1] L. Hesselink and S. Redfield, Optics Lett. 13 (1988) 877.
[2] J.K. Yamamoto and A.S. Bhalla, Mater. Res. Bull. 24 (1989) 761.
[3] H. Yoshinaga, K. Kitayama and H. Oguri, Appl. Phys. Lett. 56 (1990) 1728.
[4] H. Kogelnik, The Bell Sys. Tech. J. 48 (1969) 2909.
[5] F. Mok, M.C. Tackitt and H.M. Stoll, Optics Lett. 16 (1991) 605.
[6] J.J. Amodei and D.L. Staebler, RCA Review 33 (1972) 71.
[7] S. Wu, Q. Song, A. Mayers, D. Gregory and F.T.S. Yu, Appl. Optics 29 (1990) 1118.
[8] F.T.S. Yu and S. Jutamulia, Optical signal processing, computing and neural networks (Wiley, New York, 1992) chap. 7, p. 249.
[9] G.A. Rakuljic, V. Leyva and A. Yariv, Optics Lett. 17 (1992) 1471.
[10] B. Catanzaro, J. Ma, Y. Fainman and S.H. Lee, in: OSA Annual Meeting Technical Digest Series 23, 1992 (OSA, Washington, D.C., 1992) paper WT5.
[11] F. Ito and K. Kitayama, Optics Lett. 17 (1992) 1152.
[12] F.T.S. Yu, S. Yin, F. Zhao, H. Zhou and M. Wen, Optics Lett., submitted.
[13] F.T.S. Yu, F. Zhao, H. Zhou and S. Yin, Optics Lett., to be published.

Appendix 10.6

Cross-Talk Noise in a Wavelength-Multiplexed Reflection-Type Photorefractive Fiber Hologram

Cross-talk noise in a wavelength-multiplexed reflection-type photorefractive fiber hologram

F. T. S. Yu, F. Zhao, H. Zhou, and S. Yin

Department of Electrical and Computer Engineering, The Pennsylvania State University, University Park, Pennsylvania 16802

Received May 3, 1993

We have analyzed the cross-talk noise as affected by the wavelength spread that is due to the spectral width of the light source in a wavelength-multiplexed reflection-type photorefractive fiber hologram. The spectral bandwidth of each multiplexed channel limited by the cross-talk noise is discussed. The signal-to-noise (cross-talk) ratio is analyzed, whereby we have shown that this ratio is sensitive to the separation between adjacent multiplexed channels and to the spectral width of the light source. The cross-talk-limited storage capacity for practical photorefractive fibers is evaluated.

The upper bond of storage capacity of a thick-emulsion hologram was estimated by Van Heerden[1] to be equal to V/λ^3 (where V is the volume of the recording material and λ is the wavelength), which is as high as 10^{12} bits. Recent advances in photorefractive (PR) materials have provided a promising device for optical storage by which a massive holographic memory may be realized.[2-8] However, there are some practical limiting factors hindering the achievement of this goal. For instance, one of the limiting factors is the cross-talk effect among the multiplexed channels. In other words, for wavelength-multiplexed holograms there are always some wavelength-spread intrusions from adjacent multiplexed channels that limit the storage capacity.

It must be noted that the cross-talk noise for angular-multiplexed holograms was studied previously.[9-12] In terms of wavelength-multiplexed holograms, the effect that is due to wavelength spread was evaluated recently by Gu and Hong[13] in a study that was based on the infinitesimal linewidth of the reading beam. In this Letter we evaluate the cross-talk effect that is due to wavelength spread among the multiplexed channels in wavelength-multiplexed PR fiber holograms. Since the wavelength selectivity is rather uniform and more efficient for the reflection-type hologram, we shall focus our discussion primarily on reflection-type PR fiber holograms.

Figure 1 shows the construction of a fiber hologram with counterpropagating signal/reference beams. The laser-heated pedestal growth technique is used to fabricate the crystal fiber, whereby fibers with diameters ranging from 20 μm to 2 mm and lengths ranging from 2 mm to 1 m can be obtained. The fibers we used for storage have a diameter of 0.5–1 mm and a length of 3–20 mm. Since the light is bounced by the boundary of the fiber only a few times, we can facilitate our discussion by considering the fiber as bulky and using Kogelnik's theory[2] to gain some knowledge of the fiber hologram. Thus the diffraction efficiency (assume negligible losses) can be approximated by[2]

$$\eta = \left[1 + \frac{1 - \xi^2/\nu^2}{\sinh^2(\nu^2 - \xi^2)^{1/2}}\right]^{-1}, \tag{1}$$

in which

$$\xi = \frac{2\pi n L \Delta\lambda}{\lambda_0(\lambda_0 + 2\Delta\lambda)},$$

$$\nu = \frac{\pi n_1 L}{(\lambda_0 + \Delta\lambda)(1 + 2\Delta\lambda/\lambda_0)^{1/2}}$$

for an unslanted and a zero write-in angle case, where L is the fiber length, n is the refractive index of the crystal, n_1 is the induced refractive index that is due to recording light beams, and $\Delta\lambda$ is the wavelength mismatch of the reading beam with respect to the writing wavelength λ_0.

Figure 2 shows the diffraction efficiency as a function of wavelength spread $\Delta\lambda$ for $L = 20$ and $L = 5$ mm, respectively. It is trivial to see that η decreases rather rapidly as $\Delta\lambda$ increases and η also improves substantially as the fiber length increases. In view of the distribution profile, we have seen that the spectral bandwidth of the multiplexed channel also improves (i.e., it is narrower) when a longer fiber is used. Needless to say, the peak diffraction efficiency can be written as

$$\eta_{\text{peak}} = \eta(\Delta\lambda = 0) = \tanh^2(\pi n_1 L/\lambda_0), \tag{2}$$

which is a monotonically increasing function of the coupling strength $\pi n_1 L/\lambda_0$. It is trivial to see that, by increasing the induced refractive index n_1 and the fiber length L or using a shorter writing wavelength λ_0, we can obtain a higher peak diffraction efficiency

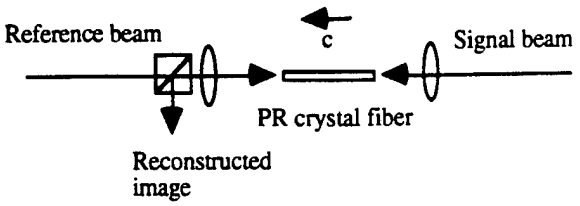

Fig. 1. Wavelength-multiplexed reflection-type fiber holographic construction.

0146-9592/93/211849-03$6.00/0

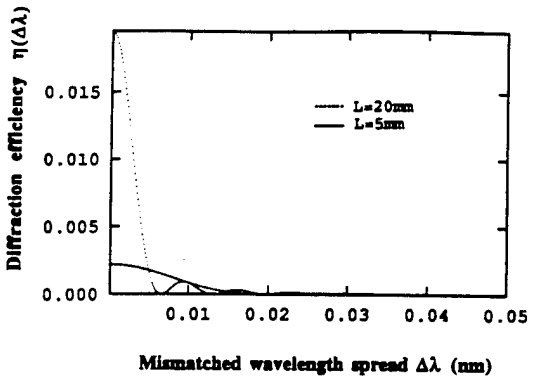

Fig. 2. Diffraction efficiency η as a function of wavelength mismatch $\Delta\lambda$. Solid curve, $\eta_{peak} = 0.2\%$ ($n_1 = 2 \times 10^{-6}$, $\lambda_0 = 670$ nm, $L = 5$ mm); dotted curve, $\eta_{peak} = 2\%$ ($n_1 = 2 \times 10^{-6}$, $\lambda_0 = 670$ nm, $L = 20$ mm).

peak. However, to ensure a large dynamic-range-limited storage capacity, n_1 should be maintained as small as possible, as pointed out by Hong *et al.*[14] The spectral bandwidth of the multiplexed holographic channel can be found by setting $\eta(\Delta\lambda) = 0$, for which we have

$$\Delta\lambda_{min} = \frac{\lambda_0^2}{2nL}[1 + (n_1 L/\lambda_0)^2]^{1/2}. \quad (3)$$

If the weak coupling condition, i.e., $(n_1 L/\lambda_0)^2 < 10^{-3}$, is imposed, $\Delta\lambda_{min}$ can be approximated by

$$\Delta\lambda_{min} \approx \frac{\lambda_0^2}{2nL}. \quad (4)$$

In order to get a sense of magnitude, if we assume that $\lambda_0 = 670$ nm, $n = 2.28$, and fiber length $L = 5$ mm, we can show that the spectral bandwidth of the channel would be $\Delta\lambda_{min} = 0.02$ nm. Notice that η in Eq. (1) (i.e., the curves of Fig. 2) is derived from the assumption of zero linewidth of the reading and the writing beams. It can be seen that if the writing beam, for example, is assumed to be a finite spectral width $\Delta\lambda_l$, then the distribution profile of η will be broader. This can be seen as the convolution of $\eta(\Delta\lambda)$ of Eq. (1) with the line shape of the light source, such that the spectral bandwidth of the multiplexed channel is

$$\Delta\lambda_{min}' = \Delta\lambda_{min} + \Delta\lambda_l.$$

Thus, for a fine-tuning multiplexed channel, a narrower spectral width of the laser is needed in the construction process.

If one regards the reconstructed hologram image from a particular channel as signal and the wavelength-spread intrusion into this channel as noise, then the signal-to-noise (cross-talk) ratio (SNR_{CT}) can be written as

$$SNR_{CT}^{(j)} = \frac{\int \text{rect}\left(\frac{\Delta\lambda}{\Delta\lambda_l}\right)\eta\, d(\Delta\lambda)}{\sum_{\substack{m=-(M-j) \\ m\neq j}}^{M+j} \int \text{rect}\left(\frac{\Delta\lambda - m\delta\lambda}{\Delta\lambda_l}\right)\eta\, d(\Delta\lambda)}, \quad (5)$$

where we assume a total number of $2M + 1$ multiplexed channels, $\delta\lambda$ is the separation between channels, and $\Delta\lambda_l$ is the spectral width of the light source. For simplicity, we assume that the recording linewidth is negligibly small, so that the cross talk would be due primarily to the reconstruction linewidth. We shall assume that the channel separation is equal to the spectral bandwidth of the channels $\Delta\lambda_{min}$, i.e., $\delta\lambda = \Delta\lambda_{min}$. In order to get a sense of magnitude, we again use the preceding data for the PR fiber; $n_1 = 2 \times 10^{-5}$, $L = 5$ mm, and $\lambda_0 = 670$ nm, for which the $\eta_{peak} = 0.2\%$ and $\Delta\lambda_{min} = 0.02$ nm. If we assume that the total number of multiplexed channels is $2M + 1 = 501$ and $\delta\lambda = \Delta\lambda_{min} = 0.02$ nm, the $SNR_{CT}^{(j)}$ can be plotted with respect to the channel number j, as shown in Fig. 3, for $\Delta\lambda_l = 1.5 \times 10^{-4}$ nm (~100 MHz) and $\Delta\lambda_l = 7.5 \times 10^{-3}$ nm (~5 GHz). From this figure we see that the SNR_{CT} values are uniformly distributed and that a narrower spectral width would produce a higher SNR_{CT}, as expected. However, there is a 10-dB drop for $\Delta\lambda_l = 5$ GHz difference between these two cases. The cross talk among the multiplexed channels would be more severe if one used a broader-spectrum beam.

To investigate further the SNR_{CT} as a function of the total number of multiplexed channels, we show two plots of SNR_{CT} with reference to the zeroth ($j = 0$) channel in Fig. 4, from which we see that the signal-to-noise ratio rapidly increases if one uses a narrower-spectrum beam and becomes independent (beyond 100) as the number of stored images increases. Notice that this effect can be seen from Eq. (1) as $\Delta\lambda$ increases. To investigate the SNR_{CT} affected by the spectral width of the light source, we have assumed two cases of channel separation, as plotted in Fig. 5. As anticipated, the farther the channel separation, the better the performance (i.e., SNR_{CT}) would be. Again we see that SNR_{CT} decreases rapidly as the linewidth of the reading beam increases.

The cross talk in a reflection-type wavelength-multiplexed fiber hologram is determined by the spectral bandwidth of the channel, which in turn determines the hologram's storage capacity. For example, using the same data and assuming the photosensitive and laser tuning ranges are of the order of $\sim 10-10^2$ nm and $\Delta\lambda_{min}$ is of the order of $10^{-2}-10^{-3}$ nm, we can estimate the cross-talk-limited storage capacity of the fiber hologram to be $\sim 10^3-10^5$ pages of holographic

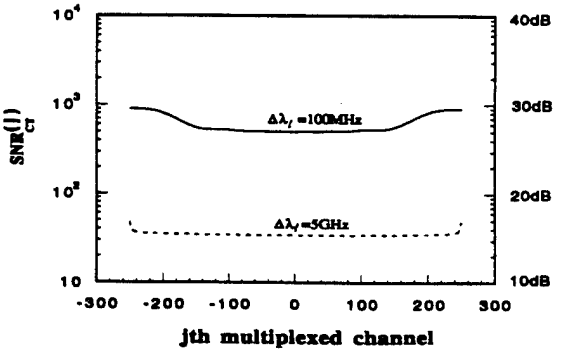

Fig. 3. Distribution of $SNR_{CT}^{(j)}$ with respect to the jth multiplexed channel.

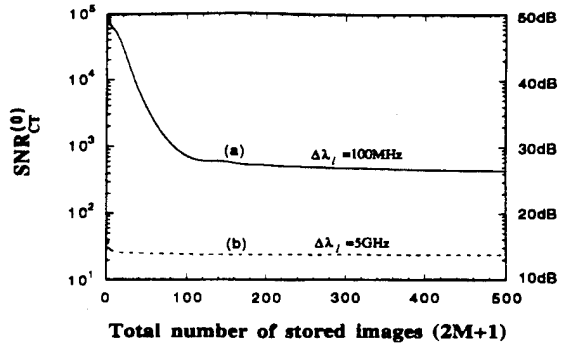

Fig. 4. $SNR_{CT}^{(0)}(j = 0)$ as a function of the total number of multiplexed channels.

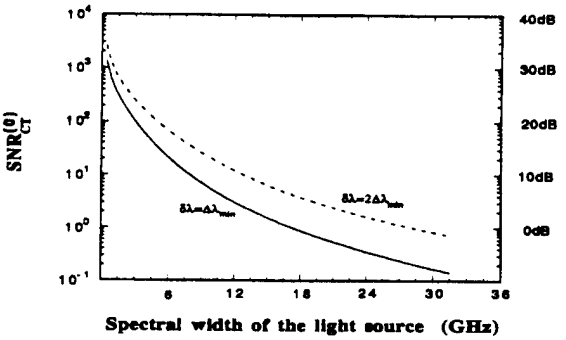

Fig. 5. $SNR_{CT}^{(0)}(j = 0)$ as a function of the linewidth $\Delta\lambda_l$ of the light source for different channels separations.

data, with a read-out SNR_{CT} ranging from 10 to 20 dB.

It must be pointed out that the cross-talk noise is not the only factor that limits the storage capacity of the fiber hologram. For example, two other major factors, i.e., the material dynamic range and the erasure of previously recorded holograms, also limit the storage capacity. Hong *et al.*[14] estimated that by consideration of the material dynamic range and with the use of proper registration methods, 1000 holograms could be recorded. Since cross-talk noise is a factor that is independent of the dynamic range and the registration method, the overall storage capacity will be the smallest number imposed by these factors. Also, the dynamic-range limitation discussed in Ref. 14 holds for wavelength multiplexing. As a result, a storage capacity of 1000 for wavelength-multiplexed fiber holograms is reasonable. We recently showed that there is no apparent cross talk between two wavelength-multiplexed PR hologram images, using a wavelength separation of ~0.02 nm (15 GHz) in a Ce:Fe:$LiNbO_3$ fiber with a narrow-linewidth tunable diode laser.[15] Incidentally, a recent Letter by Mok[16] experimentally showed that 5000 angle-multiplexed holograms could be indeed stored in a single crystal, a confirmation of the constraint of dynamic range. However, because of the lack of a suitable light source with wide tunable range and narrow linewidth, no high storage number in wavelength multiplexing has been reported.

In summary, we have analyzed the cross-talk effect and its dependence on the spectral width of the light source in a wavelength-multiplexed reflection-type PR fiber hologram. The spectral bandwidth of the multiplexed channel is derived, which is a function of the recording wavelength, the refractive index, and the length of the PR fiber. The SNR_{CT} and cross-talk-limited storage capacity are also discussed. Compared with the results of Gu and Hong,[13] the SNR_{CT} described here differs significantly as the linewidth of the light source is considered. We have found that the SNR_{CT} is sensitive to the channel separation and to the spectral width of the light source. If the minimum channel separation is used, the SNR_{CT} has been shown to be uniformly distributed in the stored holographic images. Using the minimum channel separation, we have estimated that the storage capacity of a wavelength-multiplexed PR fiber hologram can be as high as 1000 pages of holographic data, with a read-out SNR_{CT} ranging from 10 to 20 dB.

The authors acknowledge the support of the Defense Advanced Research Projects Agency through the U.S. Army Research Office under contract DAAL 03-92-G-0328.

References

1. P. J. Van Heerden, Appl. Opt. **2,** 393 (1963).
2. H. Kogelnik, Bell Syst. Tech. J. **48,** 2909 (1969).
3. F. Mok, M. C. Tackitt, and H. M. Stoll, Opt. Lett. **16,** 605 (1991).
4. J. J. Amodei and D. L. Staebler, RCA Rev. **33,** 71 (1972).
5. S. Wu, Q. Song, A. Mayers, D. Gregory, and F. T. S. Yu, Appl. Opt. **29,** 1118 (1990).
6. F. T. S. Yu and S. Jutamulia, *Optical Signal Processing, Computing and Neural Networks* (Wiley-Interscience, New York, 1992), Chap. 7, pp. 249–286.
7. G. A. Rakuljic, V. Leyva, and A. Yariv, Opt. Lett. **17,** 1471 (1992).
8. B. Catanzaro, J. Ma, Y. Fainman, and S. H. Lee, in *Annual Meeting,* Vol. 23 of 1992 OSA Technical Digest Series (Optical Society of America, Washington, D.C., 1992), paper WT5.
9. K. Bløtekjaer, Appl. Opt. **18,** 57 (1971).
10. E. G. Ramberg, RCA Rev. **33,** 5 (1972).
11. K. Wagner and D. Psaltis, Appl. Opt. **26,** 5061 (1987).
12. C. Gu, J. Hong, J. McMichael, R. Saxena, and F. Mok, J. Opt. Soc. Am. A **9,** 1978 (1992).
13. C. Gu and J. Hong, in *Annual Meeting,* Vol. 23 of 1992 OSA Technical Digest Series (Optical Society of America, Washington, D.C., 1992), paper WT2.
14. J. H. Hong, P. Yeh, D. Psaltis, and D. Brady, Opt. Lett. **15,** 344 (1990).
15. F. Zhao, H. Zhou, and F. T. S. Yu, "Wavelength-multiplexed holographic storage by using the minimum wavelength channel separation in a photorefractive crystal fiber," Opt. Commun. (to be published).
16. F. Mok, Opt. Lett. **18,** 915 (1993).

Appendix 10.7

Effects of Recording-Erasure Dynamics of Storage Capacity of a Wavelength-Multiplexed Reflection-Type Photorefractive Hologram

a reprint from Applied Optics

Effects of recording-erasure dynamics of storage capacity of a wavelength-multiplexed reflection-type photorefractive hologram

Hanying Zhou, Feng Zhao, and Francis T. S. Yu

We investigate the effects of the recording-erasure dynamics on the storage capacity of a wavelength-multiplexed reflection-type photorefractive hologram by using a coupled-recording-wave approach. A closed-form expression for the diffraction efficiency for on-Bragg incidence is derived. The dependence of the equalized diffraction efficiency on the number of recordable holograms is analyzed. The result shows that the storage capacity of a reflection-type hologram is of the same order of a transmission-type hologram but higher than the previous predictions based on an uncoupled-recording-wave theory.

1. Introduction

Photorefractive (PR) materials offer the prospect of application to massive storage, interconnection, switching, and variety of optical signal processing methods. However, in the construction of multiplexed holograms in a PR crystal the successive recordings will partially erase the previously recorded holograms. One of the problems associated with this erasure effect is that it imposes a tighter limit on the storage capacity, i.e., the total number of multiplexed holograms that can be recorded with detectable diffraction efficiencies, than do the dynamic range of the crystal index variation[1] and the cross-talk effect.[2,3] In previous analyses by Burke and Sheng[4] and Psaltis *et al.*[5] based on Kogelnik's uncoupled-recording-wave theory,[6] this limit was found to be of the order of the inverse square root of the minimum detectable diffraction efficiency, assuming equal recording and erasure time constants with small refractive-index modulation. Recently a more optimistic limit (~ 1 order of magnitude higher) was obtained by Maniloff and Johnson for angular multiplexed transmission-type holograms[7] by use of a coupled-recording-wave approach, in which the recording-erasure dynamics was taken into account.

The authors are with the Department of Electrical and Computer Engineering, Pennsylvania State University, University Park, Pennsylvania 16802.

Received 28 June 1993; revised manuscript received 15 December 1993.

0003-6935/94/204339-06$06.00/0.

The use of the coupled-recording-wave approach is indeed necessary in order to give an accurate estimation on the storage capacity of a multiplexed PR hologram. In fact, all attempts to compensate the erasure effect and to give rise to a maximized storage capacity with detectable diffraction efficiencies yield similar recording schedules,[4,5,7,8] upon which the first tens of multiplexed holograms should be exposed at much longer times as compared with the rest. Consequently, the assumption of small index modulation for the first tens of holograms is no longer satisfied during recordings, and the beam coupling and the energy transferring that are due to the phase shift of the grating formed in the PR materials occurs, resulting in a nonuniform index modulation along the crystal thickness. As we know, Kogelnik's theory for volume holograms, which is based on a uniform refractive-index modulation ratio assumption, is not valid for the case of nonuniform index modulation ratios.

Noticing recent interest in wavelength-multiplexed reflection-type PR holograms,[2,3,9,10] we apply in this paper the coupled-recording-wave approach to investigate the effects of recording-erasure dynamics on the storage capacity for this case. As energy transfer depends on the relative sign of the writing wave vectors, the behavior of a reflection-type hologram would be expected to be different from its transmission counterpart. In the following sections, first we derive a set of nonlinear coupled-wave equations that govern the holographic recording and reconstruction dynamics. A closed-form expression for the diffraction efficiency for on-Bragg incidence is then derived. Finally, the dependence of the equalized diffraction

efficiency on the number of recordable holograms is evaluated numerically.

2. Coupled-Recording-Wave Theory

The situation we consider in this analysis is that, during a hologram recording, the writing beams undergo PR two-wave mixing, producing a nonuniform refractive-index modulation ratio that varies along the thickness of the PR crystal; each successive hologram recording causes an incoherent erasure to this hologram, which means it causes a uniform decaying only in the index-modulation depth but has no effects on recorded modulation ratio structure; the readout beam is assumed very weak, so the recorded hologram can be treated as if it is fixed and not subjected to erasure during readout. The photorefractive material is assumed lossless for simplicity. The approach we adopted is similar to that used by Maniloff and Johnson[7] and Vahey,[11] and the discussion is based on the steady-state case.

Referring to Fig. 1, we consider two coherent plane waves, $R = (I_R)^{1/2}\exp(i\phi_R)$ and $S = (I_S)^{1/2}\exp(i\phi_S)$, entering the PR volume medium symmetrically from opposite faces. The interference pattern formed by the recording beams results in a refractive-index modulation, which takes the form[7,11,12]

$$\Delta n = \Delta n_0(t_r)m(z)\cos[\phi_R(z) - \phi_S(z) + \phi_{(g}], \quad (1a)$$

where ϕ_g is the grating phase shift (assumed to be constant) relative to the intensity interference pattern, $\phi_R(z) - \phi_S(z)$ is the fringe curvature, $m(z)$ is the fringe pattern contrast as defined by

$$m(z) = \frac{2[I_S(z)I_R(z)]^{1/2}}{I_S(z) + I_R(z)}, \quad (1b)$$

and $\Delta n_0(t_r)$ is the amplitude of the index perturbation. The build-up characteristic of this index perturbation depends on a number of parameters and in general has a damped oscillatory behavior.[13,14] But under certain conditions it may be described as exponential as a good approximation[13–15]:

$$\Delta n_0(t_r) = \Delta n_S[1 - \exp(-t_r/\tau_r)], \quad (1c)$$

with Δn_s denoting the saturation value of the refractive-index change of the crystal and t_r and τ_r denoting the recording time and the recording time constant, respectively.

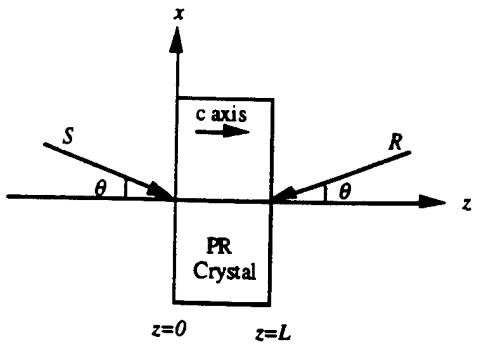

Fig. 1. Configuration for reflection-type hologram recording.

In photorefractive media that operate by diffusion only (i.e., no external static field), e.g., $BaTiO_3$, the phase shift is near $\pi/2$,[16] whereas for crystals such as $LiNbO_3$, because of photovoltaic effect, the phase shift of the grating usually has an intermediate value between 0 and $\sim\pi/2$ even without the external field.[16] The photovoltaic effect in $LiNbO_3$ also has an additional strong influence on the two-wave-mixing dynamics by the time-dependent behavior of the internal field formed by the photovoltaic effect.[17,18] For simplicity we consider in this paper only the situation with no external field and no photovoltaic effect. In any event, the sign of the phase shift is dependent on the direction of the c axis relative to the wave propagation direction. This phase shift results in the beam coupling between the writing beams, which in turn leads to a nonuniform refractive-index modulation ratio along the crystal thickness.

By substituting the above form of the refractive-index modulation equation and the total complex light field within the crystal into the scalar Maxwell wave equation and by using the standard slowly varying (field) approximation,[19] we derived the following nonlinear coupled equations:

$$S'(z, t_r) + i\Gamma_r(t_r)\frac{[I_S(z)I_R(z)]^{1/2}}{I_S(z) + I_R(z)} \times \exp\{-i[\phi_R(z) - \phi_S(z) + \phi_g]\}R(z, t_r) = 0, \quad (2a)$$

$$R'(z, t_r) - i\Gamma_r(t_r)\frac{[I_S(z)I_R(z)]^{1/2}}{I_S(z) + I_R(z)} \times \exp\{i[\phi_R(z) - \phi_S(z) + \phi_g]\}S(z, t_r) = 0, \quad (2b)$$

where

$$\Gamma_r(t_r) = \frac{\pi\Delta n_0(t_r)}{\lambda\cos\theta}, \quad (2c)$$

λ is the recording wavelength, and θ is the recording angle relative to the z axis, as shown in Fig. 1. Notice the sign difference in Eqs. (2) for beam $R(z)$, as compared with the transmission-type case.[7,12]

The quantities of interest here are $m(z)$ and $\phi_R(z) - \phi_S(z)$. We can readily find them from Eqs. (2) following a similar evaluation process given by Yeh.[19] The results are

$$m(z) = \frac{2[I_S(z)I_R(z)]^{1/2}}{I_S(z) + I_R(z)} = \frac{1}{[1 + m_1\exp(2\Gamma_r z\sin\phi_g)]^{1/2}}, \quad (3a)$$

$$\phi_R(z) - \phi_S(z) = \Gamma_r z\cos\phi_g, \quad (3b)$$

with

$$m_1 = \frac{[m_0^2 - \exp(-2\Gamma_r L \sin\phi_g)]^2}{4m_0(m_0+1)[m_0 + \exp(-2\Gamma_r L \sin\phi_g)]}, \quad (3c)$$

where $m_0 = I_R(L)/I_S(0)$ is the incident reference-to-signal intensity ratio and L is the crystal thickness. The arbitrary constant in $\phi_R(z) - \phi_S(z)$ is set to zero (owing to stationary fringes) without loss of generality. From Eqs. (3) we see that the modulation ratio (i.e., the finger-pattern contrast) is a highly nonuniform function of position z. Also notice that, because of the time dependence of Γ_r, the variables $I_R(z)$, $I_S(z)$, $\phi_R(z)$, $\phi_S(z)$, and $m(z)$ are time dependent.

To evaluate the diffraction efficiency of the PR hologram, we can rewrite a new set of coupled equations for readout beams $r(z)$ and $s(z)$, which originate from a single incident weak beam $r(z)$ at the Bragg condition:

$$s'(z) + f(z)r(z) = 0, \quad (4a)$$

$$r'(z) + f^*(z)s(z) = 0, \quad (4b)$$

where

$$f(z) = i\Gamma_e(t_e)m(z)\exp\{i[\phi_R(z) - \phi_S(z) + \phi_g]\}, \quad (4c)$$

$$\Gamma_e(t_e) = \frac{\pi\Delta n_e(t_e)}{\lambda\cos\theta}, \quad (4d)$$

with grating characteristics $m(z)$ and $\phi_R(z) - \phi_S(z)$ given by Eqs. (3). Again, notice that there is only a sign difference in Eqs. (4) for beam $r(z)$, as compared with the transmission-type case.[7,12] Also notice in Eqs. (4) that we have a new value of the amplitude of the index perturbation Δn_e for Γ_e:

$$\Delta n_e(t_e) = \Delta n_0(t_r)\exp(-t_e/\tau_e), \quad (4e)$$

with t_e and τ_e denoting the erasure time and the erasure time constant, respectively. This is because the refractive-index modulation depth decays uniformly during the successive hologram recordings; however, the recorded grating structure $m(z)$ and $\phi_R(z) - \phi_S(z)$ does not change during the process. Since all losses, including the scattering, the absorption, and the reflection, are neglected in this paper, the erasure time constant is different from the recording time constant.[7,12] In addition, although the time constants are dependent on the recording intensity (ratio) as well as on the spectral line of the light source,[12,20,21] they are treated as constants for simplicity.

The general solution of Eqs. (4) is very complicated because of the z-dependent exponential factor in the expression of $f(z)$. However, the situation can be greatly simplified if we assume $\phi_g = \pi/2$, which is the usual case for crystals such as $BaTiO_3$. Notice that the beam coupling effect is also maximum when $\phi_g = \pi/2$. Under this condition we can assume, following a similar procedure by Kogelnik,[6] the following general forms of beams $r(z)$ and $s(z)$:

$$s(z) = s_1\exp[\beta_1(z)] + s_2\exp[\beta_2(z)], \quad (5a)$$

$$r(z) = r_1\exp[\beta_1(z)] + r_2\exp[\beta_2(z)], \quad (5b)$$

where r_i and s_i are constants depending on the boundary conditions and $\beta_i(z)$ is to be determined. By substituting Eqs. (5) into Eqs. (4) and equating the summed coefficients associated with exponential $\exp[\beta_1(z)]$ and $\exp[\beta_2(z)]$ to zero, we have, respectively,

$$r_i\beta_i'(z) = -f^*(z)s_i, \qquad i = 1, 2, \quad (6a)$$

$$s_i\beta_i'(z) = -f(z)r_i, \qquad i = 1, 2, \quad (6b)$$

or

$$[\beta_i'(z)]^2 = ff^*, \qquad i = 1, 2, \quad (7a)$$

$$ff^* = \frac{\Gamma_e^2}{1 + m_1\exp(2\Gamma_r z)}, \quad (7b)$$

which has the solution

$$\beta_{1,2}(z) = \pm\beta(z) = \pm\left(\Gamma_e z - \frac{\Gamma_e}{\Gamma_r}\ln\{1 + [1 + m_1\exp(2\Gamma_r z)]^{1/2}\}\right). \quad (8)$$

Substituting back into Eqs. (5), we see that the diffracted (signal) beam can be more conveniently written with a hyperbolic function, as follows:

$$s_i(z) = c_1\sinh[\beta(z) + c_2], \quad (9)$$

with new constants c_1 and c_2, which are related to s_i, to be determined. By use of the boundary conditions $s(0) = 0$ and $r(L) = 1$ we arrive at an expression for the diffraction efficiency of the PR holograms:

$$\eta = s(L)s^*(L) = \tanh^2\left(\Gamma_e L - \frac{\Gamma_e}{\Gamma_r}\ln\left\{\frac{1 + [1 + m_1\exp(2\Gamma_r L)]^{1/2}}{1 + (1 + m_1)^{1/2}}\right\}\right). \quad (10)$$

In view of Eq. (10) two main conclusions can be drawn. First, the diffraction efficiency will never reach 100% even though the PR crystal is lossless. In fact, as Γ_r approaches infinity, the diffraction efficiency for a single exposure ($\Gamma_e = \Gamma_r$) approaches

$$\eta_\infty = \tanh^2\left[\ln\frac{(m_{1,\infty})^{1/2}}{1 + (1 + m_{1,\infty})^{1/2}}\right], \quad (11a)$$

with

$$m_{1,\infty} = \frac{m_0^2}{4(m_0 + 1)}, \quad (11b)$$

which, for example, gives a maximum diffraction efficiency $\eta_\infty \sim 88.83\%$ for $m_0 = 1$. In other words, in reflection-type PR holograms the existence of the grating phase shift limits the maximum diffraction efficiency that can be achieved. Notice that in the transmission-type situation this phase shift causes a damped behavior ($\sim 50\%$) of the sinusoidal oscillation of the diffraction efficiency.[7,12]

Second, the achievable diffraction efficiency, as can be seen from Eqs. (11), decreases as the recording reference-to-signal intensity ratio increases. Note that high beam ratios (m_0 in the hundreds) are practically used to ensure low image distortion in holographic reconstruction, and it is also the prerequisite for Eqs. (1) to be reasonably accurate for photorefractive materials.[22] In Fig. 2 we plotted the diffraction efficiency of a PR hologram as a function of recording time based on Eq. (10), for $m = 10$ and $m_0 = 100$, along with the calculations according to Kogelnik's formula[6] for non-PR holograms (i.e., $\phi_g = 0$). In view of the figure we see that as the intensity ratio increases, there is a significant drop in the achievable diffraction efficiency for PR holograms; however, the diffraction efficiency for a non-PR hologram can always reach 100%. To have a better idea of this decreasing rate, we plotted the achievable diffraction efficiency as a function of recording reference-to-signal intensity ratio m_0 in Fig. 3.

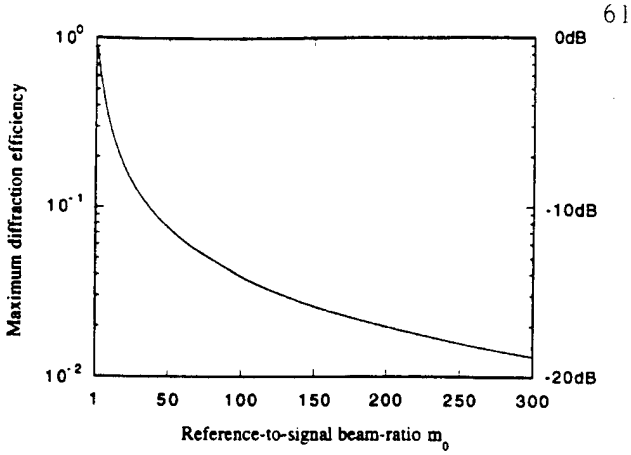

Fig. 3. Maximum achievable diffraction efficiency as a function of the recording reference-to-signal beam ratio m_0.

Multiplexing Recording Schedules and the Storage Capacity

We are now able to find the multiplexing recording schedule and the corresponding storage capacity for a wavelength-multiplexed reflection-type PR hologram by applying the above results of the coupled-recording-wave theory. Notice that, to achieve the storage capacity in a PR crystal, one has to equalize and minimize diffraction efficiencies for all multiplexed holograms. Thus the recording time for the nth hologram can be obtained with the sum of the recording times of all successive holograms as the erasure time for this exposure and then by equating the diffraction efficiencies for the nth and the $(n-1)$th holograms. By referring to Eq. (10), we have

$$\left[\frac{\pi\Delta n_0(t_{r,n-1})}{\lambda}L - \ln\left(\frac{1+\{1+m_1\exp[2\Gamma_r(t_{r,n-1})L]\}^{1/2}}{1+(1+m_1)^{1/2}}\right)\right]\exp\left(\frac{-t_{r,n}}{\tau_e}\right) = \frac{\pi\Delta n_0(t_{r,n})}{\lambda}L - \ln\left(\frac{1+\{1+m_1\exp[2\Gamma_r(t_{r,n})L]\}^{1/2}}{1+(1+m_1)^{1/2}}\right), \tag{12}$$

where $t_{r,n}$ and $t_{r,n-1}$ are the recording times for the nth and the $(n-1)$th holograms, respectively.

The recording time for each hologram can be determined numerically for a given (total) number of multiplexed holograms N. In Fig. 4 we have plotted the calculated recording times versus the total number of exposures, based on parameters $\tau_r = 120$ s, $\tau_e = 210$ s, $\phi_g = \pi/2$, $L = 2$ mm, $\lambda = 514.5$ nm, $\Delta n_S = 10^{-3}$, and $t_{r,1} = 20$ s for m_0 equal to 1, 10, and 100. The corresponding diffraction efficiencies are plotted in Fig. 5 (for up to $N = 1000$ multiplexed holograms).

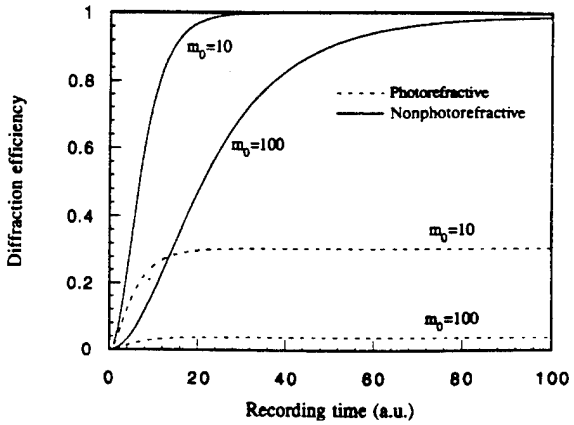

Fig. 2. Time evolution of the diffraction efficiency of a single exposure: dashed curves are based on Eq. (10) and solid curves are based on Kogelnik's formula.

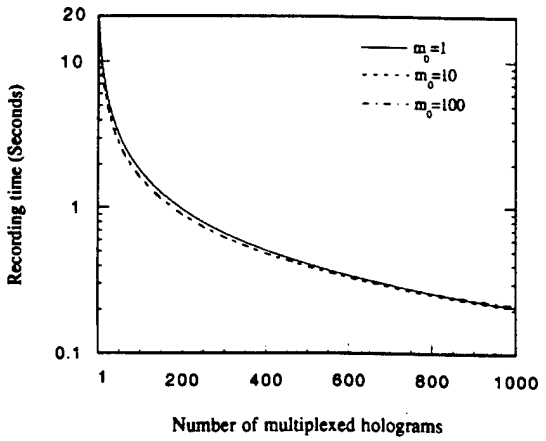

Fig. 4. Recording times versus number of the multiplexed holograms: $\tau_r = 120$ s, $\tau_e = 210$ s, $L = 2$ mm, $\lambda = 514.5$ nm, $\Delta n_S = 10^{-3}$, $t_{r,1} = 20$ s, and m_0 equal to 1, 10, and 100.

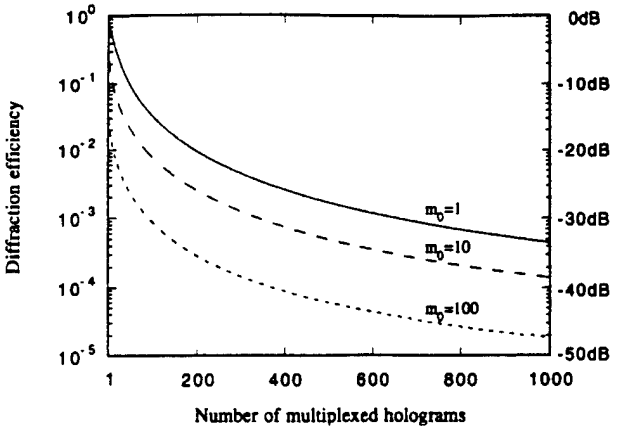

Fig. 5. Diffraction efficients versus number of the multiplexed holograms (same parameters as in Fig. 4).

In view of these figures, we note that, although the time schedules for m_0 equal to 1, 10, and 100 are almost the same (the latter two curves in Fig. 4 overlap each other), the diffraction efficiency decreases by ~ 12 times from $m_0 = 1$ to $m_0 = 100$. This implies that the storage capacity for a high beam ratio will drop rather significantly. However, as compared with the transmission-type hologram case[7] for equal intensity ratio $m_0 = 1$ (we used the same parameters as in Ref. 7), the storage capacity is roughly of the same order, which is ~ 2000 multiplexed holograms. This value is one order higher than the previous calculated results obtained with the uncoupled-recording-wave theory.[5,6] Mention must be made that, for $m_0 \neq 1$, we have no way to make a comparison with the transmission-type case at this stage, since the formulas Maniloff and Johnson derived[7] become invalid for $m_0 \neq 1$.

The above discussion on storage capacity is based on the assumption of no cross-talk noise among multiplexed holograms and no fanning noise (amplified scattering noise) in each hologram. The cross-talk noise, nevertheless, is another major limiting factor of the storage capacity. It has been shown that the storage capacity for a wavelength-multiplexed reflection-type hologram, by consideration of the cross-talk noise, is roughly 10^3–10^5 pages of holographic data.[2,3] On the other hand the fanning noise mainly affects the quality of reconstructed images,[23] although it also affects the visibility of weak reconstructed images and thus more or less limits the storage capacity. Another important consequence of the fanning noise, as mentioned in Section 2, is that it causes the time constant to deviate from its true physical value and leads to separated recording and erasure time constants for simple analysis[7,12] and thus affects the exposure time schedule for maximized storage capacity.

4. Conclusion

In summary, we have investigated the effects of recording and erasure dynamics on the storage capacity of a wavelength-multiplexed reflection-type PR hologram using a coupled-recording-wave approach. A closed-form expression for the time evolution of the diffraction efficiency was obtained for on-Bragg incidence, which predicts a lower achievable diffraction efficiency for PR materials, as compared with Kogelnik's formula for non-PR materials. The dependence of the equalized diffraction efficiency on the number of multiplexed holograms was analyzed numerically. The results have shown that the storage capacity of the reflection-type hologram is roughly of the same order of magnitude as the transmission type but higher than the previous predictions obtained by an uncoupled-recording-wave theory.

This work was supported by the Advanced Research Projects Agency through the U.S. Army Research Office under contract DAAL 03-92-G-0328.

References

1. J. H. Hong, P. Yeh, D. Psaltis, and D. Brady, "Diffraction efficiency of strong volume holograms," Opt. Lett. **15,** 344–346 (1990).
2. K. Curtis, C. Gu, and D. Psaltis, "Cross talk in wavelength-multiplexed holographic memories," Opt. Lett. **18,** 1001–1003 (1993).
3. F. T. S. Yu, F. Zhao, H. Zhou, and S. Yin, "Cross-talk noise in a wavelength-multiplexed reflection-type photorefractive fiber hologram," Opt. Lett. **18,** 1849–1851 (1993).
4. W. J. Burke and P. Sheng, "Cross-talk noise from multiple thick-phase holograms," J. Appl. Phys. **48,** 681–685 (1977).
5. D. Psaltis, A. Brady, and K. Wagner, "Adaptive optical networks using photorefractive crystal," Appl. Opt. **27,** 1752–1759 (1988).
6. H. Kogelnik, "Coupled wave theory for thick holograms," Bell Syst. Tech. J. **48,** 2909–2947 (1969).
7. E. S. Maniloff and K. M. Johnson, "Maximized photorefractive holographic storage," J. Appl. Phy. **70,** 4702–4707 (1991).
8. A. C. Strasser, E. S. Maniloff, K. M. Johnson, and S. D. D. Goggin, "Procedure for recording multiple-exposure holograms with equal diffraction efficiency in photorefractive media," Opt. Lett. **14,** 6–8 (1989).
9. G. A. Rakuljic, V. Leyva, and A. Yariv, "Optical data storage by using orthogonal wavelength-multiplexed volume holograms," Opt. Lett. **17,** 1471–1473 (1992).
10. S. Yin, H. Zhou, F. Zhao, M. Wen, Z. Yang, J. Zhang, and F. T. S. Yu, "Wavelength-multiplexed holographic storage in a sensitive photorefractive crystal using a visible-light tunable diode laser," Opt. Commun. **101,** 317–321 (1993).
11. D. W. Vahey, "A nonlinear coupled-wave theory of holographic storage in ferroelectric materials," J. Appl. Phy. **46,** 3510–3515 (1975).
12. E. S. Maniloff and K. S. Johnson, "Effects of scattering on the dynamics of holographic recording and erasure in photorefractive lithium niobate," J. Appl. Phy. **73,** 541–547 (1993).
13. K. Bløtekjaer, "Theory of hologram formation in photorefractive media," J. Appl. Phys. **48,** 2495–2501 (1977).
14. T. J. Hall, R. Jaura, L. M. Connors, and P. D. Foote, "The photorefractive effect: a review," Prog. Quantum. Electron. **10,** 77–146 (1985).
15. K. Bløtekjaer, "Limitations on holographic storage capacity of photochromic and photorefractive media," Appl. Opt. **18,** 57–67 (1979).
16. R. Hofmeister, A. Yariv, A. Kewitsch, and S. Yagi, "Simple

methods of measuring the net photorefractive phase shift and coupling constant," Opt. Lett. **18,** 488–490 (1993).
17. A. M. Glass, D. Von Der Linde, and T. J. Negran, "High-voltage bulk photovoltaic effect and the photorefractive process in $LiNbO_3$," Appl. Phys. Lett. **25,** 233–235 (1974).
18. C. Gu, J. Hong, H.-Y. Li, D. Psaltis, and P. Yeh, "Dynamics of grating formation in photovoltaic media," J. Appl. Phys. **69,** 1167–1172 (1991).
19. P. Yeh, "Two-wave mixing in nonlinear media," IEEE J. Quantum Electron. **23,** 484–519 (1989).
20. M. Horowitz, R. Daisy, and B. Fischer, "Signal-to-pump ratio dependence of buildup and decay rates in photorefractive nonlinear two-beam pumping," J. Opt. Soc. Am. B **9,** 1685–1688 (1992).
21. J. Baquedano, M. Carraascosa, L. Arizmendi, and J. M. Cabrera, "Erasure kinetics and spectral dependence of the photorefractive effect in $Fe:LiNbO_3$," J. Opt. Soc. Am. B **4,** 309–312 (1987).
22. F. Vachss and L. Hesselink, "Nonlinear photorefractive response at high modulation depths," J. Opt. Soc. Am. A **5,** 690–701 (1988).
23. H. Rajbenbach, A. Delboube, and J. P. Huignard, "Noise suppression in photorefractive image amplifiers," Opt. Lett. **14,** 1275–1277 (1989).

Appendix 10.8

Diffraction Properties of a Reflection Photorefractive Hologram

a reprint from Applied Optics

Diffraction properties of a reflection photorefractive hologram

Hanying Zhou, Feng Zhao, and Francis T. S. Yu

Diffraction properties of a photorefractive hologram have been described previously in most cases with Kogelnik's uncoupled-recording-wave-theory, which was originally derived for nonphotorefractive holograms. Despite its simplicity and good approximation, the theory has shown its practical limitations and discrepancies when the refractive-index perturbation is large. We study the diffraction properties of a reflection photorefractive hologram using a coupled-recording-wave approach. A closed-form expression for the diffraction efficiency is obtained. The important aspect of the new formula is that it predicts a lower cross-talk noise (or, a higher wavelength sensitivity) than Kogelnik's formula. This offers an explanation for the apodization phenomenon (i.e., lower cross-talk noise from the experiment as compared with the analytical result) as found by Rakuljic *et al.* [Opt. Lett. **17**, 1471–1473 (1992)].

Introduction

Thick photorefractive (PR) holograms have potential for widespread application in many areas, such as massive storage, optical interconnections, and switchings.[1–4] However, to our knowledge the diffraction properties have not yet been fully investigated,[5–8] and so far have been described mostly by Kogelnik's theory,[9] which was originally derived for non-PR holograms using an uncoupled-recording-wave approach. As applied to PR holograms, the theory shows its limitations and discrepancies when the index perturbation (i.e., coupling strength) is large. For example, the relative cross-talk noise obtained from the experiment reported by Rakuljic *et al.*[4] is much lower than in the analysis. The discrepancy is primarily caused by the beam coupling and the irreversible energy transfer affected by the phase shift of gratings formed in PR materials. The irreversible energy transfer results in a nonuniform index modulation ratio over the crystal thickness during recording, which affects the readout properties during reconstruction. In contrast, Kogelnik's theory begins with the assumption of a uniform refractive-index modulation ratio.[9]

The authors are with the Department of Electrical and Computer Engineering, Pennsylvania State University, University Park, Pennsylvania 16802.

Received 30 August 1993; revised manuscript accepted 15 December 1993.

0003-6935/94/204345-08$06.00/0.

The beam-coupling effects in a PR hologram recording have been considered by several investigators using a coupled-recording-wave approach.[5–8] For the often-encountered situation in which the readout beam is substantially weaker than the recording one, Vahey has derived the diffraction efficiency for on-Bragg incidence for an angularly multiplexed transmission-type hologram.[5] The result has been employed successfully to explain the experimental data obtained by Staebler and Amodei.[10] Maniloff *et al.*[8] have used the same result to estimate the storage capacity of an angularly multiplexed transmission PR hologram. Using a similar method for a wavelength-multiplexed reflection PR hologram case, we have recently evaluated the storage capacity and derived the diffraction efficiency for on-Bragg incidence.[7] On the other hand, for the situation in which the readout beam is incoherent with the recording beam but comparable in intensity, Yeh[11] has derived the diffraction efficiency for on-Bragg incidence for both transmission and reflection holograms by treating the reading and the writing as two simultaneous but independent two-wave-mixing processes. However, all these studies[5–8,11] have focused on the on-Bragg readout conditions. The diffraction properties for off-Bragg conditions (i.e., as a function of wavelength or angle deviations) have not yet been fully investigated to our knowledge. Nevertheless, they are important for the evaluation of the cross-talk noise and the wavelength and the angular sensitivities.

In this paper we apply the coupled-recording-wave approach to study the diffraction properties of a reflection PR hologram. First, we derive sets of

nonlinear coupled-wave equations that govern the recording and the reconstruction dynamics. A closed-form expression for the diffraction efficiency, as a function of wavelength deviation and the recording time, is then obtained. Finally, the diffraction properties for off-Bragg conditions are discussed.

Coupled-Recording-Wave Theory

Referring to the reflection PR holographic construction geometry shown in Fig. 1, we consider two coherent plane waves, with complex amplitudes $R = (I_R)^{1/2}[\exp(j\phi_R)]$ and $S = (I_S)^{1/2}[\exp(j\phi_S)]$, symmetrically entering the PR volume median from opposite faces. The nonlinear coupled equations for the recording process are the same as those considered in our previous paper[7] and can be written as

$$S'(z, t_r) - j\Gamma_r(t_r)\frac{[I_S(z)I_R(z)]^{1/2}}{I_S(z) + I_R(z)} \times \exp\{-j[\phi_R(z) - \phi_S(z) + \phi_g]\}R(z, t_r) = 0, \quad (1a)$$

$$R'(z, t_r) + j\Gamma_r(t_r)\frac{[I_S(z)I_R(z)]^{1/2}}{I_S(z) + I_R(z)} \times \exp\{j[\phi_R(z) - \phi_S(z) + \phi_g]\}S(z, t_r) = 0, \quad (1b)$$

with

$$\Gamma_r(t_r) = \frac{\pi\Delta n_0(t_r)}{\lambda_0 \cos\theta_0}, \quad (1c)$$

where λ_0 is the recording wavelength in free space, θ_0 is the recording angle (within the medium) with respect to the z axis, as shown in Fig. 1, $\Delta n_0(t_r)$ is the amplitude of the index perturbation that increases with recording time t_r,

$$\Delta n_0(t_r) = \Delta n_s[1 - \exp(-t_r/\tau_r)], \quad (1d)$$

with Δn_s denoting the saturation value of the refractive-index change of the crystal and τ_r denoting the recording time constant, and ϕ_g is the phase shift (assumed to be constant) of the recorded grating structure relative to the intensity interference pattern.

In a photorefractive medium that is operated by diffusion without an applied external field (e.g., $BaTiO_3$), the phase shift of the holographic grating ϕ_g is equal to $\pi/2$, with its sign depending on both the direction of the c axis and the sign of the dominant carrier. This phase shift results in the beam coupling between the writing beams, which in turn leads to a nonuniform refractive-index modulation ratio over the crystal thickness.

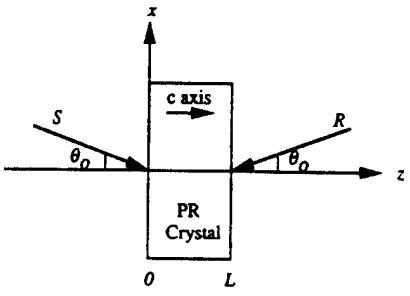

Fig. 1. Configuration for a reflection PR hologram recording.

The recorded grating structure characteristics [i.e., the grating modulation ratio $m(z)$ and the grating curvature $\phi_R(z) - \phi_S(z)$ as determined by Eqs. (1)] can be shown as[7]

$$m(z) = \frac{2[I_S(z)I_R(z)]^{1/2}}{I_S(z) + I_R(z)} = \frac{1}{[1 + m_1 \exp(2\Gamma_r z \sin\phi_g)]^{1/2}}, \quad (2a)$$

$$\phi_R(z) - \phi_S(z) = \Gamma_r z \cos\phi_g, \quad (2b)$$

where

$$m_1 = \frac{[m_0^2 - \exp(-2\Gamma_r L \sin\phi_g)]^2}{4m_0(m_0 + 1)[m_0 + \exp(-2\Gamma_r L \sin\phi_g)]}, \quad (2c)$$

with $m_0 = I_R(L)/I_S(0)$ denoting the incident reference-to-signal beam ratio and L denoting the crystal thickness. The arbitrary constant in Eq. (2b) has been set to zero without loss of generality. Figure 2 shows a plot of the modulation ratio $m(z)$ as a function of position z for various index perturbations. The influence of beam ratio m_0 on the nonuniformity of modulation ratio $m(z)$ is illustrated in Fig. 3. It is clear that the refractive-index modulation ratio can be highly nonuniform over crystal thickness if there is a nonzero grating phase shift and a large index perturbation.

For a weak-beam readout process the recorded grating structure given by Eqs. (2) can be treated as fixed and would not be subjected to erasure during readout. The weak readout beam $r(z)$, which may or may not be incident at the Bragg condition, generates a diffracted beam $s(z)$. Including a dephasing measure ϑ for Bragg mismatching, we can write the new

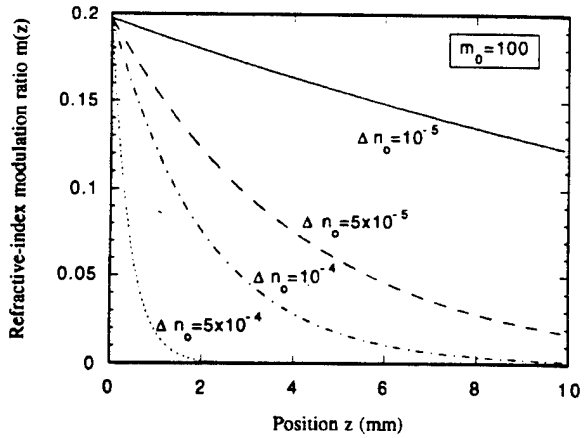

Fig. 2. Refractive-index modulation ratio $m(z)$ as a function of position z for various index perturbations Δn_0, given $\phi_g = \pi/2$, $\lambda = 614.7$ nm, $L = 10$ mm, and $m_0 = 100$.

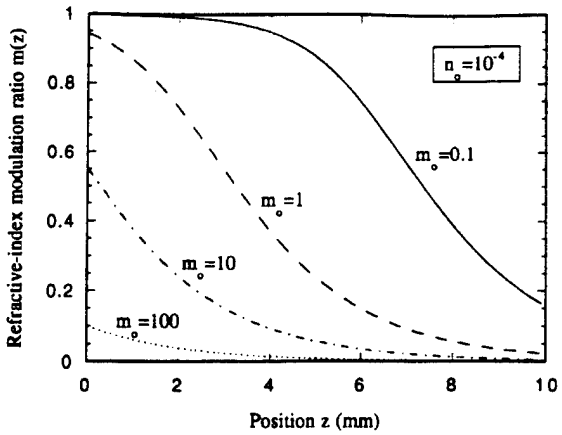

Fig. 3. Refractive-index modulation ratio $m(z)$ as a function of position z for various reference-to-signal beam ratios m_0, given $\phi_g = \pi/2$, $\lambda = 614.7$ nm, $L = 10$ mm, and $\Delta n_0 = 10^{-4}$.

coupled equations for the reconstruction process as

$$s'(z) + f^*(z)r(z) - j\vartheta s(z) = 0, \tag{3a}$$

$$r'(z) + f(z)s(z) = 0, \tag{3b}$$

where

$$f(z) = \frac{j\Gamma_e(t_e)\exp(j\Gamma_r z\cos\phi_g + j\phi_g)}{[1 + m_1\exp(2\Gamma_r z\sin\phi_g)]^{1/2}}, \tag{3c}$$

$$\Gamma_e(t_e) = \frac{\pi\Delta n_0(t_r)\exp(-t_e/\tau_e)}{(\lambda_0 + \Delta\lambda)\cos(\theta_0 + \Delta\theta)}, \tag{3d}$$

with $\Delta\theta$ and $\Delta\lambda$ denoting the angle and the wavelength deviations; ϑ is defined as

$$\vartheta = \Delta\theta K\sin\theta_0 - \frac{\Delta\lambda K^2}{4\pi n}, \tag{3e}$$

with $K = (4\pi n/\lambda_0)\cos\theta_0$ representing the grating vector of the reflection hologram. The exponential decay factor, $\exp(-t_e/\tau_e)$, with t_e and τ_e denoting the erasure time and the erasure time constant, respectively, describes incoherent erasures, that are due to successive recordings of new multiplexed holograms. Although the time constants are dependent on the recording intensity (ratio) as well as on the spectral line of the light source,[12–14] they are treated as constants for simplicity.

To obtain the solutions for Eqs. (3), we assume the following general forms for beams $r(z)$ and $s(z)$:

$$s(z) = \{s_1\exp[\beta_1(z)] + s_2\exp[\beta_2(z)]\} \times \exp[-j(\Gamma_r z\cos\phi_g + \phi_g)/2], \tag{4a}$$

$$r(z) = \{r_1\exp[\beta_1(z)] + r_2\exp[\beta_2(z)]\} \times \exp[j(\Gamma_r z\cos\phi_g + \phi_g)/2], \tag{4b}$$

where r_i and s_i are constants depending on the boundary conditions and $\beta_i(z)$ are functions of z to be determined. By substituting Eqs. (4) into Eqs. (3) and equating the summed coefficients that are associated with the exponentials of $\exp[\beta_1(z)]$ and $\exp[\beta_2(z)]$ to zero, we have

$$s_i\left[\beta_i'(z) - \frac{j\Gamma_r\cos\phi_g}{2} - j\vartheta\right] = \frac{j\Gamma_e}{[1 + m_1\exp(2\Gamma_r z\sin\phi_g)]^{1/2}}r_i, \quad i = 1, 2, \tag{5a}$$

$$r_i\left[[\beta_i'(z) - \frac{j\Gamma_r\cos\phi_g}{2}\right] = -\frac{j\Gamma_e}{[1 + m_1\exp(2\Gamma_r z\sin\phi_g)]^{1/2}}s_i, \quad i = 1, 2, \tag{5b}$$

or

$$[\beta_i'(z)]^2 - j\vartheta\beta_i'(z) + \frac{\Gamma_r^2\cos^2\phi_g}{4} + \frac{\vartheta\Gamma_r\cos\phi_g}{2} = ff^*, \quad i = 1, 2, \tag{6a}$$

$$ff^* = \frac{\Gamma_e^2}{1 + m_1\exp(2\Gamma_r z\sin\phi_g)}. \tag{6b}$$

The solutions for $\beta_i(z)$, $i = 1, 2$, are rather complicated, as shown in the appendix, but at this moment they can be written in the following simple forms:

$$\beta_{1,2}(z) = \frac{j\vartheta z}{2} \pm \beta(z), \tag{7a}$$

where

$$\beta(z) = \frac{1}{2}\int_0^z\left[-(\vartheta + \Gamma_r\cos\phi_g)^2 + \frac{4\Gamma_e^2}{1 + m_1\exp(2\Gamma_r w\sin\phi_g)}\right]^{1/2}dw. \tag{7b}$$

By substituting Eqs. (7) back into Eqs. (4), we can write the diffracted (signal) beam as

$$s(z) = c_1\exp[j(\vartheta z - \Gamma_r z\cos\phi_g - \phi_g)/2] \times \sinh[\beta(z) + c_2], \tag{8}$$

where the new constants c_1 and c_2 can be found from the boundary conditions of $s(0) = 0$ and $r(L) = 1$. The results are

$$c_1 = \frac{j\exp[-j(\vartheta L + \Gamma_r L\cos\phi_g + \phi_g)/2]}{-jA\sinh[\beta(L)] + (1 - A^2)^{1/2}\cosh[\beta(L)]}, \tag{9a}$$

$$c_2 = 0, \tag{9b}$$

where

$$A = \frac{b}{2\Gamma_e}(\vartheta + \Gamma_r\cos\phi_g), \tag{9c}$$

$$b = [1 + m_1\exp(2\Gamma_r L\sin\phi_g)]^{1/2}. \tag{9d}$$

Thus the diffraction efficiency of a reflection PR hologram can be written as

$$\eta = s(L)s^*(L) = \left| \frac{1}{-jA + (1 - A^2)^{1/2}\coth[\beta(L)]} \right|^2, \tag{10}$$

where $\beta(L)$ is given by Eqs. (A11) (see appendix).

Notice that, when the index perturbation is small, i.e., $\Gamma_r \sim \Gamma_e \sim \Gamma \to 0$, Eq. (10) reduces to Kogelnik's formula:

$$\eta = \left| -j\frac{\vartheta}{2\Gamma} + \left[1 - \left(\frac{\vartheta}{2\Gamma}\right)^2\right]^{1/2} \times \coth\left\{\frac{\Gamma L}{2}\left[1 - \left(\frac{\vartheta}{2\Gamma}\right)^2\right]^{1/2}\right\} \right|^{-2}. \tag{11}$$

Diffraction Properties of the Photorefractive Hologram

Time Evolution

It can be readily verified that, when the Bragg condition is satisfied (i.e., $\vartheta = 0$) and the phase shift of the grating is equal to $\pi/2$ (which is usually the case for PR crystals such as $BaTiO_3$), Eq. (10) reduces to[7]

$$\eta(\vartheta = 0, \phi_g = \pi/2) = \tanh^2\left(\Gamma_e L - \frac{\Gamma_e}{\Gamma_r}\ln\left\{\frac{1 + [1 + m_1 \exp(2\Gamma_r L)]^{1/2}}{1 + (1 + m_1)^{1/2}}\right\}\right). \tag{12}$$

From this equation we see that the diffraction efficiency will never reach 100% even though the crystal is lossless and also that the achievable diffraction efficiency is determined by the incident reference-to-signal beam ratio m_0 (and in general the grating phase shift ϕ_g as well):

$$\eta_\infty = \tanh^2\left[\ln\frac{(m_{1,\infty})^{1/2}}{1 + (1 + m_{1,\infty})^{1/2}}\right], \tag{13a}$$

where

$$m_{1,\infty} = m_1(\Gamma_r \to \infty) = \frac{m_0^2}{4(m_0 + 1)}. \tag{13b}$$

For example, if $m_0 = 1$, the maximum diffraction efficiency would be $\eta_\infty \approx 88.88\%$. Figure 4 shows the temporal behavior of the diffraction efficiency for $m_0 = 10$ and $m_0 = 100$ along with the calculations for non-PR holograms based on Ref. 9. Notice that as the intensity ratio increases, there is a significant decrease in the achievable diffraction efficiency for the PR holograms. However, for non-PR materials, the diffraction efficiency can reach to the maximum of 100% for sufficiently long recording time. In Fig. 5 we plotted the maximum achievable diffraction efficiency as a function of incient reference-to-signal beam ratio based on Eqs. (13), which show that the maximum diffraction efficiency decreases as m_0 increases.

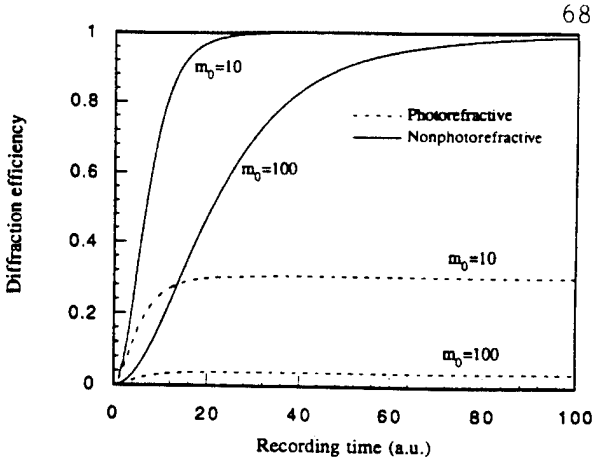

Fig. 4. Diffraction efficiency as a function of recording time (single exposure): (a) $m_0 = 10$, (b) $m_0 = 100$. In both cases, $\phi_g = \pi/2$.

Wavelength and/or Angular Sensitivity

Equation (10) also provides a description of the wavelength and/or angular sensitivities of the PR holographic grating, which are important for the evaluation of the spectral performance and the cross-talk noise problem. Taking a wavelength-multiplexed hologram as an example, we plotted the normalized diffraction efficiency as a function of wavelength deviation, which is based on Eq. (10), in Fig. 6 (solid curves) with $\theta = 0°$, $\phi_g = \pi/2$, $\lambda = 614.7$ nm, $L = 2$ mm, and $m_0 = 100$. Since the temporal aspect is not the major argument for this case and a single exposure ($\Gamma_e = \Gamma_r$) can be assumed for simplicity, we take $\Delta n_0 = 1 \times 10^{-5}$, 3×10^{-4}, and 5×10^{-4} in Figs. 6(a), 6(b), and 6(c), respectively. For comparison the normalized diffraction efficiencies for non-PR holograms (envelope only) using Kogelnik's formula[9] are also plotted in the figures with dashed curves.

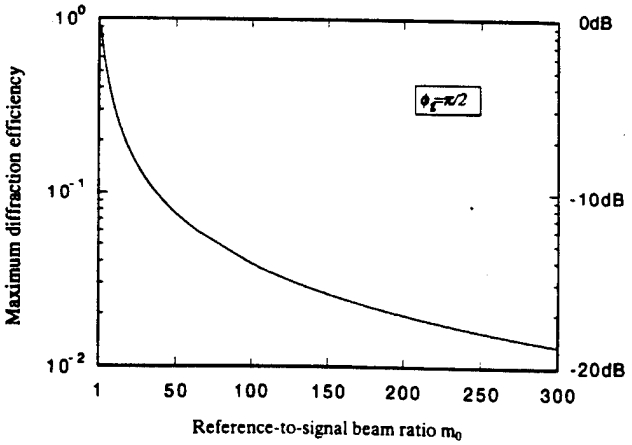

Fig. 5. Maximum achievable diffraction efficiency as a function of beam ratio m_0.

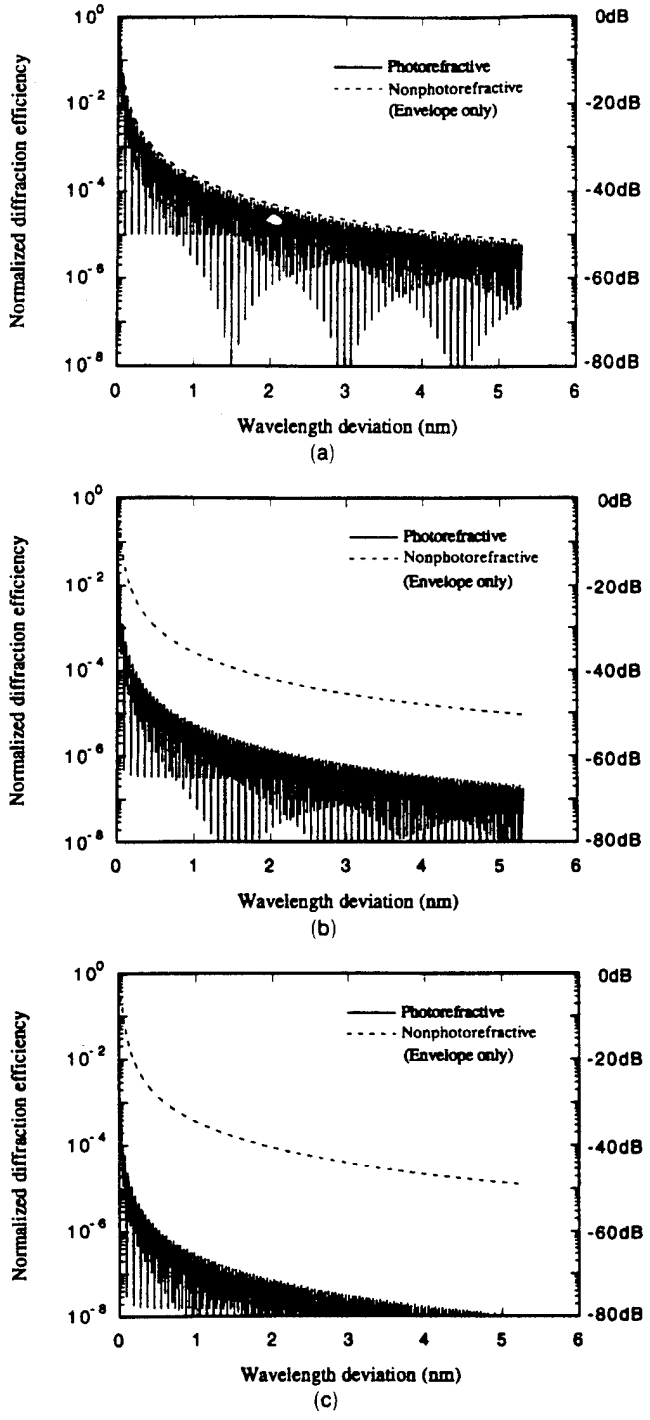

Fig. 6. Diffraction efficiencies as a function of wavelength deviation $\Delta\lambda$, given $\theta = 0°$, $\phi_g = \pi/2$, $\lambda = 614.7$ nm, $L = 2$ mm, and $m_0 = 100$: (a) $\Delta n_0 = 1 \times 10^{-5}$, (b) $\Delta n_0 = 3 \times 10^{-4}$, (c) $\Delta n_0 = 5 \times 10^{-4}$.

In view of Fig. 6 we find that for a small index perturbation, Eq. (10) behaves closely to Kogelnik's formula [see Fig. 6(a)]. However, as the index perturbation (i.e., the coupling strength) increases, Eq. (10) gives a much higher wavelength sensitivity than Kogelnik's formula [see Figs. 6(b) and 6(c)]. The discrepancy between them can be as high as two or more orders of magnitude, depending on the index perturbation and the reference-to-signal beam ratio. As a matter of fact, the envelope of Eq. (10) for a large dephasing measure ϑ is

$$\eta_{\text{envelope}} \approx \frac{1}{A^2} \approx \frac{4\Gamma_r^2}{b^2}\frac{1}{\vartheta^2}, \tag{14}$$

where b, as defined by Eq. (9d), is actually the inverse of the index modulation ratio $m(z)$ at $z = L$ [see also Eq. (3a)]. On the other hand the envelope of diffraction efficiency for non-PR holograms[9] in terms of the notation used here is

$$\eta_{\text{envelope,Kogelnik}} \approx \left(\frac{\nu}{\xi}\right)^2 = \frac{4\Gamma_r^2}{b_0^2}\frac{1}{\vartheta^2}, \tag{15}$$

where $b_0 = (m_0 + 1)/2(m_0)^{1/2}$ is the inverse of index modulation ratio $m(z)$ at $z = 0$. Notice that b_0 is also the inverse of the commonly defined uniform modulation depth. Thus for a small index perturbation (i.e., $\Gamma_r \to 0$), from Eqs. (2), (14), and (15), we have

$$\frac{\eta_{\text{envelope,Kogelnik}}}{\eta_{\text{envelope}}} \sim \left(\frac{b}{b_0}\right)^2 \sim \frac{1 + m_1(\Gamma_r \to 0)}{b_0^2} = \frac{(m_0 + 1)^2/4m_0}{b_0^2} = 1. \tag{16}$$

Therefore the diffraction efficiency for PR and non-PR holograms should approach each other, as shown in Fig. 6(a). However, for a large index perturbation, we have

$$\frac{\eta_{\text{envelope,Kogelnik}}}{\eta_{\text{envelope}}} \sim \left(\frac{b}{b_0}\right)^2 \sim \frac{m_{1,\infty}\exp(2\Gamma_r L \sin\phi_g)}{b_0^2} = \left(\frac{m_0}{m_0 + 1}\right)^3 \exp(2\Gamma_r L \sin\phi_g), \tag{17}$$

which can be as large as one or more orders, depending on the coupling strength (as well as the intensity ratio m_0 if it is close to 1). Thus the diffraction efficiency for PR holograms would be substantially smaller than that for non-PR holograms.

The result presented here thus offers an explanation for the apodization phenomenon as recently found by Rakuljic *et al.*[4] The analysis they employed for the relative cross-talk measurement is based on the distributed feedback theory, in which a uniform grating is assumed, and is basically similar to relation (15). Their experimental results gave a cross-talk measurement almost one order in magnitude smaller than the analytical result. The discrepancy, they claim, is caused by an "effective apodization whose origin is not fully understood." Notice that a higher wavelength deviation sensitivity (or lower cross-talk noise) for PR holograms would be expected than for non-PR holograms; according to the preceding discussions, one would have a theoretical prediction closer

to the experimental data if the formulas developed above were adopted. Although we do not know the exact reference-to-signal beam ratio and the index perturbation that Rakuljic *et al.* used, the calculation based on Eq. (10) with $m_0 = 100$ and $\Delta n_0 = 3 \times 10^{-4}$, together with $L = 2$ mm and $\lambda = 614.7$ nm, can serve as a good theoretical fit for their experimental data.

Conclusion

In summary, we have studied the diffraction properties of a reflection PR hologram using a coupled-recording-wave approach. A closed-form expression for the diffraction efficiency as a function of wavelength and angular deviation, as well as of temporal variation, is obtained. The new formula predicts a lower achievable diffraction efficiency and higher wavelength and angular sensitivities than Kogelnik's formula for non-PR holograms. This result offers an explanation for the apodization phenomenon previously found by Rakuljic *et al.*

Appendix

Notice that for a given dephasing measurement ϑ, the integrand of Eq. (7c) may become imaginary as the integration is carried from 0 to z. Let us rewrite Eq. (7c) as

$$\beta(z) = \beta_r(z) + j\beta_i(z), \tag{A1a}$$

with

$$\beta_r(z) = \frac{1}{2}\int_0^{z_1}\left[-\tilde{\vartheta}^2 + \frac{4\Gamma_e^2}{1 + m_1 \exp(2\Gamma_r w \sin\phi_g)}\right]^{1/2} dw, \tag{A1b}$$

$$\beta_i(z) = \frac{1}{2}\int_{z_1}^{z}\left[\tilde{\vartheta}^2 - \frac{4\Gamma_e^2}{1 + m_1 \exp(2\Gamma_r w \sin\phi_g)}\right]^{1/2} dw, \tag{A1c}$$

where $\tilde{\vartheta} = \vartheta + \Gamma_r \cos(\phi_g)$, and z_1 is the zero-crossing point of the integrand of Eq. (7c), i.e.,

$$\tilde{\vartheta} = \frac{2\Gamma_e}{[1 + m_1 \exp(2\Gamma_r z_1 \sin\phi_g)]^{1/2}}. \tag{A1d}$$

Case A

If $z_1 \geq z$, i.e., $\tilde{\vartheta} \leq 2\Gamma_e/b$ with $b = [1 + m_1 \exp(2\Gamma_r z \sin\varphi_g)]^{1/2}$, then $\beta(z)$ is a real quantity, i.e., $\beta_i(z) = 0$, and the integration limit for $\beta_r(z)$ is from 0 to z. Changing the variable by defining a new variable,

$$t = \left[-\tilde{\vartheta}^2 + \frac{4\Gamma_e^2}{1 + m_1 \exp(2\Gamma_r w \sin\phi_g)}\right]^{1/2}, \tag{A2}$$

and substituting it into Eq. (A1b) yields

$$\beta_r(z) = \frac{1}{2\Gamma_r \sin\phi_g}\left[-\frac{(4\Gamma_e^2 - \tilde{\vartheta}^2)^{1/2}}{2} \times \ln\frac{(4\Gamma_e^2 - \tilde{\vartheta}^2)^{1/2} + t}{(4\Gamma_e^2 - \tilde{\vartheta}^2)^{1/2} - t} + \tilde{\vartheta}\tan^{-1}\frac{t}{\tilde{\vartheta}}\right]_{t(w=0)}^{t(w=z)}, \tag{A3}$$

Note that $\tilde{\vartheta} \leq 2\Gamma_e/b$, and thus $\vartheta < 2\Gamma_e$, since $b \geq 1$.

To simplify the notation, we introduce the following symbols: $\gamma = [|4\Gamma_e^2 - \tilde{\vartheta}^2|]^{1/2}$, $a = (1 + m_1)^{1/2}$, $c = [|1 - m_1(\tilde{\vartheta}/\gamma)^2|]^{1/2}$, and $d = [|1 - m_1(\tilde{\vartheta}/\gamma)^2 \exp(2\Gamma_r z \sin\phi_g)|]^{1/2}$. Then, the integration limit in terms of t can be written as

$$t(w = z) = \gamma\frac{d}{b}, \qquad t(w = 0) = \gamma\frac{c}{a}, \tag{A4}$$

Now, changing back to the original variable and simplifying leads to the result

$$\beta_r(z) = \frac{\gamma z}{2} + \frac{1}{2\Gamma_r \sin\phi_g} \times \left[\gamma \ln\frac{a + c}{b + d} + \tilde{\vartheta}\tan^{-1}\frac{\tilde{\vartheta}(a^2 - b^2)}{\gamma(bd + ac)}\right]. \tag{A5}$$

Case B

If $z_1 \leq 0$, i.e., $\tilde{\vartheta} \geq 2\Gamma_e/a$ with $1 \leq a = (1 + m_1) \leq b$, then $\beta(z)$ is an imaginary quantity, i.e., $\beta_r(z) = 0$, whereas the integration limit for $\beta_i(z)$ is from 0 to z. Following a procedure similar to preceding, we obtain

$$\beta_i(z) = \frac{1}{2\Gamma_r \sin\phi_g}\left[\frac{-(\tilde{\vartheta}^2 - 4\Gamma_e^2)^{1/2}}{2} \times \ln\frac{(\tilde{\vartheta}^2 - 4\Gamma_e^2)^{1/2} + t}{(\tilde{\vartheta}^2 - 4\Gamma_e^2)^{1/2} - t} + \frac{\tilde{\vartheta}}{2}\ln\frac{\tilde{\vartheta} + t}{\tilde{\vartheta} - t}\right]_{t(w=0)}^{t(w=z)}$$

if $\vartheta > 2\Gamma_e$, (A6a)

$$= \frac{1}{2\Gamma_r \sin\phi_g}\left[-(4\Gamma_e^2 - \tilde{\vartheta}^2)^{1/2} \times \tan^{-1}\frac{t}{(4\Gamma_e^2 - \tilde{\vartheta}^2)^{1/2}} + \frac{\tilde{\vartheta}}{2}\ln\frac{\tilde{\vartheta} + t}{\tilde{\vartheta} - t}\right]_{t(w=0)}^{t(w=z)}$$

if $\vartheta \leq 2\Gamma_e$, (A6b)

Again, for $\vartheta \leq 2\Gamma_e$ the integration limit in terms of t is the same as those given by Eq. (A4), but for $\vartheta > 2\Gamma_e$ it reads as

$$t(w = z) = \gamma\frac{f}{b}, \qquad t(w = 0) = \gamma\frac{e}{a}, \tag{A7}$$

where $e = [1 + (\tilde{\vartheta}/\gamma)^2 m_1]^{1/2}$ and $f = [1 + (\tilde{\vartheta}/\gamma)^2 m_1 \exp(2\Gamma_r z \sin\phi_g)]^{1/2}$. Therefore

$$\beta_i(z) = \begin{cases} \dfrac{\gamma z}{2} + \dfrac{1}{2\Gamma_r \sin\phi_g}\left(\gamma \ln\dfrac{a+e}{b+f} + \tilde{\vartheta}\ln\dfrac{\tilde{\vartheta}b + \gamma f}{\tilde{\vartheta}a + \gamma e}\right), \\ \quad \text{if } \vartheta > 2\Gamma_e \\ \dfrac{1}{2\Gamma_r \sin\phi_g}\left(\gamma \tan^{-1}\dfrac{bc-ad}{ab+dc} + \tilde{\vartheta}\ln\dfrac{\tilde{\vartheta}b + \gamma d}{\tilde{\vartheta}a + \gamma c}\right), \\ \quad \text{if } \vartheta \le 2\Gamma_e \end{cases} \tag{A8}$$

$$\beta_i(z) = \frac{1}{2\Gamma_r \sin\phi_g}\left(-\gamma \tan^{-1}\frac{d}{b} + \frac{\tilde{\vartheta}}{2}\ln\frac{\tilde{\vartheta}b + \gamma d}{\tilde{\vartheta}b - \gamma d}\right). \tag{A10b}$$

For convenience we rewrite the final results as follows:

$$\beta(L) = \beta_r(L) + j\beta_i(L), \tag{A11a}$$

where

$$\beta_r(L) = \begin{cases} \dfrac{\gamma L}{2} + \dfrac{1}{2\Gamma_r \sin\phi_g}\left[\gamma \ln\dfrac{a+c}{b+d} + \tilde{\vartheta}\tan^{-1}\dfrac{\tilde{\vartheta}(a^2-b^2)}{\gamma(bd+ac)}\right] & \text{if } \tilde{\vartheta} \le \dfrac{2\Gamma_e}{b} \\ \dfrac{1}{2\Gamma_r \sin\phi_g}\left(\dfrac{\gamma}{2}\ln\dfrac{a+c}{a-c} - \tilde{\vartheta}\tan^{-1}\dfrac{\gamma c}{\tilde{\vartheta}a}\right) & \text{if } \dfrac{2\Gamma_e}{b} < \tilde{\vartheta} < \dfrac{2\Gamma_e}{a} \\ 0 & \text{if } \tilde{\vartheta} \ge \dfrac{2\Gamma_e}{a} \end{cases}, \tag{A11b}$$

$$\beta_i(L) = \begin{cases} 0 & \text{if } \tilde{\vartheta} \le \dfrac{2\Gamma_e}{b} \\ \dfrac{1}{2\Gamma_r \sin\phi_g}\left(-\gamma \tan^{-1}\dfrac{d}{b} + \dfrac{\tilde{\vartheta}}{2}\ln\dfrac{\tilde{\vartheta}b + \gamma d}{\tilde{\vartheta}b - \gamma d}\right) & \text{if } \dfrac{2\Gamma_e}{b} < \tilde{\vartheta} < \dfrac{2\Gamma_e}{a} \\ \dfrac{1}{2\Gamma_r \sin\phi_g}\left(\gamma \tan^{-1}\dfrac{bc-ad}{ab+dc} + \tilde{\vartheta}\ln\dfrac{\tilde{\vartheta}b + \gamma d}{\tilde{\vartheta}a + \gamma c}\right) & \text{if } \dfrac{2\Gamma_e}{a} \le \tilde{\vartheta} < 2\Gamma_e \\ \dfrac{\gamma L}{2} + \dfrac{1}{2\Gamma_r \sin\phi_g}\left(\gamma \ln\dfrac{a+e}{b+f} + \tilde{\vartheta}\ln\dfrac{\tilde{\vartheta}b + \gamma f}{\tilde{\vartheta}a + \gamma e}\right) & \text{if } \tilde{\vartheta} \ge 2\Gamma_e \end{cases}, \tag{A11c}$$

Case C

Finally, if $0 < z_1 < z$, i.e., $2\Gamma_e/b < \tilde{\vartheta} < 2\Gamma_e/a$, then $\beta(z)$ is a complex quantity in terms of z. The integration results for real and imaginary parts are similar to Eqs. (A3) and (A6b), respectively, but with new limits of the integration:

$$t(w = z_1) = 0, \quad t(w = 0) = \gamma\frac{c}{a} \quad \text{for real part;}$$

$$t(w = z) = \gamma\frac{d}{b}, \quad t(w = z_1) = 0 \quad \text{for imaginary part.} \tag{A9}$$

Therefore

$$\beta_r(z) = \frac{1}{2\Gamma_r \sin\phi_g}\left(\frac{\gamma}{2}\ln\frac{a+c}{a-c} - \tilde{\vartheta}\tan^{-1}\frac{\gamma c}{\tilde{\vartheta}a}\right), \tag{A10a}$$

with

$$\gamma = (|4\Gamma_e^2 - \tilde{\vartheta}^2|)^{1/2}, \tag{A11d}$$

$$\tilde{\vartheta} = \vartheta + \Gamma_r \cos\phi_g, \tag{A11e}$$

$$a = (1 + m_1)^{1/2}, \tag{A11f}$$

$$b = [1 + m_1 \exp(2\Gamma_r L \sin\phi_g)]^{1/2}, \tag{A11g}$$

$$c = [|1 - m_1(\tilde{\vartheta}/\gamma)^2|]^{1/2}, \tag{A11h}$$

$$d = [|1 - m_1(\tilde{\vartheta}/\gamma)^2 \exp(2\Gamma_r L \sin\phi_g)|]^{1/2}, \tag{A11i}$$

$$e = [1 + (\tilde{\vartheta}/\gamma)^2 m_1]^{1/2}, \tag{A11j}$$

$$f = [1 + (\tilde{\vartheta}/\gamma)^2 m_1 \exp(2\Gamma_r L \sin\phi_g)]^{1/2}. \tag{A11k}$$

This work was supported by the Advanced Research Projects Agency through the U.S. Army Research Office under contract DAAL 03-92-G-0328.

References

1. S. Wu, Q. Song, A. Mayers, D. A. Gregory, and F. T. S. Yu, "Reconfigurable interconnections using photorefractive holograms," Appl. Opt. **29,** 1118–1125 (1990).
2. F. T. S. Yu and S. Jutamulia, *Optical Signal Processing, Computing, and Neural Networks* (Wiley, New York, 1992), Chap. 7, pp. 249–286.
3. D. Psaltis, A. Brady, and K. Wagner, "Adaptive optical networks using photorefractive crystal," Appl. Opt. **27,** 1752–1759 (1988).
4. G. A. Rakuljic, V. Leyva, and A. Yariv, "Optical data storage by using orthogonal wavelength-multiplexed volume holograms," Opt. Lett. **17,** 1471–1473 (1992).
5. D. W. Vahey, "A nonlinear coupled-wave theory of holographic storage in ferroelectric materials," J. Appl. Phy. **46,** 3510–3515 (1975).
6. P. Yeh, "Two-wave mixing in nonlinear media," IEEE J. Quantum Electron. **23,** 484–519 (1989).
7. H. Zhou, F. Zhao, and F. T. S. Yu, "Effects of recording-erasure dynamics on storage capacity of a wavelength-multiplexed reflection-type photorefractive hologram," Appl. Opt. **33,** (1994).
8. E. S. Maniloff and K. M. Johnson, "Maximized photorefractive holographic storage," J. Appl. Phys. **70,** 4702–4707 (1991).
9. H. Kogelnik, "Coupled wave theory for thick holograms," Bell Syst. Tech. J. **48,** 2909–2947 (1969).
10. D. L. Staebler and J. J. Amodei, "Coupled-wave analysis of holographic storage in $LiNbO_3$," J. Appl. Phys. **43,** 1042 (1972).
11. P. Yeh, *Introduction to Photorefractive Nonlinear Optics* (Wiley, New York, 1993), Chap. 7, pp. 249–286.
12. E. S. Maniloff and K. S. Johnson, "Effects of scattering on the dynamics of holographic recording and erasure in photorefractive lithium niobate," J. Appl. Phys. **73,** 541–547 (1993).
13. M. Horowitz, R. Daisy, and B. Fischer, "Signal-to-pump ratio dependence of buildup and decay rates in photorefractive nonlinear two-beam coupling," J. Opt. Soc. Am. B **9,** 1685–1688 (1992).
14. J. Baquedano, M. Carraascosa, L. Arizmendi, and J. M. Cabrera, "Erasure kinetics and spectral dependence of the photorefractive effect in Fe:$LiNbO_3$," J. Opt. Soc. Am. B **4,** 309–312 (1987).

Appendix 10.9

Anisotropic Intrasignal Couplings in Photorefractive $LiNbO_3$

ANISOTROPIC INTRASIGNAL COUPLING IN PHOTOREFRACTIVE $LiNbO_3$

Dazun Zhao, Hanying Zhou, Feng Zhao, and Francis T. S. Yu
Department of Electrical Engineering
The Pennsylvania State University
University Park, Pennsylvania 16802

KEY TERMS

Photorefractive crystal, holography, intrasignal coupling

ABSTRACT

Intrasignaling coupling in a $LiNbO_3$ photorefractive crystal is studied. It is shown that the anisotropy nature of the effective electro-optic coefficient of this crystal results in an orientation-dependent intrasignal coupling. Analytical solutions for one-dimensional intrasignal coupling are derived for a-*axis and* b-*axis orientations, which enables us to estimate the maximum beam field angle and the maximum crystal thickness for a given intensity distortion due to the coupling. The results are thus illustrative to applications of this crystal in areas such as holographic data storage, interconnection, spatial mode conversion, et cetera.* © *1994 John Wiley & Sons, Inc.*

1. INTRODUCTION

Photorefractive (PR) materials have shown a wide range of applications such as large-capacity holographic memory, massive interconnection, spatial mode conversion, et cetera [1–3]. These applications, however, usually involve intrasignal coupling as light beams propagate through a PR crystal. The intrasignal coupling problem has been addressed for PR crystals such as SBN or $BaTiO_3$ [4, 5], where the coupling was found symmetric with respect to the c axis of the crystal. The $LiNbO_3$ crystal is widely used, so this article will examine the intrasignal coupling in this type of crystal, which must be orientation dependent due to its anisotropic nature in terms of the effective electro-optic coefficient. Analytical solutions for one-dimensional intrasignal coupling are derived for a-axis and b-axis orientations, which enables us to estimate the maximum beam field angle and the maximum crystal thickness for a given intensity distortion due to the coupling.

2. ORIENTATION-DEPENDENT INTRASIGNAL COUPLING

Referring to Figure 1, we assume that a number of (coherent) plane waves, each with an (external) angle θ_{mA} (or internal angle θ_m), are incident on a thick $LiNbO_3$ crystal. These plane waves can be regarded as the signal itself in a mode convertor

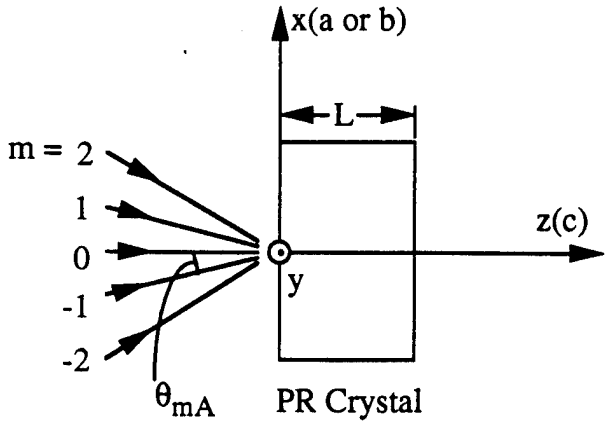

Figure 1 Geometry for intrasignal coupling in PR crystal

[3, 5], or as generated by an input pixel array in a Fourier-transform holographic system [6, 7]. These plane waves will undergo multi-wave-mixing process (intrasignal coupling) within the crystal, resulting in a (relative) intensity distortion after they have propagated through the crystal. Because the crystal is anisotropic in terms of the effective electrooptic coefficient, the intrasignal coupling in this crystal must be orientation dependent. To address this problem, we shall consider a one-dimensional signal in a $LiNbO_3$ crystal of the a-axis orientation (called case A) and of the b-axis orientation (called case B), respectively. In both cases, the c axis of the crystal is parallel to the z axis (see Figure 1), and the signal is of ordinary polarization for simplicity. Such configuration is commonly used in a reflection holographic system or in a mode conversion system for this crystal.

The complex light field inside the crystal can be written as

$$E(x, z) = \sum_m A_m(z) \exp[ik(s_m x + c_m z)], \qquad x = x \text{ or } y, \tag{1}$$

where A_m denotes the amplitude of the mth plane wave, $s_m = \sin\theta_m$, $c_m = \cos\theta_m$, and $k = 2\pi n_o/\lambda$ with n_o representing the (ordinary) refractive index of the crystal and λ the wavelength of the signal beam. The interference field of these plane waves produces a refractive index perturbation via the photorefractive effect with the result

$$\Delta n = \frac{1}{2I} \sum_m \sum_{n \neq m} u_{mn} A_m A_n^* \exp\{ik[(s_m - s_n)x + (c_m - c_n)z]\} + \text{c.c.}, \quad x = x \text{ or } y, \tag{2a}$$

where c.c. denotes the complex conjugate;

$$I = \sum_m A_m A_m^* = \sum_m I_m, \tag{2b}$$

$$u_{mn} = u_{nm}^* = -\frac{\beta}{2} r_{\text{eff}} n_o^3 E_{mn}. \tag{2c}$$

β is a ratio of Δn relative to its saturation value Δn_s (i.e., $\Delta n = \beta \Delta n_s$), E_{mn} is the space charge field induced by the mth and the nth plane waves, and r_{eff} the effective electrooptic coefficient. For $LiNbO_3$, which has a point group symmetry of $3m$, this coefficient can be found as

$$(r_{\text{eff}})_a = -r_{13} \sin\frac{\theta_m + \theta_n}{2}, \qquad \text{for case A.} \tag{2d}$$

and

$$(r_{\text{eff}})_b = -r_{22} \cos\frac{\theta_m + \theta_n}{2} - r_{13} \sin\frac{\theta_m + \theta_n}{2} \approx -r_{22} \cos\frac{\theta_m + \theta_n}{2}, \qquad \text{for case B,} \tag{2e}$$

where we have assumed the small angle approximation; that is, $-6° \leq \theta_m, \theta_n \leq 6°$.

By substituting Eqs. (1) and (2) into the scalar wave equation and using the slowly varying field approximation, the

coupled-wave equations can be derived as [4, 5, 8, 9]

$$c_m \frac{dI_m}{dz} = -\frac{4\pi n_o}{\lambda I} \sum_{n \neq m} u_{nm}^{(i)} I_m I_n, \tag{3a}$$

$$c_m \frac{d\phi_m}{dz} = \frac{2\pi n_o}{\lambda I} \sum_{n \neq m} u_{mn}^{(r)} I_n, \tag{3b}$$

where ϕ_m is the phase of the mth plane wave, and $u_{mn}^{(i)}$ and $u_{mn}^{(r)}$ are the imaginary and the real parts of u_{mn}, respectively. Because the photovoltaic field in the direction perpendicular to the c axis and the diffusion field is small compared with the saturation field, the expression for E_{mn}, when no external field is applied, would be [8]

$$E_{mn} = i \frac{4\pi n_o}{\lambda} \frac{k_B T}{e} \sin \frac{\theta_m - \theta_n}{2}, \tag{4}$$

where k_B is the Boltzmann constant, T is the absolute temperature, and e is the electron charge. In this case, u_{mn} becomes purely imaginary and its real part $u_{mn}^{(r)}$ is negligibly small. For this reason we will consider only the intensity part [i.e., Eq. (3a)] of the coupled equations in the following.

By substituting Eqs. (2) and (4) into Eq. (3), the coupled-wave equations become

$$c_m \frac{1}{I_m} \frac{dI_m}{dz} = 2\gamma_a c_m - \frac{2}{I} \gamma_a \sum_n c_n I_n, \quad \text{for case A,} \tag{5a}$$

with

$$\gamma_a = \frac{\beta}{2} r_{13} \left(\frac{2\pi n_o}{\lambda}\right)^2 n_o^4 \frac{k_B T}{e}. \tag{5b}$$

Similarly, we have,

$$c_m \frac{1}{I_m} \frac{dI_m}{dz} = \frac{2}{I} \gamma_b \sum_n s_n I_n - 2\gamma_b s_m, \quad \text{for case B,} \tag{6a}$$

with

$$\gamma_b = \frac{\beta}{2} r_{22} \left(\frac{2\pi n_o}{\lambda}\right)^2 n_o^4 \frac{k_B T}{e}. \tag{6b}$$

The solutions of Eqs. (5) and (6) are

$$I_m(z) = I_m(0) \exp\left[2\gamma_a z - \frac{2}{c_m I} \gamma_a \int_0^z \left(\sum_n c_n I_n\right) dz\right], \quad \text{for case A,} \tag{7}$$

and

$$I_m(z) = I_m(0) \exp\left[\frac{2}{c_m I} \gamma_b \int_0^z \left(\sum_n s_n I_n\right) dz - 2\gamma_b z \tan \theta_m\right], \quad \text{for case B,} \tag{8}$$

where $I_m(0)$ is the intensity of the mth plane wave at its incidence upon the crystal. Because both quantities, $\Sigma\, c_n I_n$ in Eq. (7) and $\Sigma\, s_n I_n$ in Eq. (8), are independent of m, they can be determined from Eqs. (7) and (8), respectively, by the energy conservation law. Then, by making the substitution $c_m = 1 - \delta_m$, where $\delta_m << 1$ (for small angle approximation), and after some algebra manipulations, the expression for $I_m(z)$ can be finally found as,

$$I_m(z) = I_m(0) \exp\left(-2\gamma_a z \frac{c_a - c_m}{c_m}\right), \quad \text{for case A,} \tag{9a}$$

with

$$c_a = \frac{I}{\sum_n I_n(0)/c_n}, \tag{9b}$$

and

$$I_m(z) = I_m(0) \exp(-2\gamma_b z \tan \theta_m) \times \left[\frac{I}{\sum_n I_n(0) \exp(-2\gamma_b z \tan \theta_n)}\right]^{c_b/c_m}, \quad \text{for case B,} \tag{10a}$$

with

$$c_b = \frac{\sum_n I_n(0) \exp(-2\gamma_b z \tan \theta_n)}{\sum_n I_n(0) \exp(-2\gamma_b z \tan \theta_n)/c_n}, \tag{10b}$$

where c_a and c_b represent the average of c_m for cases A and B, respectively.

In view of Eqs. (9) and (10), we see that in both cases, the relative intensity distribution of the plane waves has been changed (distorted) after they have propagated through the PR crystal. However, this change has different characteristics in two cases. For case A, the exponential quantity in Eq. (9) is cosine (of the beam field angle) dependent, which is an even function of the angle; while for case B, the exponential in Eq. (10) is tangent dependent, which is an odd function. Figures 2 and 3 show the output beam intensities as functions of crystal thickness z and of (external) beam field angle θmA, respectively. In both figures, we have used, for simplicity, seven plane waves with uniform input intensities. The adjacent angular separation is 4° in air and $\gamma_a = 4.75\ \text{cm}^{-1}$ for case A and $\gamma_b = 1.88\ \text{cm}^{-1}$ for case B [the relative value of γ_a and γ_b corresponds to the ratio of the electro-optical coefficients r_{13} and r_{22}; see Eqs. (5b) and (6b)]. From Figures 2(b) and 3(b), we see that the energy is coupled *inward* in case A from beams with larger field angles to beams with smaller ones. (The coupling will be inverted if the c-axis direction of the crystal is inverted.) In other words, the coupling is symmetric with respect to the c axis of the crystal in case A. This is similar to the intrasignal coupling behavior previously found in crystals such as $BaTiO_3$ and SBN [4, 9]. However, for case B [see Figures 2(c) and 3(c)], the energy is transferred *downward* from beams with positive field angles to those with negative ones. The intrasignal coupling has an asymmetric behavior with respect to the c axis of the crystal in this case. Quantitatively, we note that the coupling strength for case B is much larger than that for case A. This can be explained by the fact that the effective electro-optic coefficient for case B is directly proportional to the cosine of the field angle, while for case A, it is directly proportional to the sine of the field angle [see Eqs. (2d) and (2e)]. Because the field angle is

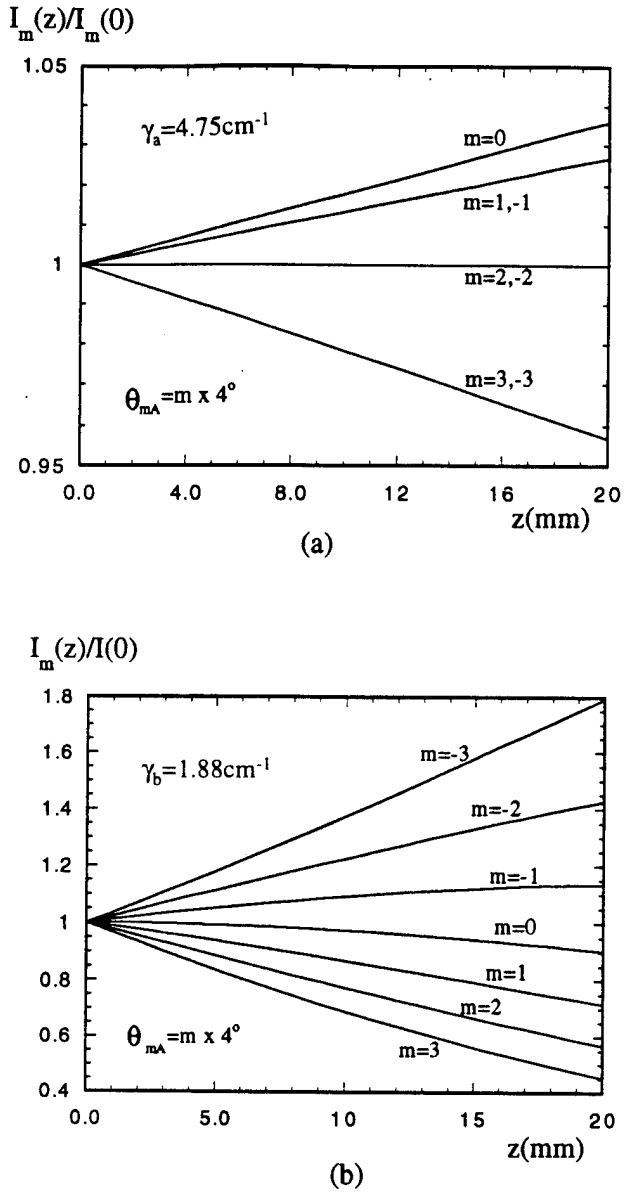

Figure 2 Energy transfer as a function of crystal thickness z. (a). Case A. (b) case B

assumed small, the effective electro-optic coefficient for case A can be considered negligible in practice.

3. DISCUSSION

We can give a rough estimation on the maximum field angle θ_M and on the maximum crystal thickness L for a given relative intensity distortion (due to the intrasignal coupling). From Eqs. (9) and (10), for a maximum relative intensity distortion less than δ; that is, $|I_m(L, \theta_M) - I_m(0)|/I_m(0) \leq \delta$, we have,

$$|L\theta_M^2| \leq 3\delta/2\gamma_a, \qquad \text{for case A,} \tag{11}$$

and

$$|L \tan \theta_M| \leq \delta/2\gamma_b, \qquad \text{for case B.} \tag{12}$$

We see that the maximum field angle θ_M (or θ_{MA}) and the crystal thickness L are mutually constrained by δ. For instance, given $\delta = 5\%$, $n = 2.28$, $\gamma_b = 0.188$ cm^{-1}, and $\gamma_a = 0.475$ cm^{-1} (corresponding to an approximated index change $\Delta n \sim 10^{-6}$), it follows that if $\theta_{MA} = 20°$, then we have $L \leq 8.76$ mm for case A and $L \leq 46$-mm for case B; or if $L = 10$ mm, then we have $\theta_{MA} \leq 17.5°$ for case B and $\theta_{MA} \leq 45°$ for case A.

4. CONCLUSION

In summary, we have investigated the intrasignal coupling in $LiNbO_3$. It has been shown that for this crystal, which has a point group symmetry of $3m$, the anisotropy nature of the effective electro-optic coefficient results in an orientation-dependent intrasignal coupling. Analytical solutions for one-dimensional intrasignal coupling are derived for the crystal of a-axis and b-axis orientations. For the a-axis-oriented crystal, the intrasignal coupling is symmetric with respect to the c axis of the crystal. On the other hand, if the crystal is b-axis oriented, the coupling is asymmetric. Quantitatively, the relative intensity change in the b-axis-oriented crystal would be much larger in the a-axis-oriented crystal. Thus, for one-dimensional applications where intrasignal coupling is unwanted, case A is preferable due to less intrasignal coupling. For two-dimensional applications, however, the intrasignal coupling is generally orientation dependent with a mixed coupling behavior of both case A and case B, and we should be cautious of the anisotropy coupling behavior of $LiNbO_3$ in any event.

Finally, it is worth noting that, in principle, the relative intensity distortion due to the intrasignal coupling can be

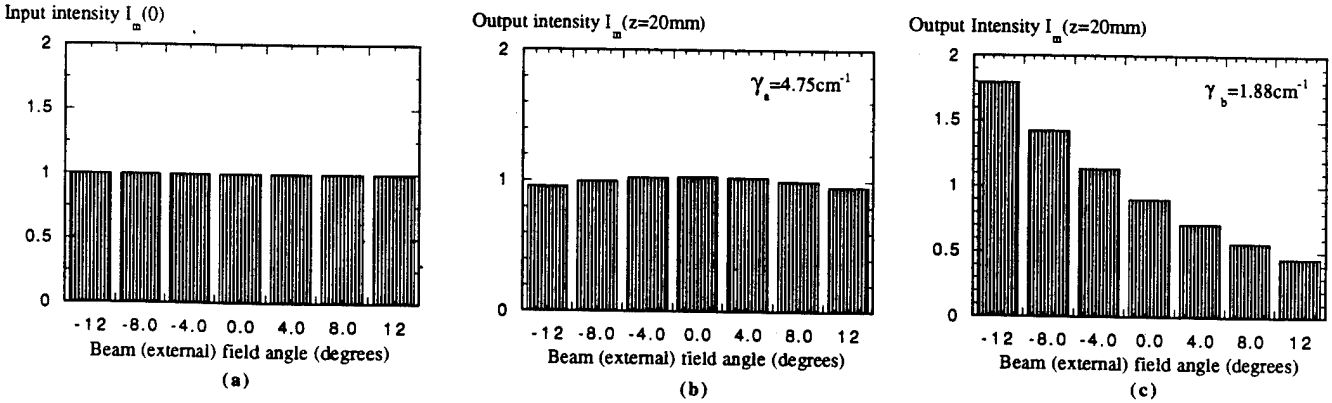

Figure 3 Energy transfer as a function of external field angle θ_{mA} for $z = 20$ mm. (a) Input beam intensity distribution. (b) Output beam intensity distribution for case A. (c) Output beam intensity distribution for case B

compensated by using a phase-conjugation mirror (PCM) as pointed by Ito, Kitayama, and Oguri [10]. However, using a PCM would complicate the system and reduce the overall light efficiency, and the intrasignal coupling in the PCM is unavoidable.

ACKNOWLEDGMENT

The authors acknowledge support by the Advanced Research Projects Agency through the U.S. Army Research Office under Contract No. DAAL 03-92-G-0328.

REFERENCES

1. S. Wu, Q. Song, A. Mayers, D. Gregory, and F. T. S. Yu, "Reconfigurable Interconnections Using Photorefractive Hologram," *Appl. Opt.*, Vol. 29, 1990, 1118–1120.
2. F. T. S. Yu and S. Jutamulia, in *Optical Signal Processing, Computing and Neural Networks*, Wiley-Interscience, New York, 1992, Chap. 7.
3. A. Chiou, P. Yeh, and C. Gu, "Spatial Mode Conversion in Photorefractive Fibers," *OSA Annual Meeting Technical Digest*, 1993, MD8.
4. J. Ma, L. Liu, S. Wu, and Z. Wang, L. Xu, and B. Shu, "Multibeam Coupling in Photorefractive SBN:Ce," *Opt. Lett.*, Vol. 13, 1988, pp. 1020–1022.
5. B. Fisher and M. Segev, "Photorefractive Waveguide and Nonlinear Mode Coupling Effects," *Appl. Phys. Lett., Vol. 54*, 1989, pp. 684–686.
6. A. Yariv, "Interpage and Interpixel Cross Talk in Orthogonal (Wavelength Multiplexed) Holograms," *Opt. Lett.*, Vol. 18, 1993, pp. 652–654.
7. P. Asthana, G. P. Nordin, A. R. Tanguay, Jr., and B. K. Jenkins, "Analysis of Weighted Fan-Out/Fan-In Volume Holographic Optical Interconnections," *Appl. Opt.*, Vol. 32, 1993, pp. 1441–1450.
8. M. Cronin-Golomb, B. Fischer, J. White, and A. Yariv, "Theory and Application of Four-Wave Mixing in Photorefractive Media," *IEEE J. Quantum Electron.*, Vol. QE-20, pp. 12–29 (1984).
9. M. Segev, Y. Ophir, and B. Fisher, "Nonlinear Multi Two-Wave Mixing, the Fanning Process and its Beaxhing in photorefractive media," *Opt. Commun.*, Vol. 77, 1990, pp. 265–274.
10. F. Ito, K. Kitayama, and H. Oguri, "Compensation of Fiber Holographic Image Distortion Caused by Intrasignal Photorefractive Coupling by Using a Phase-Conjugate Mirror," *Opt. Lett.*, Vol. 17, 1992, pp. 215–217.

Received 2-28-94

Microwave and Optical Technology Letters, 7/11, 483–486

CCC 0895-2477/94

RAPID APPROXIMATION OF CONDUCTING PROBLEMS USING A DUAL IMAGE APPROACH

Raphael Kastner
Department of Electrical Engineering-Physical Electronics
Tel Aviv University
Tel Aviv 69978, Israel

KEY TERMS

Scattering, images, equivalent Huygens sources, physical optics

ABSTRACT

Equivalent surface electric and magnetic sources can generate an approximate far field scattered off a conductor. These are exact (electric) and approximate (magnetic) images of the exciting equivalent sources. A physical-optics-type computation with improved accuracy, which also accommodates concave surfaces, is achieved.

1. FORMULATION OF THE DUAL IMAGES REPRESENTATION

A given incident field within a certain volume V can be represented by Huygens sources that obey the equivalence principle over the surface Σ enclosing the volume [1, 2]:

$$\mathbf{J}^{eq}(\mathbf{r}) = \hat{\mathbf{n}}(\mathbf{r}) \times \mathbf{H}^{inc}(\mathbf{r}), \qquad \mathbf{r} \in \Sigma, \tag{1a}$$

$$\mathbf{M}^{eq}(\mathbf{r}) = -\hat{\mathbf{n}}(\mathbf{r}) \times \mathbf{E}^{inc}(\mathbf{r}), \qquad \mathbf{r} \in \Sigma, \tag{1b}$$

where $\mathbf{n}$ points *into* V. The equivalent incident electric and magnetic currents in (1) offset the required discontinuities in the magnetic and electric fields, respectively; hence the total electromagnetic field outside the scatterer becomes identically zero. Other equivalent representations are possible, involving a different balance between the electric and magnetic sources, and generating different fields outside V. However, the evaluation of a general arrangement of sources, for example, a purely electric source representation, would require a full integral equation computation, as opposed to the straightforward expressions in (1). Each of the two sources in (1) gives rise to a portion of the total incident field, allowing for the superposition of the two solutions.

Assume now a perfect electric conductor (PEC) within V. We approach the scattering problem from the standpoint of modeling the excitation by the sources of (1), impressed at the scatterer surface Σ. Out of the many possibilities for equivalent sources over Σ induced by these sources, we choose their images. The image of the first component is indeed an exact solution: The induced current is simply the negative image of the incident electric current:

$$\mathbf{J}^{e}(\mathbf{r}) = -\hat{\mathbf{n}}(\mathbf{r}) \times \mathbf{H}^{inc}(\mathbf{r}), \qquad \mathbf{r} \in \Sigma, \tag{2}$$

where $\mathbf{n}$ is defined as before, pointing into the scatterer. Such a simple image is not available, though, for the magnetic incident current. In general, finding the current induced the magnetic current would involve the solution of an integral equation of the original complexity. However, for many cases involving large scatterers, an approximation can be prescribed for this contribution. We propose to view the scatterer locally as a part of an infinite planar sheet. Then, the equivalent magnetic current can be also imaged in it, with the image being equal to the impressed magnetic current:

$$\mathbf{M}^{e}(\mathbf{r}) = \hat{\mathbf{n}}(\mathbf{r}) \times \mathbf{E}^{inc}(\mathbf{r}), \qquad \mathbf{r} \in \Sigma. \tag{3}$$

This approximation complements Eq. (2), creating a set of the dual equivalent sources, $\mathbf{J}^e$ and $\mathbf{M}^e$ over the scatterer, which represent the effect of the induced current in the region outside the scatterer.

The far scattered field is computed directly from the sources of (2) and (3). However, one can also obtain an approximation for the actual induced electric current. This is done by computing the scattered magnetic field generated over the surface by both $\mathbf{J}^e$ and $\mathbf{M}^e$, adding it to the incident

Appendix 10.10

Tunable Interconnection Network Using a Thick Photorefractive (PR) Crystal

TUNABLE INTERCONNECTION NETWORK USING A THICK PHOTOREFRACTIVE (PR) CRYSTAL

M. Wen, S. Yin, and Francis T. S. Yu
Electrical and Computer Engineering Department
The Pennsylvania State University
University Park, Pennsylvania 16801

KEY TERMS

Optical interconnects, photorefractive crystal, wideband systems, multiplexing

ABSTRACT

A tunable interconnection network using a photorefractive (PR) crystal with an array of diode lasers is proposed. The interconnection data are wavelength multiplexed in a PR crystal reflection-type hologram. An $N \times N$ interconnection network can be realized by N holograms, for which the network can be reconfigured in real-time mode. © *1994 John Wiley & Sons, Inc.*

Optical interconnection offers the advantage of transmitting a wide-band ultrahigh-frequency signal with high flexibility and negligible cross talk. Reconfigurable optical interconnects using photorefractive (PR) materials have been recently proposed by several investigators [1–5]. PR materials offer higher diffraction efficiency and large storage capacity for massive interconnection networks. Because using wavelength multiplexing holograms in a thick recording material yields minimum cross talk as compared with the angular multiplexing technique [6, 7], the interest in wavelength multiplexing in PR crystals has been renewed [8]. Recently a technique in wavelength multiplexing transmission holograms for reconfigurable optical interconnection has been suggested by Lin [9]. However, the selectivity is strongly dependent on the write-in angle of the holograms. To alleviate this shortcoming, Wu et al. [10] have proposed a reconfigurable interconnection network using a reflection-type wavelength-tuning technique, which offers a uniform angular selectivity. There is an apparent disadvantage of this method: the angular deviation, introduced by the mismatched wavelength between the writing and the reading beams, would impose the constraint on the tuning range of the diode laser.

In this article we shall propose an $N \times N$ interconnection network using a PR crystal and an array of diode lasers. Because the wavelength multiplexed interconnection data can be reconfigured by tuning the reading wavelengths, an $N \times N$ interconnection network can be realized with N multiplexed holograms.

Let us now discuss a reflection-type wavelength multiplexed PR crystal hologram, in which two light beams propagating from opposite directions (represented by the wave vectors K_1 and K_2) would interfere within the crystal. It can be seen that a volume hologram is recorded within the crystal, as represented by wave vector K_3 as shown in Figure 1(b). If the hologram is read out by wave vector K_1, it is trivial that the wave vector K_2 will be reproduced. However, if the read-out vector differs from the writing beam vector (e.g., the wavelength of the read-out beam is not the same as that of the writing beam), then the reconstructed wave vector would differ from K_2, as denoted by K_2'. Thus we see that the diffraction efficiency is dramatically reduced. By imposing the weak coupling constraint of the holographic grating index within the crystal, the normalized diffraction efficiency of a reflection-type hologram is given by [10]

$$\eta_r \approx \left(V_r \frac{\sin \xi_r}{\xi_r} \right)^2, \tag{1}$$

where

$$V_r = \frac{\pi \Delta n d}{\lambda \sin[\cos^{-1}(\cos \alpha / n)]}, \qquad \xi_r = \frac{2\pi d \sqrt{n^2 - \cos^2 \alpha}}{\lambda^2} \Delta\lambda, \tag{2}$$

n and Δn are the refractive index and the amplitude of the induced refractive index, α is the external write-in angle as shown in Figure 1(a), d is the thickness of the crystal, and λ and $\Delta\lambda$ are the writing and the mismatching wavelengths between the reading and the writing beams. In view of Eq. (1), the diffraction efficiency as a function of the mismatched wavelength can be plotted as shown in Figure 2, where we have assumed $n = 2.28$, $d = 5$ mm, $\alpha = 85$, $\lambda = 670$ nm, and $\Delta n = 10^{-5}$. From this plot, we see that the diffraction efficiency drops rather rapidly as $\Delta\lambda$ varies. For example, if the wavelength difference between the reading and writing beams is larger than 0.2 nm, the diffraction efficiency would be less than -30 dB. Thus we see that a large number of wavelength multiplexed holograms can be stored in a PR crystal. In other

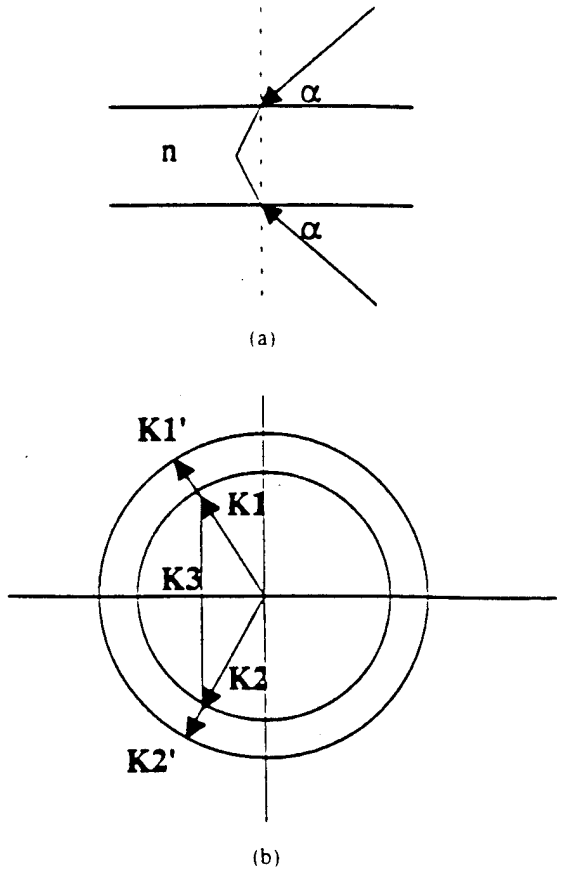

Figure 1 Construction of a reflection-type PR hologram. (a) Construction process. (b) K-vector diagram

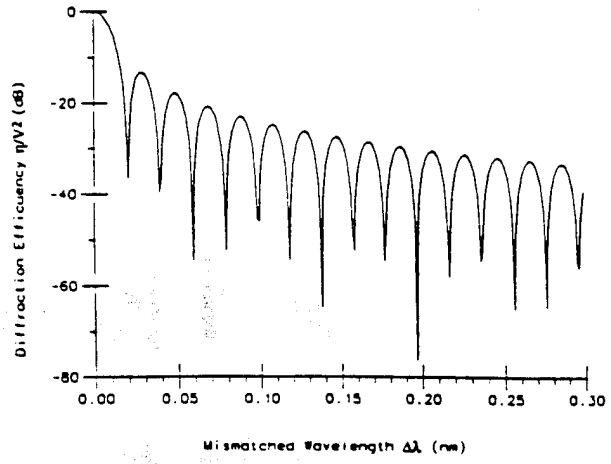

Figure 2 Normalized diffraction efficiency as a function of mismatched wavelength $\Delta\lambda$

words, if the recording wavelength separations among the multiplexed index gratings are sufficiently large, then the cross talk among channels would be minimum.

It is therefore apparent that wavelength multiplexed holograms in a PR crystal can be used for a tunable interconnection network as proposed in Figure 3, in which an array of tunable diode lasers and a recording diode laser are used. The imaging system is used to launch the array of the input beams into the PR crystal, by which the multiplexed holographic patterns can be constructed with an oblique reference beam. For example, in the training process, all the diode lasers in the input channels are turned off, and the recording diode laser is turned to λ_i ($i = 1, 2, \ldots, N$) and the reference beam is directed to the specific ith output channel (detector) at a given recording angle Θ_i. It is trivial that N multiplexed holograms, corresponding to the N output channels, can be synthesized in a PR crystal. As for the read-out process, the recording diode laser is turned off, it can be seen that the interconnections between the input and the output channels, can be simply accomplished by changing the combinations of the reading wavelengths of the diode lasers. For example, if the reading wavelength of the first diode laser is λ_1, and the wavelengths of all the other diode lasers are λ_2, then the first channel will be connected to the first output channel and all the other input channels are connected to the second output channel, and so on. Because each input channel is read out from a specific region in the PR crystal, the cross talk among the channels can obviously be avoided.

A preliminary experiment of a 2×8 interconnection network using a highly sensitive Ce:Fe:$LiNbO_3$ crystal [11] is shown in Figure 4. Because of the limited facilities, a tunable laser diode and an Ar^- laser are used as the array of light sources for the input channels. The output power of the tunable laser diode is measured to be about 3.0 mW with a wavelength of 670 nm and the intensity of the Ar^- laser is attenuated to about 3 mW. A prism is used to combine the two beams into an imaging system that is made up by a set of lenses L_1 and L_2. We have used 514.5-, 496.5-, 488.0-, 476.5-, 472.7-, 465.8-, 457.9-, and 454.5-nm wavelengths for the interconnections between the first input channel (represented by the Ar^- laser) and the ith ($i = 1, 2, \ldots, 8$) output channel. As for the interconnections between the second input channel (represented by the diode laser) and the ith output channel, the recordings are implemented using a wavelength tuning

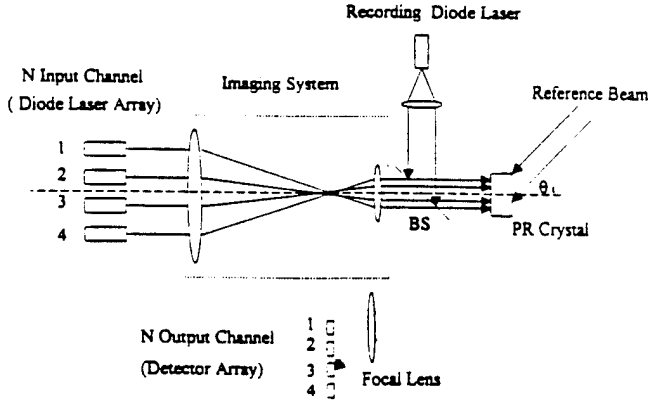

Figure 3 An $N \times N$ interconnection network using a PR crystal

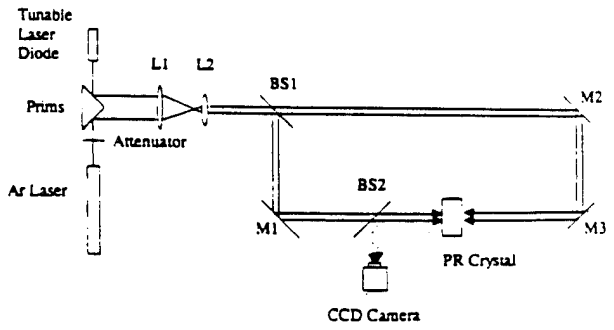

Figure 4 A 2×8 interconnection network

beam is changed by simply rotating the set of mirrors M_2 and M_3, by which the angle between the adjacent output channels is maintained to about 1°. Thus we see that the interconnections between the input and the output channels can be realized by simply combining of the reading wavelengths, as depicted (in part) in Figure 5. Figure 5(b) shows a set of output patterns using a 514.5-nm reading wavelength from the Ar^- laser. In another word, the Ar^- laser is connected to the first output channel. Thus by tuning the diode laser at $\Delta\lambda = 0.2$ nm/step, it can be seen that the laser diode can be sequentially connected to the ith ($i = 1, 2, \ldots, 8$) output channels. For example, the output pattern at the upper left corner of Figure 5(b) represents that both the Ar^- laser and the diode laser are connected to the first output channel. The next pattern to the right indicates that the Ar^- laser is connected to the first output channel and the diode laser is connected to the third output channel, and so on. Figure 5(c) shows a set of the output results using 670-nm reading wavelength from the diode laser, in which we see that the diode laser is connected to the second output channel. Thus by tuning the reading wavelength of the Ar^- laser, the Ar^- laser can be sequentially connected to the ith ($i = 1, 2, \ldots, 8$) output channels. As for the diffraction efficiencies for the eight multiplexed holograms recorded by the laser diode, we have seen in Figure 6 that the diffraction efficiency is relatively uniform because the change of the write-in angle is small. The diffraction efficiencies of the recorded holograms are measured to be about 0.14%.

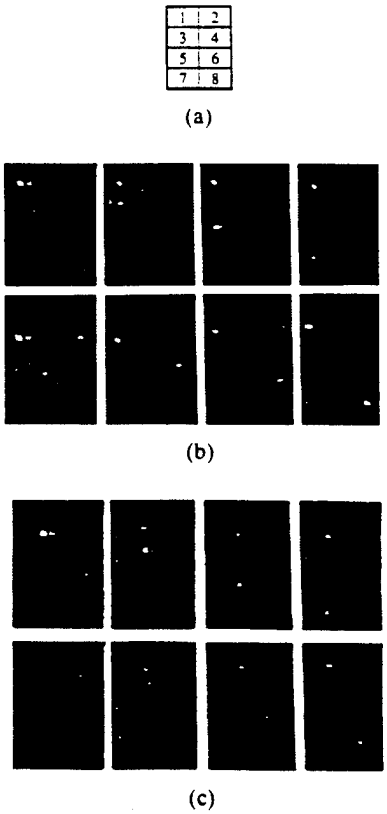

Figure 5 Experimental results obtained from the setup of Figure 4. (a) Eight output channels. (b) Interconnection patterns obtained for (Ar^- laser) $\lambda_a = 514.5$ nm, while the diode laser is tuned at $\Delta\lambda = 0.2$ nm/step. (c) Interconnection patterns obtained for (laser diode) $\lambda_d = 670$ nm while the Ar^- laser is tuned at $\lambda = 514.5, 496.5, \ldots$.

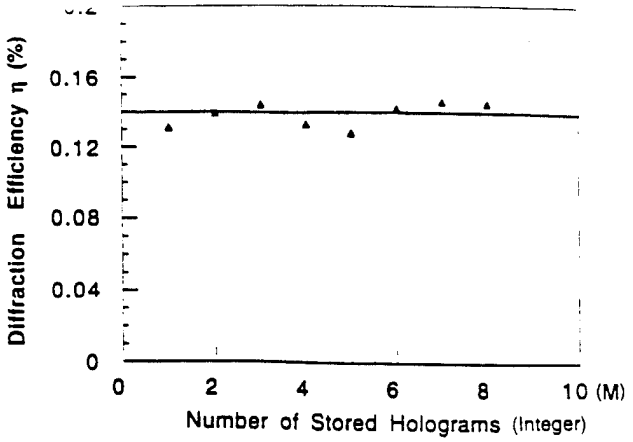

Figure 6 Diffraction efficiency of the holograms recorded with a tunable laser diode

In conclusion, we have proposed an $N \times N$ interconnection network using a PR crystal with an array of tunable diode laser. We have shown that by using a wavelength multiplexing technique, an $N \times N$ interconnection network can be realized by using N multiplexed holograms, instead of N^2 holograms if the angular multiplexing scheme is used. In other words, by using an equal-volume PR crystal with the same tuning range of the laser diode, the wavelength multiplexing interconnection capacity would be N times larger than the angular multiplexing hologram. One of the obvious advantages of using an array of the tunable diode lasers is that the interconnection network can be reconfigured in the real-time mode. The rate of reconfiguration would be primarily imposed by the time response of the PR crystal.

ACKNOWLEDGMENT

We acknowledge the support of the Defense Advanced Research Projects Agency through the U.S. Army Research Office under Contract No. DAAL 03-92-G0328.

REFERENCES

1. P. Yeh, A. Chiou, and J. Hong, *Appl. Opt.*, Vol. 31, 1992, p. 5536.
2. Q. W. Song, M. C. Lee, P. J. Talbot, and E. Tam, *Opt. Lett.*, Vol. 16, 1991, p. 1228.
3. D. J. Brady and D. Psaltis, *Appl. Opt.*, Vol. 30, 1991, p. 2324.
4. K. Rastani and W. M. Hubbard, *Appl. Opt.*, Vol. 31, 1992, p. 598.
5. E. S. Maniloff and K. M. Johnson, *Opt. Eng.*, Vol. 29, 1990, p. 225.
6. G. A. Rakuljic, V. Leyva, and A. Yariv, *Opt. Lett.*, Vol. 17, 1992, p. 1471.
7. F. T. S. Yu, F. Zhao, H. Zhou, and S. Yin, *Opt. Lett.*, to be published.
8. S. Yin, H. Zhou, F. Zhao, M. Wen, J. Zhang, and F. T. S. Yu, *Opt. Commun.*, to be published.
9. F. Lin, in *Technical Digest, Topical Meeting on Optical Computing*, Optical Society of America, Washington, DC, 1989.
10. S. Wu, Q. Song, A. Mayers, D. A. Gregory, and F. T. S. Yu, *Appl. Opt.*, Vol. 29, 1990, p. 1118.
11. S. Yin and F. T. S. Yu, *IEEE Photon. Technol. Lett.*, Vol. PTL-5, 1993, p. 581.

Received 6-30-94

Microwave and Optical Technology Letters, 7/18, 858–860

CCC 0895-2477/94

Appendix 10.11

Ce:Fe:$LiNbO_3$ Photorefractive Crystal: Material Properties and Applications

Ce:Fe:$LiNbO_3$ Photorefractive Crystal: Material Properties and Applications

(Invited)

F. T. S. Yu, A. S. Bhalla, S. Yin, F. Zhao, Z. Wu, and D. M. Salerno*
Department of Electrical Engineering
Pennsylvania State University
University Park, Pennsylvania 16802

Abstract — A specially doped photorefractive (PR) crystal Ce:Fe:$LiNbO_3$, and the effect due to Ce and Fe dopants are reported. We have found that the double-doped crystal exhibits higher PR sensitivity, larger dynamic range, broader spectral bandwidth, and lower scattering noise. It is about 10-times higher in PR sensitivity in the red light region (633nm), as compared with the reported data [1]. We have also discovered anomalous enhancement of PR effects which occur at 57°C, 70°C and 110°C. The anomalies are primarily due to possible structural phase-transitions of the crystal at these temperatures. Several applications of this specially doped PR (Ce:Fe:$LiNbO_3$) crystal (both bulk and fiber) are also provided.

I. Introduction

Photorefractive lithium niobate ($LiNbO_3$) based materials have received broad promising applications in recent years, such as optical signal processing, random-access memories, large capacity interconnections, switching, etc. [2]. In these applications, high PR sensitivity and low scattering noise materials are needed. It is well known that these PR properties are influenced by doping, annealing, and other crystalline processes. For example, photo-induced charge transport process in $LiNbO_3$ can be greatly enhanced by transition-metal-dopants in different valence states. Fe, Cu, Cr, Mn, Ce, etc., dopants have been used to improve the PR properties of lithium niobate based materials [1, 3-5]. However, based on the approach by Yeh [6], the PR response time of a $LiNbO_3$ based material is in the order of a few seconds, which is much slower than the actual limit, which is in the order of milliseconds. On the other hand, light-induced scattering noise (e.g., initiated by crystalline imperfections and non-uniform doping) through high (PR) gain amplification would affect the signal-to-noise ratio (SNR) of the material. Therefore to broaden the application of the $LiNbO_3$ based materials, PR sensitivity should be improved and scattering noise has to be minimized.

II. Crystal Preparation

Both bulk and single crystal fiber $LiNbO_3$ based materials doped with Ce, Fe and Ce:Fe have been grown in the Material Research Laboratory (MRL) at the Pennsylvania State University [7], in which the conventional Czochralski technique has been used to grow the bulk crystals, and the Laser Heated Pedestal Growth (LHPG) technique is used to fabricate the single crystal fibers.

By using the Czochralski process, a single crystal seed is dipped into a Platinum crucible containing the melt and then slowly withdrawn. The temperature of the crucible is heated by RF sources to about 1260°C. During the withdraw process, the melt solidifies onto the seed, for which the crystal in initiated by adjusting the input heat of the melt to control the crystal diameter. Crystals of 60mm in diameter and 50mm in thickness have been grown. The samples are poled to exhibit a single domain by heating the crystal to the Curie temperature (1220°C), where the crystals become paraelectric, in which a DC field (0.5~5V/cm) is applied for approximately 1 hour. To obtain a higher PR sensitivity, the crystals are annealed in vacuum chamber at ~800°C, for about 2-3 hours.

By using the laser-heated growth process, the tip of a small source crystal rod is uniformly heated with a high intensity CO_2 laser beam using a reflexicon with a parabolic mirror. By dipping the crystal seed into the molten zone the fiber growth can be initiated by pulling the fiber crystal (at rates of a few millimeters per minute) away from the melt, while feeding the source rod at a commensurate steady-state rate. Advantages of the LHPG technique include fast growth rate, no poling is needed, long crystalline fiber can be obtained, etc. Single crystal fibers of $LiNbO_3$ and SBN of diameters ranging from 100-1000μm have been successfully grown by using this technique.

III. Characterization of Photorefractive Properties

Photorefractive sensitivity is one of the most important figures of merit of a PR material. For holographic applications, the PR sensitivity is defined as the energy density needed to give rise to a 1% diffraction efficiency for a 1mm thick storage material [1],

$$S = \frac{d(\eta^{1/2})}{dW}\frac{1}{L}, \qquad (1)$$

where η is the diffraction efficiency, W is the total incident energy density, and L is the thickness of the crystal. Thus, once we know the dynamic diffraction efficiency η and the

corresponding input optical power W, we can proceed by Eq. (1) to obtain the PR sensitivity S.

The photorefractive recording time-constant determines the speed of a PR hologram formation, which is crucial to any real-time applications of the PR crystal. The build-up of the space-charge field can be shown, by using the Kukhtarev's model [5], to exhibit an exponential behavior. Hence the evolution of the diffraction efficiency can be expressed as [1]:

$$\eta(t) = \eta_{max}\left(1 - e^{-t/\tau}\right), \qquad (2)$$

where η_{max} is the saturation value of the diffraction efficiency, and τ is the response time-constant (or recording time constant). The time-constant can be measured from the evolution of the diffraction efficiency. For practical applications, a large diffraction efficiency and a fast time-constant are needed.

The maximum refractive index change Δn_{max} of the PR crystal is referred to as the material dynamic range, which determines the maximum number of holograms that can be stored in the crystal.

It has been shown by Kogelnik [8] that the photo-induced refractive index change Δn is related to the diffraction efficiency η by

$$\eta = \exp\left(-\frac{\alpha L}{\cos\theta_i}\right)\sin^2\left(\frac{\pi L \Delta n}{\lambda \cos\theta_i}\right), \qquad (3)$$

for transmission hologram, where α is the optical absorption coefficient, L is the crystal thickness, λ is the wavelength of the incident light, and $2\theta_i$ is the internal angle between the two incident beams. The dynamic range can be determined from Eq. (3) by measuring the saturation diffraction efficiency.

We have experimentally characterized the PR properties for three samples doped with Fe, Ce, and Ce:Fe, respectively, as tabulated in Table 1. Figure 1 shows the schematic of the experimental setup, in which a 10mW He-Ne laser is used to provide the writing beams. The power of the signal beam I_1 and reference beam I_2 are about the same, i.e., I_1=I_2=2mW. The sizes of the two beams are about 1.5mm in diameter, and the external angle between them is about 7°. Extra-ordinary polarized lights are used, and the *c*-axis of the crystal is oriented at the incident plane. Note that this orientation allows the use of the largest electro-optic tensor element γ_{33}. An electronic shutter is placed in the reference arm, with a chopping rate of 1Hz and duty-cycle of 50%.

Figure 2 shows the evolution of the diffraction efficiency for the three samples, in which the lower envelop represents the diffraction efficiency evolution. It is therefore trivial that the recording time-constants τ, the diffraction efficiencies η_{max}, the PR sensitivities S, and the dynamic ranges Δn_{max} can be measured, and the results are tabulated in Table 1. From these results we see that the sample with double-doping gives rise to the best overall PR properties. As compared with

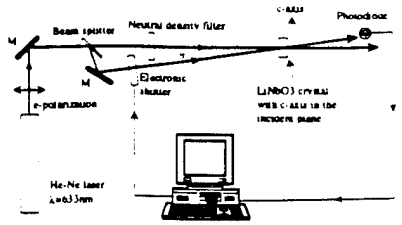

Fig. 1. Schematic of the experimental setup for photorefractive property characterization.

reported data by Günter and Huignard [1], our results show that there is about a 10-fold increase in the PR sensitivity. To our knowledge, this is the highest PR sensitivity that has been reported for $LiNbO_3$ based crystal in the red light region.

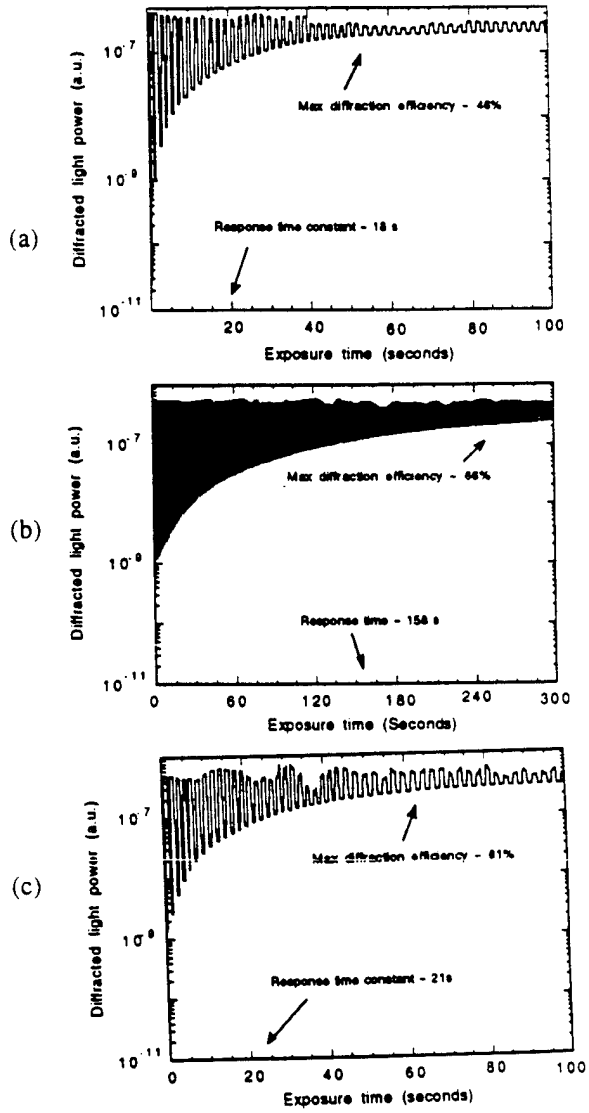

Fig. 2. Development of the photorefractive process. The lower envelop represents the diffraction evolution.
(a) $Fe:LiNbO_3$; (b) $Ce:LiNbO_3$; and (c) $Ce:Fe:LiNbO_3$.

Table 1. Photorefractive properties of $LiNbO_3$ with Fe, Ce, and Ce:Fe dopants

	Fe:$LiNbO_3$	Ce:$LiNbO_3$	Ce:Fe:$LiNbO_3$
Doping concentration	Fe:0.08mol%	Ce:0.08mol%	Ce:0.08mol%, Fe:0.08mol%
Response time constant τ (seconds)	18	158	21
Dynamic range Δn_{max}	1.4×10^{-4}	1.9×10^{-4}	1.8×10^{-4}
Inverse of PR sensitivity S^{-1} (mJ/cm)	17	97	14
Maximum diffraction efficiency η_{max}	51%	66%	61%

IV. Low Temperature Phase-Transitions

One important advantage of $LiNbO_3$ is the high Curie point (~1220°C), which makes it very robust against temperature perturbations. In fact, all samples of $LiNbO_3$ show the high temperature phase-transition. Intrinsic $LiNbO_3$ samples show only one phase-transition, however doped $LiNbO_3$ based materials have been found to exhibit some low temperature transitions [9-10]. Notice that the doped $LiNbO_3$ crystals remain in the ferroelectric domain at low temperature phase-transitions, which have not been fully understood and no report has been given on the influence of the PR properties due to the low temperature phase-transitions

In this section, we will present our preliminary investigation on the PR effect (two-wave coupling constant, and phase-conjugate reflectivity) as affected by the low temperature phase-transitions of the Ce:Fe:$LiNbO_3$ crystal. Figure 3 shows the experimental setup, in which a Ce:Fe:$LiNbO_3$ crystal is mounted in a temperature (controlled) oven. The size of the sample is $10\times10\times1$ (mm^3), and the doping concentrations for both Ce and Fe are the same amount, 0.08mol%. The crystal c-axis is oriented at the incident plane, where the extra-ordinary polarized laser beam is used. A He-Ne laser provides the incident beams, with pump beam I_1 and signal beam I_2. In our experiment, the intensities of the incident beam are I_1=4mW, and I_2=10μW, respectively. The strong pump beam is perpendicularly incident on the crystal, and the external angle between I_1 and I_2 is about 7°. An electronic shutter is placed in the pump arm, by which the pump beam can be modulated.

It has been shown by Yeh [6] that the two-beam coupling constant Γ can be approximated by

$$\Gamma \approx \frac{1}{L}\ln\left[\frac{I_2'(L) \quad \text{with} \quad \text{pump}}{I_2(L) \quad \text{without} \quad \text{pump}}\right], \tag{4}$$

under the undepleted (pump) condition, where L is the crystal thickness. $I_2(L)$ and $I_2'(L)$ are the transmitted signal intensity with and without the pump beam.

Since the temperature range between 20°C and 120°C is important to the holographic thermal fixing process, we have measured the (saturation) coupling constant Γ as a function of the crystal temperature and result is depicted in Figure 4(a). Thus we see that there are three peaks of coupling constant at 57°C, 70°C and 110°C that show possible structural phase-transitions at these temperatures. The largest Γ occurs at about 57°C and has about 45% increase in the coupling constant. We note that these phase-transition temperatures are similar to those reported by Ismailzade, *et al.* [9] and Engelmann, *et al.* [10].

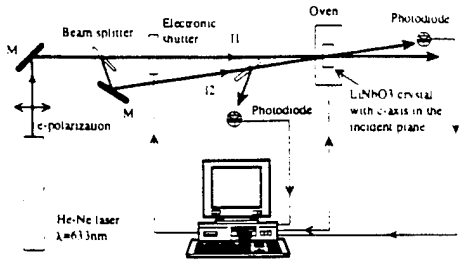

Fig. 3. Experimental setup for the measurement of low temperature phase transitions.

We have also measured the phase-conjugate reflectivity R as a function of the crystal temperature between 20°C and 120 °C and result is plotted in Figure 4(b). R is defined as the ratio of the phase-conjugate beam intensity to the signal beam intensity. This phase-conjugate beam is primarily due to the four-wave mixing process occurred among the pump, back reflection and signal beams. Again, we observe the peak reflectivities R at the same phase-transition temperatures as the coupling constants Γ, and the largest R is at about 70°C, which has about 300% increase in the reflectivity. We can also see that the peaks are about 3~4°C wide (full-width half maximum).

We would point out that, since the temperature gradient across the crystal section and the temperature fluctuations caused by the ambient air turbulence may be as large as several degrees Centigrade, the above mentioned peaks may in fact be much higher and narrower than what we have observed. We suggest further study of the phase-transitions and their impact on the PR properties of $LiNbO_3$ based materials, which include transmission electronic microscopy

(TEM), DTA, DSC, dielectric constant measurement, and others.

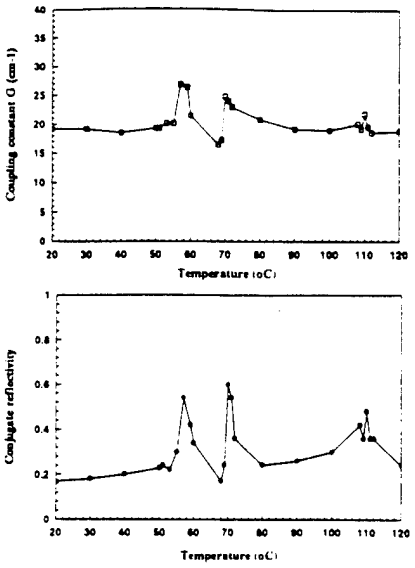

Fig. 4. Temperature dependency of the two-wave coupling constant Γ and phase-conjugate reflectivity R.

V. Applications of PR Ce:Fe:$LiNbO_3$ Crystal (Bulk and Fiber)

A). High capacity wavelength-multiplexed image correlator

Optical pattern recognition is a viable field in optical signal processing, machine vision, target tracking, etc. As compared with the classic Vander Lugt filter, a PR crystal based image correlator has the advantages of real-time processing, large capacity and less stringent alignment requirement. We shall propose a reflection-type wavelength-multiplexed spatial filter, as applied to a high capacity correlator, as shown in Figure 5, in which a 1-cm cube z-cut Ce:Fe:$LiNbO_3$ crystal is used for the filter synthesis. A tunable diode laser (New Focus Model 6102 with a tuning range of 12nm at 670nm central wavelength) is used as the light source, for which reference targets can be sequentially recorded in the crystal. In read-out process, a target is displayed on the input spatial-light modulator (SLM), by which a correlation peak can be observed if the correct read-out wavelength is used.

Proof-of-concept experiments have been conducted as shown in Figure 6, in which a set of "P", "S", "U", "R", and "M" letters are used as the reference targets. In this experiment, we use a 0.1nm laser tuning step with a 10-second exposure for each hologram construction. The reconstructed holographic images and the corresponding correlation peaks are shown in Figure 6(b) and (c),

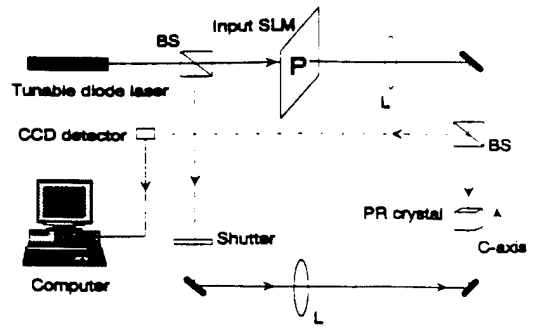

Fig. 5. Wavelength-multiplexed reflection correlator.

respectively. In view of these results, we see that the holographic images are faithfully reconstructed, by which a large-capacity optical correlator, in principle, can be developed using a reflection-type wavelength-multiplexed (PR) spatial filter.

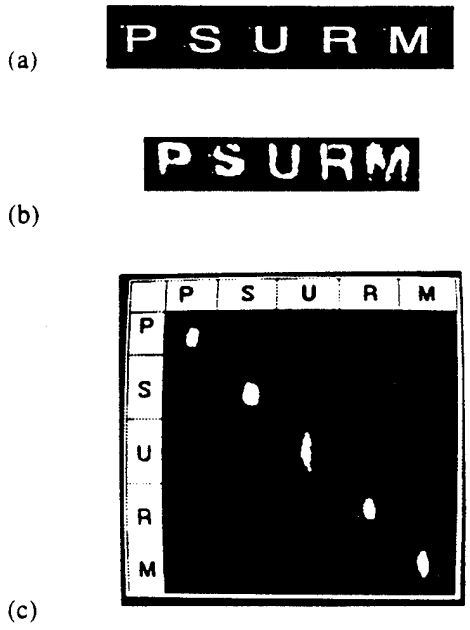

Fig. 6. Experimental results of the reflection wavelength-multiplexed correlator. (a) Input letter images; (b) Reconstructed images; (c) Auto correlation peaks.

B). Tunable narrow-band in-fiber Bragg filter using PR crystal fiber

PR processes have been extensively studied in bulk materials for a variety of applications to optical signal processing and other photonic technologies. Unfortunately, the lack of availability of large single crystals severely limits the use of PR materials in practical applications.

On the other hand, PR fibers provide long length structure that can be utilized for some new applications, such

as high capacity fiber bundle memories, electro-optic fiber switches, fiber optic interconnections, and others [11-14].

Because of high electro-optic coefficient of the PR materials, it is possible to develop electrically tunable fiber optic switches. One of the major advantages of fiber switches must be its physical form, in which it can be easily coupled with fiber links in a fiber-optic network. Mention must be made that photonic switches have been used in fiber optic communication and reconfigurable networks. However, the integrated-optic photonic switches are difficult to fabricate and not convenient to interface with optical fibers. We shall now propose an electronic tunable (Bragg-diffraction) fiber switch using a Ce:Fe:$LiNbO_3$ fiber, as follows: Figure 7 shows a sketch of a fiber switch, in which an axial holographic grating is constructed by the counter-propagating beams (i.e., reflection-type fiber hologram) within the PR fiber [7, 12-14]. This axial grating can in fact be thermally fixed by heating the crystal fiber to about 150°C followed by a uniform illumination at room-temperature. Since the axial index grating acts as a notch filter, the wavelength that does not matched with the grating will be rejected (i.e., transmitted). It is apparent that by taking advantage of the high electro-optic constant (e.g., 30.8×10^{-12}m/V for $LiNbO_3$) of the PR fiber, the distribution of the index grating and the birefringence of the fiber can be varied by the applied electric field patterns within the fiber. In other words, the Bragg diffraction condition of the index grating can be manipulated by an external field patter, for which the matched wavelength of the grating can be shifted. Since the electro-optic effect takes place in a PR material almost instantaneously (e.g., $<10^{-12}$ s for $LiNbO_3$), the tunable fiber switches would be very fast in the order of GHz to THz.

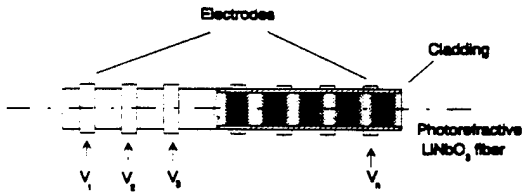

Fig. 7. A sketch of a tunable fiber switch.

The spectral bandwidth of the fiber switch can be shown to be inversely proportional to the length of the fiber [13],

$$\Delta\lambda = \frac{\lambda_o^2}{2nL}, \tag{5}$$

where λ_o is the wavelength in vacuum, n is the refractive index of the fiber, and L is the fiber length. To have a feeling of magnitude, we assume L=5cm, λ_o=1.5μm, and n=2.28, for which we have $\Delta\lambda=1.0\times10^{-11}$m (i.e., 1.3GHz), which is matched with the channel bandwidth of the fiber optic communication networks.

The wavelength shift $\delta\lambda$ due to the external electric field induced index deviation Δn can be estimated by

$$\frac{\Delta\lambda}{\lambda_o} = \frac{\Delta n}{n}, \tag{6}$$

where

$$\Delta n = -\frac{1}{2} n^3 \gamma_{eff} \Delta E .$$

Here ΔE is the variation of the applied electric field, and γ_{eff} is the (effective) electro-optic coefficient of the fiber. In order to have a feeling of magnitude, we assume a PR (Ce:Fe:$LiNbO_3$) fiber, n=2.28, $\gamma_{eff}=30.8\times10^{-12}$m/V, λ_o=1.5μm, and ΔE=100V/mm, for which we have $\Delta n=1.8\times10^{-5}$ and $\delta\lambda=1.2\times10^{-11}$m (1.6GHz). Therefore we see that, by applying a specific electric field pattern along the fiber, a high speed fiber optic switch can be developed. The major merits of the proposed electro-optic fiber switch must be the high SNR, low loss and high extinction ratio, for which may warrant a wide variety of applications, particular to optical fiber networks.

VI. Conclusion

We have presented a specially doped $LiNbO_3$ crystal (both bulk and fiber) and the PR effect due to dopants. We have found that double-doped Ce:Fe:$LiNbO_3$ crystal exhibits higher PR sensitivity, larger dynamic range, wider spectral bandwidth, and lower scattering noise, for which the crystal (bulk and fiber) would offer a variety of promising applications. In this study, we have found several anomalous PR sensitivities in the specially doped material, which occur at 57°C, 70°C and 110°C crystal temperatures. These anomalies are primarily due to the possible structural phase-transitions of the crystal. The application of this specially doped crystal to wavelength-multiplexed spatial filters is experimentally demonstrated, in which we have shown that a large capacity correlator using a tunable diode laser is feasible. We have also proposed an application of using this double-doped PR fiber to photonic switching. Owing to the high electro-optic coefficient of the material, a high speed electro-optic fiber switch in principle can be developed. In short, the specially doped (Ce:Fe:$LiNbO_3$) material is at the threshold of practical reality, there is much that remains to be done before it becomes a wide spread of application.

★ D. M. Salerno is with the Photonics Group, U.S. Army Missile Command, Redstone Arsenal, AL 35898-5248.

Acknowledgment

The support from Advanced Research Projects Agency through the U. S. Army Research Office under Contract No. DAAL 03-92-G-0328 and from Army Research Laboratory under Contract No. DAAL 01-93-K-0059 are acknowledged.

REFERENCES

[1] P. Günter, and J.-P. Huignard, ed., *Photorefractive Materials and Their Applications I*, Berlin: Springer-Verlag, 1989, ch. 3, pp.7-74.

[2] for example, F. T. S. Yu, and S. Jutamulia, *Optical Signal Processing, Computing and Neural Networks*, New York: Wiley-Interscience, 1992, ch. 7, pp. 249-286.

[3] E. Krätzig, and R. Sommerfeldt, "Influence of dopants on photorefractive properties of $LiNbO_3$ crystals," in *SPIE Proceedings*, vol. 1273, pp. 2-11, 1990.

[4] A. Ashkin, G. D. Boyd, J. M. Dziedzic, R. C. Smith, A. A. Ballman, J. J. Levinstein and K. Nassau, "Optically induced refractive index inhomogenities in $LiNbO_3$ and $LiTaO_3$," *Appl. Phys. Lett.*, vol. 9, pp. 72-74, 1966.

[5] N. V. Kukhtarev, V. B. Markov, S. G. Odulov, M. S. Soskin and V. L. Vinetskii, "Holographic storage in electro-optic crystals, I. steady-state, and II. Beam coupling - light amplification," *Ferroelectrics*, vol. 22, pp. 949-964, 1979.

[6] P. Yeh, "Two-wave mixing in nonlinear media," *IEEE J. Quantum Electron.*, vol. QE-25, pp. 484-519, 1989.

[7] F. T. S. Yu, S. Yin, and A. S. Bhalla, "Wavelength-multiplexed holographic construction using a Ce:Fe: doped photorefractive fiber with a tunable visible-light laser diode," *IEEE Photon. Tech. Lett.*, vol. 5, pp. 1230-1233, October 1993.

[8] H. Kogelnik, "Coupled wave theory for thick hologram gratings," *The Bell Sys. Tech. J.*, vol. 48, pp. 2909-2947, 1969.

[9] I. G. Ismailzade, V. I. Nesterenko, F. A. Mirishi, "X-ray study of lithium niobate at high temperatures," *Sov. Phys.-Crystallogr.*, vol. 13, pp. 25-28, July 1968.

[10] H. Engelmann, N. Krämer, H. Yuanfu, L. Rongchuan, and U. Gonser, "Investigation of anomalous tranitions in LiNbO3 by Mössbauer spectroscopy," Ferroelectrics, vol. 69, pp217-222, 1986.

[11] S. Yin, H. Zhou, F. Zhao, M. Wen, Z. Yang, and F. T. S. Yu, "Wavelength-multiplexed holographic construction using a $Ce:Fe:LiNbO_3$ crystal with a tunable visible-light diode laser," *Opt. Comm.*, vol. 101, pp. 317-321, September 1993.

[12] F. T. S. Yu, F. Zhao, H. Zhou, and S. Yin, "Cross-talk in a reflection-type wavelength-multiplexed photorefractive fiber hologram," *Opt. Lett.*, vol. 18, pp. 1849-1851, November 1993.

[13] F. Zhao, H. Zhou, S. Yin, and F. T. S. Yu, "Wavelength-multiplexed holographic storage by using the minimum wavelength-channel separation," *Opt. Comm.*, vol. 103, pp. 159-162, November 1993.

[14] S. Wu, A. Mayers, S. Rajan, and F. T. S. Yu, "Use of photorefractive fiber in optical interconnections and switching," *Appl. Opt.*, vol. 29, pp. 1059-1061, March 1990.

Appendix 10.12

Steady-State Nondegenerate Four-Wave Mixing in Photorefractive Ce:Fe:$LiNbO_3$

Steady-state nondegenerate four-wave mixing in photorefractive Ce:Fe:$LiNbO_3$

F. Zhao, Z. Wu, F. T. S. Yu

Department of Electrical Engineering

The Pennsylvania State University

University Park, Pennsylvania 16802

D. K. McMillen

U.S. Army Missile Command

Redstone Arsenal, Alabama 35898-5248

Abstract

In this paper, nondegenerate four-wave mixing in a Ce:Fe:$LiNbO_3$ photorefractive (PR) crystal is studied as a function of the crystal temperature. We show that an efficient steady-state frequency-varied conjugate wave (FVCW) can be generated at an elevated temperature. We show that the optimum temperature is ~120°C, at which there is about a 10 fold increase in the steady-state intensity of the FVCW compared with room temperature (20°C). We have found that the temperature dependency is primarily due to the reduction of light-induced scattering by thermally activated ions neutralizing the noise grating in the crystal. We also show that, at the higher temperature, steady-state phase-conjugate waves at both the pump wavelengths can be obtained, which is useful for applications such as polychromatic complex spatial filtering and wavefront correction.

1. Introduction:

It is well known that phase conjugate optics offers significant contributions to optical signal processing, including wavefront correction and complex spatial filtering [1-3]. Among the methods of producing a phase-conjugate wave, four-wave mixing in a photorefractive (PR) material is the most common technique since it requires a lower power source than other methods. Most of the work on four-wave mixing in photorefractive media has focused on the degenerate case, in which the phase conjugate wave has the same wavelength as all other mixing beams. A frequency-varied phase conjugate wave (FVCW) is required for high capacity filter synthesis (such as wavelength-multiplexed filters for correlators and neural network weight matrix). For FVCW, the phase conjugate wave is derived from a different wavelength than the input writing beam. A transient FVCW was generated by way of nondegenerate four-wave mixing (NFWM) in an Fe doped $LiNbO_3$ crystal by Bao, *et al.* [4], but a steady-state conjugate wave intensity was difficult to obtain due to the transient energy transfer effect [5] and light-induced scattering [6]. However, at a higher temperature, the thermally activated ions within the PR crystal can neutralize the electronic gratings [7-10], which reduces the light-induced scattering effect in the crystal [11]. It is therefore apparent that an efficient steady-state nondegenerate phase-conjugation can be obtained by operating the PR crystal at a higher temperature [12].

In this paper, we shall investigate the temperature dependency of steady-state FVCW generation with a specially doped Ce:Fe:$LiNbO_3$ photorefractive crystal. We will first present a background of NFWM in a photorefractive medium.

2. Background:

Unlike the four-wave mixing process by way of the third-order nonlinear susceptibility $\chi^{(3)}$, the phase-conjugation in a PR crystal is characterized by the light-

induced space charge field E_{SC} [13]. As a result of the presence of the space charge field, a change in the refractive index is induced by means of the Pockel's effect [14],

$$\Delta n \approx \frac{1}{2} n_o^3 \gamma_{eff} E_{SC}, \tag{1}$$

where n_0 is the normal refractive index of the PR crystal, and γ_{eff} is the effective electro-optic coefficient.

In the NFWM process depicted in Figure 1, pump beam #1 and the probe beam are assumed to be the same wavelength (frequency), i.e., $\lambda_p=\lambda_1$, while pump beam #2 has a different wavelength λ_2. By using the law of energy conservation, the wavelength of the output beam can be shown to be [15],

$$\lambda_c = \lambda_2. \tag{2}$$

In view of Eq. (1), the index perturbation due to the wave mixing can be shown to be:

$$\Delta n = \frac{1}{2}\Delta n_I e^{i\phi_I} \frac{A_1 A_p^*}{I_o} exp\left[-i\left(\vec{k}_1 - \vec{k}_p\right)\cdot\vec{r}\right] + \frac{1}{2}\Delta n_{II} e^{i\phi_{II}} \frac{A_c A_2^*}{I_o} exp\left[-i\left(\vec{k}_c - \vec{k}_2\right)\cdot\vec{r}\right] + c.c., \tag{3}$$

where $\vec{k}_i$ and A_i (i=1,2,p,c) are the wave vectors and wave amplitudes, respectively, I_0 is the total incident intensity, Δn_i and ϕ_i (i=I, II) are the refractive index change magnitude and phase shift, respectively, and *c.c.* represents the remaining unessential complex conjugate terms. Following the work of Cronin-Golomb, *et al.* [13], on degenerate four-wave mixing in PR media, one can show that the output field is proportional to the amplitude of the two pump beams and the phase-conjugate of the probe beam, , such that,

$$A_c \propto A_1 A_2 A_p^* \left(1 - e^{i\Delta\vec{k}\cdot\vec{r}}\right), \tag{4}$$

where $\vec{r}$ is the interaction length of the mixing beams inside the crystal, and $\Delta\vec{k}$ is the phase mismatch among the mixing beams, i.e.,

$$\Delta\vec{k} = \vec{k}_1 - \vec{k}_p - \vec{k}_2 + \vec{k}_c. \tag{5}$$

It can be seen from Eqs. (2) and (4), that the output beam A_c is essentially the phase-conjugate of the probe beam, where we have assumed that both the pump beams are plane waves. We note that the wavelength of the phase-conjugate wave A_c is different from that of the probe beam, therefore A_c is referred to as the frequency-varied phase conjugate wave (FVCW) [4].

In four-wave mixing applications, phase matching ($\Delta\vec{k}$=0) is the primary factor for achieving a high efficiency output phase-conjugate wave. With the NFWM geometry shown in Fig. 1, the phase matching condition is found to be:

$$\alpha = \frac{1}{2}\theta - \mathrm{Sin}^{-1}\left(\frac{\lambda_2}{\lambda_1}\mathrm{Sin}\frac{\theta}{2}\right) \tag{6}$$

where θ is the angle between the probe beam A_p and pump beam #1, and α is the angular deviation of the output wave with respect to the probe beam . Notice that the incident angle of the pump beam #2 is also α.

From the preceding, it is trivial to see that from NFWM, as shown in Fig. 1, a frequency-varied phase-conjugate replica of the probe beam can be generated. However, at room temperature, only a transient phase-conjugate wave is obtained [4, 5], because of a transient energy transfer and light-induced scattering effects. Nevertheless, we shall

show that a steady-state FVCW can be obtained when the PR crystal is operated at a higher temperature.

2. Nondegenerate four-wave mixing as a function of temperature:

Figure 2 shows the nondegenerate four-wave mixing architecture that we have used for our study, in which an X-cut Ce:Fe:$LiNbO_3$ PR crystal with a dimension of 10× 10×1mm^3 (X:Y:Z) is inserted within a small temperature controllable oven. The crystal is in fact a single domain crystal which is grown along the c-axis by using the conventional Czochralski method. The doping concentrations for both the Ce and Fe are about 0.08mol%. In order to produce a strong PR effect, the doped crystal was annealed in a vacuum chamber at ~800°C, for about 2 hours. The sample is aligned in the experiment such that the *c*-axis is oriented in the incident plane (i.e., extra-ordinary polarization writing waves are used). A programmable temperature controller (Omega CN2002) is used to control the temperature of the oven, such that the variation of the temperature can be maintained within 1°C over a period of 1 hour. A He-Ne laser (λ=633nm) is used to provide pump beam #1 and the probe beam, with powers of 4mW and 12μW, respectively. However, pump beam #2 (about 85mW) is from an Ar^+ laser (λ=488nm) for the NFWM experiment. Note that pump beam #1 is normally incident to the crystal, while the angle θ between pump beam 1 and the probe beam is about 7°. Since the sizes of all the mixing beams are about 3mm in diameter, a 3mm iris is placed in front of the photodetector (PD) to block unwanted scattered light. An x-y plotter is used, as shown in the figure, to record the evolution of the phase-conjugate wave as a function of time.

Note that pump beam #1 and the probe beam will interfere, forming a phase grating inside the crystal by means of the photorefractive effect. After exposing the crystal for about 4 minutes, pump beam #2 is introduced, after which the frequency-varied phase conjugate wave (FVCW) can be observed in the direction slightly deviated from the counter propagation of the probe beam. We adjusted the incident angle of pump

beam #2 to obtain an optimum phase-conjugate wave output, for which the deviation angle α is measured to be about 1.6°, that is quite agreeable with the phase matching condition as described by Eq. (5).

The time evolution of the FVCW for various crystal temperatures was measured, and the evolution at room temperature (20°C) is shown in Fig. 3. From this figure we see that the intensity of the FVCW increases to a peak value at about 1 minute and then exponentially decays to about zero. The width (half power points) of the peak is measured to be about 20 seconds.

We have found that much of the energy of the incident beams goes into scattered light depleting over half of the incident power. This causes the energy of the FVCW to be essentially lost to the scattered light.

However, at higher temperatures, the evolution of the FVCW is quite different, as can be seen in Fig. 4. From this figure we see that the FVCW rises to a peak value about the same as that at room temperature, drops to a valley, and then rises again to a steady-state level which is about 10 times higher than that at room temperature. In previous experiments, we have found that the scattered light is greatly reduced at the higher temperature which may explain why the intensity of the FVCW is maintained at the higher steady-state value instead of dropping to about zero. At steady-state, a phase-conjugate wave of 633nm is also observed, at the counter propagation direction of the probe beam, with a (phase-conjugate) reflectivity of about 30%.

The steady-state intensities of the FVCW at various crystal temperatures have been measured and plotted in Fig. 5, in which we see that there is an optimum value of about 120°C.

3. Discussion:

We have shown a strong temperature dependence of the FVCW in a specially doped Ce:Fe:$LiNbO_3$ PR crystal. The dependency is primarily due to the neutralization

of the electronic space charge fields with the thermally activated ions, as described by several authors [7-10]. In the course of the neutralization, two dynamic processes have been initiated within the PR crystal: First, pump beam #2 interacts with its own phase-conjugate wave (i.e., FVCW) to form a new diffraction grating which couples additional energy into the FVCW through two-beam coupling effect [14]. Second, the light-induced self-diffraction (scattering) gratings would gradually build up, which leads to energy losses as scattered light. In other words, the first dynamic process involves holographic gratings constructed through the interference between the mixing beams, while the second dynamic process involves gratings formed by the random scattered light and the light beam itself. Although the second dynamic process is a slower process [16], it is more temperature dependent than the first process [11]. Thus we see that, for the nondegenerate four-wave mixing process, the interaction between pump beam #2 and the FVCW will dominate the initial stage, which gives rise to the first peak of the FVCW evolution, as can be seen in Fig. 4. However at room temperature, the light-induced scattering would gradually dominate the process, by which the FVCW would lose its energy in the form of scattered light. Thus we see that the FVCW decays rapidly to a small steady-state value, as shown in Fig. 3. As the temperature increases, the thermally activated ionic charges become more mobile and they will drift to screen the electric field of photoinduced electrons. The space charge fields are characterized by the neutralization due to these mobile ions. Although the electronic space charge fields of both the two dynamic processes can be neutralized, the neutralization of the electronic space charge field of the light induced scattering is dominant, which will lead to a reduction in the scattering loss, as will be reported in a follow-up paper [11]. As can be seen in Fig. 4, the neutralization by the thermally activated ions indeed reduces the scattering loss in a thermally stabilized Ce:Fe:$LiNbO_3$ crystal, which gives rise to a strong steady-state FVCW at higher temperatures. In fact, by further increasing the crystal temperature, the scattering loss will be reduced further to a certain extent.

However, when the crystal temperature is above 120°C, more thermally activated ions are generated. Thus not only the light-induced scattering grating is completely neutralized, but also the main diffractive holographic grating, which leads to a decrease in the steady-state intensity. As a matter of fact this observation is quite consistent with the work on thermal fixing in a PR crystal reported by Amodei, *et al* [7,8].

By the way, the output phase-conjugate wave at 633nm, in the counter propagation direction of the probe beam, can be explained by the degenerate four-wave mixing process as follows: pump beam #1 interacts with the probe beam inside the PR crystal to generate a phase grating due to the PR effect. Since there is a strong reflection from the back surface of the crystal due to the high refractive index (n) of $LiNbO_3$, a degenerate four-wave mixing process occurs among pump beam #1, the probe beam, and the reflected beam. This mixing gives rise to a phase conjugate wave in the counter propagating direction of the probe beam. At a higher temperature, the thermally activated ions would reduce the light-induced scattering, by which a higher intensity output phase-conjugate wave at 633nm is generated. As in contrast with room temperature, the intensity of the phase-conjugate wave is significantly reduced by the strong light-induced scattering from all the mixing beams, there is no significant phase-conjugate wave produced at 633nm.

4. Concluding remarks:

Our study shows evidence and an explanation for the strong temperature dependence of the NFWM in a specially doped Ce:Fe:$LiNbO_3$ photorefractive crystal. We have found that an optimum steady-state FVCW output occurs at 120°C, which is attributed to the reduction of light-induced scattering due to neutralization of the electronic space charge field by thermally activated ions. The reduction in scattering allows more energy to go into the FVCW. We have also shown that a degenerate phase-conjugate wave is simultaneously generated at the higher temperature (e.g., 120°C). We

further notice that there are potential uses of NFWM in specially doped Ce:Fe:$LiNbO_3$ PR crystals at an elevated temperature. For example, it can be used for wavefront correction, tunable complex spatial filtering, and others.

Acknowledgments:

The authors acknowledge the support of the Advanced Research Projects Agency through the U.S. Army Research Office under contract No. DAAL03-92-G-0328 and the U.S. Army Missile Command through the U.S. Army Research Laboratory under contract No. DAAL01-93-k-0059.

References:

1. A. Yariv, IEEE J. Quan. Electron., **QE-14** (1978) 650
2. B. Ya. Zel'dovich, V. I. Popovichev, V. V. Gagul'skiy, and F. S. Faizullov, Sov. Phys. JETP, **15** (1972) 109
3. F. T. S. Yu, and S. Jutamulia, "Optical Signal Processing, Computing, and Neural Networks," Chapter 7, (John Wiley & Sons, New York, 1992)
4. C. Bao, J. Zhang, and S. Wang, Appl. Opt., **26** (1988) 652
5. N. Kuktarev, V. Markov, and S. Odulov, Opt. Comm., **23** (1977) 338
6. Z. Wu, J. Wan, G. Zhang, S. Liu, Z. Mou, Y. Lu, and Y. Xu, Chinese Phys., **8** (1988) 664
7. J. J. Amodei, and D. L. Staebler, Appl. Phys. Lett., **18** (1971) 540
8. J. J. Amodei, W. Phillips, and D. L. Staebler, Appl. Opt., **11** (1972) 390
9. H. Vormann, G. Weber, S. Kaphan, and E. Krätzig, Solid State Comm., **40** (1981) 543
10. M. Carrascosa, and F. Agulló-López, J. Opt. Soc. Am. B, **7** (1990) 2317
11. F. T. S. Yu, F. Zhao, H. Zhou, Z. Wu, and D. K. McMillen, "Temperature dependence of the light induced self-diffraction (scattering) in photorefractive Ce:Fe:$LiNbO_3$," in preparation.
12. Z. Wu, S. Jiang, Z. Li, H. Wang, Z. Lou, and Y. Xu, Technical Digest of CLEO/QELS'90, CTuW28 (1990)
13. M. Cronin-Golomb, B. Fisher, J. O. White, and A. Yariv, IEEE J. Quan. Electron., **QE-20** (1984) 12
14. for example, P. Yeh, IEEE J. Quan. Electron., **QE-25** (1989) 484
15. Y. R. Shen, "Principles of Nonlinear Optics," Chapter 14, (John Wiley & Sons, New York, 1984)
16. H. Rajbenbach, A. Delboulbe, and J. P. Huignard, Opt. Lett., **14** (1989) 1275

Figure captions:

Fig.1 The schematic of nondegenerate four-wave mixing (NFWM) in a photorefractive medium. λ_i (i=1,2,p,c) represent the wavelengths of the mixing beams. If $\lambda_1 = \lambda_p$, then $\lambda_c = \lambda_2$ and the output is a phase conjugate replica of the probe beam. Note $\lambda_c \neq \lambda_p$.

Fig.2 The schematic of the experimental setup. Beams ① and ② are the FVCW at 488nm and phase conjugate wave at 633nm, respectively. M: mirror; BS: beam splitter; PD: photodetector. The crystal c-axis is along the z axis.

Fig.3 The intensity evolution of the FVCW at room temperature (20°C) as a function of time.

Fig.4 The intensity evolution of the FVCW at 121°C as a function of time.

Fig.5 The steady-state intensity of the FVCW as a function of the crystal temperature.

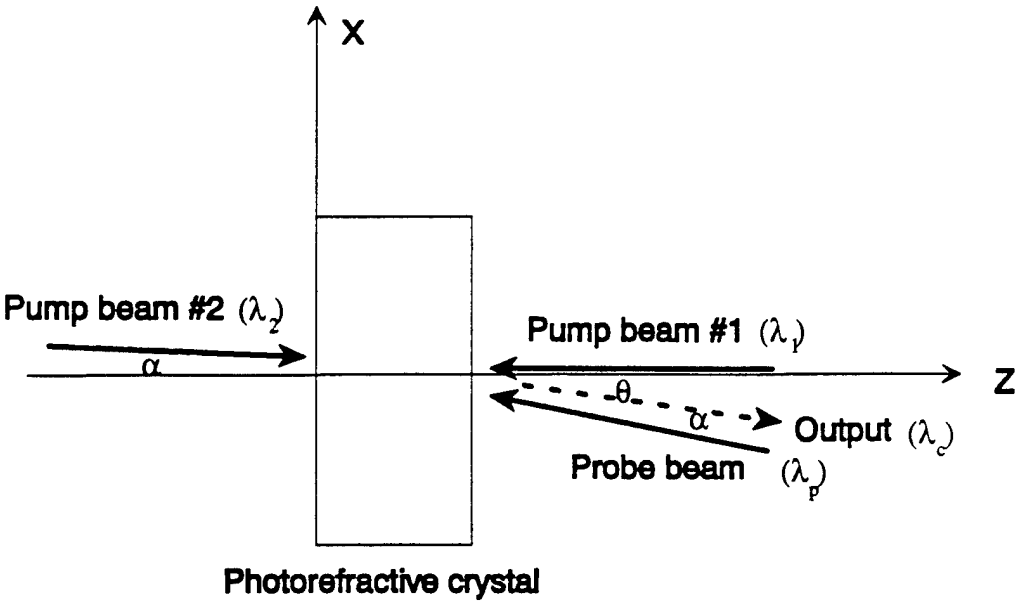
X
Pump beam #2 (λ_2)
α
Pump beam #1 (λ_1)
Z
θ
α
Output (λ_c)
Probe beam (λ_p)
Photorefractive crystal

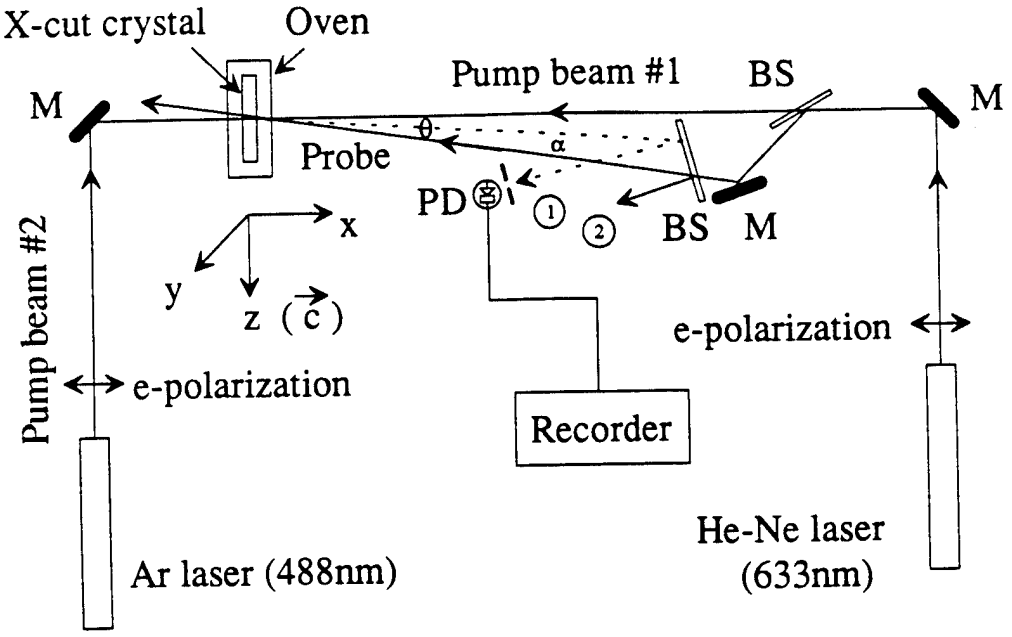
X-cut crystal
Oven
Pump beam #1
BS
M
M
Probe
θ
α
PD
1
2
BS
M
x
y
z (c)
Pump beam #2
e-polarization
e-polarization
Recorder
He-Ne laser
(633nm)
Ar laser (488nm)

Fig. 2

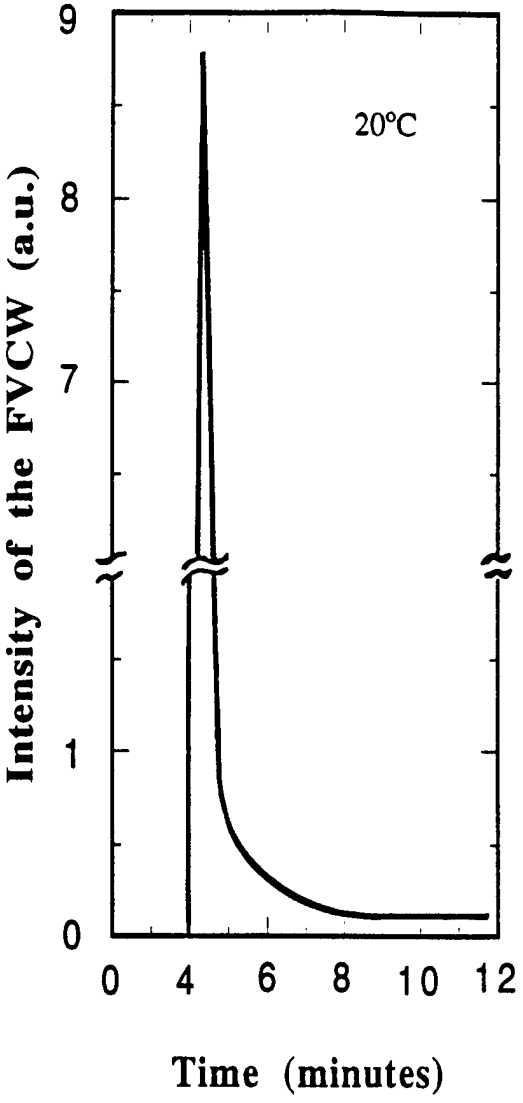

Fig. 3

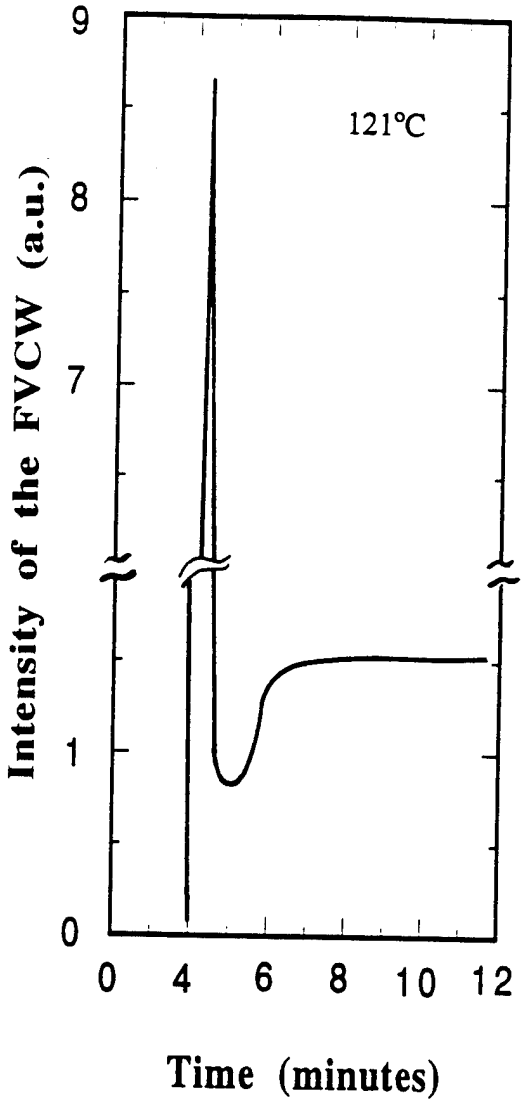

Fig. 1

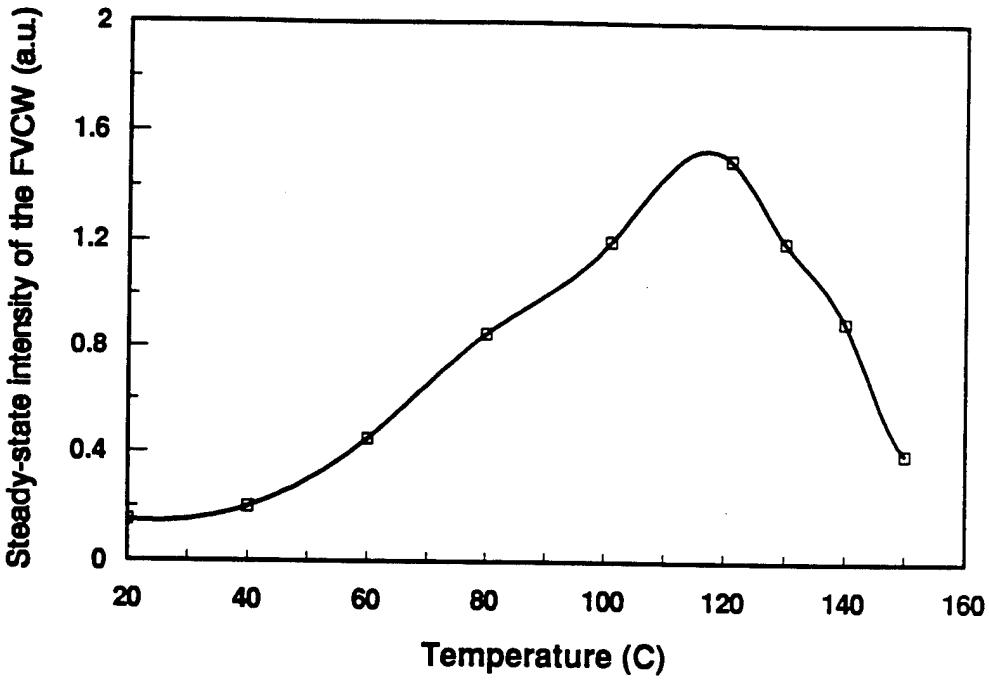
Steady-state intensity of the FVCW (a.u.)
2
1.6
1.2
0.8
0.4
0
20
40
60
80
100
120
140
160
Temperature (C)

Fig. 5

Appendix 10.13

Anomalies of Photovoltaic Current in Ce:Fe: Doped $LiNbO_3$ Crystal at 55°C and 75°C Temperatures

Anomalies of photovoltaic current in Ce: Fe: doped $LiNbO_3$ crystal at 55°C and 75°C temperatures

Francis T. S. Yu, Jianzhong Zhang, Shizhuo Yin, Zhongkong Wu

Department of Electrical Engineering

The Pennsylvania State University

University Park, PA 16802

ABSTRACT

KEY WORDS: Photovoltaic effect, photorefractive crystal

The anomalies of photovoltaic current in Ce: Fe: doped $LiNbO_3$ crystal at 55°C and 75°C temperatures have been investigated. Experiments show that there are about two-fold increase in the photovoltaic current at these temperatures, which is consistent with the anomalies observation in a two-wave mixing experiment reported previously.

The anomalies coupling coefficient in a two-wave mixing experiment using a specially doped Ce:Fe:$LiNbO_3$ crystal at 55°C and 75°C temperatures has been observed in our previous reports.[1] However, since these anomalies are primarily due to effect between the induced electric field $\vec{E}$ and the photovoltaic current $\vec{J}$ [2], we shall investigate the anomalies of photovoltaic current at these temperatures.

It is well known that photorefractive effect can be easily described by the Kukhtarev equations,[3] as given by

$$\frac{dn}{dt} = \frac{dN_D^+}{dt} - \frac{1}{e}\nabla\vec{j}, \tag{1}$$

$$\frac{dN_D^+}{dt} = (s \cdot I + \beta)(N_D - N_D^+) - \gamma_R \cdot n \cdot N_D^+, \tag{2}$$

$$\vec{j} = e \cdot \mu \cdot n \cdot (\vec{E} - \frac{k_B T}{e}\nabla \ln n) + p \cdot I \cdot \vec{e}_c, \tag{3}$$

$$\nabla(\varepsilon_0 \cdot \vec{E}) = 4\pi e(n + N_A - N_D^+), \tag{4}$$

where n is the density of free electron in the conduction band, N_d and N_d^+ are donor and the ionized donor densities, $\vec{E}$ is the induced electric field, s is the cross section of photoionization, β is the rate of thermal generation, γ_R is the recombination constant, μ is the mobility of the electron in the crystal, and p is the photovoltaic constant. Suppose that the interference pattern in a two-wave mixing take the following form

$$I = I_o \cdot [1 + M \cdot \cos(Kz)], \tag{5}$$

the free electron density would be

$$n = n_0 \cdot [1 + m \cdot \cos(Kz)] \tag{6}$$

By substituting Eqs.(5) and (6) into Eq.(3), the induced electric field can be written as.

$$E = \frac{\frac{J}{\sigma_0} + E_D \cdot m \cdot \sin(Kz) - E_{ph} \cdot [1 + M \cdot \cos(Kz)]}{1 + m \cdot \cos(Kz)} \tag{7}$$

Where

$$\sigma_0 = e \cdot \mu \cdot n_0, \tag{8}$$

$$E_D = \frac{k_B T}{e} K, \tag{9}$$

and $$E_{ph} = \frac{p}{\sigma_0}. \tag{10}$$

From the preceding Eq.(7), we see that the photo-induced electric field depends on the photovoltaic current. Thus, we may expect photovoltaic current anomalies at temperatures near the anomalies observed with two-wave mixing[1].

To show the anomalies photovoltaic current, experiments are conducted and shown in Fig.1, in which an Ar+ laser is used to illuminate the crystal along the a-axis of the crystal. The photovoltaic current is measured by using a low-noise current pre-amplifier with an x-y recorder. Since the photovoltaic current from the crystal is in the order of a few pA, a copper chamber is used to isolate the specimen from external interference as shown in the figure. To vary the crystal temperature, an electric oven is used within the isolating chamber. The photovoltaic current also depends on its previous illumination history, we have found that a negative photoconductivity can be measured if the crystal

had been long exposed to the laser light. When the crystal is heated to about 250°C for about 30 minutes, it can erase the previous influences due to laser illumination. The photovoltaic currents from room temperature(30°C) to 300°C are measured. The experimental results are shown in Fig.2, in which we see that two anomalies peak currents occurred at 55°C and at 75°C. The anomalies observation is in fact consistent with what we have reported in our previous article[1]. Although the photocurrent shows anomalies, the absorption of the crystal doesn't change with temperature. The lack of change indicates that the increase in photovoltaic current is not due to the increase of absorption, but rather there may be structural changes at anomalous temperatures.

When the crystal is heated above 180°C, the photovoltaic current increases very rapidly, However, the absorption change of the crystal is negligibly small. We believe that the rapid increase of photovoltaic current is primarily due to the detrapping of electrons in the crystal. In other words, when the crystal is illuminated by the laser, electrons in Fe^{2+} ions are excited into the conduction band, and then trapped by Fe^{3+} ions. As the temperature increases above 180°C, the electrons are detrapped from the recombination center that causes the rise in photocurrent. Note that rapid increase in photovoltaic current at higher temperatures would cause the erasure of photorefractive grating.

Reference:

[1] Feng Zhao et. al, " Photorefractive enhancement near 57°C, 70°C, and 110°C in cerium-iron-doped single crystal lithium niobate " Submitted to **Applied Optics**.

[2] A. M. Glass, et.al "Excited state polarization, bulk photovoltaic effect and the photorefractive effect in electrically polarized media" **Journal of Electronic Materials**, Vol.4, No.5, pp915-943(1975)

[3] N. V. Kukhtarev. et.al. "Holographic storage in Electrooptic crystal. I steady state" **Ferroelectrics**, Vol.22, pp949-960(1979)

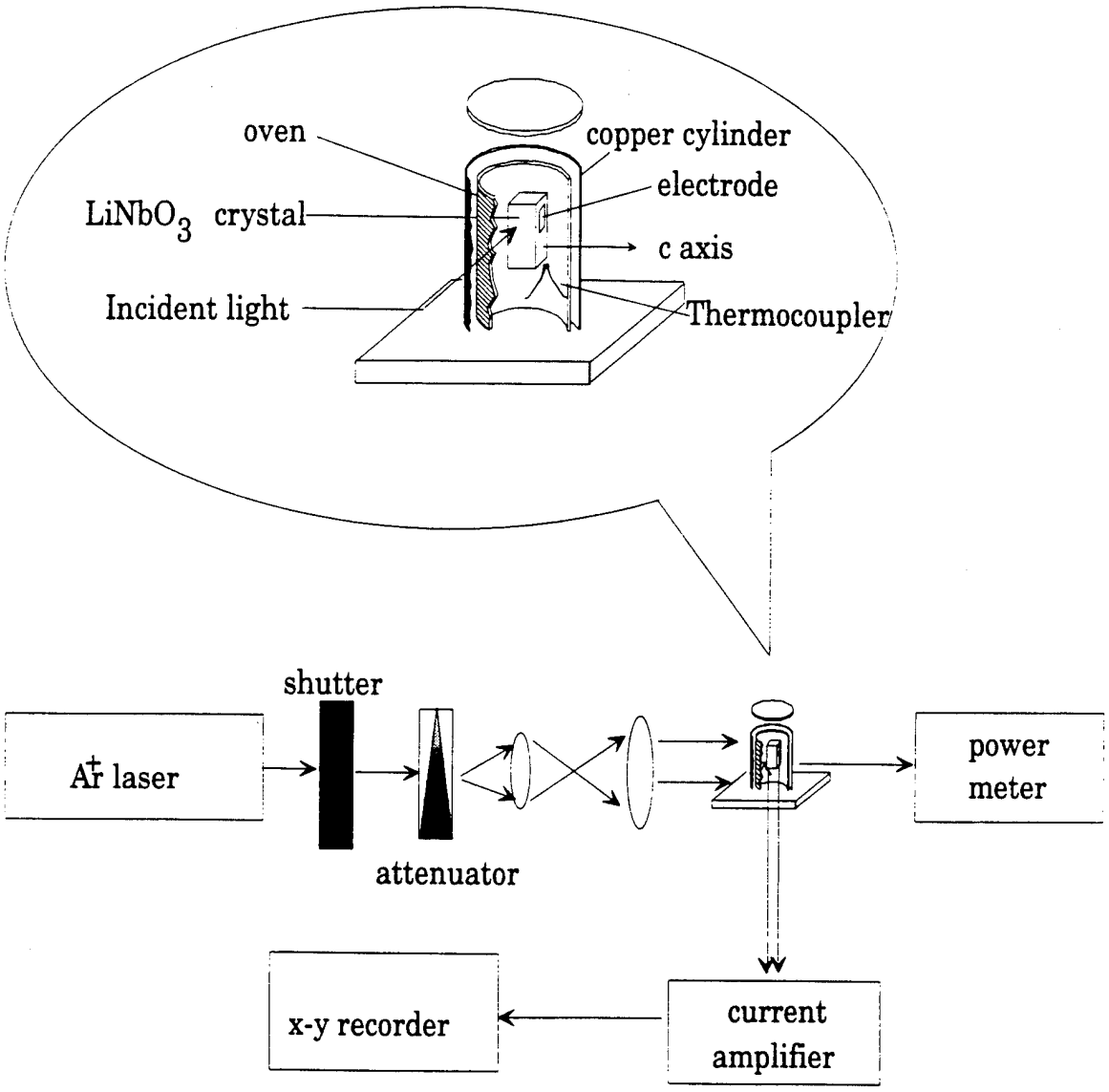

Fig.1 Experimental setup

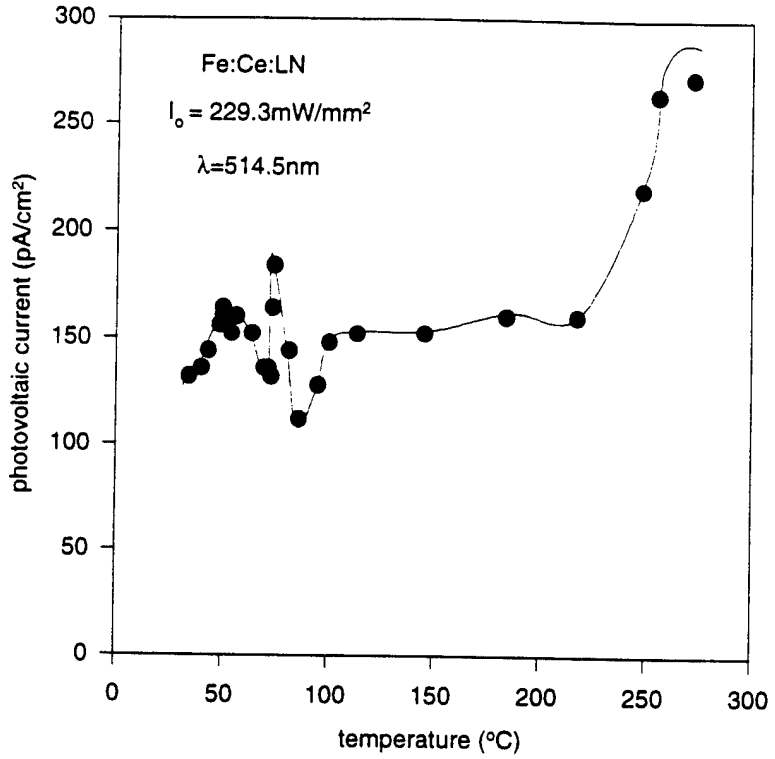

Fig.2 Photovoltaic current of Fe:Ce:LN crystal at different temperatures

Appendix 10.14

Temperature Dependence of Light-Induced Scattering and Noise Suppression in Ce:Fe:$LiNbO_3$ Photorefractive Crystal

Temperature dependence of light-induced scattering and noise suppression in Ce:Fe:$LiNbO_3$ photorefractive crystal

Feng Zhao, Hanying Zhou, Zhongkang Wu, and Francis T. S. Yu

Department of Electrical Engineering

The Pennsylvania State University

University Park, Pennsylvania 16802

Deanna K. McMillen

Photonics Group

U. S. Army Missile Command

Redstone Arsenal, Alabama 35898-5248

Abstract

The temperature dependence of light-induced scattering and noise suppression in a Ce:Fe:$LiNbO_3$ crystal is studied. Taking thermally activated ions into account in Kukhtarev's equations, we show that by lifting the crystal temperature, the light-induced electronic space charge field may be neutralized by thermally activated ions, leading to a reduction in the scattering noise. We have experimentally confirmed that raising the crystal temperature cause a reduction in scattering noise consistent with the calculations. The signal-to-noise ratio (SNR) evolution in a photorefractive two-wave amplification process is also analysized. Experimental demonstration of the enhancement of SNR is provided using the Ce:Fe:$LiNbO_3$ crystal.

I. Introduction:

The photorefractive (PR) effect has been extensively studied in recent years, and has shown promise for a variety of applications [1]. Light-induced scattering (beam-fanning) is a well-known photorefractive phenomena in which a coherent laser beam is scattered asymmetrically as it passes through a PR crystal. A typical scattering pattern in a $LiNbO_3$ crystal with an extra-ordinary polarization laser beam is shown in Fig.1. The light-induced scattering was first observed by Ashkin *et al.* in 1966 [2], and was later attributed to photorefractive amplification (two-beam coupling) [3,4] of light scattered from crystal imperfections in the volume and at the surfaces. Direct experimental evidence of this two-beam coupling model has been given by Zhang *et al.* using an iron-doped $LiNbO_3$ PR crystal [5].

The light-induced scattering can be useful, for example, in self-pumped phase conjugators [6], photorefractive oscillators [7], optical limiting [8], etc., where a strong and fast light-induced scattering is desirable. However, it is an unwanted side-effect in many other cases such as image amplification [9], volume holographic storage [10,11], and multiplexed filter synthesis [12], where the scattering not only causes energy loss in the main beam (signal beam), but also contributes to noise, which results in a poor signal-to-noise ratio (SNR). Therefore, minimizing the light-induced scattering is an important issue for these applications. However, only limited efforts have been given to this end [13,14,15], in which either a high power pulsed laser, or a mechanically rotated crystal is involved.

In this paper, we shall investigate the temperature dependence of light-induced scattering in a photorefractive $LiNbO_3$ crystal with the goal of noise suppresion. We will focus our attention on $LiNbO_3$ crystals, since, compared with other PR crystals such as barium titanate ($BaTiO_3$) and strontium barium niobate ($Sr_xBa_{1-x}Nb_2O_6$), lithium niobate has no structural phase transformation near room temperature. It is therefore possible for us to operate $LiNbO_3$ in a higher temperature region (e.g., 60°-150°C).

It has been shown by several authors that during the holographic thermal fixing process in $LiNbO_3$, thermally activated ionic charges become mobile and neutralize the photo-induced electronic grating [16,17]. Vormann *et al.* [18] have identified hydrogen ions (protons) as the dominant ionic charges in $LiNbO_3$ at the high temperature. Since the noise grating is of no difference from other gratings, it is thus expected that by elevating the crystal temperature, the light-induced (electronic) scattering grating would be weakened by the same mechanism at high temperature. Assume initial signal is larger than the initial noise, than in a two-wave-mixing process, it is expected that the scattering noise grating would be neutralized before the desired signal gratings. Apparently, one advantage of this technique is that the photorefractive response speed can be enhanced, since the mobility of the photo-induced electrons increases as the temperature increases [19].

This paper is organized as follows: In section II, we present the theoretical background of scattering noise suppression by raising the crystal temperature. We will solve Kukhtarev's equations taking into account the thermally activated ions and show that the light-induced scattering grating can be neutralized by these ions. In section III, experimental results of reducing the light-induced scattering in a Ce:Fe:$LiNbO_3$ crystal in the temperature range between 20°C and 120°C will be provided. The data are analyzed and we will see that the experimental results are in good agreement with the theoretical model. Finally, a discussion on SNR enhancement and concluding remarks will be given.

II. Theoretical background:

When a single laser beam passes through a PR crystal, it produces scattered light (intrinsic scattering) from defects or imperfections within the PR crystal. The scattered lights will experience photorefractive gain through, according to commonly accepted models, a two-wave mixing process, and thereby reduce the transmitted beam intensity. Since we are not particularly concerned about the spatial structure of the scattered light

pattern, we assume an isotropic scattering process for simplicity and use a simple two-wave mixing model instead of the multi two-wave mixing model [20, 21]. Under these conditions, the transmitted beam intensity can be approximately described by [4, 22]:

$$I(t) = I(0)\frac{1+m_o}{1+m_o\, exp\left[\Gamma_{eff}(t)d\right]}, \tag{1a}$$

with effective two-beam-coupling coefficient Γ_{eff} given by

$$\Gamma_{eff}(t) = \frac{\pi}{m\lambda\cos\theta}\gamma_{eff}\, n^3\, \mathcal{Im}(E_{sc}), \tag{1b}$$

where *I(0)* is the initial transmitted light intensities, m_o is the ratio of the incident beam to the initial effective scattering intensity and $m = 2\sqrt{m_o}/(1+m_o)$ is the modulation depth, d is the crystal thickness, γ_{eff} is the effective electro-optic coefficient of the crystal, E_{sc} is the complex amplitude of the space-charge field within the crystal, $\mathcal{Im}$ represents the imaginary part of E_{sc}, λ is the laser wavelength in free-space, n is the normal refractive index of the crystal, and θ is an average angle between the scattered light and the input beam.

Note that in general, the space charge field E_{sc} receives contributions from two sources, i.e., the electrons and ions. At room temperature the photo-induced electronic field will dominate. This is because both the number and mobility of the ions are strongly temperature dependent, and at room temperature, there is simply not enough kinetic energy for ions to have significant mobility and the influence of the ionic field can be ignored. As a result, the build-up of the space-charge field E_{sc} is simply the build-up of photoinduced electronic field, and exhibits a single exponential behavior for small beam ratio m_o [19, 23].

When the crystal is at higher temperatures, in addition to the optically (and thermally) excited electrons, thermally excited ions (protons) become mobile and will contribute to the space-charge field. The mobile ions move in a way to neutralize the

electronic one [17,18,24,25]. By including both the optical excitation of electrons and thermal excitation of protons in Kukhtarev's material equations [19], it can be shown that (see Appendix) the growth of the net space charge field E_{sc} is proportional to the difference between the electronic donor grating amplitude D_1 and the proton grating amplitude H_1. From Eq.(A6), we have

$$E_{sc} = \frac{e}{iK\varepsilon}(D_1 - H_1)$$
$$= \frac{eB}{iK\varepsilon}\left[\frac{A_h - \Gamma_h}{\alpha_1\alpha_2} + \frac{A_h - \Gamma_h + \alpha_1}{\alpha_1(\alpha_1 - \alpha_2)}exp(-\alpha_1 t) + \frac{\Gamma_h - A_h - \alpha_2}{\alpha_2(\alpha_1 - \alpha_2)}exp(-\alpha_2 t)\right], \quad (2a)$$

with

$$\alpha_{1,2} = \frac{1}{2}\left\{(\Gamma_h + \Gamma_e - i\Gamma_{ph}) \mp \left[(\Gamma_h - \Gamma_e + i\Gamma_{ph})^2 + 4A_hA_e\right]^{1/2}\right\}, \quad (2b)$$

where the meaning of notations Γ_h, Γ_e, Γ_{ph}, A_h, A_e, and B are defined in the Appendix (see Eq.(A4)), with subscripts h, e, and ph denote protonic, electronic, and photovoltaic related material parameters.

In view of Eq.(2), we can see that the time evolution of the space charge field E_{sc} is composed of two exponential terms characterized by α_1 and α_2. Note that when the temperature is not too high (<150°C), α_1 and α_2 can be simplified to be:

$$\alpha_1 \approx \Gamma_e - i\Gamma_{ph}, \quad (3a)$$

$$\alpha_2 \approx \Gamma_h. \quad (3b)$$

Therefore, we see that the first exponential (which is a function of α_1) is mainly due to the contribution from electronic grating, and the second exponential (which is a function of α_2) approximately corresponds to the thermally activated ions.

One can imagine that due to the difference in effective mass of electrons and protons, the photoinduced electrons and thermally activated protons will have different mobility and time constants in the crystal lattice. The time constants are in fact the inverse of the real part of α_1 and α_2. Figure 2 illustrates typical time constants of the

electronic and ionic gratings as a function of temperature. One can observe that the build-up rate of the ionic grating has a much stronger temperature dependence than the electronic counterpart, and becomes comparable to that of the electronic one when the temperature is above ~80°C. As indicated in the figure, it will take several hundreds years for a proton grating to build up at room temperature, but only several minutes at near 100 °C. This explains why the protons do not contribute to the space-charge field at room temperature, while at higher temperatures, grows fast enough to affect the photorefractive process.

In short, in the high temperature region, the net space-charge field E_{sc} will be weakened due to the neutralization of the electronic grating by the thermally excited ionic charges. As a result, the effective coupling constant Γ_{eff} of the light-induced scattering process becomes smaller, leading to an increase in the transmitted light intensity $I(t)$, as given by Eq.(1). In the next section, we shall provide some experimental results to support above analyses.

III. Experimental results:

Figure 3 shows the experimental setup that we used for our study. A single laser beam passes through a Ce:Fe:$LiNbO_3$ crystal which is housed in a temperature controllable oven. The size of the crystal is about 10×10×2 mm^3 (Y:Z:X). The Ce:Fe:$LiNbO_3$ crystal is in fact a single domain crystal which is grown along the *c*-axis by using the conventional Czochralski method from congruent melt. The doping concentrations for both the Ce and Fe are about 0.08mol%. The crystal was annealed in a vacuum chamber at ~800°C for about 2 hours. The sample is aligned so that the c-axis is in the incident plane (i.e., extra-ordinary polarization wave is used). A programmable temperature controller (Omega CN2002) is used to control the oven. The temperature variation was less than 1°C over a period of 1 hour for all experiments. The input laser beam is provided by a He-Ne laser of wavelength λ=633nm. The power of the laser beam

is about 40mW in front of the sample. As shown in the Fig.3, the laser beam is spatially filtered to produce a fundamental Gaussian beam, with a diameter of approximately 3mm. A 3mm iris is placed between the crystal and the photodiode to block scattered light, so that only the transmitted signal beam intensity is recorded. A computer is used to control the temperature of the crystal and for data acquisition from the photodiode.

The time evolution of the transmitted beam intensity was recorded at various temperatures. Figure 4 shows the results at three temperatures: 20°C, 60°C and 120°C. As can be seen from this figure, at the lower temperatures, the transmitted beam intensity $I_t(t)$ decreases as the time increases, which means the light-induced scattering gradually builds up and causes energy loss in the transmitted beam. This scattering loss is considerable (~ 45%) at room temperature (20°C). By raising the operating temperature, the scattering loss was reduced to be about 14% at 60°C and nearly zero at 120°C. The corresponding scattering patterns (at steady-state) are shown in Fig.5, from which we see that the scattering noise is evidently reduced by increasing the crystal temperature.

To demonstrate the validity of the our theoretical analysis in the preceding section, we plotted, in Fig.6, the theoretical fit using Eqs. (1) and (2) to the experimental data. The parameters we used for the theoretical fit are listed in Table 1. Most values of the parameters are in the typical range for $LiNbO_3$ from previous publications. The activation energy of electrons, $\varepsilon_e = 0.11eV$, however, is little lower than the reported data (0.18eV) [26] but is still reasonable due to the fact that our sample of $LiNbO_3$ crystal is heavily doped with Fe, which could result in a decreased activation energy of electrons [27]. The initial scattering noise to input beam ratio m_o is assumed to be 5×10^{-3}, which corresponds to a scattering light intensity of about 20μW. We also assume an average angle (θ=4°) between the scattered lights and the input beam. As can be seen from Figs.4 and 6, the theoretical evaluation given by Eqs. (1) and (2) agrees well with the experimental results.

IV. Signal-to-noise ratio enhancement

So far we have demonstrated that the light-induced scattering noise in a single beam case can be effectively suppressed by increasing the operating temperature. However, it would be of no practical use if the main grating (the signal grating) is also significantly suppressed. To explore the possibility of scattering noise suppression without much sacrifice in the signal beam, we have to consider a real situation with the presence of a main grating in addition to the noise grating, and examine the signal-to-noise ratio (SNR).

Let us consider a fundamental photorefractive process, i.e., two-wave-mixing, for example. Assume that a strong reference beam and a weak signal beam form a signal grating in the PR crystal. The scattered lights from both beams interact with the strong reference beam and, as a result, create an effective noise grating. Since both the signal beam and the scattered lights are amplified by the strong reference beam via photorefractive two-wave mixing, their intensity growths are governed by the same equation [28] as,

$$I_s(t) = I_s(0)\frac{1+m_{so}}{1+m_{so}^{-1}\,exp\left[-\Gamma_{eff}(t)d\right]}, \qquad s = s,n, \tag{5}$$

and therefore the evolution of *SNR* is

$$SNR(t) = \frac{I_s(t)}{I_n(t)} = SNR(0)\cdot\frac{1+m_{so}}{1+m_{no}}\cdot\frac{1+m_{no}^{-1}\,exp\left[-\Gamma_{eff}(t)d\right]}{1+m_{so}^{-1}\,exp\left[-\Gamma_{eff}(t)d\right]}, \tag{6}$$

where $SNR(0)=I_s(0)/I_n(0)$ is the initial signal-to-noise ratio, m_{so} and m_{no} are the initial signal-to-reference and noise-to-reference beam ratios, respectively. In Fig.7, we plotted the SNR development at different temperatures, 20°C, 60°C and 120°C. Figure 7(a) shows the SNR development for an initial $SNR(0)$=100, from which we see that there is a 16dB increase in SNR if the temperature increases from 20°C to 120°C. Even for a small

initial *SNR(0)*=2, as depicted in Fig. 7(b), there is still a 4dB improvement in SNR.

Figure 8 shows the experimental result of an amplified letter-image "PSU" at different temperatures. At each temperature, the exposure time was set long enough (>15 minutes) to reach photorefractive saturation, i.e., the maximum amplification. We can see from Fig. 8 that, at 120°C, the amplified image has the best signal-to-noise ratio; while at 20°C, although the amplified image has the strongest intensity, it exhibits the worst signal-to-noise ratio. In general, a compromise can be made between the signal level and SNR, as the thermally activated ionic charges also neutralize the signal grating, leading to an decrease in the signal level.

Above results indicate that it is possible to achieve a higher SNR above room temperature. In fact, as long as the initial signal-to-reference ratio (m_{so}) is larger than the initial noise-to-reference ratio (m_{no}), then, the growth of the scattering noise in a two-wave-mixing process will be always slower than the growth of the signal beam [29]. This will in principle guarantee the enhancement of the SNR in a two-wave-mixing process. Of course, one can expect that exists an optimum operation temperature region, which may vary with the initial signal-to-noise ratios as well as the material characteristics.

V. Discussion and conclusion remarks:

Since the light-induced scattering noise is initialized by material intrinsic scattering centers, such as crystal imperfection and inhomogenities including photorefractive centers, one can, of course, reduce the intrinsic scattering by using materials with better optical qualities. However, even with a crystal of perfect optical quality, there exists a minimum scattering density, i.e., the dopant's density, which also determines the photorefractive effect. The initial scattering noise due to these photorefreactive centers can be very small (10^{-3}~10^{-4}), but it can be amplified via strong photorefractive gain (exponential gain can be as high as 40). Therefore, it is very

important to have an effective way to eliminate this amplified noise even when the crystal is of good optical quality.

Metion must also be made that although this noise suppression technique requires operating in a higher temperature region, this study suggests a possible approach to achieve room temperature operation by special doping and processing of the PR crystal, such that both the number and mobilities of the ions are increased. By introducing dopants with shallow ionic energy levels, noise suppression at room temperature might be possible.

In summary, we have investigated the temperature dependent light-induced scattering in $LiNbO_3$. The scattering noise in a signal beam case has been effectively reduced by increasing the temperature. The signal-to-noise ratio in a two-wave-mixing case is examined for different temperatures. The results suggest a new noise suppression technique by raising the crystal temperature, which is important in applications such as image amplification, holographic memeory, and multiplexed filter synthesis.

VI. Acknowledgment:

The authors acknowledge the support of the Advanced Research Projects Agency through the U.S. Army Research Office under contract No. DAAL03-92-G-0328 and the U.S. Army Missile Command through the U.S. Army Research Laboratory under contract No. DAAL01-93-k-0059.

VII. Appendix: Solution to the Kukhtarev's material equation at high temperature

Including both optically and thermally excited electrons and protons in $LiNbO_3$ crystal, the Kukhtarev's material equations can be extended to [9, 19, 25],

$$\dot{n} = \dot{D} - \frac{1}{e}\frac{\partial j_e}{\partial x}, \tag{A1a}$$

$$\dot{D} = -\dot{A} = (s + \sigma I / h\nu)D - rnA, \tag{A1b}$$

$$\frac{\partial E}{\partial x} = \frac{\rho}{\varepsilon}, \tag{A1c}$$

$$H = -\frac{1}{e}\frac{\partial j_h}{\partial x}, \tag{A1d}$$

$$j_e = e\mu_e nE + D_e e\frac{\partial n}{\partial x} + e\sigma L_{ph} DI/h\nu, \tag{A1e}$$

$$j_h = e\mu_h HE - D_h e\frac{\partial H}{\partial x}, \tag{A1f}$$

where we have used the following notations: n, H: free electron and proton densities; j_e, j_h: the corresponding current densities; $D_e = D_{eo}\, exp[-\varepsilon_e/k_BT]$, $D_h = D_{ho}\, exp[-\varepsilon_h/k_BT]$ and $\mu_e = (e/k_BT)D_e$, $\mu_h = (e/k_BT)D_h$: their diffusion constants and mobilities, respectively; D, A: electronic donor and acceptor densities; $s = s_o\, exp[-\varepsilon_D/k_BT]$: thermal generation rate of donors; σ: photoionization cross section; r: recombination constant of acceptor; L_{ph}: photovoltaic transport length; I and hν: optical intensity and photon energy; E: space-charge field induced by charge distribution; ρ: photoinduced charge density; e: electronic charge.

Assume the intensity distribution of an illumination is of the form:

$$I = I_o\left(1 + \frac{1}{2}me^{iKx} + c.c.\right), \tag{A2}$$

where K is the grating vector, $c.c.$ denotes complex conjugate, and $m = 2\sqrt{m_o}/(1+m_o)$ is the modulation depth with initial intensity ratio $m_o << 1$. Then, the spatial variation of all other quantities is expected to follow the intensity pattern as:

$$[\ ] = [\ ]_o + \frac{1}{2}[\ ]_1 e^{i(Kx+\phi)} + c.c., \tag{A3}$$

where [ ] stands for n, H, j_e, j_h, D, A and E. $[\ ]_1$ are the complex amplitudes of the spatial modulation of these quantities containing possible phase shifts relative to the intensity pattern.

For not very high intensity, we have $\rho \approx (H_1 - D_1)e$. Thus, the amplitude of the space-charge field E_1 can be easily found if the amplitudes of the electronic grating D_1 and the ionic grating H_1 are known. Substituting relations represented by Eq.(A3) into

Eq.(A1) and following the standard linearization procedure, one obtains the following coupled equations for H_1 and D_1 under the usual quasi-equilibrium condition ($\dot{n} = 0$):

$$\dot{D}_1 = -\left(\Gamma_e - i\Gamma_{ph}\right)D_1 + A_e H_1 - B, \tag{A4a}$$

$$\dot{H}_1 = -\Gamma_h H_1 + A_h D_1, \tag{A4b}$$

where:

$$A_e = \mu_e n_o e/\varepsilon, \tag{A4c}$$

$$A_h = \mu_h H_o e/\varepsilon, \tag{A4d}$$

$$\Gamma_e = A_e + \beta n_o D_e K^2, \tag{A4e}$$

$$\Gamma_h = A_h + D_h K^2, \tag{A4f}$$

$$\Gamma_{ph} = K\sigma L_{ph} I_o/h\nu, \tag{A4g}$$

$$B = -imD_o\Gamma_{ph} + D_e K^2 \frac{m\sigma D_o I_o}{rA_o h\nu}, \tag{A4h}$$

$$n_o = \frac{\left(s + \sigma I_o/h\nu\right)D_o}{rA_o}, \tag{A4i}$$

$$\beta = 1/D_o + 1/A_o, \tag{A4j}$$

$$H_o = H_{oo}\, exp\left(-\varepsilon_h/k_b T\right). \tag{A4k}$$

The coupled equation (A4) can be de-coupled as:

$$\ddot{D}_1 + \left(\Gamma_h + \Gamma_e - i\Gamma_{ph}\right)\dot{D}_1 + \left(\Gamma_h\Gamma_e - A_h A_e - i\Gamma_h\Gamma_{ph}\right)D + \Gamma_h B = 0, \tag{A5a}$$

$$\ddot{H}_1 + \left(\Gamma_h + \Gamma_e - i\Gamma_{ph}\right)\dot{H}_1 + \left(\Gamma_h\Gamma_e - A_h A_e - i\Gamma_h\Gamma_{ph}\right)H_1 + A_h B = 0. \tag{A5b}$$

By using the initial conditions: $H_1(t=0)=D_1(t=0)=0$, the solutions can be found to be:

$$D_1 = -B\left[\frac{A_h}{\alpha_1\alpha_2} + \frac{A_h}{\alpha_1(\alpha_1 - \alpha_2)}exp(-\alpha_1 t) - \frac{A_h}{\alpha_2(\alpha_1 - \alpha_2)}exp(-\alpha_2 t)\right], \tag{A6a}$$

$$H_1 = -B\left[\frac{\Gamma_h}{\alpha_1\alpha_2} + \frac{\Gamma_h - \alpha_1}{\alpha_1(\alpha_1 - \alpha_2)} exp(-\alpha_1 t) - \frac{\Gamma_h - \alpha_2}{\alpha_2(\alpha_1 - \alpha_2)} exp(-\alpha_2 t)\right], \qquad \text{(A6b)}$$

where

$$\alpha_{1,2} = \frac{1}{2}\left\{\left(\Gamma_h + \Gamma_e - i\Gamma_{ph}\right) \mp \left[\left(\Gamma_h - \Gamma_e + i\Gamma_{ph}\right)^2 + 4A_hA_e\right]^{1/2}\right\}. \qquad \text{A(6c)}$$

References

[1] P. Gunter and J.-P. Huignard, in "Photorefractive materials and their applications II," Chapter 6, (Springer-Verlag, New York, 1988).

[2] A. Ashkin, G. D. Boyd, J. M. Dziedzic, R. C. Smith, A. A. Ballman, J. J. Levinstein and K. Nassau, "Optically-induced refractive index inhomogeneities in $LiNbO_3$ and $LiTaO_3$," Appl. Phys. Lett., **9**, 72 (1966).

[3] V. V. Voronov, I. R. Dorosh, Yu. S. Kuz'minov, and N. V. Tkachenko, "Photoinduced light scattering in Cesium-doped variant Strotnium Niobate crystals," Sov. J. Quantum Electron., **10**, 1346 (1980).

[4] M. Segev, Y. Ophir, and B. Fischer, "Nonlinear multi two-wave mixing, the fanning process and its bleaching in photorefractive media," Opt. Comm., **77**, 265 (1990).

[5] G. Zhang, Q. Li, P. Ho, S. Lin, Z. Wu, and R. R. Alfano, "Dependence of speckle size on the laser beam size via photo-induced light scattering in $LiNbO_3$:Fe," Appl. Opt., **25**, 2955 (1986).

[6] J. Feinberg, "Self-pumped, continuos-wave phase conjugator using photorefractive fanout," Opt. Lett., **13**, 856 (1982).

[7] J. O. White, M. Cronin-Golomb, B. Fischer and A. Yariv, "Coherent oscillation by self-induced gratings in the photorefractive crystal $BaTiO_3$," Appl. Phys. Lett., **40**, 450 (1982).

[8] M. Cronin-Golomb and A. Yariv, "Optical limiters using photorefractive nonlinearities," J. Appl. Phys., **57**, 4906 (1985).

[9] N. V. Kukhtarev, V. B. Markov, S. G. Odulov, M. S. Soskin and V. L. Vinetskii, "Holographic storage in electrooptic crystals, II. Beam coupling - light amplification," Ferroelectrics, **22**, 961 (1979).

[10] F. H. Mok, "Angle-multiplexed storage of 5000 holograms in lithium niobate," Opt. Lett., **18**, 915 (1993).

[11] S. Yin, H. Zhou, F. Zhao, M. Wen, Z. Yang, and F. T. S. Yu, "Wavelength multiplexed holographic storage in a sensitive photorefractive crystal using a visible-light tunable diode laser," Opt. Comm., **101**, 317 (1993)

[12] F. T. S. Yu, S. Yin, Z. H. Yang, "Thick volume photorefractive crystal wavelength-multiplexed reflection-type matched filter," Optical Memory and Neural Network, to be published (1994).

[13] H. Rajbenbach, A. Delboulbe, and J. P. Huignard, "Noise suppression in photorefractive image amplifiers," Opt. Lett., **14**, 1275 (1989).

[14] W. S. Rabinovich , B. J. Feldman and G. C. Gilbreath, "Suppression of photorefractive beam fanning using achromatic gratings," Opt. Lett., **16**, 1147 (1991).

[15] J. Joseph, P. K. C. Pillari and K. Singh, "A novel way of noise reduction in image amplification by two-beam coupling in photorefractive $BaTiO_3$ crystal," Opt. Comm., **80**, 84 (1990).

[16] W. Meyer, P. Wurfel, R. Munser, and G. Muller-Vogt, "Kinetics of fixing of phase holograms in $LiNbO_3$," Phys. Stat. Sol. (A), **53**, 171 (1979).

[17] J. J. Amodei and D. L. Staebler, " Holographic pattern fixing in electro-optic crystals," Appl. Phys. Lett., **18**, 540 (1971).

[18] H. Vormann, G. Weber, S. Kapphan and E. Kratzig, "Hydrogen as origin of thermal fixing in $LiNbO_3$:Fe," Solid State Comm., **40**, 543 (1981).

[19] N. V. Kukhtarev, V. B. Markov, S. G. Odulov, M. S. Soskin, and V. L. Vinetskii, "Holographic storage in electrooptic crystals, I. Steady state" Ferroelectrics, **22**, 949 (1979).

[20] M. Yu, S. G. Odoulov and B. I. Sturman, "Polarization-anisotropic scattering lines in $LiNbO_3$," Appl. Phys., **B56**, 223 (1993).

[21] M. Segev, D. Engin, A. Yariv and G. Valley, "Temporal evolution of fanning in photorefractive materials," Opt. Lett., **18**, 956 (1993).

[22] R. A. Rupp and F. W. Drees, "Light-induced scattering in photorefractive crystals," Appl. Phys., **B39**, 223 (1986).

[23] G. C. Valley and M. B. Klein, "Optimal properties of photorefractive materials for optical data processing," Opt. Eng., **22**, 704 (1983).

[24] P. Hertel, K. H. Ringhofer and R. Sommerfeldt, "Theory of thermal hologram fixing and application to $LiNbO_3:Cu^2$," Phys. Stat. Sol., **A104**, 855 (1987).

[25] M. Carrascosa and F. Agullo-Lopez, "Theoretical modeling of the fixing and developing of holographic gratings in $LiNbO_3$," J. Opt. Soc. Am. B, **7**, 2317 (1990).

[26] W. Josch, R. Munser, W. Ruppel and P. Wurfel, "The photovoltaic effect and the charge transport in $LiNbO_3$," Ferroelectricity, **21**, 623 (1978).

[27] I. B. Barkan, M. V. Entin and S. I. Marennikov, "Conductivity of Fe-doped $LiNbO_3$ crystals," Phys. Stat. Sol., **A44**, K91 (1977).

[28] P. Yeh, "Two-wave-mixing in nonlinear media," IEEE J. Quan. Electron., **QE-25**, 484 (1989).

[29] M. Horowitz, R. Daisy, and B. Fischer, "Signnal-to-pump ratio dependence of buildup and decay rates in photorefractive nonlinear two-beam coupling," J. Opt. Soc. Am. B, **9**, 1685 (1992).

Figure Captions:

Fig.1. A typical light-induced scattering pattern in $LiNbO_3$ crystal with an extra-ordinary polarized laser beam.

Fig.2. Time constants of the electron and the proton gratings in $LiNbO_3$ crystal as a function of temperature.

Fig.3. Experimental schematic for observation of a single beam light-induced scattering.

Fig.4. Experimental results of time evolution of the transmitted beam intensity *I(t)*. As the transmitted light decreases, the scattering noise gradually builds up.

Fig.5. Theoretical fits to the experimental data presented in Fig.4

Fig.6. Corresponding steady-state scattering patterns at 20°C, 60°C and 120°C.

Fig.7. Evoluiton of signal-to-noise ratio (SNR) at different temperatures.
(a): Initial SNR(0)=100. (b): Initial SNR(0)=2.

Fig.8. Amplified letter-image "PSU" at 20°C, 100°C and 120°C.

Table caption:

1. Parameters choice for fitting the experimental data according to Eqs.(1) to (3).

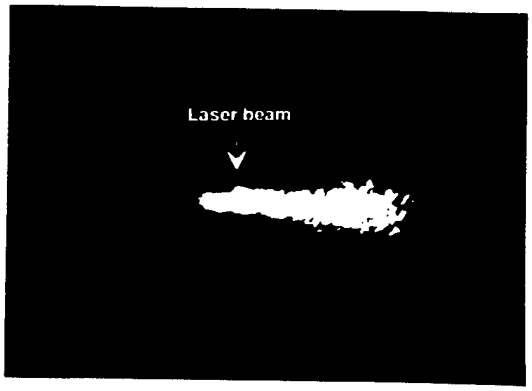
Laser beam

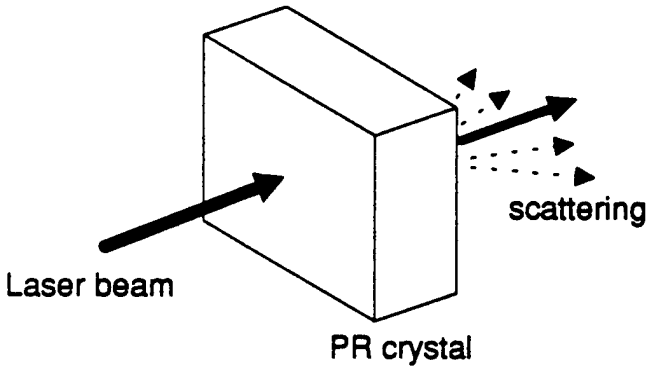
scattering
Laser beam
PR crystal

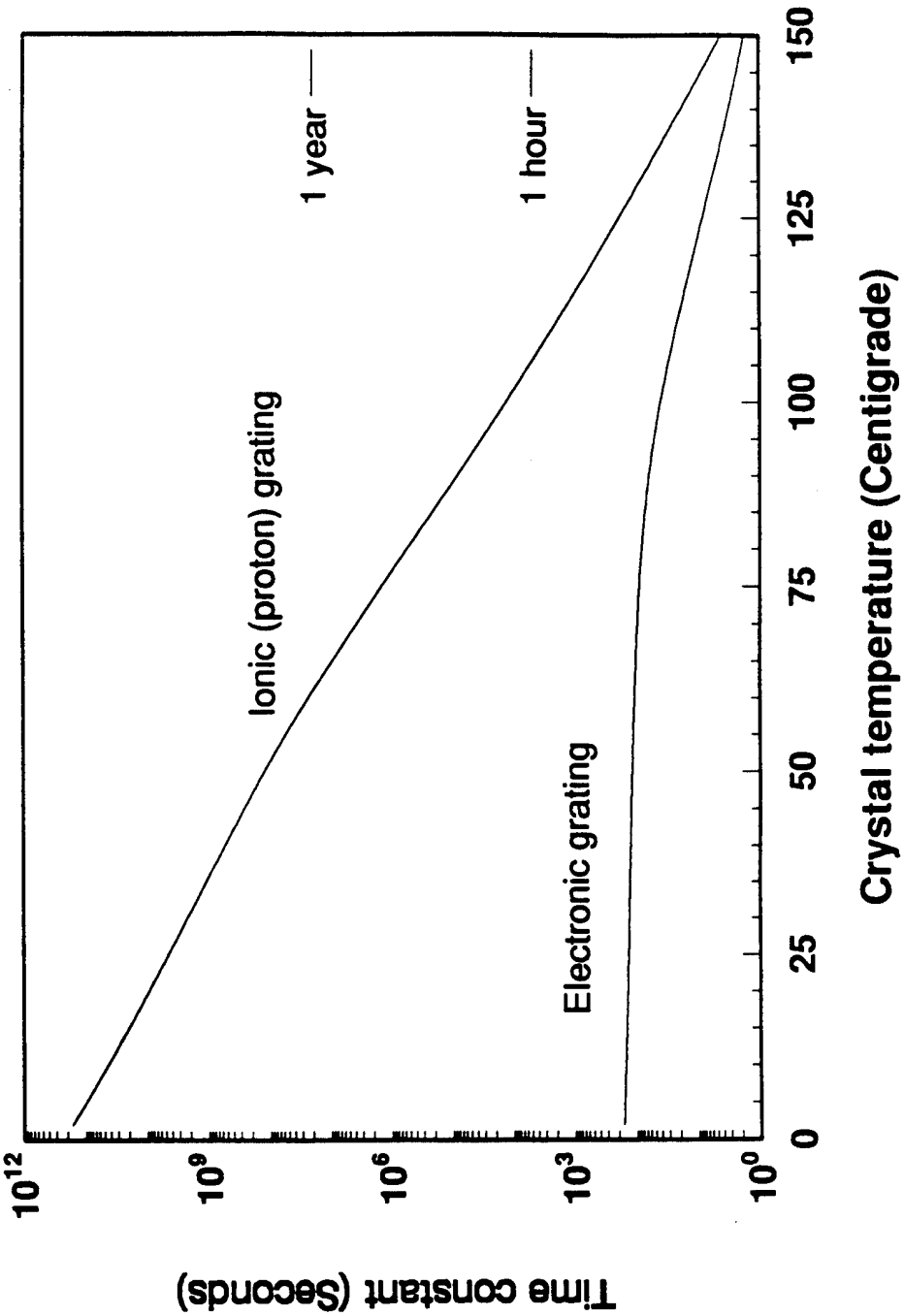
Time constant (Seconds)
10^{12}
10^{9}
10^{6}
10^{3}
10^{0}
0
25
50
75
100
125
150
Crystal temperature (Centigrade)
1 year
1 hour
Ionic (proton) grating
Electronic grating

Fig. 2

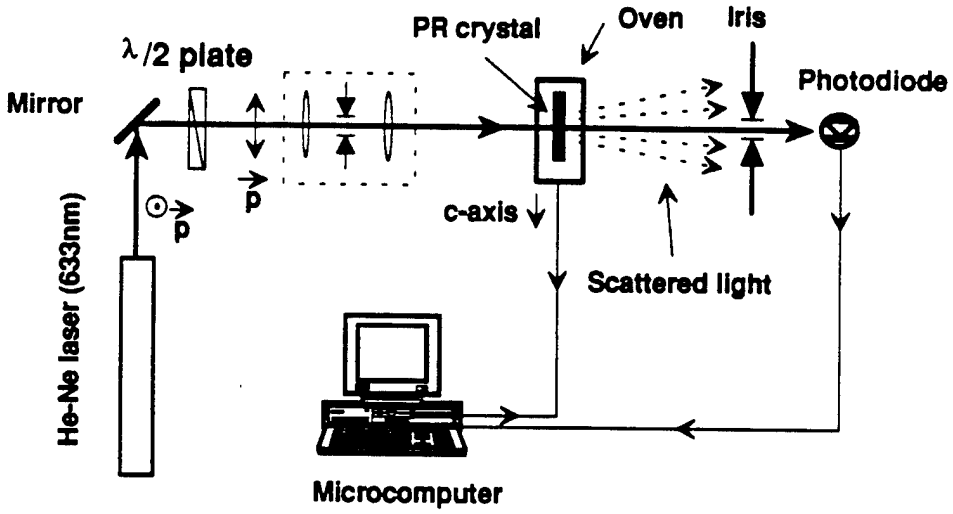
λ/2 plate
PR crystal
Oven
Iris
Photodiode
Mirror
p
p
c-axis
Scattered light
He-Ne laser (633nm)
Microcomputer

Fig 3

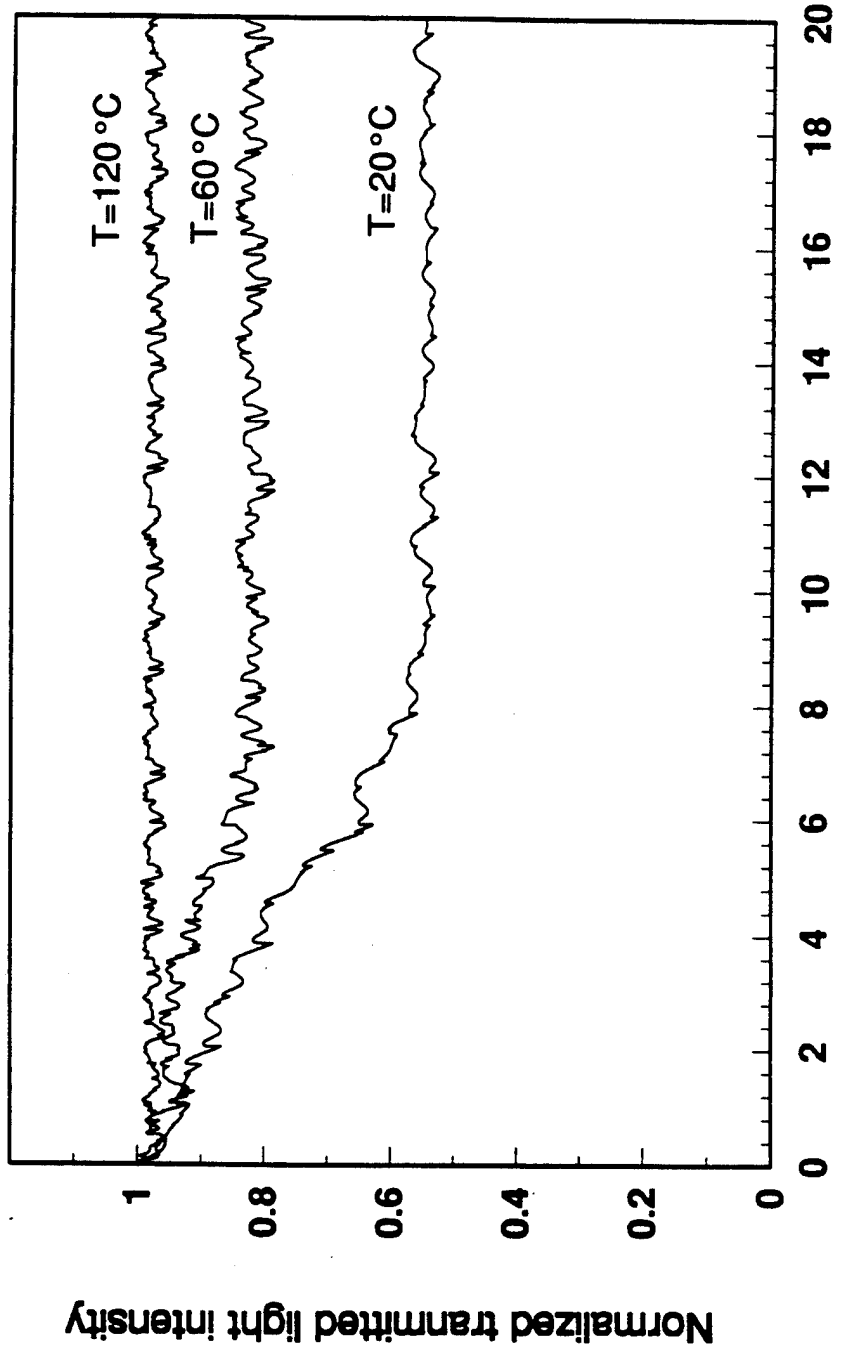
T=120°C
T=60°C
T=20°C
Normalized transmitted light intensity
Time (Minutes)
0
0.2
0.4
0.6
0.8
1
0
2
4
6
8
10
12
14
16
18
20

Fig. 4

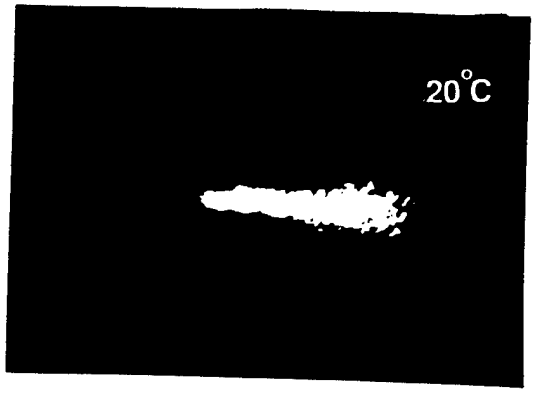

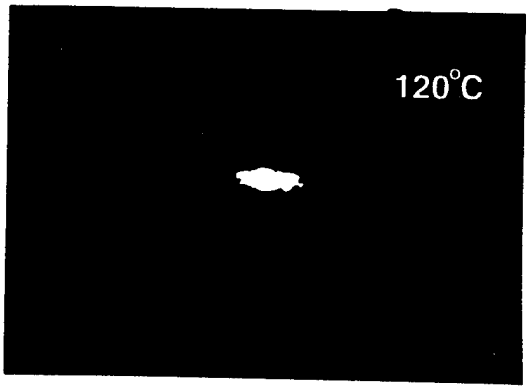

Fig 5

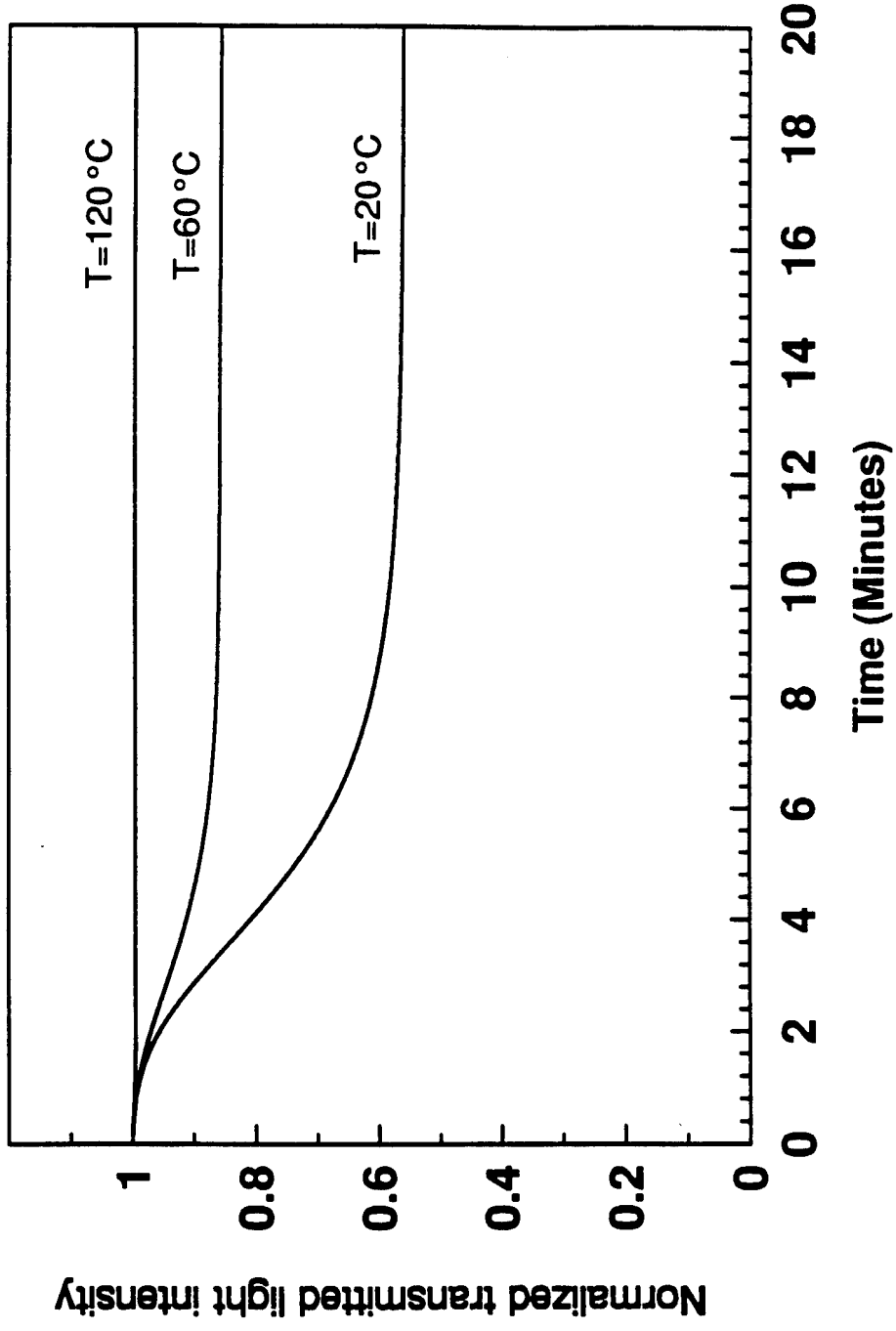
T=120°C
T=60°C
T=20°C
Normalized transmitted light intensity
1
0.8
0.6
0.4
0.2
0
0
2
4
6
8
10
12
14
16
18
20
Time (Minutes)

Fig. 6

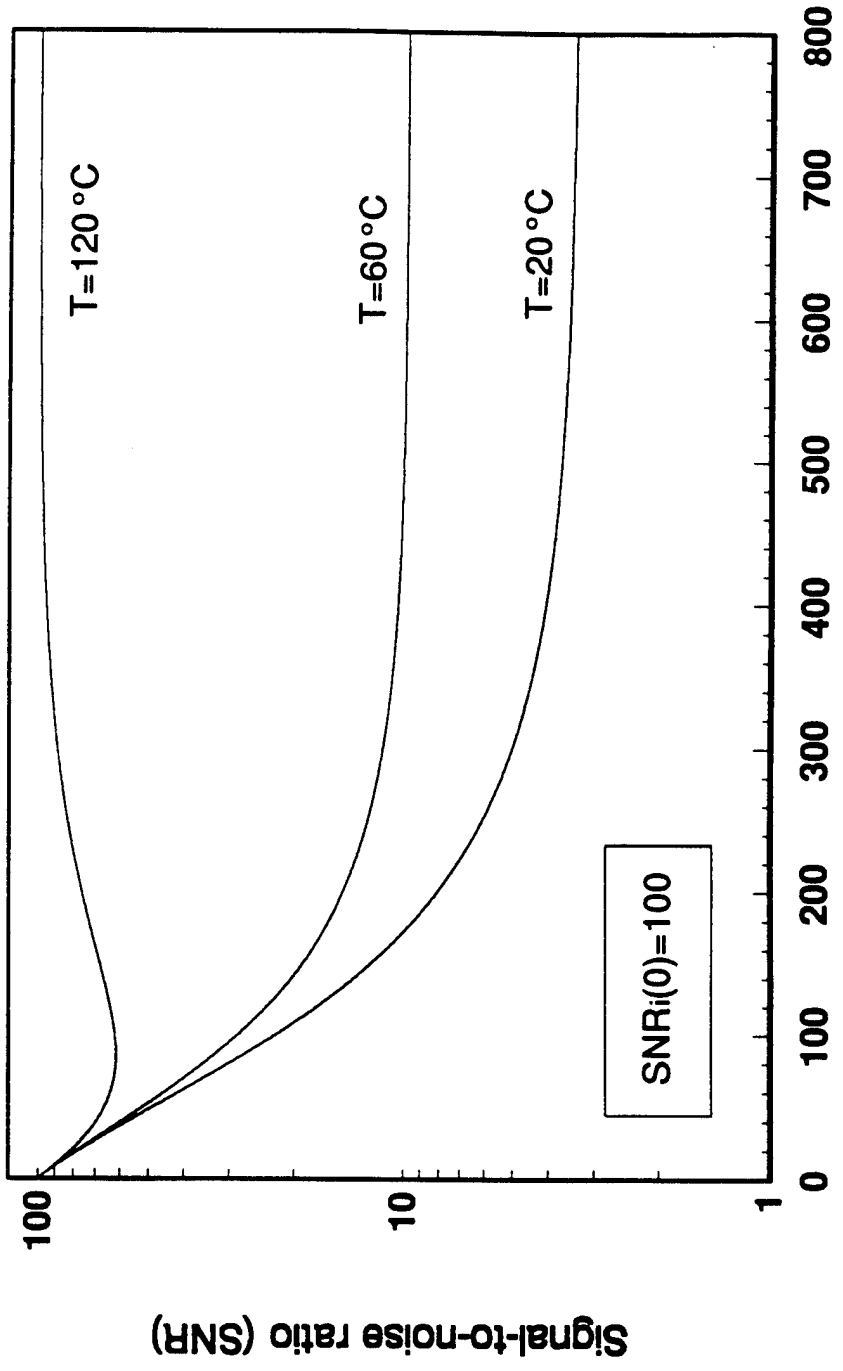
T=120 °C
T=60 °C
T=20 °C
SNRi(0)=100
100
10
1
0
100
200
300
400
500
600
700
800
Time (Seconds)
Signal-to-noise ratio (SNR)

Fig. 7 (a)

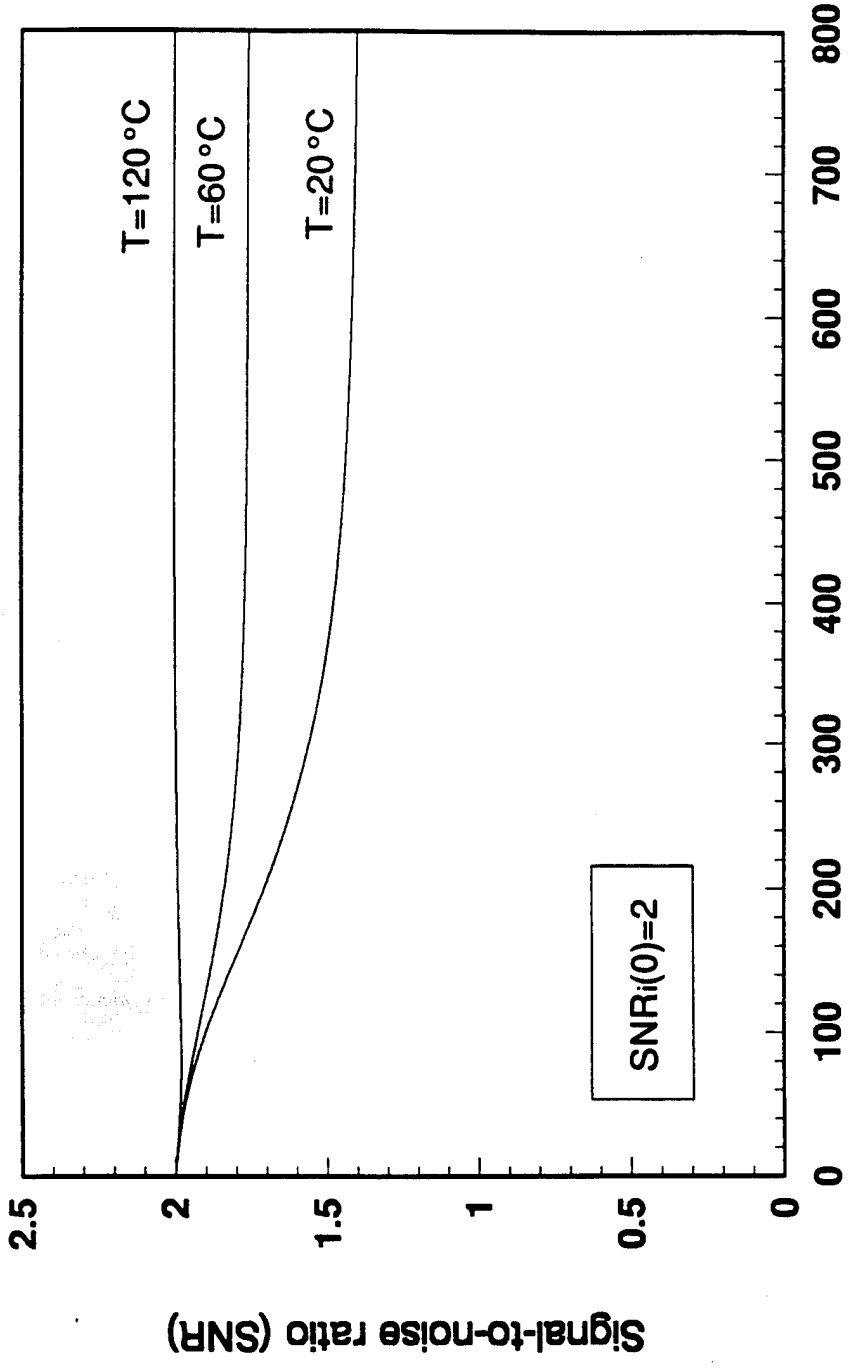
T=120 °C
T=60 °C
T=20 °C
SNRi(0)=2
Signal-to-noise ratio (SNR)
Time (Seconds)
2.5
2
1.5
1
0.5
0
0
100
200
300
400
500
600
700
800

Fig. 7 (b)

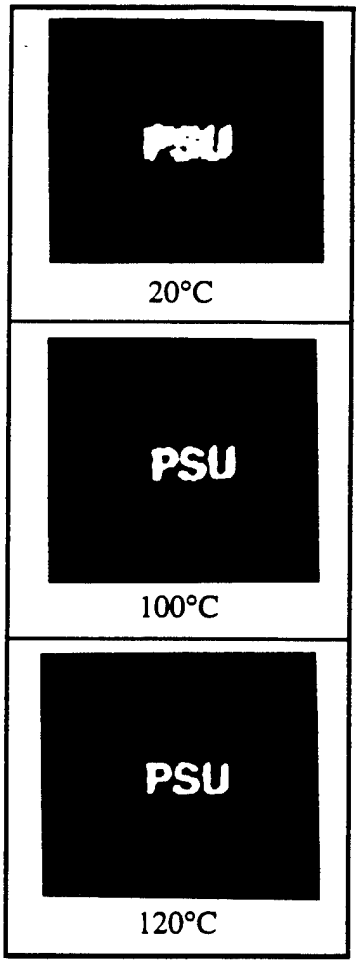

Fig. 8

$D_{oe}=6.5\times10^{-5}\ m^2s^{-1}$	$D_o=2\times10^{24}\ m^{-3}$	$\varepsilon_r=28.0$	$\varepsilon_e=0.12eV$	$\sigma=1\times10^{-24}\ m^2$	$I_o=4\times10^{3}\ Wm^{-2}$
$D_{oh}=8.1\times10^{-6}\ m^2s^{-1}$	$A_o=7\times10^{25}\ m^{-3}$	$K=2.3\times10^{6}\ m^{-1}$	$\varepsilon_h=1.1eV$	$L_{ph}=5\times10^{-10}\ m$	$n=2.2$
$s_o=4\times10^{10}\ s^{-1}$	$H_{oo}=1\times10^{25}\ m^{-3}$	$\gamma_{eff}=31\times10^{-12}\ mV^{-1}$	$\varepsilon_D=1eV$	$r=10^{-15}\ m^3s^{-1}$	$\lambda=6.33\times10^{-9}\ m$

Tab. 1

Appendix 10.15

Bragg Diffraction Limited Photorefractive (PR) Crystal Based Correlators

Bragg diffraction limited photorefractive (PR) crystal based correlators

Francis T. S. Yu and Shizhuo Yin

Department of Electrical Engineering

The Pennsylvania State University

University Park, PA 16802

Tel. (814) 863-2989

Fax. (814) 865-7065

E-mail: s3y@ecl.psu.edu

Abstract

Although thick volume photorefractive (PR) crystal offers the promising application to large storage capacity holographic memories, the thickness of the material also impairs the shift-invariant properties of the correlator. We have in this paper discussed the influence of the angular and the wavelength selectivity in a thick PR crystal filter. The shift-tolerances of Bragg diffraction limited PR based correlators are analyzed, which include the Vander Lugt (VLC), joint transform (JTC), and reflection-type (RC) correlators. We have shown that the RC correlator, in terms of shift-tolerance, performs the best. Simple experiment to illustrate the shift-invariant capability of PR based reflection-type correlator is also provided.

1. Introduction.

In recent years, the use of photorefractive (PR) crystals to synthesize large capacity spatial filters[1] has played a crucial role in the development of real-time correlators[2-11]. The salient features of using the thick PR materials for the matched filter implementation must be the large information capacity, the real-time addressability, the high diffraction efficiency, and the high angular and wavelength selectivities. However, the thick PR crystals also impose the Bragg diffraction limitation, which reduces the shift-invariant capability of a PR based correlator.

In this paper, we shall briefly discuss the Bragg diffraction limitation in a thick PR crystal. The influences of Bragg diffraction on the angular and the wavelength selectivities are provided, in which we have shown that the reflection-type wavelength-multiplexed matched filter would be the best choice. Comparison among the thick PR crystal based correlators, which includes the VLC, JTC, and RC, are analyzed. We have shown that the reflection-type PR based correlator performs the best in terms of the shift-tolerance among these three correlators.

2. Bragg diffraction limitation

Bragg diffraction limitation in a thick PR crystal can be shown with the k vector diagram[12] as depicted in Fig. 1. The recorded spatial grating vector **k** is shown as

$$\mathbf{k} = \mathbf{k}_0 - \mathbf{k}_1, \quad (1)$$

where $\mathbf{k}_o$ and $\mathbf{k}_1$ are the writing wave vectors. If the recorded hologram is read out by a wave vector $\mathbf{k}_2$ (where the scattered wave vector is denoted by $\mathbf{k}_3$), then the optical path difference (OPD) of the scattered light from two points within the crystal can be written as

$$\mathbf{OPD} = \mathbf{k} \bullet \mathbf{r} - (\mathbf{k}_2 - \mathbf{k}_3) \bullet \mathbf{r}, \quad (2)$$

where $\mathbf{r}$ represents the displacement vector between two points and • denotes the dot product. In view of Eq. (1), we see that

$$\mathbf{OPD} = \Delta\mathbf{k} \bullet \mathbf{r}, \quad (3)$$

where

$$\Delta\mathbf{k} = \mathbf{k}_0 - \mathbf{k}_1 - \mathbf{k}_2 + \mathbf{k}_3, \quad (4)$$

is known as the dephasing wave vector,[12] which corresponds to the Bragg diffraction (dephasing) limitation. In other words, if the reading beam is not matched with the writing beam, the OPD will be non-zero. The field of the scattered light from the crystal, as a function of (scattered) wave vector k_3, can be expressed as

$$\mathbf{A}(\mathbf{k}_3) = \int_v \mathbf{e}^{i\Delta\mathbf{k}\bullet\mathbf{r}} \mathbf{dv}, \quad (5)$$

where the integration is over the entire volume of the crystal. We note that the preceding equation is valid under the weak diffraction condition, such that the multiple diffraction within the crystal can be neglected.

3. Angular and wavelength selectivities

It is apparent to see that, from the Eq. (5), the performance of the PR matched filter would be severely limited by the Bragg diffraction. Since the angular and the wavelength selectivities of a multiplexed matched filter are limited by the Bragg diffraction condition, the shift-tolerance of the matched filter (related to the Bragg mismatch) will be affected by these selectivities.

Let us now consider the unslanted spatial filter synthesis for a transmission-type and a reflection-type spatial filter, as depicted in Fig. 2. By using the Kogelnik's coupled wave theory[13], the normalized diffraction efficiency can be shown as [14]

$$\eta_t = \frac{\mathrm{Sin}^2(v_t^2 + \xi_t^2)^{1/2}}{1 + \frac{\xi_t^2}{v_t^2}}, \qquad (6)$$

$$\eta_r = \frac{1}{1 + \frac{1 - \xi_r^2/v_r^2}{\mathrm{Sh}^2(v_r^2 - \xi_r^2)^{1/2}}}, \qquad (7)$$

where the subscripts t and r denote the transmission-type and the reflection-type holographic filters,

$$v_t = \frac{\pi \Delta n d}{\lambda \mathrm{Cos}\theta}, \qquad \xi_t = \frac{2\pi n d \mathrm{Sin}\theta}{\lambda}\Delta\theta,$$
$$v_r = \frac{\pi \Delta n d}{\lambda \mathrm{Sin}\theta}, \qquad \xi_r = \frac{2\pi n d \cos\theta}{\lambda}\Delta\theta,$$

n and Δn are the refractive index and the amplitude of its variation, d is the thickness of the crystal, and θ and $\Delta\theta$ are the internal construction angle and its variation. Under the

assumption of weak coupling condition, i.e., $|v|<<|\xi|$, the normalized diffraction efficiency η can be approximated as:

$$\eta_t \approx v_t^2 \mathrm{Sinc}^2\xi_t, \qquad (8)$$

$$\eta_r \approx v_r^2 \mathrm{Sinc}^2\xi_r. \qquad (9)$$

Based on Eqs. (8) and (9), the angular selectivity for the transmission and the reflection-type holographic filters can be shown as [14]

$$\left\{\frac{1}{\Delta\alpha}\right\}_t = \frac{\mathrm{Sin}\alpha\mathrm{Cos}\alpha}{\sqrt{n^2-\mathrm{Sin}^2\alpha}}\frac{d}{\lambda}, \qquad (10)$$

$$\left\{\frac{1}{\Delta\alpha}\right\}_r = \frac{\mathrm{Sin}\alpha\mathrm{Cos}\alpha}{\sqrt{n^2-\mathrm{Cos}^2\alpha}}\frac{d}{\lambda}, \qquad (11)$$

where 2α is the external construction angle, as shown in Fig. 2. By referring to the Eqs (10) and (11), the variation of the angular selectivity for the transmission-type and reflection-type holographic filters as a function of the external construction angle are plotted in Fig. 3 (a), in which we see that the peak selectivity occurs at $2\alpha = 90^\circ$ and decreases rapidly at both ends.

Similarly, the wavelength selectivity for the transmission-type and the reflection-type holographic filters can be shown to be[14]

$$\left\{\left|\frac{\lambda}{\Delta\lambda}\right|\right\}_t = 1+\frac{2}{\dfrac{\mathrm{Sin}\alpha/n}{\mathrm{Sin}[\mathrm{Sin}^{-1}(\dfrac{\mathrm{Sin}\alpha}{n})-\dfrac{\lambda}{d\mathrm{Sin}\alpha}]}-1}. \qquad (12)$$

$$\left\{\left|\frac{\lambda}{\Delta\lambda}\right|\right\}_r = \frac{\sqrt{n^2-\mathrm{Cos}^2\alpha}}{\lambda}d. \qquad (13)$$

The corresponding wavelength selectivity for the transmission-type and the reflection-type filters, as a function of external write-in angle, are plotted in Fig. 3 (b). In this figure, we see that the wavelength selectivity for the reflection-type hologram is higher than the transmission type, and the selectivity for the reflection-type is relatively uniform as a function of the construction angle. Although the wavelength selectivities for both the reflection-type and the transmission-type filters increases as the thickness of the crystal filter increases, the reflection-type filter increase far more rapidly as compared with the transmission-type. In addition, the wavelength selectivity for the transmission-type filter would not significantly until the construction angle 2α reaches to 90°. In view of these results, it is apparent that reflection-type filter would be more preferable for the wavelength-multiplexed matched filter. To have a sense of magnitude, given that the crystal thickness d = 7 mm, construction angle $2\alpha = 180^{\circ}$, and the construction wavelength λ = 0.7 μm, the wavelength selectivity for a reflection type crystal matched filter, $\{\lambda/\Delta\lambda\}_r$, will be in the order of 10^4. This represents recording about one-thousand multiplexed matched filter within a 7 mm thick PR crystal with currently commercial available tunable light source.

Lets us now investigate the shift tolerance of a PR matched filter as influenced by the angular and the wavelength selectivities. By referring to the matched filtering system of Fig. 4, a shift of the input target at the input plane will cause a change in the read-out angle at the Fourier plane (i.e., the matched filter plane). When the change of the read-out angle is large, the intensity of the read-out beam decreases rapidly due to the high angular selectivity (i.e., the Bragg diffraction limitation of the PR filter). In other words, the higher the angular selectivity of the PR filter, the lower the shift tolerance of PR filter will be. Thus, to have a larger shift-invariant property in a thick PR filter, a minimum angular selectivity is needed. From Eqs. (10) and (11), we see that the minimum angular

selectivity (which approaches to zero) occurs at angle $2\alpha = 0^{\circ}$ and $2\alpha = 180^{\circ}$, respectively. Since the wavelength selectivity for the reflection-type filter has the highest value at $2\alpha = 180^{\circ}$ while the angular selectivity is minimum (as it can be seen in Fig. 3 (a)), the reflection-type wavelength-multiplexed PR filter will be the best choice for large storage capacity and optimum shift-tolerant property.

4. Shift-invariant limited correlators

In this section, we shall investigate the shift-invariant property for three types of commonly used PR based correlators; named the VLC, the JTC, and the RC.

First, let us consider a PR based VLC shown in Fig. 5. Under the paraxial approximation, the corresponding Bragg diffraction wave vectors can be written as

$$\begin{cases} \mathbf{k}_0 = -\dfrac{\mathbf{x}_0}{\lambda \mathbf{f}}\hat{\mathbf{u}} + \dfrac{\mathbf{n}}{\lambda}\left(1 - \dfrac{\mathbf{x}_0^2}{2\mathbf{n}^2\mathbf{f}^2}\right)\hat{\mathbf{z}}, \\ \mathbf{k}_1 = -\dfrac{\mathbf{x}_1}{\lambda \mathbf{f}}\hat{\mathbf{u}} + \dfrac{\mathbf{n}}{\lambda}\left(1 - \dfrac{\mathbf{x}_1^2}{2\mathbf{n}^2\mathbf{f}^2}\right)\hat{\mathbf{z}}, \\ \mathbf{k}_2 = -\dfrac{\mathbf{x}_2}{\lambda \mathbf{f}}\hat{\mathbf{u}} + \dfrac{\mathbf{n}}{\lambda}\left(1 - \dfrac{\mathbf{x}_2^2}{2\mathbf{n}^2\mathbf{f}^2}\right)\hat{\mathbf{z}}, \\ \mathbf{k}_3 = -\dfrac{\mathbf{x}_3}{\lambda \mathbf{f}}\hat{\mathbf{u}} + \dfrac{\mathbf{n}}{\lambda}\left(1 - \dfrac{\mathbf{x}_3^2}{2\mathbf{n}^2\mathbf{f}^2}\right)\hat{\mathbf{z}}, \end{cases} \tag{14}$$

where $\mathbf{k}_0$ and $\mathbf{k}_1$ are the writing vectors, $\mathbf{k}_2$ and $\mathbf{k}_3$ are the reading and the diffracted wave vectors, respectively, n is the refractive index of the crystal, λ is the wavelength of the light source, f is the focal length of lens, and $\hat{\mathbf{u}}$ and $\hat{\mathbf{z}}$ represent the transversal and the longitudinal unit wave vectors, respectively. With reference to the momentum conservation and the infinite extension in the u direction, the dephasing wave vectors for the transversal and the longitudinal directions can be shown as

$$\Delta k_u = x_1 - x_0 + x_3 - x_2 = 0, \quad (15)$$

$$\Delta k_z = \frac{1}{2n\lambda f^2}\left(x_1^2 - x_0^2 + x_3^2 - x_2^2\right), \quad (16)$$

By substituting Eq. (15) into Eq. (16), we have

$$\Delta k_z = \frac{1}{n\lambda f^2}(x_1 - x_0)(x_0 - x_3). \quad (17)$$

Let us assume that the read out beam $\mathbf{k}_2$ is shifted with respect to the writing beam $\mathbf{k}_1$, that is

$$x_2 = x_1 - S, \quad (18)$$

where S represents the shift of the input target. By substituting Eq. (18) into Eq. (15), we have

$$x_0 - x_3 = x_1 - x_2 = S. \quad (19)$$

By substituting Eq. (19) into Eq. (17), we see that the dephasing wave vector in the z direction would be

$$\Delta k_z = \frac{1}{n\lambda f^2}(x_1 - x_0)S. \quad (20)$$

At the input plane x_1, the writing beams (i.e., the reference and the object beams) are represented by $q_0(x_0) = \delta(x_0 - X_0)$ and $q_1(x_1)$, respectively. If the crystal filter is read-out by a shifted object, represented by $q_2(x_2)=q_1(x_1-S)$ (i.e., autocorrelation case), the

output correlation peak intensity can be calculated by integrating Eq. (5) overall all $\mathbf{k}_0$ and $\mathbf{k}_1$ with weighting factors $q_0(x_0)$ and $q_1(x_1)$, respectively, i.e.,

$$I(x_3)=\left|\int_{-\infty}^{\infty}dx_o\int_{-\infty}^{\infty}dx_1\int_{-\infty}^{\infty}du\int_{-d/2}^{d/2}dz\,\delta(x_0-X_0)q_1^*(x_1-S)q_1(x_1)e^{i\Delta\mathbf{k}\bullet\mathbf{r}}\right|^2, \qquad (21)$$

It is apparent that by substituting Eq. (20) into Eq. (21), the output correlation peak intensity as a function of the shift distance can be shown to be[11]

$$R(S)=\left|\int|q_1(x_1)|^2\mathrm{Sinc}(\frac{\pi d}{n\lambda}\frac{S(x_1-X_o)}{f^2})dx_1\right|^2. \qquad (22)$$

where d is the thickness of the PR crystal, f is the focal length, λ is the wavelength, and X_o is the location of the input reference point-source. In view of the preceding result, we see that the intensity is modulated by a broad Sinc factor with a width as given by

$$W=\frac{2n\lambda f^2}{Sd}. \qquad (23)$$

In order to keep the target object within this width, it is clear that the Sinc factor has to be sufficiently broad as compared with the width of the target and the location of the input reference point source, that is

$$\frac{W}{2}\geq X_o+\frac{X}{2}. \qquad (24)$$

where X is the width of the input target.

Notice that in a PR based VLC, it is required that the location of the point source should satisfy the following condition[1], that is

$$X_{o\min} = \frac{5}{2}X. \quad (25)$$

In view of Eqs. (24) and (25), we have

$$W \geq 6X \quad (26)$$

Thus by substituting Eq. (26) into Eq. (23), we have the following object shift constraint

$$S \leq \frac{n\lambda f^2}{3Xd}, \quad (27)$$

which is inversely proportional to the thickness of the PR filter. In other words, the thinner the PR filter, the higher the shift-tolerance will be. However the thinner the PR filter the lower the storage capacity will be. If the product of the width of input target and the maximum permissible shift (i.e., $S_{max} = \frac{n\lambda f^2}{3Xd}$) is defined as the figure-of-merit(FOM) for the shift tolerance of the correlator, then the FOM for the VLC can be shown to be

$$FOM_{VLC} = XS_{max} = \frac{n\lambda}{3d} f^2, \quad (28)$$

which is inversely proportional to the thickness of the PR filter, and proportional to λ and the square of the focal length.

Let us now consider a PR crystal based JTC as shown in Fig. 6, where q_0 and q_1 are the reference and input targets. Similar to Eq. (14), the corresponding Bragg diffraction wave vectors can be written as

$$\begin{cases} \mathbf{k}_o = -\dfrac{\mathbf{x}_o}{\lambda \mathbf{f}}\hat{\mathbf{u}} + \dfrac{\mathbf{n}}{\lambda}\left(1 - \dfrac{\mathbf{x}_o^2}{2\mathbf{n}^2\mathbf{f}^2}\right)\hat{\mathbf{z}}, \\ \mathbf{k}_1 = -\dfrac{\mathbf{x}_1}{\lambda \mathbf{f}}\hat{\mathbf{u}} + \dfrac{\mathbf{n}}{\lambda}\left(1 - \dfrac{\mathbf{x}_1^2}{2\mathbf{n}^2\mathbf{f}^2}\right)\hat{\mathbf{z}}, \\ \mathbf{k}_2 = \dfrac{\mathbf{x}_2}{\lambda \mathbf{f}}\hat{\mathbf{u}} - \dfrac{\mathbf{n}}{\lambda}\left(1 - \dfrac{\mathbf{x}_2^2}{2\mathbf{n}^2\mathbf{f}^2}\right)\hat{\mathbf{z}}, \\ \mathbf{k}_3 = -\dfrac{\mathbf{x}_3}{\lambda \mathbf{f}}\hat{\mathbf{u}} - \dfrac{\mathbf{n}}{\lambda}\left(1 - \dfrac{\mathbf{x}_3^2}{2\mathbf{n}^2\mathbf{f}^2}\right)\hat{\mathbf{z}}, \end{cases} \tag{29}$$

Using similar evaluation as for the VLC, the output correlation intensity distribution can be shown to be

$$I(x_3) = \left| \int_{-\infty}^{\infty} dx_o \int_{-\infty}^{\infty} dx_1 \int_{-\infty}^{\infty} du \int_{-d/2}^{d/2} dz\, q_o^*(x_o - h) q_1(x_1 + h) e^{i\Delta \mathbf{k} \bullet \mathbf{r}} \right|^2, \tag{30}$$

where 2h is the separation between the input targets, d is the thickness of the crystal. Again, we assume that the PR crystal is infinitely extended in the $\hat{u}$ direction. By virtue of the momentum conservation, i.e., $\Delta k_u = 0$, the preceding equation can be reduced to

$$I(x_3) = \left| \int_{h-X/2}^{h+X/2} q_o(x_o - h) q_1(x_o + h) \mathrm{Sinc}(\pi d \Delta k_z) dx_o \right|^2, \tag{31}$$

where the dephasing wave vector in the z direction is given by

$$\Delta k_z = \frac{(x_o - h)(x_3 + h)}{n \lambda f^2}, \tag{32}$$

and X represents the width of the input target. Suppose the read out beam #2 is just a shifted version of the conjugate beam of the beam #0, and $q_0(x_0)$ and $q_1(x_1)$ have the same light field distribution (i.e., autocorrelation case), then the output correlation peak intensity as a function of the target displacement S can be shown as

$$R(S) = \left| \int |q_1(x_o - h)|^2 \, \mathrm{Sinc}\left(\frac{\pi d}{n\lambda} \frac{(x_o - h)(2h - S)}{f^2} \right) dx_o \right|^2. \qquad (33)$$

Again, we see that the peak intensity is modulated by a broad Sinc factor due to the Bragg diffraction limitation. The width of the Sinc factor is given by

$$W = \frac{2n\lambda f^2}{(2h - S)d}. \qquad (34)$$

To keep the target within the width of the Sinc factor, W is required to be broader than the width of the input targets, i.e.,

$$W = \frac{2n\lambda f^2}{(2h - S)d} \geq X. \qquad (35)$$

Thus for a given object width X, the maximum distance 2h between two objects can be determined by setting W = X and S=0, for which we have

$$2h_{max} = \frac{2n\lambda f^2}{Xd}. \qquad (36)$$

When the read-out beam is shifted by a distance S closer to the input object, the distance between the zeroth order and the first order diffraction would be 2h-S. To avoid the overlapping between the two diffraction orders, the separation between them should be greater than twice the target X, that is

$$2h - S \geq 2X. \qquad (37)$$

By substituting Eq.(36) into Eq. (37), we see that the maximum permissible target translation would be

$$S_{max} = \frac{2n\lambda f^2}{Xd} - 2X. \quad (38)$$

Thus, shift tolerance FOM for the JTC can be written as

$$FOM_{JTC} = XS_{max} = \frac{2n\lambda f^2}{d} - 2X^2, \quad (39)$$

which is inversely proportional to the thickness of the PR crystal and it decreases rapidly as the width of the target X increases.

Similarly, for the reflection-type (RC) correlation shown in Fig. 7, the Bragg diffraction wave vectors can be written as

$$\begin{cases} \mathbf{k}_o = -\dfrac{\mathbf{n}}{\lambda}\hat{\mathbf{z}}, \\ \mathbf{k}_1 = -\dfrac{\mathbf{x}_1}{\lambda \mathbf{f}}\hat{\mathbf{u}} + \dfrac{\mathbf{n}}{\lambda}(1 - \dfrac{\mathbf{x}_1^2}{2\mathbf{n}^2\mathbf{f}^2})\hat{\mathbf{z}}, \\ \mathbf{k}_2 = -\dfrac{\mathbf{x}_2}{\lambda \mathbf{f}}\hat{\mathbf{u}} + \dfrac{\mathbf{n}}{\lambda}(1 - \dfrac{\mathbf{x}_2^2}{2\mathbf{n}^2\mathbf{f}^2})\hat{\mathbf{z}}, \\ \mathbf{k}_3 = \dfrac{\mathbf{x}_3}{\lambda \mathbf{f}}\hat{\mathbf{u}} - \dfrac{\mathbf{n}}{\lambda}(1 - \dfrac{\mathbf{x}_3^2}{2\mathbf{n}^2\mathbf{f}^2})\hat{\mathbf{z}}, \end{cases} \quad (40)$$

where $\mathbf{k}_o$ and $\mathbf{k}_1$ are the writing vectors, $\mathbf{k}_2$ and $\mathbf{k}_3$ are the reading and the diffracted wave vectors, respectively. With reference to the momentum conservation, the transversal and the longitudinal dephasing wave vectors can be written as

$$\Delta k_u = \frac{x_1}{\lambda} - \frac{x_2 + x_3}{\lambda} = 0, \quad (41)$$

$$\Delta k_z = \frac{1}{n\lambda}\frac{x_3(x_1 - x_3)}{f^2}. \quad (42)$$

In view of Eqs. (41) and (42), the output correlation intensity distribution can be written as

$$I(x_3) = \left| \int_{-\infty}^{\infty} dx_o \int_{-\infty}^{\infty} dx_1 \int_{-\infty}^{\infty} du \int_{-d/2}^{d/2} dz\, \delta(x_0) q_2^*(x_2) q_1(x_1) e^{i\Delta \mathbf{k} \bullet \mathbf{r}} \right|^2, \qquad (43)$$

Again if $q_2(x_2)$ is just a shifted version of $q_1(x_1)$, that is

$$q_2(x_2) = q_1(x_1 - S) \qquad (44)$$

the corresponding correlation peak intensity as a function of shift distance S can be shown to be

$$R(S) = \left| \int |q_1(x_1)|^2 \, \mathrm{Sinc}\left[\frac{\pi d}{n\lambda} \frac{S(x_1 - S)}{f^2} \right] dx_1 \right|^2, \qquad (45)$$

in which width of the Sinc factor is given by

$$W = \frac{2n\lambda}{dS} f^2. \qquad (46)$$

Again, to maintain the target within the Sinc factor, we have

$$\frac{W}{2} \geq S + \frac{X}{2} \qquad (47)$$

By substituting Eq. (46) into Eq. (47), we have

$$SX \leq \frac{2n\lambda}{d} f^2 - 2S^2. \qquad (48)$$

Since the shift variable S can be positive or negative quantity, S should be maintained within a half of the maximum permissible translation S_{max}. Thus by substituting $S = S_{max} / 2$ into Eq. (48), we obtain

$$(FOM)_{RC} = XS_{max} = \frac{4n\lambda}{d} f^2 - S_{max}^2, \quad (49)$$

which is inversely proportional to the thickness of the PR filter and it decreases as the maximum permissible shift distance increases.

To summarize the results that we have obtained, the FOM for the three types of correlators are tabulated in Table 1. Figure 8 shows the plots of the FOM for the three types of PR based correlators, in which we see that the RC offers a better shift tolerance as compared with the VLC and the JTC. In fact, the FOM for RC is about two-fold higher than that of the JTC and about one-order better than that of the VLC. As an example, if we assume that the thickness of the PR filter is d = 1cm, n = 2.2, f =300 cm, X = 5 cm, λ = 0.5 μm, then the maximum permissible shift distance for the RC can be shown as S_{max} = 4.3 cm, which is considered large for most of the practical optical correlators[15].

5. Experimental demonstration

To demonstrate the shift-tolerance of the RC, a 1 cm^3 Ce:Fe: doped $LiNbO_3$ crystal[14] has been used for the reflection-type matched filter synthesis as shown in Fig. 9. By tuning the wavelength at $\Delta\lambda$ = 0.1 nm per step with 10 second per exposure, a set of wavelength-multiplexed reflection-type matched filter is synthesized. After the PR filter construction, an input target can be used to reconstruct the reference beam by simply scanning the wavelength of the light source. If the input target is matched with one-of recorded matched filters, a sharp correlation peak can be detected by a CCD camera as shown in the figure.

Thus, we see that multi-target detection can be done by tuning the wavelength of the light source so that the spectral contents of the multiplexed filter can be exploited.

For shift-invariant demonstration of the RC, a set of Roman letters shown in Fig. 10 (a) are used as the training targets for the wavelength-multiplexed matched filter synthesis. Notice that the "letter" is centered at the optical axis and recorded one-by-one during the construction of the PR filter. The corresponding reconstructed holographic images obtained with the specific spectral line are shown in Fig. 10 (b). To test the shift-invariant property of the PR filter, the five input "letters" are inserted at the input plane at the same time as shown in Fig. 10 (a). Notice that, these letters have been shifted with respect to the recorded PR filter. The corresponding correlation peak intensities for each spectral lines are detected by the CCD camera as tabulated in Table 2. By properly thresholding these detected peak intensities, a set of correlation peaks corresponding to the recorded spectral contents is depicted in Fig. 11. From these results, we see that the PR based RC can indeed preserve the shift-invariant property by using a wavelength-multiplexed reflection-type PR filter.

6. Conclusion

The Bragg diffraction limitation in a thick PR matched filter has been studied, in which we have shown that the angular and the wavelength selectivities are affected by the thickness of the PR filter. We have also investigated the Bragg diffraction limitation as imposed on the PR crystal based correlators, which include the VLC, the JTC, and the RC. We have shown that, in terms of shift-tolerance, the RC performs the best. We have found out that the figure-of-merit for the RC is about two-fold higher than that for the JTC and ten-fold higher than that for the VLC.

References:

[1] A. Vander Lugt, "Signal detection by complex spatial filtering," IEEE transactions on information theory **IT-10**, 139-145 (1964).

[2] D. M. Pepper, J. Auyeung, D. Fekete, and A. Yariv, "Spatial convolution and correlation of optical field via degenerate four-wave mixing," Opt. Lett. **3**, 7-9 (1978).

[3] Q. He, P. Yeh, L. Hu, S. Lin, T. Yeh, T. Tu, S. Yang, and K. Hsu, "Shift invariant photorefractive joint transform correlator using Fe: LiNbO3 crystal plates," Appl. Opt. **32**, 3113-3115 (1993).

[4] R. Young and C. Chatwin, "Design and simulation of a synthetic discriminant function filter for implementation in an updateable photorefractive correlator," SPIE **1701**, 239-263, Orlando, FL (1992).

[5] D. Liu, T. Chao, and L. Cheng, "Novelty filtered optical correlator using photorefractive crystal," SPIE **1701**, 105-110, Orlando, FL (1992).

[6] M. Wen, S. Yin, Purwosumarto P., F. T. S. Yu, "Wavelet matched filtering using a photorefractive crystal," Opt. Commun. **99**, 325-330 (1993).

[7] D. Liu, K. Luke, and L. Cheng, "GaAs-based photorefractive time-integrating correlator," SPIE **1702**, 205-209, Bellingham, WA (1992).

[8] C. Chang, H. Yau, Y. Tong, and N. Puh, "Rotational invariant pattern recognition with the method of circular harmonics using a BaTiO3 crystal," Opt. Commun. **87**, 219-222 (1992).

[9] S. Faria, A. Tagliaferri, S. Bos, A. Paulo, "Photorefractive optical holographic correlation using a $Bi_{12}TiO_{20}$ crystal at $\lambda = 0.633$ μm," Opt. Commun. **86**, 29-33 (1991).

[10] F. T. S. Yu, S. Wu, A. Mayers, and S. Rajan, "Wavelength-multiplexed refection-type matched spatial filtering using $LiNbO_3$," Opt. Commun. **81**, 343-346 (1991).

[11] F. T. S. Yu, S. Yin, and Z. H. Yang, "Thick volume photorefractive crystal wavelength-multiplexed reflection-type matched filter," Optical memory and neural networks **3**, 207-214 (1994).

[12] F. T. S. Yu and S. Jutamulia, *Optical signal processing, computing, and neural networks*, Wiley-Interscience, New York, Ch. 7, 249 (1992).

[13] H. Kogelnik, "Coupled wave theory for thick hologram gratings," Bell. Syst. Tech. J. **48**, 2909-2947 (1969).

[14] S. Yin, H. Zhou, M. Wen, J. Zhang, and F. T. S. Yu, "Wavelength-multiplexed holographic construction using a Ce:Fe: doped $LiNbO_3$ crystal with a tunable visible-light diode laser," Opt. Commun. **101**, 317-321 (1993).

[15] S. Jutamulia, *Optical Correlator*, SPIE milestone series, Vol. 76, SPIE optical engineering press, Bellingham, Wash., (1993).

Captions:

Figures:

Fig. 1. Bragg diffraction vectors

Fig. 2. Unslanted volume filter construction

(a) Transmission-type filter;

(b) Reflection-type filter.

Fig. 3. (a) Angular selectivity (dashed line for the transmission-type and solid line for the reflection type filter)

(b) Wavelength selectivity (dashed line for the transmission-type and solid line for the reflection type filter)

Fig. 4. A thick PR matched filtering system

Fig. 5. A PR crystal based VLC

Fig. 6. A PR crystal based JTC

Fig. 7. A PR crystal based reflection-type wavelength-multiplexed correlator (RC)

Fig. 8. Figure of merit as a function of target translation S or target width X for different types of correlators.

Fig. 9. Experimental set-up of a PR crystal based RC.

Fig. 10. (a) The input training objects;

(b) The corresponding reconstructed images.

Fig. 11. Output correlation peak intensities shown the shift-invariant property with the spectral content.

Table Captions:

Table 1 Shift-tolerance figure-of-merit

Table 2 Normalized correlation peak intensities

Types of PR based correlators	FOM
Vander-Lugt correlator	$XS_{max} = \frac{n\lambda}{3D} f^2$
Joint transform correlator	$XS_{max} = \frac{2n\lambda}{D} f^2 - 2X^2$
Reflection correlator	$XS_{max} = \frac{4n\lambda}{D} f^2 - S_{max}^2$

Table 1

Reference images / Target images	P	S	U	R	M
P	1.00	0.62	0.33	0.91	0.43
S	0.49	1.00	0.30	0.33	0.45
U	0.50	0.73	1.00	0.46	0.43
R	0.70	0.60	0.57	1.00	0.60
M	0.10	0.09	0.11	0.21	1.00

Table 2

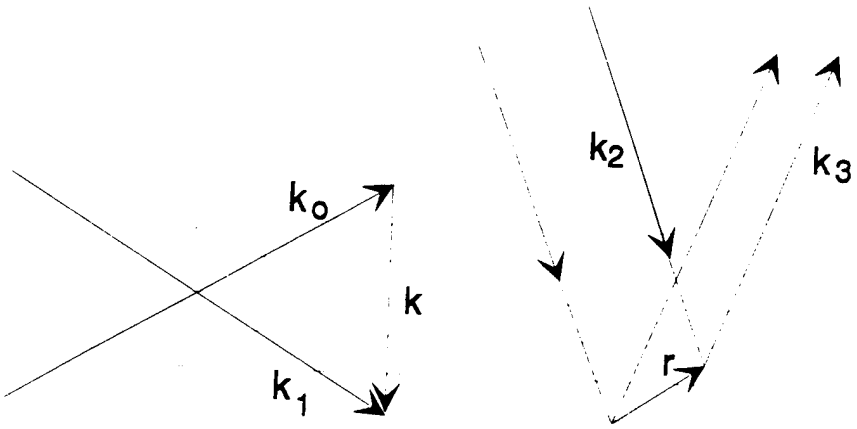

Fig. 1

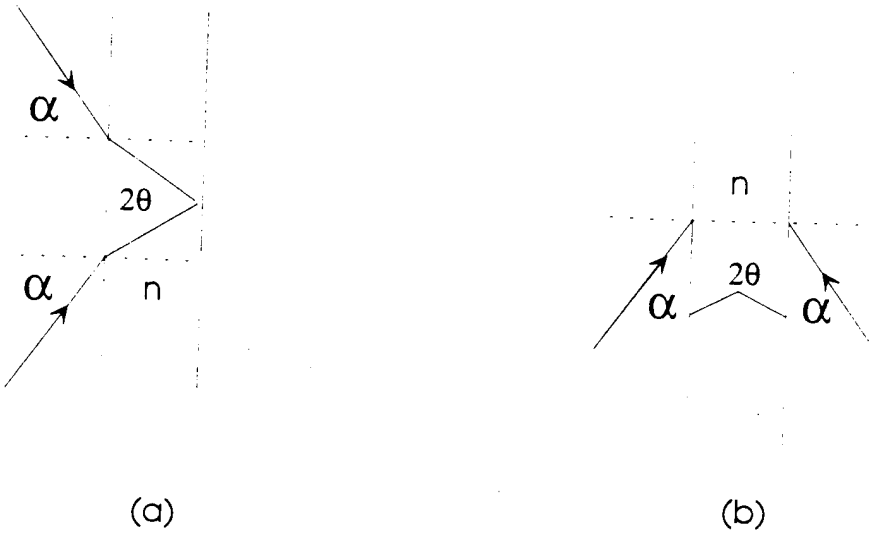

Fig. 2

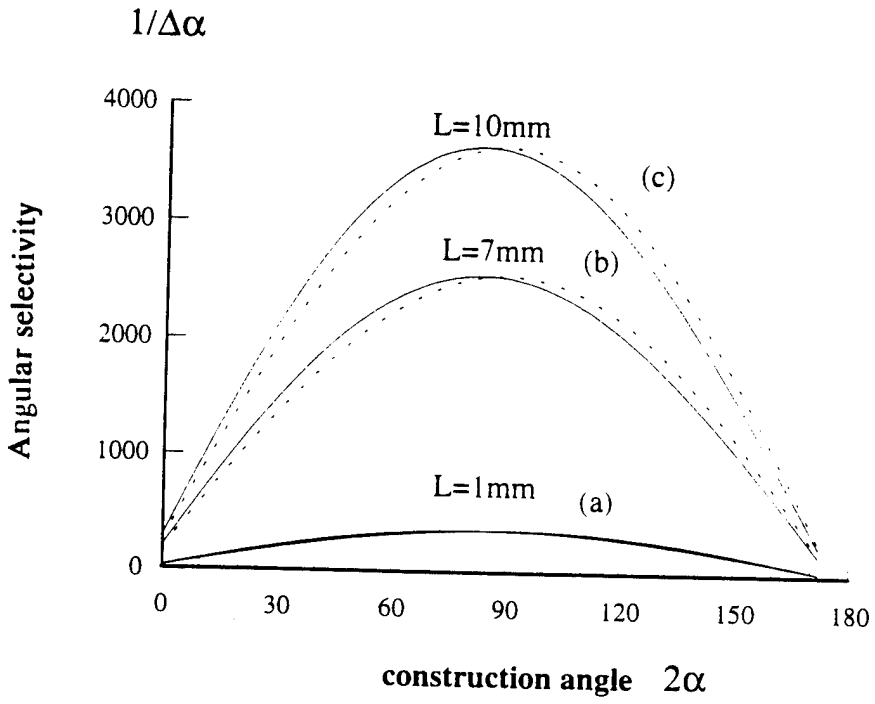
1/Δα
4000
3000
2000
1000
0
Angular selectivity
L=10mm
(c)
L=7mm
(b)
L=1mm
(a)
0
30
60
90
120
150
180
construction angle 2α

(a)

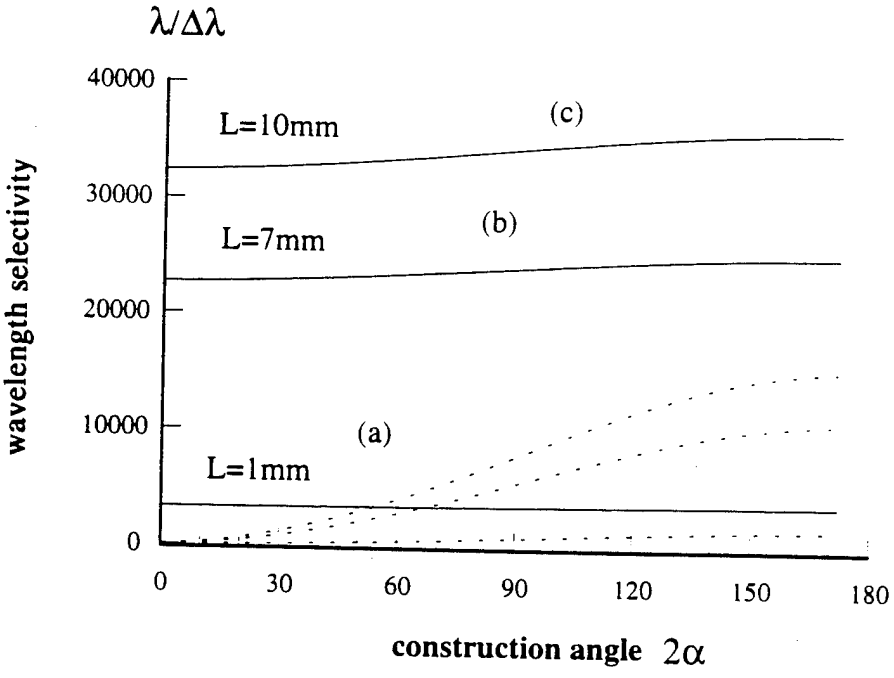
λ/Δλ
40000
30000
20000
10000
0
wavelength selectivity
L=10mm
(c)
L=7mm
(b)
(a)
L=1mm
0
30
60
90
120
150
180
construction angle 2α

(b)

Fig. 3

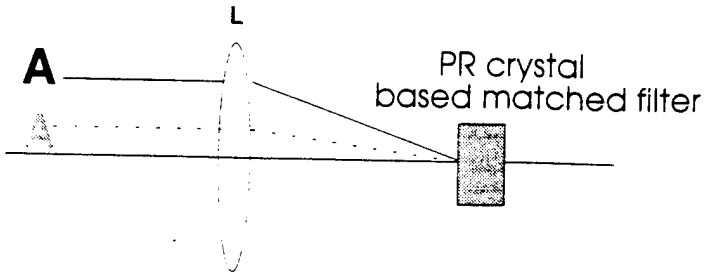

Fig. 4

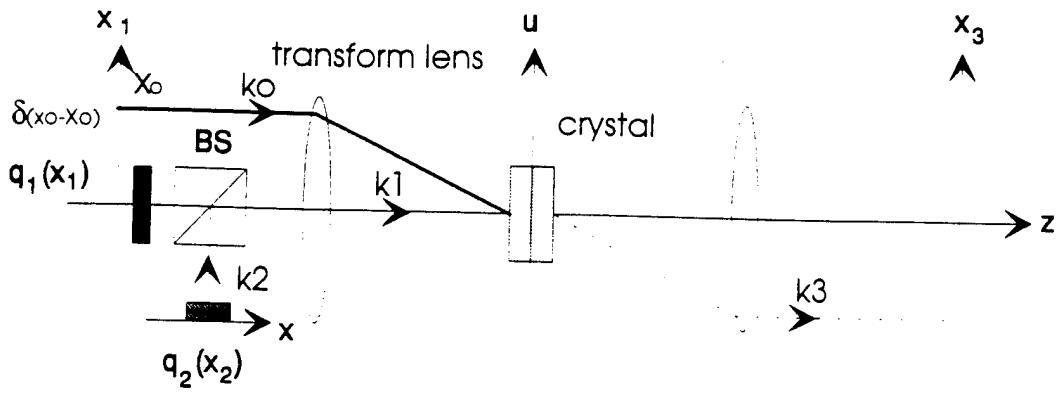
x 1
u
x3
transform lens
xo
ko
δ(xo-xo)
BS
crystal
q1(x1)
k1
z
k2
k3
x
q2(x2)

Fig. 5

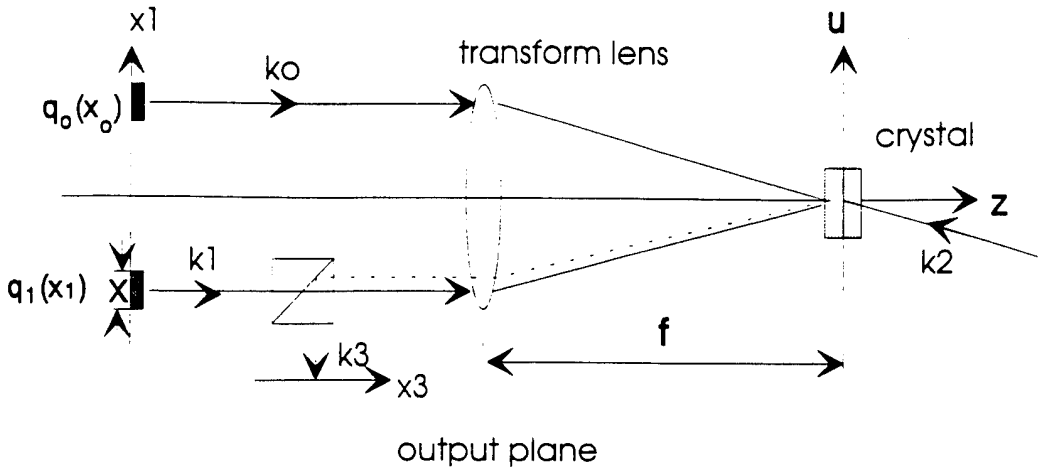
x1
ko
transform lens
u
$q_o(x_o)$
crystal
z
k1
$q_1(x_1)$
k2
f
k3
x3
output plane

Fig. 6

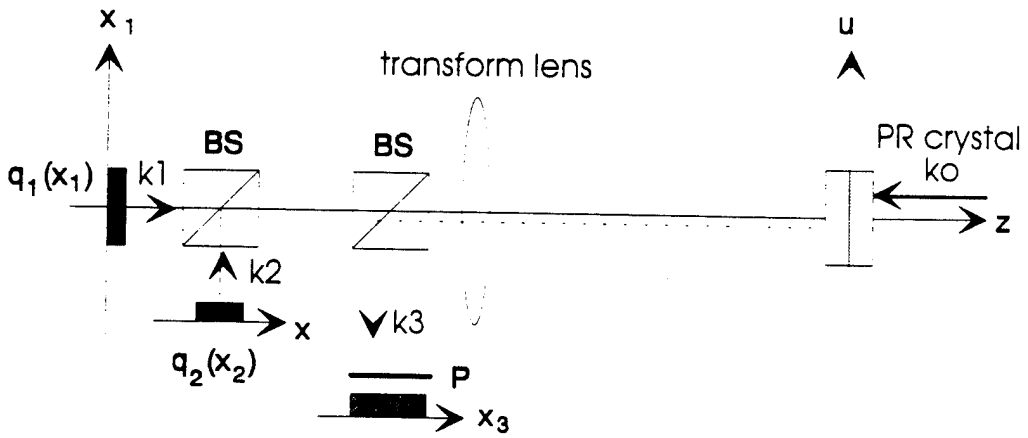
x 1
u
transform lens
BS
BS
PR crystal
ko
q1(x1)
k1
z
k2
x
k3
q2(x2)
P
x3

Fig. 7

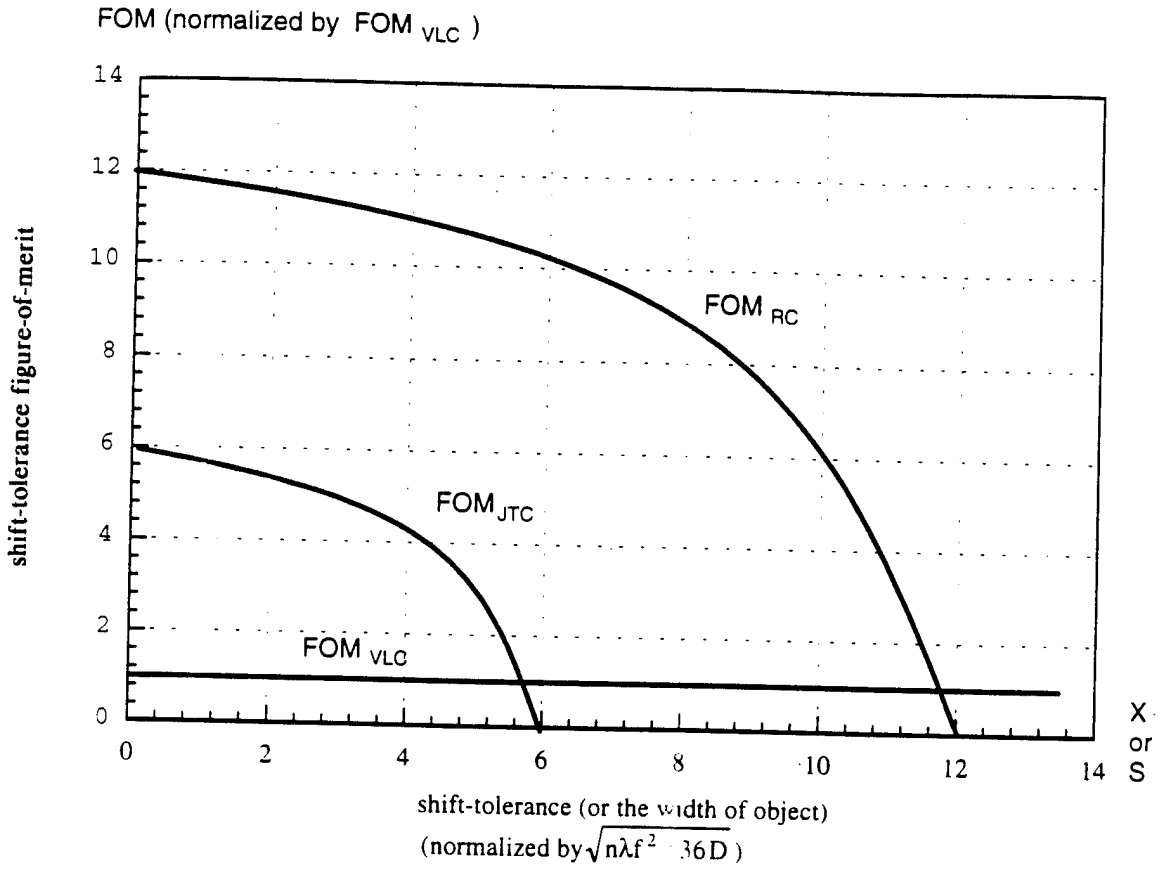
FOM (normalized by FOM VLC)
shift-tolerance figure-of-merit
14
12
10
8
6
4
2
0
FOM RC
FOM JTC
FOM VLC
0
2
4
6
8
10
12
14
X or S
shift-tolerance (or the width of object)
(normalized by √(nλf² 36D))

Fig. 8

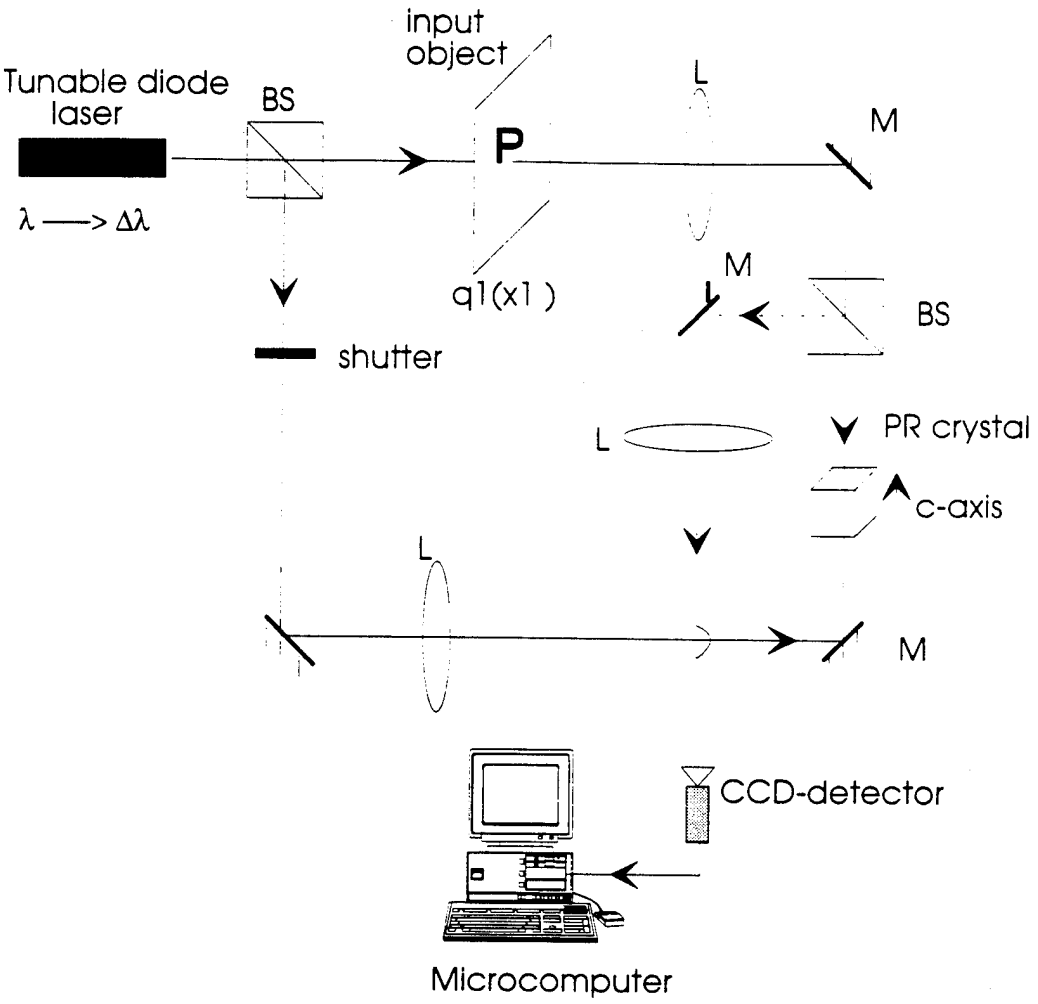
input
object
Tunable diode
laser
BS
P
L
M
λ ——> Δλ
q1(x1)
M
BS
shutter
L
PR crystal
c-axis
L
M
CCD-detector
Microcomputer

Fig. 9

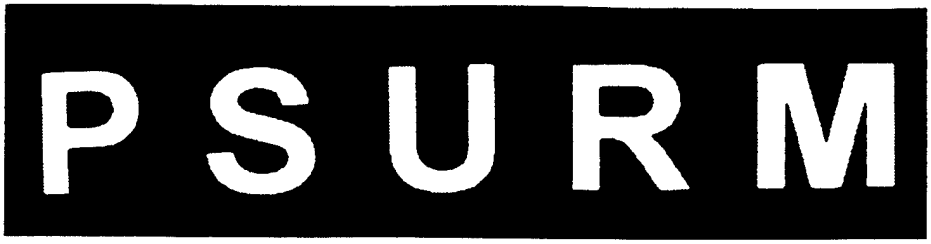

(a)

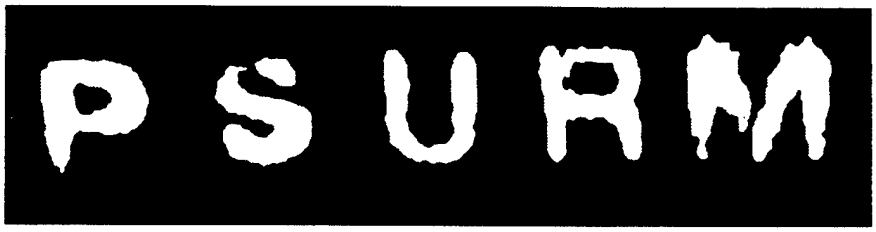

λ = 670.0 nm, 670.1 nm, 670.2 nm, 670.3 nm, 670.4 nm

(b)

Fig. 10

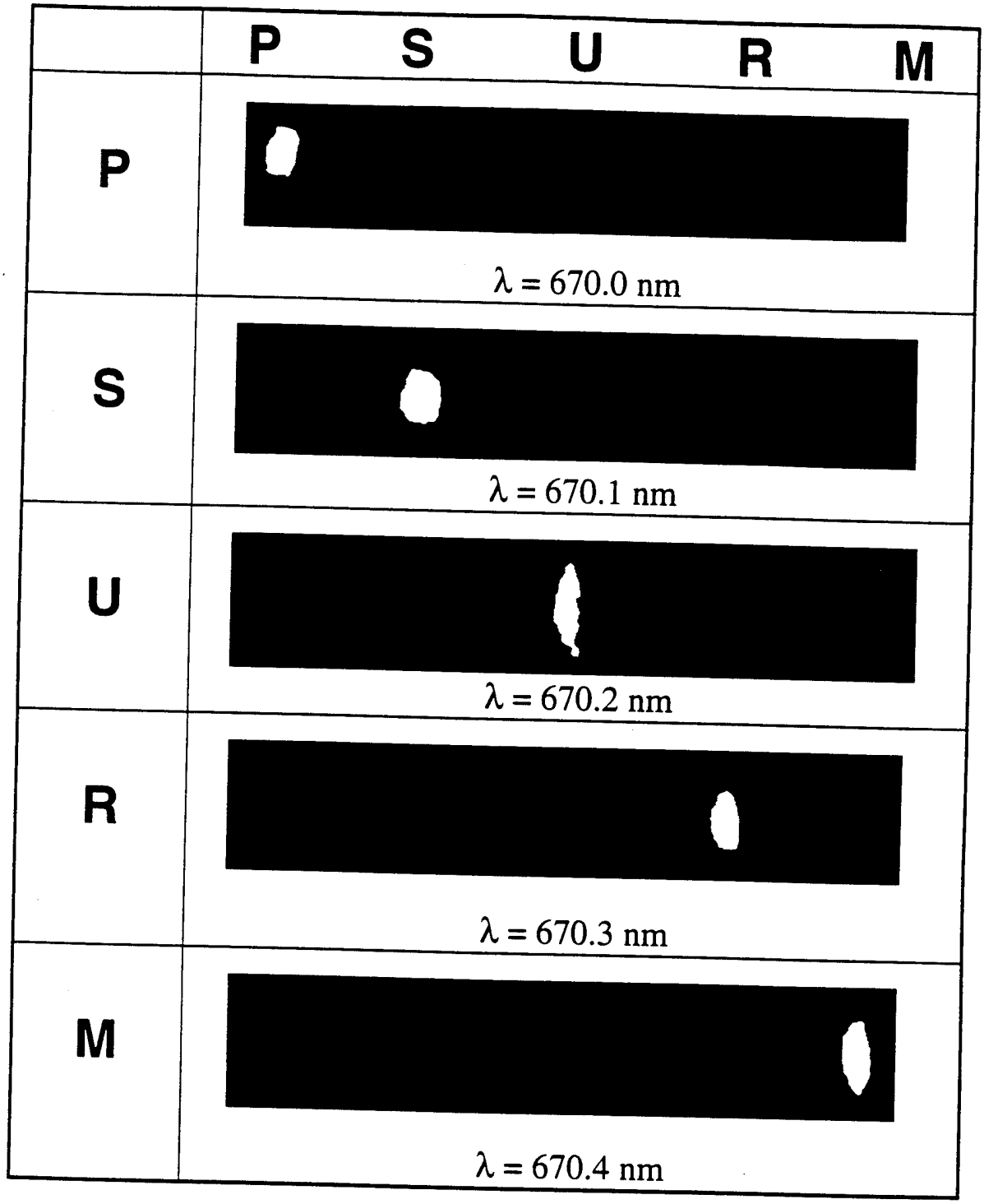

Fig. 11

Appendix 10.16

Wavelet Matched Filtering Using a Photorefractive Crystal

Optics Communications 99 (1993) 325–330
North-Holland

OPTICS
COMMUNICATIONS

Wavelet matched filtering using a photorefractive crystal

Meiyuan Wen, Shizhuo Yin, Purwosumarto Purwardi and Francis T.S. Yu
Electro-Optics Center, Electrical and Computer Engineering Department, The Pennsylvania State University, University Park, PA 16802, USA

Received 3 November 1992; revised manuscript received 27 January 1993

A pattern identification technique using the wavelet matched filter (WMF) based on the photorefractive (PR) crystal has been proposed. The essential merit of using the WMF is that it offers better signal discrimination than the conventional matched filter (CMF). Since a large number of WMFs can be synthesized in a PR crystal, fingerprint identification was chosen as the application. Simulated and experimental results are provided.

1. Introduction

Over the years, fingerprint identification systems based on the optical correlation technique have been reported by several investigators [1,2]. More recently, real time fingerprint identification systems using a prism as the input device have been reported by Shimizu et al. [3], Gerhart et al. [4] and Gamble et al. [5]. Alternatively, Farrant et al. [6] described a hybrid fingerprint identification system that used a magneto-optic spatial light modulator (SLM) to generate the spatial filters and Fielding et al. [7] have suggested an optical fingerprint verification system using binary joint transform correlation. In this paper we will present a wavelet matched filtering system which uses a photorefractive (PR) crystal for fingerprint identification. Since the PR crystal is capable of storing a large number of WMFs, the proposed system provides a large capacity which fingerprint identification requires in real time mode.

2. Wavelet transform and filtering

Wavelet transform (WT) analysis is a viable alternative to Fourier transform (FT) analysis for pattern recognition. For instance, WT was utilized for multiresolution image analysis by Mallat [8] and several optical implementations of WT have been reported by Zhang et al., Sheng et al., Szu et al., and Yang et al. [9–12]. A two-dimensional WT of a signal $s(x, y)$ is given as

$$w(a_x, a_y, b_x, b_y) = \mathrm{WT}\{s(x, y)\}$$
$$= \iint s(x, y)\, h^*_{ab}(x, y)\, \mathrm{d}x\, \mathrm{d}y\,, \tag{1}$$

where the asterisk represents the complex conjugation of the wavelet which is defined as

$$h_{ab}(x, y) = \frac{1}{\sqrt{a_x a_y}}\, h\left(\frac{x-b_x}{a_x}, \frac{y-b_y}{a_y}\right). \tag{2}$$

This function is obtained by translating and dilating the anlyzing wavelet function $h(x, g)$. Thus the WT of eq. (1) can also be written as

$$w(a_x, a_y, b_x, b_y) = \frac{1}{\sqrt{a_x a_y}} \int_{-\infty}^{\infty} \int_{-\infty}^{\infty} s(x+b_x, y+b_y)$$
$$\times h^*(x/a_x, y/a_y)\, \mathrm{d}x\, \mathrm{d}y$$
$$= \frac{1}{\sqrt{a_x a_y}}\, s(x, y) * h^*(x/a_x, y/a_y)\,, \tag{3}$$

where $*$ denotes the correlation operation, which is essentially the cross correlation between the signal and the dilated analyzing wavelet. Further $h(x/a_x, y/a_y)$ can be interpreted as a band pass filter which is governed by the dilation (a_x, a_y). Thus both the dominant frequency and the bandwidth of the filter can be adjusted by changing the dilation of $h(x/a_x,$

y/a_y). Or in other words, the WT is essentially a filtered version of the input signal $s_t(x, y)$, and the correlation of two WTs with respect to the input signals would be the estimation of the similarity between the two signals. Due to the inherent local feature selection of the WT [13], the WMF would generally offer a higher discriminability than the CMF.

If we take the WT of the target signal $s_t(x, y)$ to be

$$w_t(a_x, a_y, b_x, b_y) = \frac{1}{\sqrt{a_x a_y}} s_t(x, y) * h^*\left(\frac{x}{a_x}, \frac{y}{a_y}\right), \tag{4}$$

then the frequency domain representation of the WT is

$$W_t(u, v) = \mathcal{F}\{w_t(a_x, a_y, b_x, b_y)\}$$
$$= \frac{1}{\sqrt{a_x a_y}} S_t(u, v) H_a^*(u, v), \tag{5}$$

where $\mathcal{F}\{\ \}$ denotes the FT operation and

$$S_t(u, v) = \mathcal{F}\{s_t(x, y)\}$$

$$H_a(y, v) = \mathcal{F}\{h(x/a_x, y/a_y)\}. \tag{6}$$

Similarly, the frequency domain representation of the WT of the reference signal $w_r(a_x, a_y, b_x, b_y)$ can be written as

$$W_r(u, v) = \mathcal{F}\{w_r(a_x, a_y, b_x, b_y)\}$$
$$= \frac{1}{\sqrt{a_x a_y}} S_r(u, v) H_a^*(u, v), \tag{7}$$

where

$$S_r(u, v) = \mathcal{F}\{s_r(x, y)\}. \tag{8}$$

If the WT of the reference signal is used to generate the CMF, then the matched filtering function is essentially the complex conjugation of eq. (7), that is

$$\mathrm{CMF}_w(u, v) = W_r^*(u, v) = \frac{1}{\sqrt{a_x a_y}} S_r^*(u, v) H_a(u, v). \tag{9}$$

If the WT of the target signal is inserted at the input plane of an optical correlator [14], the correlation between the WT of the target and the WT of the reference can be obtained at the output plane, that is

$$o_w(x', y') = \mathcal{F}^{-1}\{\mathrm{CMF}_w(u, v)\, W_t(u, v)\}$$
$$= w_r(x', y') * w_t(x', y'). \tag{10}$$

In order to simplify the operation of such a wavelet correlator, it is desirable to use the original target signal, instead of its WT, as the input of the correlator. Thus we see that the complex light field behind the matched filter can be written as

$$O_w(u, v) = W_t(u, v)\, W_r'^*(u, v)$$
$$= (1/a_x a_y) S_t(u, v) H_a(u, v) S_r^*(u, v) H_a^*(u, v)$$
$$= S_t(u, v)\mathrm{WMF}(u, v), \tag{11}$$

where

$$\mathrm{WMF}(u, v) = (1/a_x a_y) S_r^*(u, v) |H_a(u, v)|^2 \tag{12}$$

is defined as the wavelet matched filter. It can be synthesized with the CMF and the scaled modulus of the dilated wavelet spectrum of eq. (6). It is apparent that, if the input is the original target pattern and the CMF is replaced by such a WMF, the output result would be the correlation of WT of the target and the WT of the reference. It is therefore trivial that if these two WTs are identical, we would expect a high correlation peak intensity at the output plane.

3. Pattern recognition with wavelet matched filter

The generation of the WMFs is the key issue in the construction of a WT correlator. Although the WMFs can be synthesized by computer generated hologram (CGH), the synthesis is rather complicated. The WMFs can also be generated sequentially using a SLM. In this case, however, only one filter can be loaded at a time, which limits the data throughput of the system. To alleviate these shortcomings, we propose an optical wavelet correlator using a photorefractive (PR) crystal, in which a large number or WMFs can be stored.

The recording system for a WMF correlator is shown in fig. 1a, in which the reference signal s_r is located at the input plane. Let us assume that the scaled moduli of the wavelet spectra are sequentially generated by the SLM located at the back focal plane of lens L1, the emerging light field can be synchronously imaged onto the crystal by the imaging lens L2. Thus a large number of WMFs can be recorded in

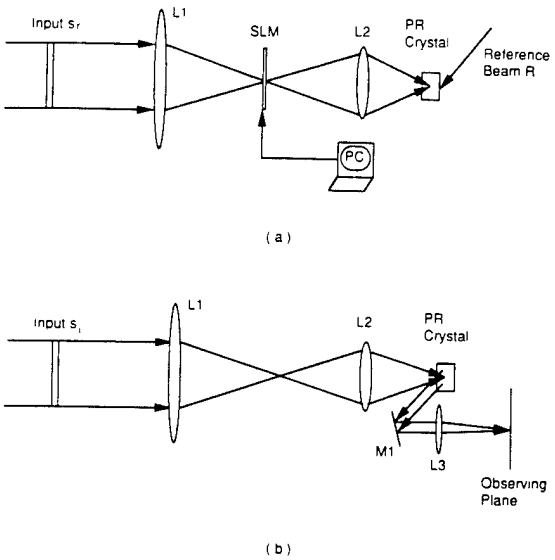

Fig. 1. An optical wavelet correlator using a PR crystal. (a) Reflection type WMFs synthesis, (b) correlation with a PR WMF.

the PR crystal as a set of reflective holograms by means of angular multiplexing. The light intensity within the crystal can be written as

$$I=\sum_{n=1}^{N}|S_r|H_n|^2+R_n|^2$$

$$=|S_r|^2\sum_{n=1}^{N}|H_n|^4+\sum_{n=1}^{N}|R_n|^2$$

$$+S_r^*\sum_{n=1}^{N}|H_n|^2R_n+S_r\sum_{n=1}^{N}|H_n|^2R_n^*, \qquad (13)$$

where S_r and H_n are the Fourier transforms of the reference signal and the dilated analyzing wavelets, respectively, R_n is the reference beam, and N is the total number of the wavelets.

By referring to fig. 1b, if a target object s_t is inserted at the input plane, the reflected (i.e. reconstructed) light field from the crystal will be

$$O(u,v)=KS_tI=KS_t\left(\sum_{n=1}^{N}|S_r|H|^2+R_n|^2\right)$$

$$=KS_t\left(|S_r|^2\sum_{n=1}^{N}|H|^4+\sum_{n=1}^{N}|R_n|^2\right)$$

$$+KS_tS_r^*\sum_{n=1}^{N}|H|^2R_n+KS_tS_r\sum_{n=1}^{N}|H|^2R_n^*, \qquad (14)$$

Fig. 2. The fingerprint used to obtain the autocorrelation.

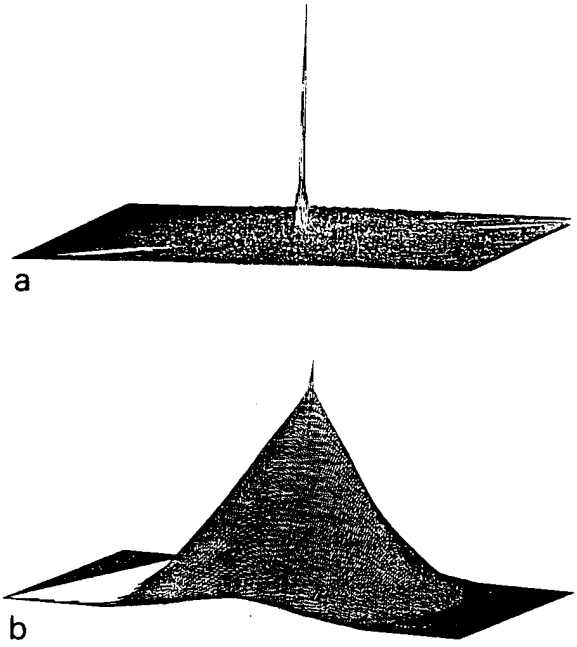

Fig. 3. Computer simulated results. (a) Autocorrelation distribution using a WMF ($a_x=0.05, a_y=0.05$) and (b) using a CMF.

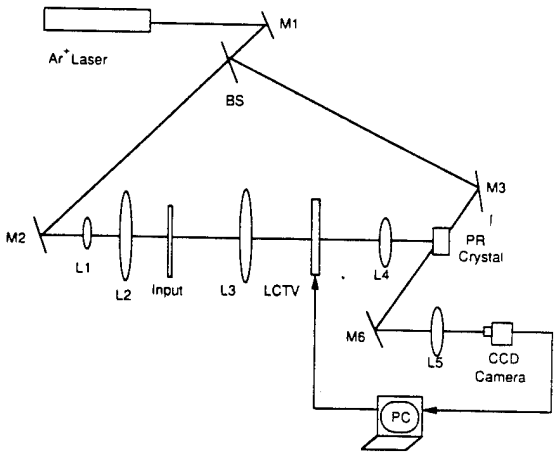

Fig. 4. An optical wavelet correlator for fingerprint identification.

where K is a proportionality constant. Thus by inverse Fourier transforming this equation, the correlation between the w_t and w_r can be obtained. If the input object s_t is identical to the reference signal s_r, then an array of autocorrelation peaks will be produced at the back focal plane of lens L3. Since this system is essentially a multichannel correlator, the correlations between the input signal and all the WMFs can be performed in real time.

4. Simulated and experimental demonstration

To verify the feasibility of the wavelet matched filtering using a PR crystal, a computer simulation was undertaken. A set of fingerprints, one of them is depicted in fig. 2, were used as the reference and target patterns. Since the major feature of typical fingerprints is a parallel circular type striation pattern, a mexican hat-like analyzing wavelet is chosen, as given by

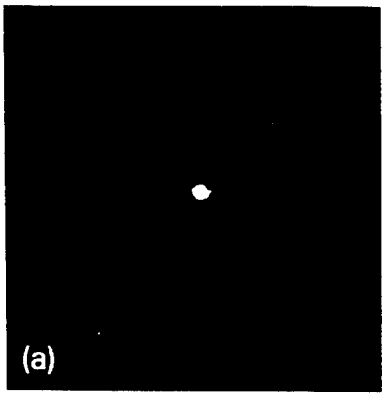

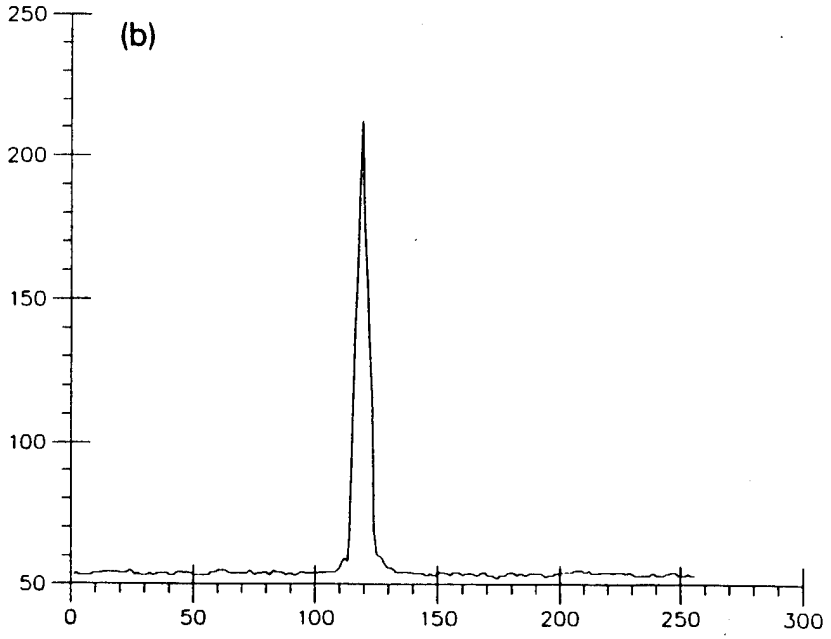

Fig. 5. Autocorrelation output using a WMF (a_x=0.05, a_y=0.05). (a) Photograph of the autocorrelation peak and, (b) profile of the autocorrelation peak.

$$h(x, y) = (1 - x^2 - y^2) \exp(-x^2 - y^2) . \quad (15)$$

Its dilated version is written as

$$h(x/a_x, y/a_y) = [1 - (x/a_x)^2 - (y/a_y)^2] \times \exp[-(x/a_x)^2 - (y/a_y)^2] , \quad (16)$$

which is a real symmetric function. The corresponding Fourier spectrum is given by

$$H_a(u, v) = \mathcal{F}\{h(x/a_x, y/a_y)\} = (\pi/16) a_x a_y [(a_x x)^2 + (a_y y)^2] \times \exp[-\tfrac{1}{4}(a_x x)^2 - \tfrac{1}{4}(a_y y)^2] . \quad (17)$$

If we let $a_x = a_y = a_0$, then eqs. (16) and (17) reduce to circularly symmetric functions, as given by

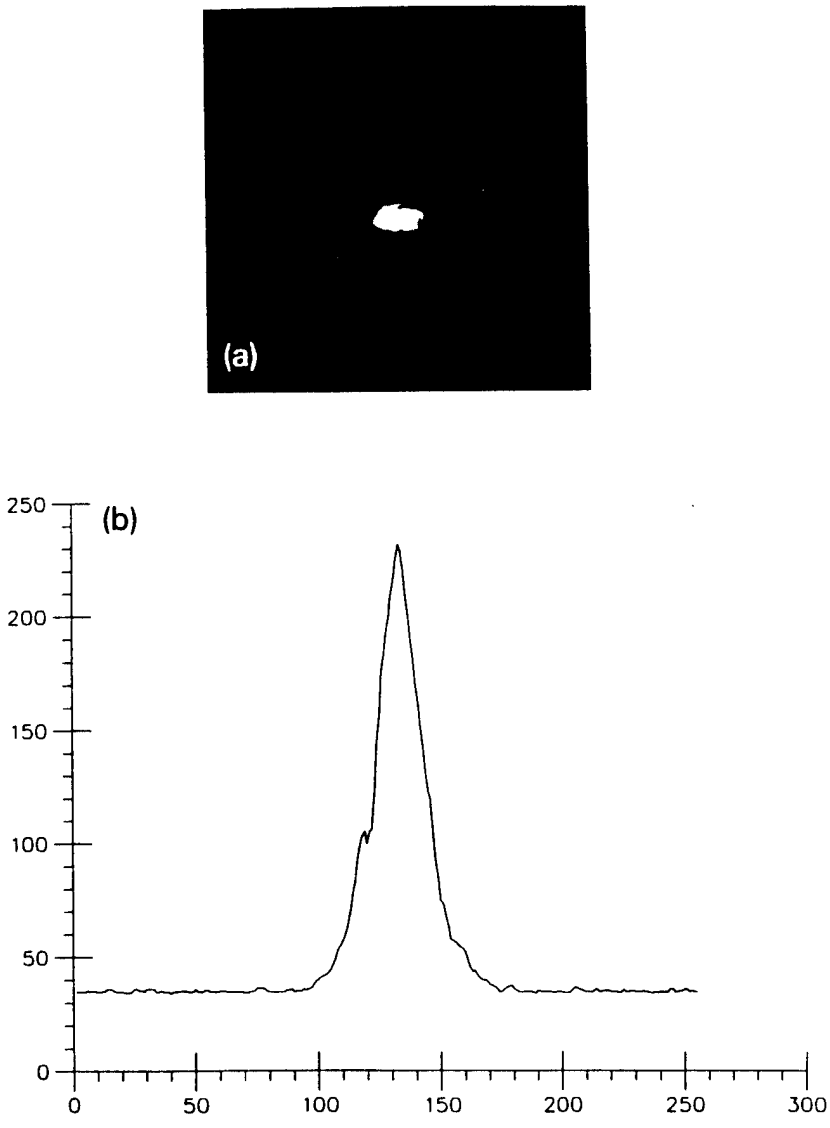

Fig. 6. Autocorrelation output using a CMF. (a) Photograph of the autocorrelation peak and (b) profile of the autocorrelation peak.

$$h(x/a_0, y/a_0) = [1-(x/a_0)^2-(y/a_0)^2] \times \exp[-(x/a_0)^2-(y/a_0)^2], \quad (18)$$

and

$$H_a(u, v) = (\pi/16)a_0^4(u^2+v^2)\exp[-\tfrac{1}{4}a_0^2(x^2+y^2)]. \quad (19)$$

The WMF with this wavelet can be expressed as

$$\mathrm{WMF}(u, v) = (1/a_0^2)S_r^*(u, v)|H_a(u, v)|^2, \quad (20)$$

where $H_a(u, v)$ is defined by eq. (19) and $S_r(u, v)$ is the FT of the reference fingerprint as given in fig. 2. If we chose $a_0 = 0.05$, and the same fingerprint was used as the input, a sharp autocorrelation peak was obtained, as shown in fig. 3a. In comparison with the autocorrelation obtained with the CMF, as depicted in fig. 3b, the optical wavelet correlator offered obviously better performance (i.e., better signal discriminability). Since the signal discriminability is affected by the dilation of the analyzing wavelet, in principle, an optimum WMF can be found, which depends on the features of the input signal.

The optical system used to demonstrate the use of WMFs as applied to the fingerprint identification is shown in fig. 4. The fingerprint shown in fig. 2 was taken as the reference signal. Needless to mention that a SLM or a prism may be used to introduce the fingerprint into the system. However for simplicity, fingerprint transparencies are used in our experiment. An Ar^+ laser that emanates a wavelength of 514 nm was used as the light source and a liquid crystal television (LCTV) panel was used to display the wavelet filters. We used a $LiNbO_3$ crystal of about size $5\times6\times7$ mm^2 for the WMFs system. In reconstruction, the read-out light field was detected by a CCD camera and the correlation distribution was displayed on a TV monitor. Figure 5 shows the output autocorrelation peak obtained with a WMF, and fig. 6 is obtained with a CMF. From these results, once again, we see that the WMF performed better than the CMF. In both cases (with a WMF and a CMF), no correlation peaks were observed when other fingerprints were used as the input.

4. Conclusions

We have demonstrated a wavelet matched filtering system using a PR crystal. We have shown that the WMF performs better than the CMF. Since the performance of the wavelet matched filtering is affected by the dilation of the analyzing wavelet, an optimum dilation of the analyzing wavelet function can be found, which depends upon the feature of the input signal. The major advantage of the proposed system is that a large number of WMFs can be stored in a PR crystal, and therefore, the correlations of an input signal with respect to all the stored WMFs can be implemented in real time.

Acknowledgements

We acknowledge the partial support of DARPA through the U.S. Army Research Office under contract DAAL03-92-G-0328.

References

[1] D.H. McMahon, G.L. Johnson, S.L. Teeter and C.G. Whitney, IEEE Trans. Comput. C-24 (1975) 358.
[2] G.R. Mangasaryan, B.E. Khaikin and V.S. Khitrova, Optics Comm. 22 (1977) 169.
[3] A. Shimizu and M. Hase, Trans. Inst. Electronic Comm. Eng. Japan D J67D (1984) 627.
[4] L.A. Gerhardt, J.B. Attili, D.H. Crockett and A.M. Presler, Proc. Int. Carnahan Conf. on Security Technology (1986) 251.
[5] F.T. Gamble, L.M. Frye and D.R. Grieser, Appl. Optics 31 (1992) 652.
[6] D. Farrant, B.F. Oreb, J.P. Modde and P. Hariharan, Proc. Soc. Photo-Opt. Instrum. Eng. 1053 (1989) 110.
[7] K.H. Fielding, J.L. Horner and C.K. Makekau, Opt. Eng. 30 (1992) 1958.
[8] S.G. Mallat, Trans. IEEE on Acous. Speech and Sig. Proc. ASSP-37 12 (1989) 2091.
[9] Y. Zhang, Y. Li, E.G. Kanterakis, A. Katz and X.J. Lu, Optics Lett. 17 (1992) 210.
[10] Y. Sheng, T. Lu and D. Roberge, Opt. Eng. 31 (1992) 1859.
[11] H. Szu, Y. Sheng and J. Chen, Appl. Optics 31 (1992) 3267.
[12] X. Yang, H.H. Szu, Y. Sheng and H.J. Caulfield, Opt. Eng. 31 (1992) 1846.
[13] J.M. Combes, A. Grossmann and Ph. Tchamitchian, eds. Wavelets, 2nd Ed. (Springer, Berlin, 1990).
[14] F.T.S. Yu, Optical information processing (Wiley, New York, 1983).

Appendix 10.17

Application of a Fiber-Speckle Hologram to Fiber Sensing

Application of a fiber-speckle hologram to fiber sensing

Francis T. S. Yu, Shizhuo Yin, Jianzhong Zhang, and Ruyan Guo

A sensitive fiber-speckle field sensor using a Ce:Fe-doped $LiNbO_3$ photorefractive fiber hologram is introduced. We have shown that the sensitivity of this photorefractive fiber specklegram sensor can be of the order of 0.05 μm. The proposed system would offer the widespread use of practical fiber-sensing applications.

Fiber-optic sensing has been shown to be one of the more important sensing technologies in recent years.[1] A new type of fiber sensor called the fiber specklegram sensor (FSS) was proposed recently.[2,3] In other words, by taking advantage of the sensitivity of the complex speckle field that exits from a multimode fiber, a highly sensitive FSS can be developed.

In previous papers[2,3] we proposed a multimode fiber-sensing system using photorefractive bulk crystal to construct a fiber-speckle hologram. However, using the bulk material for construction of the fiber-speckle hologram has some practical limitations: First, the physical size of the photorefractive (PR) crystal usually makes it awkward and inefficient for coupling with the sensing fiber. Second, the separation between the sensing fiber and the crystal hologram[2,3] is vulnerable to misalignment and environmental changes. Third, bulk crystal is more expensive compared with equivalent-length PR fiber.[4,5] Fourth, the large dimension of the bulk material makes the fiber specklegram sensing system rather large, which limits its practical application.

To alleviate these limitations, in this Note we demonstrate a FSS using a PR fiber (as the fiber specklegram recording material) as shown in Fig. 1. The sensing fiber is a step-index multimode silica fiber with a 50-μm core diameter, and the PR fiber is a specially doped Ce:Fe $LiNbO_3$ crystal fiber with a 7-mm length and 0.7-mm diameter. The doping levels of Ce and Fe are ~300 and 500 ppm, respectively. Two interesting features of this specially doped material are its high photosensitivity so that the photorefractive effect can be initiated with a low-power (5-mW) laser diode and that its spectral response covers all the visible spectral lines.[6]

In view of Fig. 1 we see that a reflection-type fiber specklegram can be constructed.[7] It is trivial that the reference beam can be reconstructed if one uses the same fiber speckle field. To introduce the transversal displacement on the sensing fiber, a cylindrical rod affixed with a piezoelectric driver, as illustrated in Fig. 1, is used as the bending device. The bending radius (i.e., the distance between bending points A and B) is ~2 mm. The normalized correlation peak intensity as a function of transversal displacement is plotted in Fig. 2. From this figure we see that it exhibits a fairly linear relationship of 0- to 1.4-μm transversal displacement, for which it can be used for submicrometer displacement sensing. The dynamic range of this fiber specklegram sensing system is ~1.3 μm, in which the sensitivity of measurement can be as high as 0.05 μm. We stress that the sensitivity can be improved if higher-mode sensing fiber is used.

In conclusion, we have demonstrated a highly sensitive FSS using a multimode sensing fiber coupled with a PR fiber. The experiment shows that the sensitivity of the PR FSS (in terms of transversal displacement) can be of the order of 0.05 μm or even higher if a higher-mode sensing fiber is used.

The authors are with The Pennsylvania State University, University Park, Pennsylvania 16802. F. T. S. Yu, S. Yin, and J. Zhang are with the Department of Electrical Engineering, and R. Guo is with the Material Research Laboratory.

Received 19 November 1993; revised manuscript received 8 April 1994.

0003-6935/94/225202-02$06.00/0.

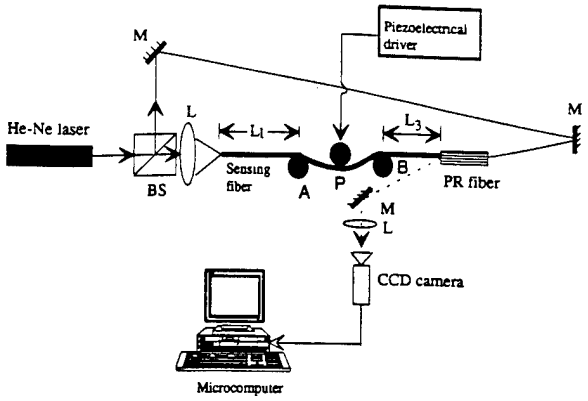

Fig. 1. Experimental setup of the PR FSS system. M, mirror; L, lens; BS, beam splitter; L_1, L_3, fiber lengths; P, bending point.

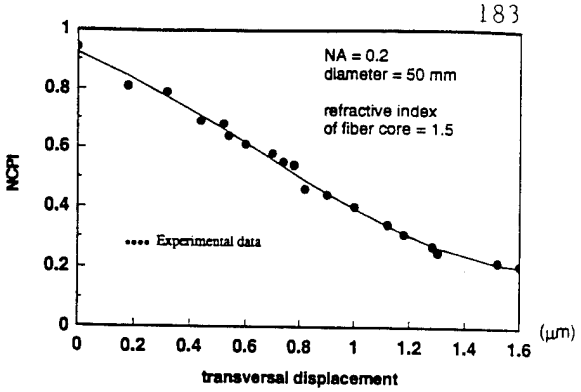

Fig. 2. Normalized correlation peak intensity (NCPI) value as a function of transversal displacement. NA, Numerical aperture.

Compared with the intensity FSS technique as reported in the previous paper,[8] the sensitivity of the PR FSS is ~1 order higher. This high sensitivity is primarily due to the complex amplitude-field analysis compared with the intensity-field analysis of the system.[8]

In short, the proposed PR FSS offers the advantage of higher sensitivity, compact size, direct-coupling architecture, and more robustness during environmental changes. Because of the simplicity of the PR FSS system and its economical operation, we expect the proposed PR FSS to have widespread practical applications, such as in acoustic wave sensing and structure fatigue monitoring.

The authors acknowledge the support of the Advanced Research Projects Agency through the U.S. Army Research Office under contract DAAL 03-92-G-0328.

References

1. E. Udd, *Fiber Optic Sensors* (Wiley, New York, 1991), Chap. 1, p. 1.
2. S. Wu, S. Yin, and F. T. S. Yu, "Sensing with fiber specklegrams," Appl. Opt. **30,** 4468–4470 (1991).
3. S. Wu, S. Yin, S. Rajan, and F. T. S. Yu, "Multichannel sensing with fiber specklegrams," Appl. Opt. **31,** 5975–5983 (1992).
4. R. S. Feigelson, "Growth of fiber crystals," in *Crystal Growth of Electronic Materials,* E. Kaldis, ed. (North-Holland, Amsterdam, 1985), pp. 127–144.
5. J. K. Yamamoto and A. S. Bhalla, "Growth of $Sr_{1-x}Ba_xNb_2O_6$ single crystal fiber," Mater. Res. Bull. **24,** 761–765 (1989).
6. S. Yin and F. T. S. Yu, "Specially doped $LiNbO_3$ crystal holography using a visible-light low-power laser diode," IEEE Photon. Technol. Lett. **5,** 581–582 (1993).
7. F. T. S. Yu and S. Yin, "Holographic storage and interconnection using a Ce:Fe-doped $LiNbO_3$ photorefractive crystal fiber with a tunable visible-light laser diode," Opt. Memory Neural Networks **1,** 289–301 (1992).
8. F. T. S. Yu, M. Wen, S. Yin, and C. Uang, "Submicrometer displacement sensing using inner-product multimode fiber speckle fields," Appl. Opt. **32,** 4685–4689 (1993).

Appendix 10.18

A Content-Addressable Polychromatic Neural Net Using a (Ce:Fe) Doped $LiNbO_3$ Photorefractive Crystal

ELSEVIER

15 April 1994

OPTICS COMMUNICATIONS

Optics Communications 107 (1994) 300–308

Full length article

A content-addressable polychromatic neural net using a (Ce:Fe)-doped $LiNbO_3$ photorefractive crystal

Francis T.S. Yu, S. Yin, C.-M. Uang

Department of Electrical and Computer Engineering, Pennsylvania State University, University Park, PA 16802, USA

Received 1 April 1993; revised manuscript received 27 October 1993

Abstract

A polychromatic neural net using a (Ce:Fe)-doped $LiNbO_3$ photorefractive crystal is presented. This neural net is a two-level high-content addressable memory. The first level is a polychromatic Hamming net for color image classification, and the second level is a mapping net, based on a photorefractive crystal associative memory. The major advantage of this neural net is the large storage capacity and it requires a fewer interconnection links. Experimental demonstrations are provided, in which is shown that the proposed neural net is consistent with the theoretical model.

1. Introduction

It is well known that the associative memory, such as used in the Hopfield model and the inter-pattern association (IPA) model [1,2], has a variety of applications to content addressable memory (CAM), optimization computing, error-correction code, pattern recognition, and intelligent control. These models have the advantages of simple and easy implementation. However, they also suffer some limitations for practical applications. For example, they have a lower storage capacity, require a huge interconnection links, are unstable, sometimes converge to a wrong exemplar, and are not effective for hetero-association. On the other hand, models such as the Hamming net [3,4] have the advantages of high storage capacity, fewer interconnection links, and strong convergency to a correct exemplar. Furthermore, the currently available LCTVs are built with color liquid-crystal panels which makes them particularly suitable for implementation of polychromatic neural networks. By introducing a color encoding technique in conjunction with a conventional white light source the polychromatic neural network can be synthesized. Since each triad of an LCTV pixel element consists of three R, G, and B pixel elements, the storage capacity of the polychromatic neural net can be increased by three times as compared with a regular black and white neural network. A typical Hamming net is shown in Fig. 1. It essentially contains two networks: the first layer is a Hamming layer and the next layer is a MAX net. We will discuss how to expand it to a color architecture in detail in the next section. Unfortunately, a Hamming net does not include the usual associative memory that limits the practical applications.

In this paper, we shall propose a two-level high-content addressable polychromatic neural net, in which the first level is a polychromatic Hamming net (for color image classification) and the second level is a mapping net using a photorefractive crystal for the construction of a hetero-associative memory.

0030-4018/94/$07.00
SSDI 0030-4018(93)E0556-U

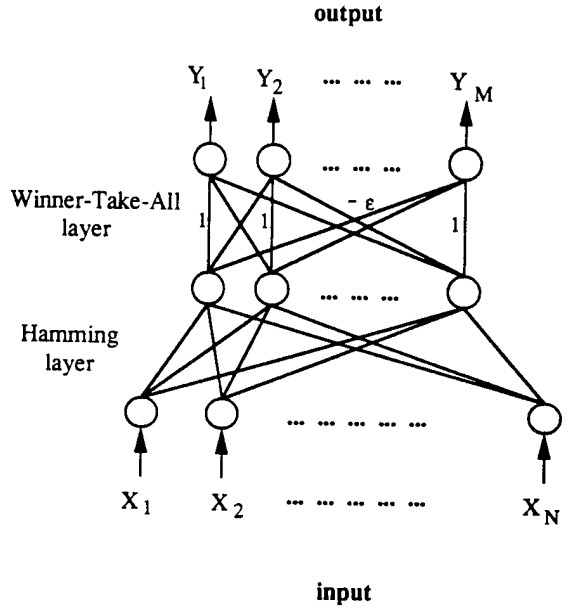

Fig. 1. A schematic diagram of the neural network (Hamming net+WTA).

2. Polychromatic Hamming net

A schematic optical set-up diagram of the polychromatic neural network [5] is shown in Fig. 2, which has two liquid crystal television (LCTV) panels tightly cascaded for displaying the input pattern and the interconnection weight matrix (IWM).

Let us denote the light intensity of the red, the green, and the blue components in a color pixel element as $I_R(x, y)$, $I_G(x, y)$, and $I_B(x, y)$, respectively. The color intensity light field from the LCTV panel can be written as

$$I(x, y) = I_R(x, y) + I_G(x, y) + I_B(x, y) , \qquad (1)$$

where (x, y) represents the spatial coordinate of the liquid crystal panel. Eq. (1) is provided for the concept for color decomposition and the composition, by which each image pixel can be decomposed and composed with the primary colors as illustrated in Fig. 3. For example, a set of reference color patterns are decomposed into primary color pattern, which can be used as the training sets for the construction of the color IWMs (i.e., IWM_R, IWM_G, and IWM_B). By combining this set of IWMs, a multicolor IWM can be displayed on panel LCTV2, as shown in Fig. 2. Apparently, if a color pattern is fed into LCTV1, the summed signal detected by the color CCD would be the output of the color Hamming net. If this output is sent to a color winner-take-all (WTA) layer and then selecting the maximum input node, a classification of the input color pattern can be made.

Let M be the number of the color exemplars stored in the neural net, for which each exemplar has N pixels. We assume that the first layer (i.e., the Hamming layer) has N input and M output neurons, which corresponds to N pixels and M classes, respectively. If

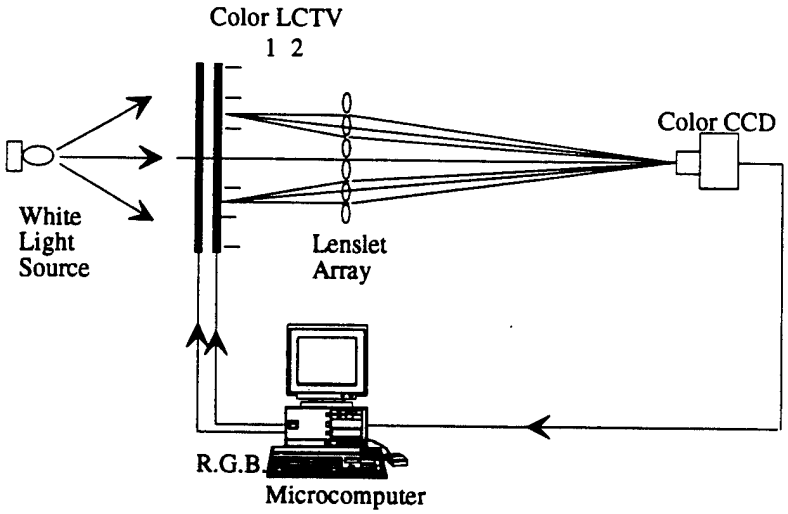

Fig. 2. A color LCTV based polychromatic Hamming net.

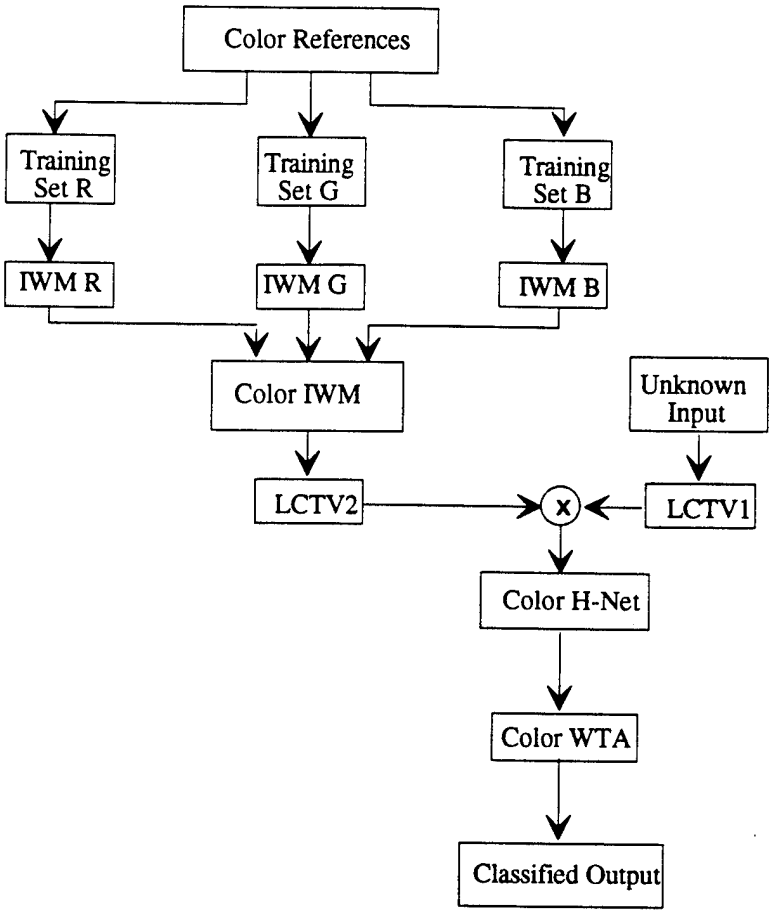

Fig. 3. Block diagram of color decomposition and composition.

an input color pattern, X_i, is loaded into the neural net classifier, it is decomposed into primary color patterns as given by

$$X_{iC} = \Theta_C[X_i], \quad (1 \leqslant i \leqslant N, C = \mathrm{R, G, B}), \tag{2}$$

where $\Theta_{C=\mathrm{R,G,B}}$ denotes the color decomposition operation on red, green, and blue, respectively. And the interconnection weights in the Hamming layer are determined by

$$W_{ijC} = X_{iC}^{(j)}, \quad (1 \leqslant j \leqslant M, \quad C = \mathrm{R, G, B}), \tag{3}$$

where W_{ijC} is the primary color interconnection weight from the ith input neuron to the jth output neuron, X_{iC} is the value (which can be either $+1$ or -1) of the ith pixel in the jth exemplar of the primary color, and M is the number of classes. The output of the Hamming layer in each channel is given by

$$U_{jC}(0) = \sum_C \frac{1}{2}\left(\sum_{i=1}^{N} W_{ijC} X_{iC} + N\right),$$

$$(1 \leqslant j \leqslant M, C = \mathrm{R, G, B}), \tag{4}$$

where $\Sigma_{C=\mathrm{R,G,B}}$ denotes the primary color composition operation, and N is the number of input neurons. When an exemplar matches exactly with the input pattern, the corresponding output of the neuron representing the exemplar reaches a maximum value, N, in each channel. On the other hand, if all the pixels in an exemplar are different from the corresponding pixels of the input pattern, the corresponding output of the neuron representing the exemplar would be zero in each channel. In general, the output $U_{jC}(0)$ would have a value between 0 and N in each channel, which is equal to the number of bits of the input pattern that matches the bits of the jth exemplar, i.e.,

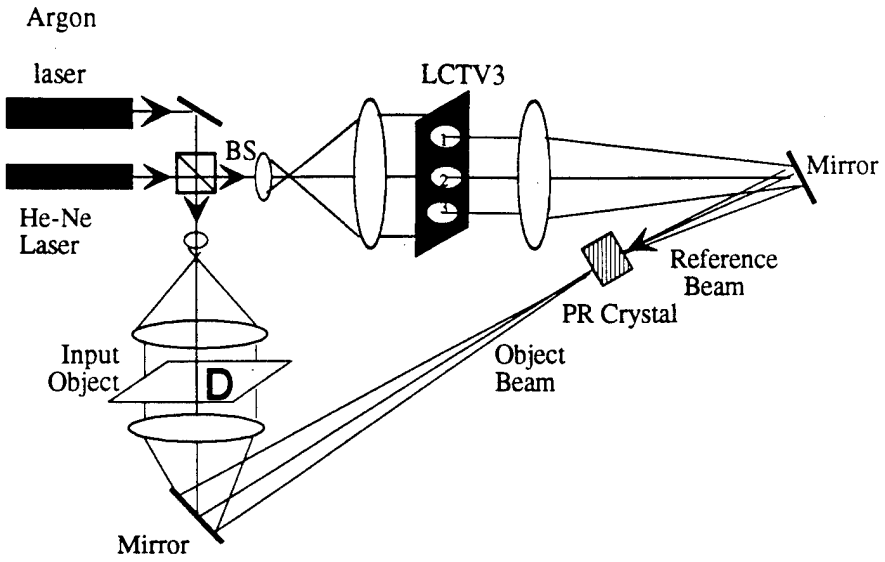

Fig. 4. Polychromatic holographic recording in a (Ce:Fe)-doped $LiNbO_3$ photorefractive crystal.

$$U_{jC}(0)=N-\mathrm{HD}_C, \quad (1\leqslant j\leqslant M,\ C=\mathrm{R,G,B}), \tag{5}$$

where HD_C represents the Hamming distance in each channel.

However in the MAX Net (second) layer, it requires a high dynamic range and successive iteration to produce a maximum output node. Nevertheless, if the Hamming distance between an exemplar and the input pattern is larger than a specific value, (e.g., $N/2$, half of the total input bits), it is not necessary to send a non zero signal to the second layer. Thus by introducing a parameter α, $(0<\alpha<1)$, such that αN is the maximum Hamming distance that gives rise to a non zero output signal from the first layer, the output of the modified Hamming layer can be expressed as [4]

$$\begin{aligned} U_j(0) &= \sum_C f\left(\sum_{i=1}^{N} W_{ijC}X_{iC}\right) \\ &= N-\mathrm{HD}/\alpha, \quad \mathrm{HD}<\alpha N \\ &= 0, \quad \mathrm{HD}\geqslant\alpha N, \quad (1\leqslant j\leqslant M,\ C=\mathrm{R,G,B}), \end{aligned} \tag{6}$$

where $f(\ )$ is a hard limiter thresholding function. By using the preceding scheme, the Hamming distance between the input and the exemplar can be enlarged by a factor of $1/\alpha$, for which the high dynamic range requirement imposed on the spatial light modulators (SLMs) and the number of iterative cycles in the MAX Net can be reduced. Thus, the overall performance of the modified Hamming Net can be improved.

The winner-take-all or MAX Net layer has M input and M output neurons, in which the interconnection weight between the jth input and kth output neurons can be written as

$$\begin{aligned} t_{ijC} &= 1, \quad j=k, \\ &= -\epsilon, \quad j\neq k, \\ &(\epsilon<1/M,\ 1\leqslant j,k\leqslant M,\ C=\mathrm{R,G,B}), \end{aligned} \tag{7}$$

where ϵ is known as the *inhibition constant*. When an output signal from the Hamming layer is fed to the MAX Net layer, the iteration can be carried out as given by

$$\begin{aligned} U_{kC}(n+1) &= g\left(\sum_{j=1}^{M} t_{jkC}U_{jC}(n)\right) \\ &= g\left(U_{kC}(n)-\epsilon\sum_{j\neq k}U_{jC}(n)\right), \\ &(1\leqslant j,k\leqslant M,\ C=\mathrm{R,G,B}), \end{aligned} \tag{8}$$

where $g(\ )$ represents a nonlinear operator (e.g., a sigmoid function). We note that, by using this analog nonlinear thresholding operation, it can suppress the value of the output signal when the argument becomes negative. Thus by modifying Eq. (8), we have

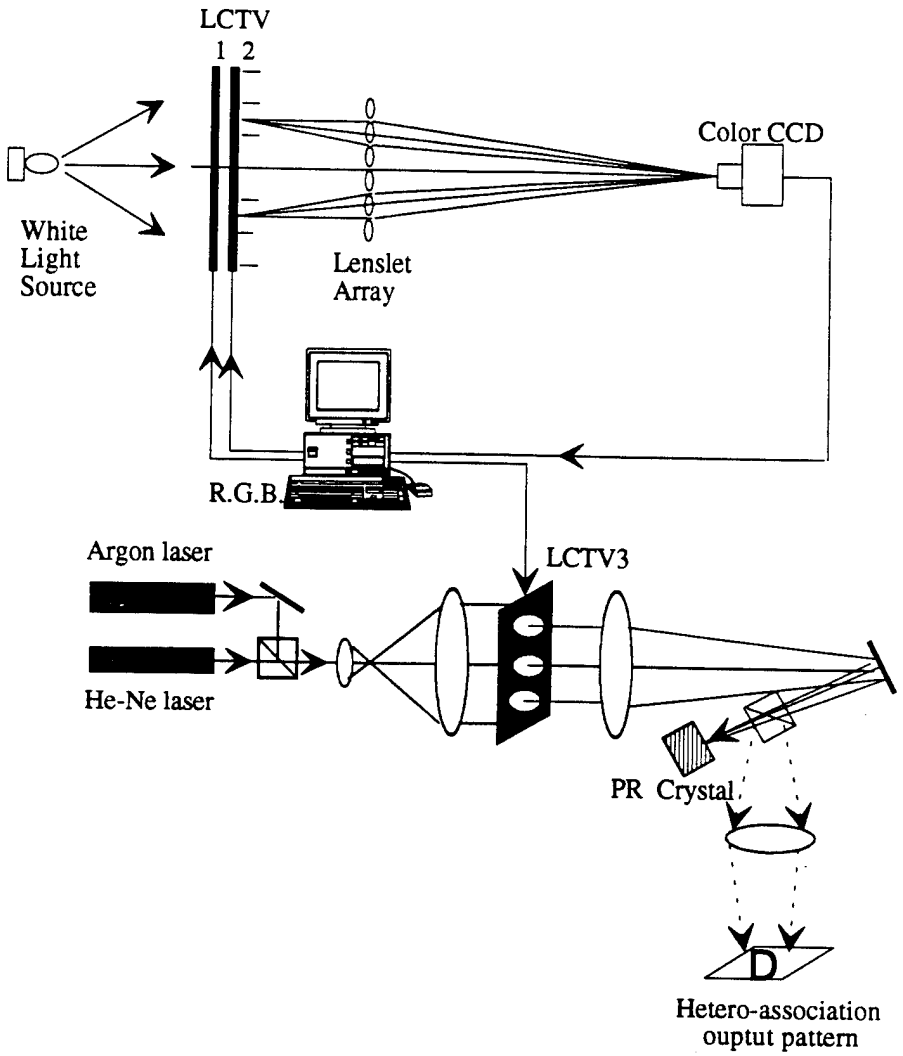

Fig. 5. Experimental set-up of the polychromatic two-level content-addressable neural net.

$$U_{kC}(n+1)=g\Big(U_{kC}(n)+\epsilon U_{kC}(n)$$

$$-\epsilon U_{kC}(n)-\epsilon\sum_{j\neq k}U_{jC}(n)\Big)$$

$$=g\Big(aU_{kC}(n)-\frac{1}{N}\sum U_{jC}(n)\Big),$$

$$(1\leqslant j,k\leqslant M,\ C=\mathrm{R,G,B})\ , \qquad (9)$$

where $a=(1+\epsilon)/(\epsilon N)$ is a factor used to control the convergent speed of the iteration, for it can be implemented in practice. Since the second term of Eq. (9) represents the average intensity of the nth iteration cycle, the output neurons, whose values are below the average would have been zero.

3. Two-level high-content polychromatic neural net

The polychromatic Hamming net described in the preceding section offers the advantages of large storage capacity and fewer interconnection links. However, it does not include the usual associative memory, which is important in some applications such as

error-correction code and pattern recognition. To alleviate this problem, we propose a two-level high-content polychromatic neural net. The first level of the proposed neural net is a polychromatic Hamming net and the second level is a mapping net, which has the ability of mapping the maximum output from the Hamming net to the desired output pattern. Important mapping process can be done by using either auto-association or hetero-association memory, for pattern recognition or pattern translation, respectively.

In our proposed implementation, the second mapping level is essentially a holographic interconnection system, in which a set of Fourier holograms are recorded using the outputs from the polychromatic Hamming net as the read-out training set as shown in Fig. 4. In the read-out process, the object beam is blocked while the reference beam will be used to reconstruct the stored exemplars. Since a different input position corresponds to the different reference beam angle, an angular multiplexed crystal hologram can be used [6]. Thus, a one-to-one correspondence between the reading angles and the output stored exemplar can be established in the second level. Since the different input pattern corresponds to a different output position (i.e., reading angle for the second level) from the Hamming net, the content-addressable network can be developed using this two-level neural net. In the proposed neural net, a (Ce:Fe)-doped $LiNbO_3$ photorefractive crystal is used as the large-capacity recording medium [7,8]. One of the advantages of this (Ce:Fe)-doped $LiNbO_3$ PR crystal is that it is sensitive to the entire visible-light spectral lines (e.g., the sensitivity is about 15 mJ/cm^2 for 1% diffraction efficiency), which makes it rather easy to construct a polychromatic holographic associative memory. Furthermore, since the PR crystal hologram is a two-dimensional parallel write-in and read-out process [7], the read-out process from the PR crystal memory can be, theoretically speaking, at the speed of light. Therefore, the addressing speed of the proposed neural net can also be very fast.

4. Experimental demonstration

The proposed polychromatic neural net is depicted in Fig. 5, in which a PR holographic mapping set is connected in tandem with a LCTV polychromatic Hamming net. For experimental demonstration, we

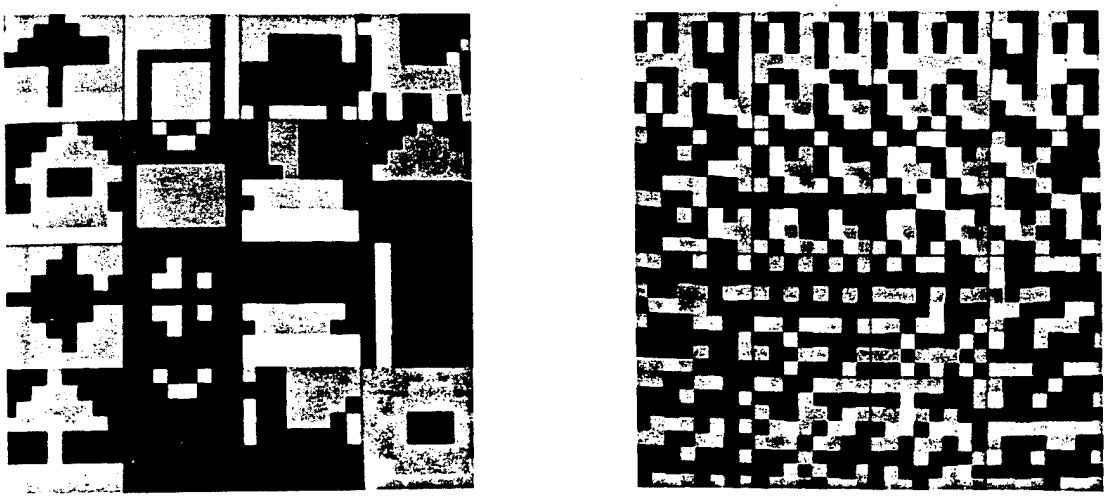

(1) (2)

Fig. 6. Experimental results: (1) sixteen training object pattern; (2) IWM of the first level; (3) (4) (5) three input object patterns; (6) (7) (8) the corresponding output results from the MAX Net; (9) (10) (11) the corresponding hetero-association output patterns obtained from the second level.

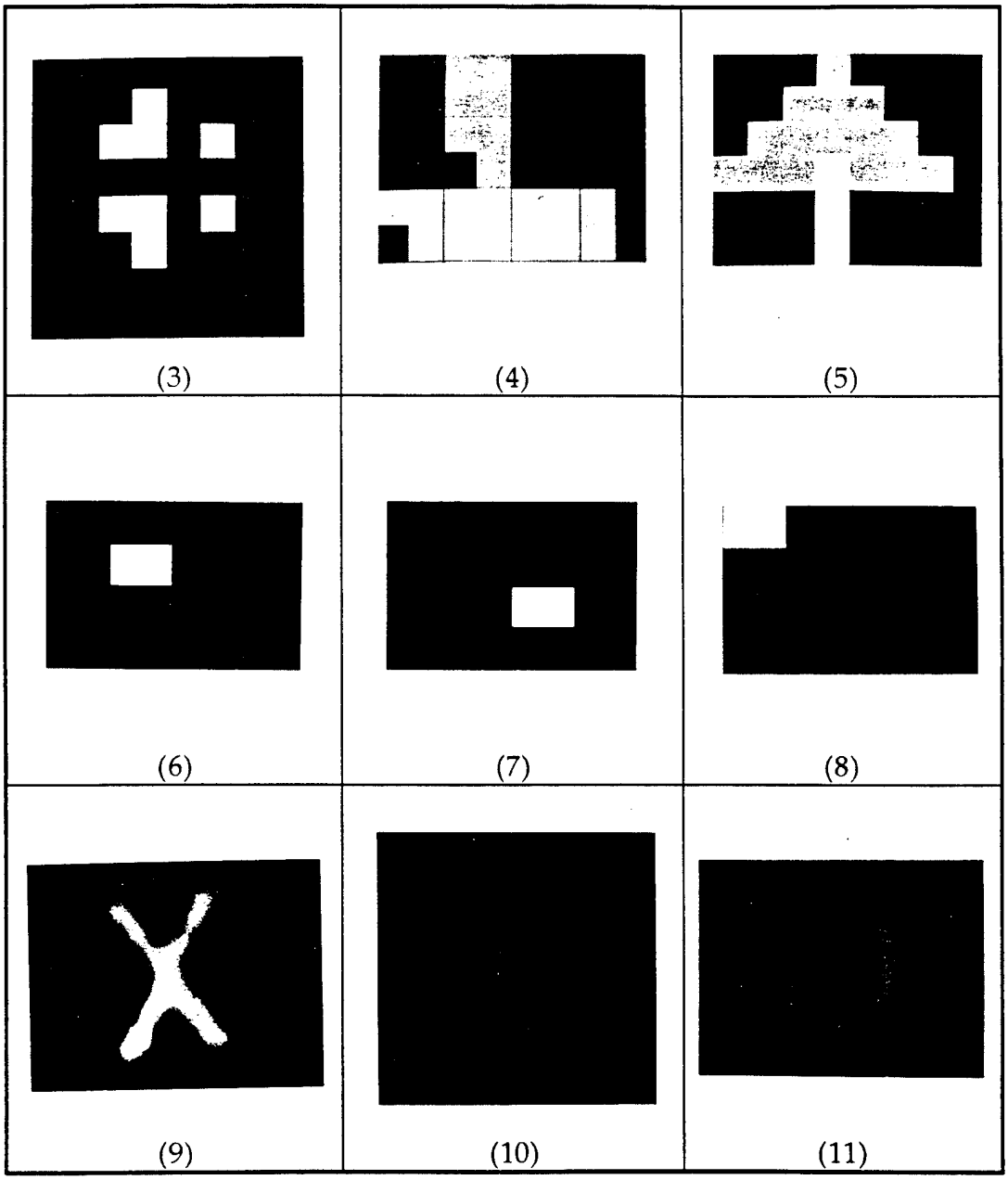

Fig. 6. Continued.

have used training set pattern as shown in Fig. 6(1) for the construction of the IWM in the Hamming net level, as shown in Fig. 6(2). The pixel arrangement of the input pattern, the IWM, and the contents of each subIWM is shown in Figs. 7a, b, and c, respectively. Now let us assume that the input objects of Figs. 6(3), 6(4), and 6(5) are sequentially presented to the proposed neural net (i.e., LCTV1) and the IWM of Fig. 6(2) is displayed on the LCTV2. To match the physical size of the submatrix of the IWM, the input object is enlarged by which the input pattern-pixel is of the same size as the submatrix. Since

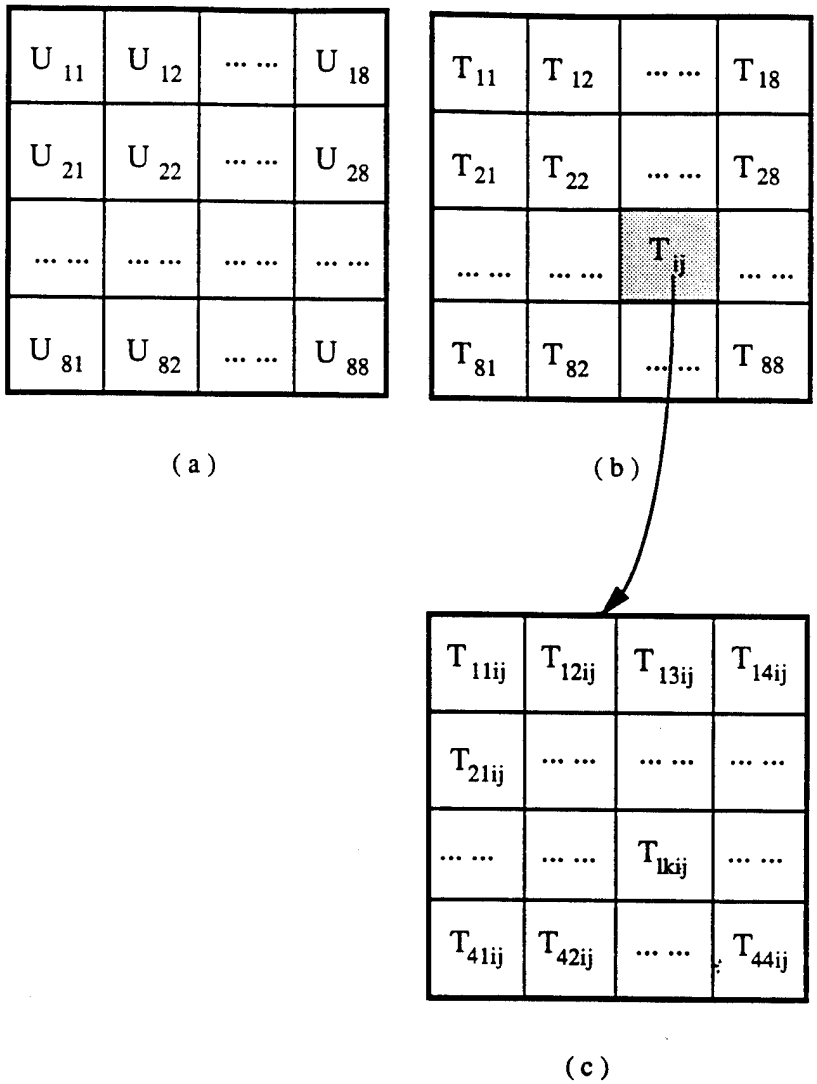

Fig. 7. A diagram of pixel arrangement of neural net, (a) input pattern; (b) interconnection weight matrix; (c) the content of each subIWM.

the emerging light field from LCTV panels 1 and 2 represents the pattern–submatrix pixel multiplication, the summation part of Eq. (6) can be carried out by a lenslet array on a color CCD camera. In other words, the polychromatic vector–matrix multiplication is performed with a LCTV system, by which the Hamming net output can be obtained using a CCD camera. By applying the winner-take-all (WTA) algorithm of the Max Net (i.e., carried out by a microcomputer), the output of the Hamming layer can be obtained by taking about two to three cycles of iterations if one uses a simplified WTA system as described by Yang et al. [4]. Figs. 6(6), 6(7), and 6(8) show a set of Max Net outputs, which correspond to the input objects of Figs. 6(3), 6(4), and 6(5), respectively.

To demonstrate an application of this proposed neural net to the hetero-association memory, we use an associative training set of color patterns as recorded in the PR crystal in the second level. The het-

ero-associated patterns corresponding to the input patterns Figs. 6(3), 6(4), and 6(5) are the red letter "X", green letter "V", and blue letter "D", which are recorded accordingly in a PR crystal hetero-associative hologram, as shown in Fig. 5. In our experiment, a specially doped (Ce:Fe:) $LiNbO_3$ based crystal is used for the construction of an angular multiplexed reflection-type hologram. A HeNe laser of $\lambda = 633$ nm and an Ar^+ laser of $\lambda = 515$ nm, $\lambda = 488$ nm, are used for the coherent sources, and the size of the crystal was measured to be about 1 cm^3 cube. The orientation of the crystal is in z-cut direction and the construction angle between the object and the reference beams is about 170°. The exposure time used for each of the PR hetero-association holograms (i.e., from each output spot of the MAX Net) is about 1 second. Notice that in the read-out process (i.e., operation of the second level) the object beam has been blocked, so the reflected hologram images can be read-out by the angular multiplexed reference beams from the LCTV3, as shown in the Fig. 5. For example, if the input object pattern of Fig. 6(3) is presented to the LCTV1 of the neural net, then a transparent spot, resulting from the MAX Net output shown in Fig. 6(6), will be registered on the LCTV3, for which the transmitted polychromatic coherent light is used to read-out the hetero-association PR hologram, as shown in Fig. 6(9) (i.e., a red letter "X").

Similarly, if the input object patterns of Figs. 6(4) and 6(5) are presented to the proposed content addressable neural net, the corresponding hetero-association exemplars of "V" and "D" (in green and in blue) can be observed at the output plane, as shown in Figs. 6(10) and 6(11), respectively.

5. Conclusion

In conclusion, we have proposed a two-level content-addressable polychromatic neural net. The architecture is basically the combination of a polychromatic Hamming net with a mapping net, which is based on a hetero-association PR crystal holographic memory. The proposed neural net is not only increasing the storage capacity and reducing the interconnection links, but also provides the content addressable capability at the second mapping net level. Since a $LiNbO_3$ crystal volume hologram has a very large storage capacity, the number of the output neurons from the second mapping net level can be very large, which is in the order of 10^6. We have also experimentally demonstrated that the proposed content addressable polychromatic neural net can indeed perform the pattern translation in color.

References

[1] J.J. Hopfield, Proc. Natl. Acad. Sci. USA 9 (1982) 2554.
[2] T. Lu, X. Xu, S. Wu and F.T.S. Yu, Appl. Optics 29 (1990) 284.
[3] R.P. Lippman, IEEE ASSP Mag. 4-12, 1987.
[4] X. Yang and F.T.S. Yu, Appl. Optics 31 (1992) 3999.
[5] F.T.S. Yu, T. Lu, X. Yang and D.A. Gregory, Optics Lett. 15 (1990) 863.
[6] H. Kogelnik, Bell Syst. Tech. J. 48 (1969) 2909.
[7] P. Günter and J.P. Huignard, Photorefractive materials and their applications I (Springer, Berlin, 1988).
[8] S. Yin and F.T.S. Yu, IEEE Photonics Technology Lett. 5 (1993) 581.